Local and Global Features of Resonant Third-Order Interactions Amongst Surface Gravity Waves

Dylan Barratt

St Cross College

University of Oxford

A thesis submitted for the degree of

Doctor of Philosophy

July 2021

This thesis is dedicated to:

Ann Margaret Barratt and *Audrey Patton* for always supporting my education, *Seraina Anne Dual* for her love and encouragement, and *Tongbeum Kim* for igniting my interest in research.

Acknowledgements

I have been fortunate to enjoy the excellent supervision of Professor Thomas A. A. Adcock and Professor Ton S. van den Bremer during my time at the University of Oxford. I have been told that the foundations of a successful thesis rest upon two pillars, the topic and the supervisors. By this measure, my thesis has benefited from the firmest of foundations and I remain immensely grateful to my supervisors for their unwavering guidance and support. Professor Paul H. Taylor at The University of Western Australia has been a continuous source of insight and experience during this investigation; the influence of his ideas can be felt at numerous points in this thesis, strengthening the work in every instance. I have been reliant upon a particular simulation tool, *OceanWave3D*, to complete most of the simulations in this thesis and Professor Harry B. Bingham at the Technical University of Denmark (DTU) has been an invaluable collaborator in all matters of simulation. I unreservedly recommend *OceanWave3D* to anyone interested in the high-fidelity simulation of ocean waves. I began this thesis with no background in ocean wave mechanics and the discussions I have enjoyed with Peter S. Tromans of Ocean Wave Engineering Ltd. are amongst the most interesting and thought-provoking that I have experienced. This work has been made possible by the studentship I received from the Engineering and Physical Sciences Research Council (EPSRC) of the UK Government and I gratefully acknowledge further resources provided by the *DeRisk* project of Innovation Fund Denmark and the High Performance Computing (HPC) clusters at DTU.

Abstract

The formation of 'rogue' or 'freak' waves at the ocean surface is an important consideration for engineering design since such waves represent the worst-case scenario for structures in the ocean. Extreme wave events can be formed by the linear mechanism of dispersion, due to constructive interference between propagating wave components with different frequencies and directions. Nonlinear energy transfers between wave components can, however, alter the shape, kinematics and lifespan of an extreme wave event. The relative importance of linear and nonlinear mechanisms in the formation of extreme wave events remains an active area of interest. This thesis seeks to characterise the local nonlinear interactions which occur during the formation of an isolated group of steep surface gravity waves. We also consider the impact of steepness, finite depth, spreading and the spectral tail on the dominant interactions of an isolated wave group. To perform our investigation, we use a fully-nonlinear potential flow solver, *OceanWave3D*. We also perform simulations using the Modified Nonlinear Schrödinger (MNLS) equation of Trulsen et al. (2000, *Phys. Fluids*, vol. 12, pp. 2432–2437) and compare the results with *OceanWave3D* to assess the fidelity. Lastly, we simulate random seas and assess whether the global spectral changes are consistent with our local observations based on isolated wave groups. If an isolated wave group is narrow-banded, we find that the dominant interactions resemble a third-order degenerate quartet, resulting in energy transfers at $\pm 35^\circ$ to the spectral peak. As the wave spectrum broadens, the qualitative agreement with a degenerate quartet worsens and we observe energy transfers at $\pm 55^\circ$ to the spectral peak. We find that the the $\pm 35^\circ$ and $\pm 55^\circ$ energy transfers are both suppressed by finite depth but

the $\pm 35^{\circ}$ interactions are more severely suppressed, effectively disappearing at $k_p d = 1.36$. In contrast, the $\pm 55^{\circ}$ interactions are more resilient to a reduction in depth and remain prominent at $k_p d = 1.36$. An isolated wave event with high directional spreading will focus for a comparatively shorter amount of time due to linear dispersion, reducing energy transfers in an integral sense. We find that high directional spreading also tends to reduce the rate of energy transfer between wave components. Similarly, we find that truncation of the tail of the spectrum tends to augment the rates of energy transfer between wave components, accompanied by rapid redevelopment of the spectral tail. Thus, we concluded that directional spreading and the high-wavenumber tail of the spectrum play an important role in establishing a form of spectral equilibrium that reduces nonlinear energy transfers for an isolated wave event. Our comparison between the MNLS equation and *OceanWave3D* reveals that the MNLS equation generally captures the formation of an isolated wave group of surface gravity waves. However, the equation performs better if the linear dispersion relation is exact, rather than truncated at the fifth-order. The exact version of the dispersion operator also allows the arbitrary-depth linear dispersion relation to be included in the equation. We find that the classic MNLS equation of Trulsen et al. (2000) performs well at finite depths ($k_p d$) between 5.59 and 1.36 if the exact dispersion operator is combined with the the arbitrary-depth linear dispersion relation and the bottom boundary condition is applied at finite depth. Despite the existence of several intermediate-depth MNLS formulations, our results suggest that modification of the coefficients to the nonlinear terms is not required within this range of depths. Lastly, our simulations of random seas supports our observations based on isolated wave groups. We find that truncation of the spectral tail also tends to augment the energy transfers of a random sea, accompanied by redevelopment of spectral tail and augmented values of the free-surface kurtosis. Thus, we con-

clude that the spectral tail also plays an important role in establishing the spectral equilibrium of random seas and care should be taken when truncating the tail for the purposes of simulation/experiment. Our results suggest that the accumulation of local spectral distortions caused by individual wave groups could play an important role in determining the global spectral evolution of a random sea.

Contents

1 Introduction

The introduction outlines the motivation for this thesis and identifies several specific objectives that have been addressed. This thesis follows an integrated format where each chapter represents a separate full-length research paper. A complete list of publications is included in the introduction together with a synopsis of the thesis chapters.

1.1 Thesis Outline

Offshore structures, including wind turbines and wave energy devices, must be designed to withstand the loads imposed by ocean waves. An understanding of wave mechanics is also necessary to maximise the energy output and life expectancy of such devices. Ocean waves can be well-represented with linear mechanics if the waves are dispersed and not very steep, providing a simple means of analysis. However, steep waves can feature prominent nonlinear interactions that significantly influence the shape, lifespan and kinematics of a focused wave event. This thesis focuses on the nonlinear interactions which arise amongst steep ocean waves. This work is concerned exclusively with waves at the surface of the ocean, termed surface gravity waves, and the methods are based upon a constant density body of water as the propagation medium. Consideration is given to the characteristics of nonlinear interactions at the 'local' scale of an individual wave as well as the 'global' scale of a wave field. Four specific objectives have been identified:

1 *To characterise the nonlinear wave-wave interactions which dominate the spectral evolution of a steep wave group formed by dispersive focusing.*

2 *To determine the impact of steepness, finite depth, spreading and the spectral tail on the dominant nonlinear interactions of a steep wave group.*

3 *To assess the suitability of the Modified Nonlinear Schrödinger (MNLS) equation for simulating steep wave groups.*

4 *To determine whether our local observations, based on individual wave groups, are consistent with the global statistics of a random wave field.*

1.2 Synopsis of Thesis Chapters

The contents of the thesis chapters are described here in brief.

Chapter 2. Literature review

I have included an overview of fundamental wave theory with emphasis on the role of nonlinear wave-wave interactions.

Chapter 3. High-fidelity potential flow simulations of steep wave groups

I installed and configured the *OceanWave3D* simulation tool in our research group and used it to perform a series of high-fidelity potential flow simulations using the High Performance Computing (HPC) cluster of the Technical University of Denmark (DTU). I have performed a comprehensive assessment of the numerical error of the simulations, including the effect of: grid resolution, order of finite differencing, Courant-Friedrich-Lewy (CFL) condition, symmetry plane and the 'deep-water' assumption. I implemented a novel third-order correction for the initial conditions and also determined a way to minimise the formation of second-order error waves. I observed and investigated the occurrence of resonant third-order interactions and determined that the interactions are responsible for the formation of 'wing waves', obliquely propagating waves which form at the edge of the wave group and influence the group shape and kinematics. I confirmed that the wing waves are a physical process related to wave-wave interactions and not a numerical artefact using various numerical checks, including energy conservation and reversing the simulations.

Specific outcomes:

O3.1 Selected numerical parameters for the potential flow simulations including: grid size, order of finite differencing and Courant-Friedrichs-Lewy (CFL) condition.

O3.2 Verified the results against an HOS scheme and ensured energy conservation within 0.024% over the entirety of each simulation.

O3.3 Confirmed that the implemented symmetry plane adds negligible additional diffusivity despite the use of asymmetric stencils.

O3.4 Found that a depth of $k_p d = 5.592$ represents an adequate approximation for infinitely deep water in this application.

O3.5 Implemented an approximate correction scheme for the third-order bound harmonics and minimised the formation of both second and third-order error waves.

O3.6 Revealed that energy transfers at $\pm 35°$ to the spectral peak results in the formation of 'wing waves' and explained the impact on group shape.

O3.7 Confirmed that the observed spectral evolution is due to physical processes and not a numerical artefact by demonstrating that the simulations are reversible.

Chapter 4. Directional energy transfers due to nonlinear interactions

The results of chapter 3 provide confidence that the *OceanWave3D* simulations are a reliable means of analysis for steep groups of surface gravity waves. Based on further potential flow simulations, I explored some features of third-order interactions for a single test case, classifying the interactions and analysing growth-rates. I showed that the directional energy transfers, up until nonlinear focus, resemble a degenerate quartet, a form of narrow-banded interaction in which one of the participating components is repeated. However, after focus the comparison with a degenerate quartet worsens and non-degenerate interactions appear to dominate. I found that the third-order interactions augment the kinematics of the wave group by transferring energy to high-wavenumber components while extending the lifespan of the focused events. Access to kinematics data is a somewhat unique feature of *OceanWave3D* since most potential flow solvers avoid calculating the internal kinematics (Higher-Order Spectral (HOS) schemes only solve for parameters at the free surface, typically in waters of infinite depth). This chapter also considers the

effect of finite depth on the spectral evolution of steep wave groups since the three-dimensional domain of *OceanWave3D* allows the depth to be specified. I found that the quasi-degenerate and non-degenerate interactions exhibit different sensitivities to depth. While both forms of interaction are suppressed by a reduction in depth, the quasi-degenerate interactions are more severely suppressed and almost disappear for a depth of $k_p d = 1.363$, consistent with previous analytical results. The sensitivity of the quasi-degenerate interactions appears to be caused by detuning of the interactions by the return current which develops beneath the wave group (a Doppler-shift effect discussed in previous analytical studies and supported by our simulations). The depth of $k_p d = 1.363$ is a critical value for finite-depth effects since analytical results have predicted the complete suppression of third-order interactions for a unidirectional and monochromatic wave field at this depth. Our simulations of three-dimensional wave groups, in contrast, show that the non-degenerate interactions continue to occur at a depth of $k_p d = 1.363$ and dominate the evolution of the spectrum. Contraction of the spectrum in the k_y-direction has been associated by previous studies with the 'wall-of-water' effect, forming a steep, long-crested event. My simulations show that the spectral contraction in the k_y-direction persists at intermediate depths and, thus, the 'wall-of-water' effect may be expected to also occur at intermediate depths.

A major focus of chapter 4 is the emphasis upon *spectral equilibrium*—I consider features of the wave spectrum which tend to increase/reduce the rates of energy transfer between wave components. In particular, I investigated the effects of directional spreading and the high-wavenumber tail of the spectrum on the spectral evolution of focused wave groups. Increasing the directional spreading of a wave group reduces the focused time span of the wave group due to linear mechanisms. However, my results also indicate that the peak rate of energy transfer is reduced by directional spreading. Furthermore, my simulations indicate that the energy transfers of wave groups with low-spreading appear to be largely permanent, i.e., the changes do not reverse after focus, while the spectral changes of wave groups with high spreading appear to be largely temporary, i.e., many of the spectral changes

reverse after focus. Thus, my results suggest that sea states with low directional spreading will result in focused wave events with localised spectral distortions that contribute to the evolution of the sea state. In contrast, a sea state with high spreading will result in focused wave events with temporary localised distortions of the spectrum that contribute less significantly to the evolution of the sea state. Thus, spreading appears to be a feature of spectral equilibrium which reduces directional energy transfers during a focused wave event. Some studies also ignore the spectral tail, choosing to only include the wave components in the spectral peak, to simplify the analysis. My simulations indicate that removing the spectral tail causes the tail to redevelop during the simulation, augmenting the nonlinear features of the wave event and increasing the observed rates of energy transfer. Thus, the high-wavenumber tail also appears to be a feature of spectral equilibrium which reduces rates of energy transfer and the nonlinear features of a steep wave group. Ignoring the spectral tail in the generation of initial conditions for a simulation can lead to artificially augmented energy transfers. Physical processes which can suppress the development of the spectral tail also exist, e.g., ice sheets disproportionately dissipate the energy of high-wavenumber components, which could suppress the spectral tail. Wave blocking by currents can also suppress the spectral tail at a particular location, i.e., high-wavenumber components propagate slower than low-wavenumber components and a current flowing in the opposite direction can 'block' high-wavenumber components while allowing low-wavenumber components to propagate through, suppressing the spectral tail locally. Initial conditions which do not include the spectral tail should thus be treated with caution, while physical mechanisms which suppress the tail could result in higher rates of energy transfer and focused wave events with more prevalent nonlinear features.

Specific outcomes:

O4.1 Classified interactions as being quasi-degenerate during focus and non-degenerate after focus.

O4.2 Demonstrated and analysed augmented kinematics due to third-order interac-

tions.

O4.3 Showed that nonlinear interactions extend the lifespan of the focused wave groups.

O4.4 Provided additional supporting evidence that quasi-degenerate interactions are suppressed by depth due to detuning by the return current.

O4.5 Revealed that non-degenerate interactions are more depth resilient and and remain prevalent at the critical depth of $k_p d = 1.363$.

O4.6 Showed that the 'wall-of-water' effect still occurs in waters of intermediate depth.

O4.7 Showed that directional spreading reduces rates of energy transfer, in addition to reducing energy transfers in an integral sense.

O4.8 Showed that the spectral distortions of a steep wave group may be more permanent/temporary dependent upon the spreading of the background sea state.

O4.9 Demonstrated that ignoring the tail of the spectrum causes the tail to be redeveloped during the simulation, artificially augmenting energy transfers.

O4.10 Highlighted that physical mechanisms which suppress the spectral tail, e.g., ice sheets and currents, could result in higher rates of energy transfer during focused wave events.

Chapter 5. MNLS simulations of steep wave groups

The results of chapters 3 and 4 provide a database of high-fidelity potential flow simulations of focusing groups. I have used these results to test the suitability of the Modified Nonlinear Schrödinger (MNLS) equations of Trulsen & Dysthe (1996) and Trulsen *et al.* (2000) to simulate focused wave groups with directional spreading. The MNLS is significantly less computationally expensive than a potential flow solver—a case which requires 300 hours of CPU time with *OceanWave3D* can be done in approximately 30min with the MNLS equation. However, the MNLS equation assumes that the wave field can be represented by a modulated carrier wave.

Thus, the MNLS equation features bandwidth and spreading limits that may limit its applicability to engineering design. I coded my own pseudo-spectral solver for the MNLS equation and verified the solver with a series of numerical checks and comparisons against my potential flow simulations. I also implemented two different types of dispersion operator for the MNLS equation, based on exact and truncated versions of the linear dispersion relation, and assessed the performance of the two operators. The exact version of the dispersion operator has been presented by Trulsen *et al.* (2000) and the authors state that the exact operator should improve the resolution of four-wave interactions, reduce energy leakage and extend the bandwidth limits of the equation. To test the bandwidth limits, I deliberately introduced misalignment between the selected carrier wave of the MNLS equations and the direction of wave group propagation. I also selected characteristic wavenumbers for the carrier wave above and below the spectral peak. I found that the exact dispersion operator does significantly extend the bandwidth limits of the MNLS equation and also reduces energy leakage in certain cases. A comparison with our potential flow results confirmed that the MNLS simulations captured the most prominent physical processes that arose during nonlinear evolution, suggesting that the equation may be suitable for most engineering design purposes. As part of this chapter, I also tested the depth limits of the MNLS equation. Although the equation is typically used for waters of infinite depth, the bottom boundary condition does allow for a finite-depth domain. The exact dispersion operator of Trulsen *et al.* (2000) also allows arbitrary-depth linear dispersion relation to be used. I find that the MNLS equation provides excellent finite-depth results under these conditions, accurately capturing the spectral evolution of steep wave groups at depths as shallow as $k_p d = 1.363$. This result is particularly surprising since a variety of finite-depth MNLS formulations have been developed and these formulations typically modify the coefficients of the nonlinear terms, reducing the magnitude of the coefficients as depth decreases. Our results suggest that modification of the coefficients for the nonlinear terms is not necessary for depths in the range of $k_p d$ between 5.592 and 1.363—implementation of the arbitrary-depth dispersion relation and application of the bottom-boundary

condition at finite depth appear to suffice. Application of the bottom boundary condition at finite depths primarily influences the return current that develops beneath the wave group. Strengthening of the return current is known to suppress the modulation instability due to 'detuning', which effectively reduces nonlinear energy transfers as depth decreases. Our results suggest that the MNLS equation can capture this physical process without further modifications to the coefficients of the nonlinear terms if the dispersion operator and bottom boundary conditions have been appropriately configured.

Specific outcomes:

O5.1 Found that the exact and truncated versions of the MNLS dispersion operator both perform well if the carrier wave is aligned with the direction of wave propagation and the characteristic wavenumber coincides with the spectral peak.

O5.2 Revealed that the truncated dispersion operator is however slightly more diffusive, reducing the amplitude at focus by 1% compared with the exact operator.

O5.3 Demonstrated that the exact dispersion operator significantly enhances the bandwidth limits of the equation if the carrier wave is misaligned with the wave direction or the characteristic wavenumber does not coincide with the spectral peak.

O5.4 Determined that the truncated dispersion operator peforms well if the misalignment between the carrier wave and direction of wave propagation is less than 10°.

O5.5 Found that the truncated operator is particularly sensitive to the selection of the carrier wavenumber, with aggravated energy leakage if a characteristic wavenumber below the spectral peak is selected.

O5.6 Determined that the exact dispersion operator peforms well if the misalignment between the carrier wave and direction of wave propagation is less than 30°.

O5.7 Showed that the exact dispersion operator shows almost no sensitivity to the selection of the carrier wavenumber up to 10% above/below the spectral peak.

O5.8 Found that the MNLS formulation of Trulsen *et al.* (2000) performs well for $k_p d$ between 5.592 and 1.363 if the arbitrary-depth dispersion relation is used and the bottom boundary condition is applied at finite depth.

Chapter 6. MNLS simulations of random seas

The results of chapter 5 effectively verify my MNLS code and I have used the code to simulate random seas with the results presented in chapter 6. Random seas capture certain effects not incorporated by a wave group based on quasi-determinism, including the natural variability of dispersive focusing, proximity between multiple wave groups and the global evolution of the background sea state. In particular, I investigate the impact of the spectral tail on the kurtosis evolution of random seas. Chapter 4 demonstrates that the spectral tail can play a significant role in creating a form of *spectral equilibrium* that suppresses nonlinear energy transfers at the local scale of an individual wave event. In chapter 6, I investigate whether the spectral tail can significantly influence the nonlinear energy transfers at the global scale of a random sea. I focus upon the dynamic kurtosis of the free surface because this parameter is indicative of the build-up of phase correlation, an immediate consequence of nonlinear energy transfers between wave components. Our results indicate that the spectral tail does significantly impact the kurtosis evolution of random seas. I define a narrow-banded wave spectrum and truncate the tail at two different wavenumbers. For the 'Short Tail' (ST) case, I truncate the tail at $2.4k_p$, where k_p represents the wavenumber of the spectral peak. For the 'Long Tail' (LT) case, I truncate the tail at $6k_p$. I find that case ST exhibits a kurtosis peak that is 10% higher than case LT. The augmented kurtosis for case ST is accompanied by spectral changes that are more prominent and more rapid than those of case LT. I observe that case ST redevelops the spectral tail during the simulation and develops directional spreading in the tail during to directional energy transfers, consistent with our observations based on an individual wave group. Thus, I find that the

spectral tail also plays in important role in the spectral equilibrium of a random sea. Fedele (2015) provided a theoretical model for the evolution of dynamic kurtosis in random seas with directional spreading. I compare our kurtosis results for cases ST and LT with the theory of Fedele (2015) and find that the model provides an excellent estimate of the peak kurtosis value. However, I find that the bandwidth parameter used in the theory of Fedele (2015) must account for the spectral tail to capture the differences between cases ST and LT. I find that the bandwidth parameter proposed by Goda (1985) appears to be suitable for this purpose.

Ultimately, I have investigated the impact of third-order resonance between wave components at two different scales in this thesis, the local scale of an individual wave event (chapters 3, 4 and 5) as well as the global scale of a random sea (chapter 6). I find that the features of spectral equilibrium may be shared between these two different scales, creating conditions that augment or reduce nonlinear energy transfers at both the local and global scales.

Specific outcomes:

O6.1 Demonstrated that truncation of the spectral tail can impact the kurtosis evolution of random seas.

O6.2 Found that augmented kurtosis due to truncation of the tail is accompanied by more prominent and more rapid spectral changes due to nonlinear energy transfers, including downshifting of the spectal peak and an increase in bandwidth.

O6.3 Revealed that the truncated tail tends to redevelop during the simulation accompanied by an increase in directional spreading due to directional energy transfers in the tail.

O6.4 Concluded that the spectral tail does play an important role in the spectral equilibrium of a random sea and truncation of the tail for simulation/experiment should be handled with care to avoid artificially augmented energy transfers.

O6.5 Confirmed that the MNLS equation with an exact dispersion operator can

be assumed to estimate the kurtosis evolution of random seas despite the bandwidth limits of the equation.

O6.6 Determined that the theory of Fedele (2015) provides an excellent estimate for the peak kurtosis value if the bandwidth parameter accounts for the spectral tail.

O6.7 Demonstrated that the bandwidth parameter of Goda (1985) appears to provide a suitable choice, consistent with the recommendations of Serio *et al.* (2005).

Appendix A. Comparison of methods for removing the bound harmonics

In this thesis, I have extensively investigated the energy transfers which occur between free wave components due to third-order resonant interactions. To analyse such energy transfers, the free wave components must be isolated from the higher-order bound harmonics which arise amongst steep waves. I have used the method of *phase separation* first implemented by Baldock *et al.* (1996) and later used by Gibbs & Taylor (2005). I specifically use the four-phase version of phase separation as described by Fitzgerald *et al.* (2014). In Appendix A, I compare the four-phase technique against another method for removing the bound harmonics, based on a three-dimensional (3D) fast Fourier transform. The comparison is based upon our own wave group simulations with OceanWave3D, as described in chapters 3 and 4. I show excellent agreement between the two techniques for removing the bound harmonics, verifying our implementation of the phase separation technique. Thus, our analysis of the free-wave components, as described in chapters 3 and 4, features negligible contamination by bound harmonics. Note that the MNLS formulation entirely excludes bound harmonics, thus the phase separation technique is not used in chapters 5 and 6.

1.3 List of Publications

The contents of chapters 3, 4 and 5 have already been published as peer-reviewed journal papers and the contents of chapter 6 will soon be submitted. Appendix A

has also been published as a peer-reviewed conference paper. Thus, I have published three first-author journal papers and one first-author conference paper based on this thesis, at the time of submission.

Chapter 3 (published)

Barratt, D., Bingham, H. B., and Adcock T. A. A. (2020) Nonlinear evolution of a steep, focusing wave group in deep water simulated with *OceanWave3D*. *J. Offshore Mech. Arct. Eng.* **142**, 021201. https://doi.org/10.1115/1.4044989

Chapter 4 (published)

Barratt, D., Bingham, H. B., Taylor, P. H., van den Bremer, T. S., and Adcock T. A. A. (2020) Rapid spectral evolution of steep surface wave groups with directional spreading. *J. Fluid Mech.* **907**, A30.
https://doi.org/10.1017/jfm.2020.835

Chapter 5 (published)

Barratt, D., van den Bremer, T. S., and Adcock T. A. A. (2021) MNLS simulations of surface wave groups with directional spreading in deep and finite depth waters. *J. Ocean Eng. Mar. Energy* **7**, pp. 261–275.
https://doi.org/10.1007/s40722-021-00201-2

Chapter 6 (to be submitted)

Barratt, D., van den Bremer, T. S., and Adcock T. A. A. (2021) The impact of the spectral tail on the kurtosis of random seas.

Appendix A

Barratt, D., Bingham, H. B., Taylor, P. H., van den Bremer, T. S., and Adcock T. A. A. (2020) Linearization of the Wave Spectrum: A Comparison of Methods. 39^{th} *International Conference on Ocean Offshore and Arctic Engineering* (OMAE2020). Paper No. 18820. https://doi.org/10.1115/OMAE2020-18820

Note: Barratt et al. (2020, *J. Offshore Mech. Arct. Eng.*, 142) was nominated for the Best Paper Award at the OMAE2019 conference and an abstract based on Barratt et al. (2020, *J. Fluid Mech.*, 907) also won the Tuck Fellowship award at the IWWWFB20 conference.

2 Literature Review

The design of offshore structures relies upon accurate estimations of wave crest height and kinematics, for the assessment of loads. The formation of extreme ocean waves, sometimes termed 'rogue' or 'freak' waves, thus remains a topic of interest as the 'worst case scenario' a structure may encounter in the ocean. Nonlinear interactions between wave components can result in rapid spectral changes influencing the shape, kinematics and lifespan of a wave event. In this literature review, some of the characteristic features of nonlinear wave-wave interactions are presented. The focus is restricted to surface gravity waves propagating through water.

2.1 Terminology

Several terms of particular importance are defined in this subsection:

- *Isolated wave group*: A single wave group surrounded by otherwise quiescent water. We calculate the linear components of the wave groups using an inverse Fourier transform. Thus, the wave field is homogeneous in space. We tune the phases of the individual linear components to form the wave group with constructive interference while the surface elevation tends to zero away from the location of the wave group. Figure 2.1 depicts an example of the isolated wave groups considered in this thesis.

- *Focusing wave group*: In this study, we consider wave groups formed by dispersive focusing. We calculate the linear wave field at the time of focus—the time at which all the linear wave components are in-phase at one spatial location. We then use the linear dispersion relation to 'rewind' the linear components in time, calculating the wave field several wave periods before focus is expected to occur, providing the initial conditions for our simulations. Exact second order correction and an approximate third order correction are then applied to the surface elevation and velocity potential to account for the bound harmonics. The wave field is then marched forward in time with a nonlinear solver.

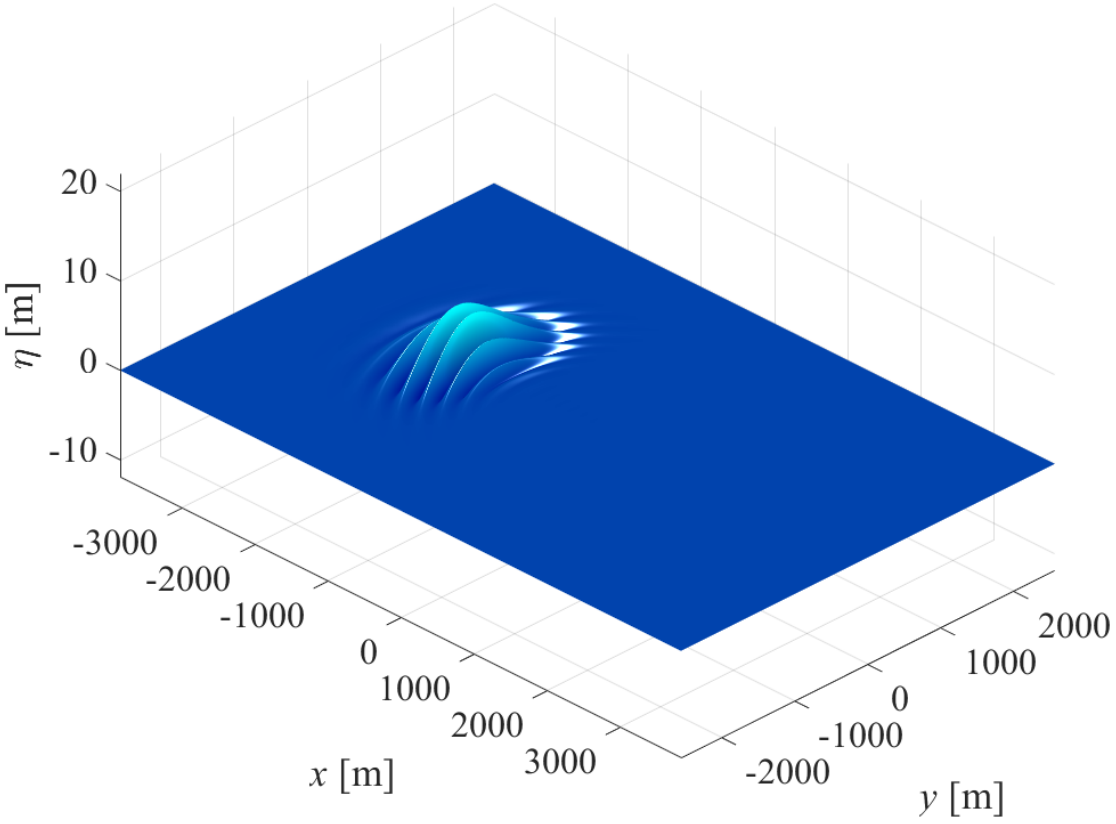

Figure 2.1: Surface elevation (η) of an isolated wave group calculated 20 characteristic wave periods (T_p) before focus.

- *Wall-of-water effect*: observed by Gibbs & Taylor (2005), the 'wall-of-water' effect refers to the change in group shape that can occur for a steep wave group due to nonlinear interactions. Gibbs & Taylor (2005) as well as Adcock & Taylor (2016) observed that the bandwidth of the wave spectrum tends to increase in the k_x-direction as the wave group approaches focus, causing the wave group to contract in the direction of propagation. Simultaneously, Gibbs & Taylor (2005) and Adcock & Taylor (2016) observed that the bandwidth of the spectrum tends to reduce in the k_y-direction, causing the wave group to broaden laterally. Both studies also observed that the largest crest tends to move towards the front of the wave group, preceded by a relatively shallow trough. The combined effect of longitudinal contraction, lateral broadening and a large crest at the front of the group has been termed the 'wall-of-water' effect.

- *Wing wave*: a feature due to nonlinear interactions, influencing the shape of

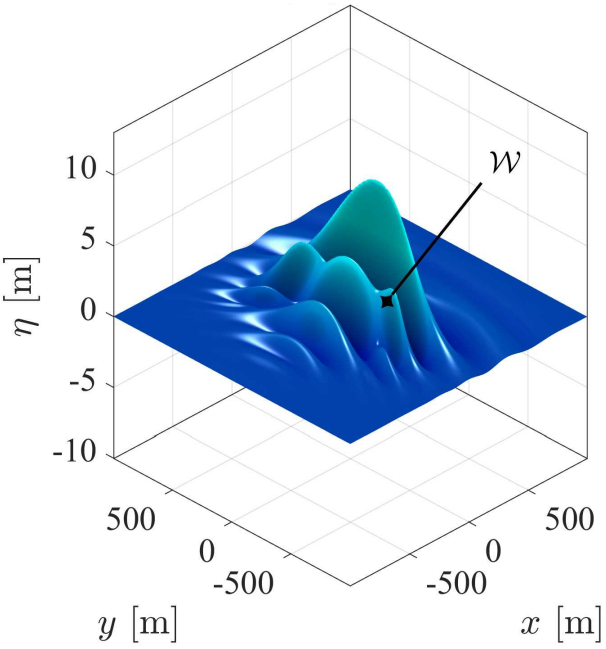

Figure 2.2: 'Wing waves' (denoted by $\mathcal{W}$) formed at the edge of a wave group due to energy transfers to oblique components.

a wave group. We have observed that energy transfers to oblique components results in the formation of shoulder-like protrusions at the edge of the wave group. Figure 2.2 depicts an example of wing waves for an isolated wave group. The wing waves propagate at an oblique angle to the wave group at a speed which is slower than the group speed.

- *Exact dispersion operator*: This thesis incorporates two versions of the Modified Nonlinear Schrödinger (MNLS) equation: presented in Trulsen & Dysthe (1996) and Trulsen *et al.* (2000) respectively. Both formulations use the linear dispersion relationship to relate the frequency (ω) and wavenumber (k) of each wave component, $\omega^2 = gk$, based on the gravitational constant g. Both formulations also require that an inverse Fourier transform in terms of wavenumber (k) be applied to a temporal evolution equation based on ω to calculate the dispersion operator. Trulsen & Dysthe (1996) use a Taylor series expansion to express ω in terms of k based on the linear dispersion relation, truncating the series at the fifth order followed by an analytical inverse Fourier transform—thus, we refer to the dispersion operator of Trulsen & Dysthe (1996) as 'truncated'. In contrast, Trulsen *et al.* (2000) directly evaluate the inverse Fourier transform with numerical methods, avoiding truncation

of the linear dispersion relation—thus, we refer to the dispersion operator of Trulsen *et al.* (2000) as 'exact'. The Taylor series approach of the truncated operator is bandwidth limited, i.e., the dispersion operator becomes less accurate for wave components away from the characteristic wavenumber. In contrast, the exact dispersion operator is not bandwidth limited, improving the resolution of dispersion for the full wave spectrum.

- *Local and global scales*: in this thesis, the 'local scale' refers to the spatial scale of an individual wave group, typically around 3–10 characteristics wavelengths (λ_0) or approximately 1 km. The 'global scale' refers to the spatial scale of a random sea, typically around 90–140 characteristics wavelengths (λ_0) or approximately 20–30 km.

- *Narrowbanded and broadbanded wave groups*: these terms refer to the bandwidth of the wave spectrum and are, in practice, somewhat qualitative. The wave spectrum is obtained by performing a two-dimensional Fourier transform on the surface elevation of the wave field. A 'narrowbanded' wave spectrum is characterised by a concentration of large amplitude wave components around a spectral peak, resulting in a comparatively small bandwidth. In contrast, a 'broadbanded' wave spectrum is characterised by a more even distribution of amplitudes around a larger number of wave components, including components with a significantly different wavenumber to the spectral peak.

- *Quasi-degenerate and non-degenerate interactions*: This thesis is focused on the lowest order of nonlinear interaction that can arise for surface gravity waves in deep water, third order interactions. Such interactions arise between four wave components (k_1, k_2, k_3, k_4) which fulfil a set of two resonance conditions first described by Phillips (1960). A simplified version of four-wave interaction is the *degenerate* interaction which includes only three unique wave components, i.e., one of the wave components participates twice in the interaction ($k_1 = k_2$). In this thesis, we consider a class of interaction we term *quasi-degenerate*; this interaction consists of four unique wave components but two

of the components possess a similar wavenumber ($k_1 \approx k_2$). Lastly, we consider non-degenerate interactions which consist of four wholly unique wavenumber components ($k_1 \neq k_2 \neq k_3 \neq k_4$).

- *Spectral equilibrium*: this expression refers to attributes of the wave spectrum that tend to reduce the rates of energy transfer between wave components. For example, a typical wave spectrum tends to include a large number of high-wavenumber components with a small amplitude in the 'tail' of the spectrum. The combined energy of these components may only account for a small percentage of the total energy of the wave-field. However, the presence/absence of these components can have a significant impact on the rates of energy transfer within the wave spectrum, as this thesis demonstrates. Thus, the presence of the tail components can be said to reduce the rate at which the wave spectrum changes, contributing to the equilibrium of the spectrum.

2.2 Potential Flow Treatment of Surface Gravity Waves

This thesis relies upon simulations of ocean waves as a means of investigation and all of the simulation tools are based upon potential flow, described here briefly. For an incompressible Newtonian fluid, mass conservation yields the continuity equation:

$$\nabla \cdot \boldsymbol{u} = 0, \tag{2.1}$$

and momentum conservation yields the Navier-Stokes (NS) equations:

$$\frac{\partial \boldsymbol{u}}{\partial t} + \boldsymbol{u} \cdot \nabla \boldsymbol{u} = -\frac{\nabla P}{\rho} + \nu \nabla^2 \boldsymbol{u} + g, \tag{2.2}$$

where $\boldsymbol{u}$ denotes the three-dimensional velocity vector and P denotes the scalar mechanical pressure for a fluid of density ρ and kinematic viscosity ν. Here, ∇ represents the *del operator*, $\nabla = (\partial/\partial x, \partial/\partial y, \partial/\partial z)$. The governing equations can be greatly simplified by invoking the physical assumption of *irrotationality*, $\nabla \times \boldsymbol{u} = 0$, which implies that fluid particles do not rotate about their own principal axes.

The advection term in (2.2) can, thus, be simplified by the vector identity:

$$\boldsymbol{u} \cdot \nabla \boldsymbol{u} = \frac{1}{2}\nabla(\boldsymbol{u} \cdot \boldsymbol{u}) - \boldsymbol{u} \times \cancelto{0}{(\nabla \times \boldsymbol{u})}. \tag{2.3}$$

Furthermore, the combined conditions of incompressibility ($\nabla \cdot \boldsymbol{u} = 0$) and irrotationality ($\nabla \times \boldsymbol{u} = 0$) render the diffusion term in (2.2) identically zero, as can be seen from the vector identity:

$$\nabla^2 \boldsymbol{u} = \nabla\cancelto{0}{(\nabla \cdot \boldsymbol{u})} + \nabla \times \cancelto{0}{(\nabla \times \boldsymbol{u})}. \tag{2.4}$$

The simplified governing equations can, thus, be reformulated for mathematical convenience in terms of a 'velocity potential' (ϕ) scalar function, $\boldsymbol{u} = \nabla\phi(x, y, z, t)$, which yields the Laplace equation as the condition for continuity throughout the physical domain,

$$\nabla^2\phi = 0 \quad \text{for} \quad -\infty < z < \eta, \tag{2.5}$$

forming an elliptic boundary value problem that reduces momentum conservation to a dynamic boundary condition applied at the free-surface,

$$\frac{\partial\phi}{\partial t} + g\eta + \frac{1}{2}\nabla\phi \cdot \nabla\phi = 0 \quad \text{at} \quad z = \eta, \tag{2.6}$$

accompanied by another free-surface boundary condition which ensures that fluid particles at the free-surface remain at the free surface:

$$\frac{\partial\eta}{\partial t} + \nabla\phi \cdot \nabla\eta = \frac{\partial\phi}{\partial z} \quad \text{at} \quad z = \eta. \tag{2.7}$$

For the scenario of 'deep water', an asymptotic boundary condition is also applied at the bottom of the domain specifying no-normal-flow (an impermeable end-wall/seabed):

$$\frac{\partial\phi}{\partial z} \to 0 \quad \text{at} \quad z \to -\infty. \tag{2.8}$$

Equations (2.5) to (2.8) form the governing equations of potential flow and have been used extensively to model and analyse ocean waves. The primary difficulties

of solving (2.5) to (2.8) arise from the *a priori* unknown location of the surface elevation (η) as well as the nonlinearity of the free-surface boundary conditions (2.6) and (2.7).

2.3 Energy Conservation for Surface Gravity Waves

The total energy of a potential flow field is a conserved quantity, in the abscence of external forcing such as surface tension, wind-energy input and energy dissipation by breaking. The total energy within a volume ($\mathcal{V}$) may, thus, be decompartmentalised into kinetic energy (E_K):

$$E_K = \frac{1}{2}\rho \int\int\int |\nabla\phi|^2 \mathrm{d}\mathcal{V}, \tag{2.9}$$

and potential energy (E_P):

$$E_P = \frac{1}{2}\rho g \int\int \eta^2 \mathrm{d}s, \tag{2.10}$$

subject to the constraint:

$$\frac{\mathrm{d}}{\mathrm{d}t}[E_K + E_P] = 0. \tag{2.11}$$

For convenience, the volume integral expressed in (2.9) may be reformulated in terms of a surface integral, allowing both the kinetic and potential energy to be evaluated at the free-surface with no regard for the interior domain. Combination of a vector identity with the continuity condition,

$$\nabla \cdot (\phi(\nabla\phi)) = \phi\nabla \cdot (\nabla\phi) + \nabla\phi \cdot \nabla\phi, \tag{2.12}$$

yields:

$$E_K = \frac{1}{2}\rho \int\int\int \nabla \cdot (\phi(\nabla\phi))\mathrm{d}\mathcal{V}, \tag{2.13}$$

which can be reformulated in terms of Gauss's divergence theorem and the exact kinematic free-surface boundary condition to obtain a surface integral that can be evaluated numerically:

$$E_K = \frac{1}{2}\rho \int\int \phi\big|_{z=\eta} \frac{\partial\eta}{\partial t}\,\mathrm{d}s. \tag{2.14}$$

2.4 Linear Theory and Gaussian Seas

The linear theory of surface gravity waves seeks to describe the free-surface as a summation of independent propagating harmonics, as explained by Holthuijsen (2007). Variation of the surface elevation (η) in space (x, y) and time (t) can, thus, be described by a superpositioning process:

$$\underline{\eta}(x, y, t) = \sum_{i}^{N} \sum_{j}^{M} \underline{a}_{ij} \cos(\omega_i t - k_i x \cos\theta_j - k_i y \cos\theta_j + \underline{\alpha}_{ij}), \tag{2.15}$$

with random sampling of the component amplitudes ($\underline{a}_{ij}$) and phases ($\underline{\alpha}_{ij}$) from a Raleigh distribution and uniform distribution respectively while the direction of propagation (θ_j) is determined by the spread of the underlying spectrum. Consequently, the surface elevation at a particular point in space or time is also a randomly distributed variable ($\underline{\eta}$) following a Gaussian distribution. Furthermore, the angular frequency (ω) and wavenumber (k) share the same index (i) since the linear dispersion relationship, $\omega^2 = gk \tanh kd$, prescribes a unique relationship between frequency and wavenumber for a given depth (d) and gravitational acceleration (g). Two further fundamental assumptions underlie the linear approach: (1) 'stationarity' of the wave spectrum in time and (2) 'homogeneity' of the wave spectrum in space. Energy transfer between wave components, which would cause a transient and localised alteration of the wave spectrum, is thus precluded by linear theory and all harmonics are expected to propagate in agreement with the linear dispersion relationship. The superpositioning process expressed in (2.15), in terms of surface elevation, yields an exact solution to the Laplace equation in (2.5), in terms of velocity potential. Linear theory, thus, conserves mass exactly. However, linear theory only satisfies a first-order approximation to the free-surface boundary conditions (2.6) and (2.7).

2.5 Exact Second-Order Theory

Higher-order approaches to satisfying the free-surface boundary conditions (2.6) and (2.7) result in the appearance of 'bound harmonics' which do not obey the linear

dispersion relationship. However, at the second order, energy transfer between components does not occur since resonant triad interactions are not possible for surface gravity-waves in deep water, as noted by Phillips (1960). Thus, the assumptions of stationarity and homogeneity of the wave spectrum remain valid according to second-order theory. Exact formulations based on the mode-coupling approach have been provided by Longuet-Higgins (1962), Sharma & Dean (1981), Dalzell (1999) and Forristall (2000) to calculate the second-order bound harmonics corresponding to a linear wave spectrum, which provides a complete description of second-order theory. The potential flow solver *OceanWave3D* requires a numerical domain of finite extent and, thus, cannot simulate surface waves in infinitely deep water. Dalzell (1999) provides a finite-depth (d) version of second-order theory that considers two intersecting wave trains (indexed as $j = 1, 2$) and provides expressions for both surface elevation and velocity potential, both adopting a similar form. The form of the second-order velocity potential, for two intersecting waves, can be expressed in an expanded form using the notation of Longuet-Higgins (1962):

$$\phi = [\alpha\phi_{10} + \beta\phi_{01}]\big|_{z=\eta} + [\alpha^2\phi_{20} + \beta^2\phi_{02}]\big|_{z=0} + [\alpha\beta\phi_{11}]\big|_{z=0} \,, \tag{2.16}$$

featuring the first-order linear harmonics (ϕ_{10}, ϕ_{01}) of the two waves which should be evaluated at the free-surface ($z = \eta$), to avoid second-order error waves, and can be calculated with the finite-depth expression of Dalzell (1999):

$$[\alpha\phi_{10} + \beta\phi_{01}] = \sum_{j=1}^{2} a_j \frac{g}{\omega_j} \frac{\cosh\{|k_j|(z+d)\}}{\cosh\{|k_j|d\}} \sin\psi_j. \tag{2.17}$$

and a phase (ψ_j) variation, for each of the two 'free' waves,

$$\psi_j = \omega_j t - k_j x\cos\theta_j - k_j y\cos\theta_j + \alpha_j, \tag{2.18}$$

that adheres to the linear dispersion relationship, which remains valid for second-order theory.

Self-interaction terms of the second order (ϕ_{20}, ϕ_{02}) also appear in the expanded form

of (2.16) and should be evaluated at the mean water level ($z = 0$). However, second-order self-interactions are negligible for depths approaching the deep-water limit, as indicated by the quartic power of the exponential function in the denominator:

$$[\alpha^2\phi_{20} + \beta^2\phi_{02}] = \sum_{j=1}^{2} a_j^2 \frac{3\omega_j}{8} \frac{\cosh\{2|k_j|(z+d)\}}{\sinh^4\{|k_j|d\}} \sin(2\psi_j). \tag{2.19}$$

Lastly, second-order cross-interactions (ϕ_{11}) between the two intersecting waves appear in the expanded form of (2.16), also for evaluation at the mean water level ($z = 0$). Significant bound harmonics can arise from cross-interactions between steep waves, even in deep-waters, and can be categorised into two types:

$$\begin{aligned}[\alpha\beta\phi_{11}] = {} & a_1 a_2 A_p(k_1, k_2) \frac{\cosh\{|k_1 + k_2|(z+d)\}}{\cosh\{|k_1 + k_2|d\}} \sin(\psi_1 + \psi_2), \qquad \textit{Superharmonics,} \\ & + a_1 a_2 A_m(k_1, k_2) \frac{\cosh\{|k_1 - k_2|(z+d)\}}{\cosh\{|k_1 - k_2|d\}} \sin(\psi_1 - \psi_2), \qquad \textit{Subharmonics,}\end{aligned} \tag{2.20}$$

where the functional coefficients A_p and A_m are known as 'interaction kernels' with a complete mathematical description in Dalzell (1999). The phase of neither the *superharmonics*, $\psi_1+\psi_2$, nor the *subharmonics*, $\psi_1-\psi_2$, adhere to the linear dispersion relationship and propagate with a dynamic governed by the free wave components. The *superharmonics* manifest with an effective wavenumber of k_1+k_2 and, thus, appear as a short-wavelength modification to the linear velocity potential. Conversely, the *subharmonics* manifest with an an effective wavenumber of $k_1 - k_2$ and, thus, appear as a long-wavelength modification to the linear velocity potential. The larger length scale of the subharmonics results in greater depth sensitivity than observed for the superharmonics. Figure 2.3 depicts the second-order velocity potential for a focused wave group, used as the initial condition for potential flow simulations of an extreme wave in this thesis, and calculated with the expressions of Dalzell (1999). Two cases of finite depth have been plotted, $k_p d = 5.6$ and $k_p d = 22.4$, both considered to be in 'deep water' ($k_p d > \pi$). As can be seen, a small but discernible difference exists between the two deep-water cases, on the scale of the wave-group,

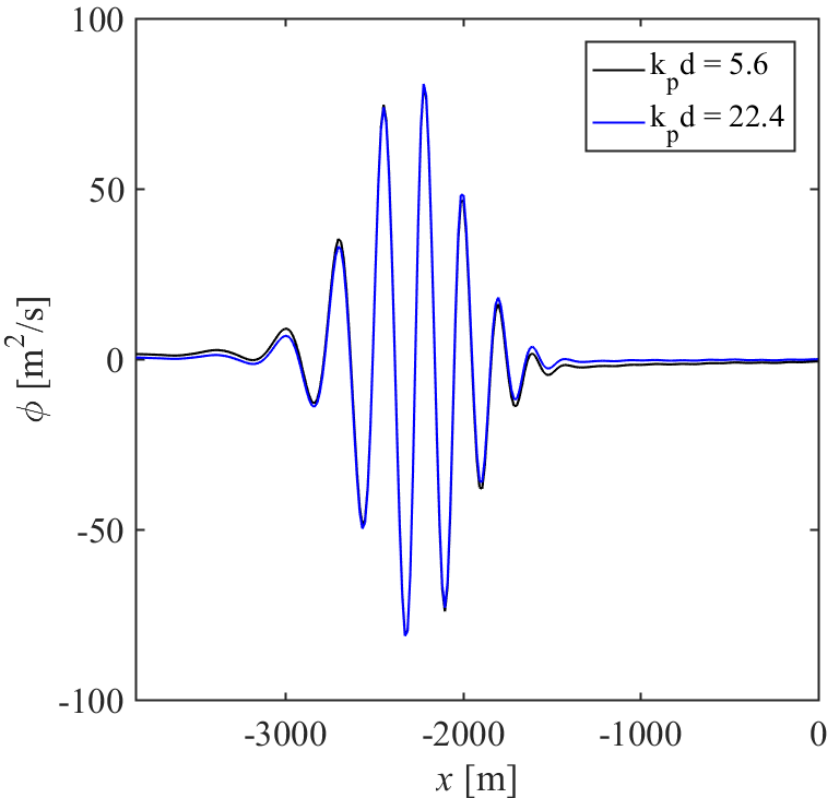

Figure 2.3: Second-order velocity potential for a focused wave group using the formulation of Dalzell (1999) for finite-depth cases of $k_p d = 5.6$ and $k_p d = 22.4$.

demonstrating the depth sensitivity of the second-order subharmonics.

2.6 Approximate Third-Order Bound Wave Theory

A third-order approach to satisfying the free-surface boundary conditions results in the appearance of more bound harmonics than described by second-order theory. However, the possibility of energy transfer between components of the wave spectrum also arises in the form of resonant quartet interactions, as described by Phillips (1960). Evolution of the wave spectrum due to resonant third-order interactions significantly influences the formation of an extreme wave, a central theme of this thesis, and the fully-nonlinear potential flow code *OceanWave3D* has been shown to accurately capture third-order resonance effects. An exact description of the third-order bound harmonics, based on the perturbation expansion approach, has also been presented by Madsen & Fuhrman (2012). However, an approximate description of the third-order bound harmonics is sufficient for correction of the initial conditions for the simulations since the third-order harmonics are small for the initially dispersed group and the absolute error, thus, negligible. An approximation

for the third-order bound harmonics has also been proposed by Walker *et al.* (2004) based on a Stokes-type expansion for a regular wave, shown here to the third order for the surface elevation (η):

$$\eta(t) = a\cos\theta(t) + C_{22}a^2\cos 2\theta(t) + C_{31}a^3\cos\theta(t) + C_{33}a^3\cos 3\theta(t), \tag{2.21}$$

where a and $\theta(t)$ are the amplitude and phase describing the linear surface (η_L):

$$\eta_L(t) = a\cos\theta(t). \tag{2.22}$$

The coefficients, C, encapsulate the depth-sensitivity of each term and a complete list can be found in Appendix A of Walker *et al.* (2004). Approximations for the third-order terms in the Stokes expansion have also been provided by Walker *et al.* (2004) in terms of the *Hilbert transform*, denoted by $\mathcal{H}$, which introduces a 90° phase-shift into the operand. The third-order *principal harmonic* of surface elevation (η_{31}) can, thus, be approximated as:

$$\begin{aligned}\eta_{31} &= C_{31}a^3\cos\theta(t) \\ &= -\frac{3(1+3S+3S^2+2S^3)}{8(1-S)^3}k_0^2\eta_L(\eta_L^2 + [\mathcal{H}\{\eta_L\}]^2),\end{aligned} \tag{2.23}$$

and the third-order *superharmonic* of surface elevation (η_{33}) as:

$$\begin{aligned}\eta_{33} &= C_{33}a^3\cos 3\theta(t) \\ &= +\frac{3(1+3S+3S^2+2S^3)}{8(1-S)^3}k_0^2\eta_L(\eta_L^2 - 3[\mathcal{H}\{\eta_L\}]^2),\end{aligned} \tag{2.24}$$

where $S = \mathrm{sech}(2k_0d)$ and k_0 is the characteristic wavenumber.

The corresponding velocity potential associated with the third-order surface elevation terms may be obtained with a scaling argument. Noting the scaling relation

between velocity potential and surface elevation, described by Lannes (2013):

$$\phi \sim \frac{g}{\omega}\eta, \tag{2.25}$$

and the 90° phase-shift expected between surface elevation and velocity potential, an approximation can, thus, be obtained for the third-order principal harmonic of the velocity potential (ϕ_{31}):

$$\phi_{31} = D_{31}\frac{g}{\omega_0}\mathcal{H}\{\eta_{31}\}, \tag{2.26}$$

as well as the third-order superharmonic of the velocity potential (ϕ_{33}):

$$\phi_{33} = D_{33}\frac{g}{\omega_0}\mathcal{H}\{\eta_{33}\}, \tag{2.27}$$

where ω_0 is the characteristic frequency and the coefficients D_{31} and D_{33} are proportionality constants which may be set to unity or tuned according to numerical/experimental data.

2.7 Resonant Third-Order Interactions

Exact third-order resonance for deep-water waves has been shown by Phillips (1960) to occur between four wave components that satisfy the conditions:

$$\boldsymbol{k}_1 \pm \boldsymbol{k}_2 \pm \boldsymbol{k}_3 \pm \boldsymbol{k}_4 = 0, \tag{2.28}$$

and with the same combination of signs,

$$\omega_1 \pm \omega_2 \pm \omega_3 \pm \omega_4 = 0, \tag{2.29}$$

consistent with the deep-water linear dispersion relationship,

$$\omega_i{}^2 = gk_i. \tag{2.30}$$

Here, the wavenumber and angular frequency of each component are denoted with $\boldsymbol{k}_i$ and ω_i and the gravitational constant is denoted with g. Third-order resonance allows energy to be transferred between wave components, altering both the component amplitudes and phase speeds. This thesis extensively investigates the impact of third-order resonance on the evolution of steep wave groups, as well as the evolution of random seas.

2.8 Degenerate and Quasi-Degenerate Quartets

A quartet of interacting wave components is termed 'degenerate' if only three unique wave components are involved—one of the components participates twice in the interaction (e.g., $\boldsymbol{k}_1 = \boldsymbol{k}_2$). A degenerate quartet forms the basis of stability analyses for a regular/monochromatic wave, assuming that $\boldsymbol{k}_1$ and $\boldsymbol{k}_2$ both equate to the characteristic wavenumber $\boldsymbol{k}_0$ of the regular wave. The remaining two components, $\boldsymbol{k}_3$ and $\boldsymbol{k}_4$, act as lower and upper sidebands which ultimately result in instability. In this thesis, we focus upon narrow-banded JONSWAP and Gaussian wave spectra. The concentration of energy around the spectral peak means that we anticipate interactions in which $\boldsymbol{k}_1$ and $\boldsymbol{k}_2$ resemble the characteristic wavenumber $\boldsymbol{k}_0$ (the wavenumber of the spectral peak) but may not strictly equate, i.e., we expect $\boldsymbol{k}_1 \approx \boldsymbol{k}_2 \approx \boldsymbol{k}_0$ for our narrow-banded wave groups, rather than $\boldsymbol{k}_1 = \boldsymbol{k}_2 = \boldsymbol{k}_0$ as expected for a regular/monochromatic wave. Interactions of the form $\boldsymbol{k}_1 \approx \boldsymbol{k}_2$ are not strictly degenerate. However, interactions with $\boldsymbol{k}_1 \approx \boldsymbol{k}_2$ can be expected to share some characteristics with strictly degenerate interactions $\boldsymbol{k}_1 = \boldsymbol{k}_2$. Thus, we use the term 'quasi-degenerate' for interactions of the form $\boldsymbol{k}_1 \approx \boldsymbol{k}_2$. For example, we consider a quartet comprised of $\boldsymbol{k}_1$ and $\boldsymbol{k}_2$ components related by a small deviation $\delta\boldsymbol{k}$ with $|\delta\boldsymbol{k}| \ll |\boldsymbol{k}_1|$:

$$\boldsymbol{k}_2 = \boldsymbol{k}_1 + \delta\boldsymbol{k}. \tag{2.31}$$

From the wavenumber resonance condition in (2.28), follows:

$$\boldsymbol{k}_4 = 2\boldsymbol{k}_1 - \boldsymbol{k}_3 + \delta\boldsymbol{k}. \tag{2.32}$$

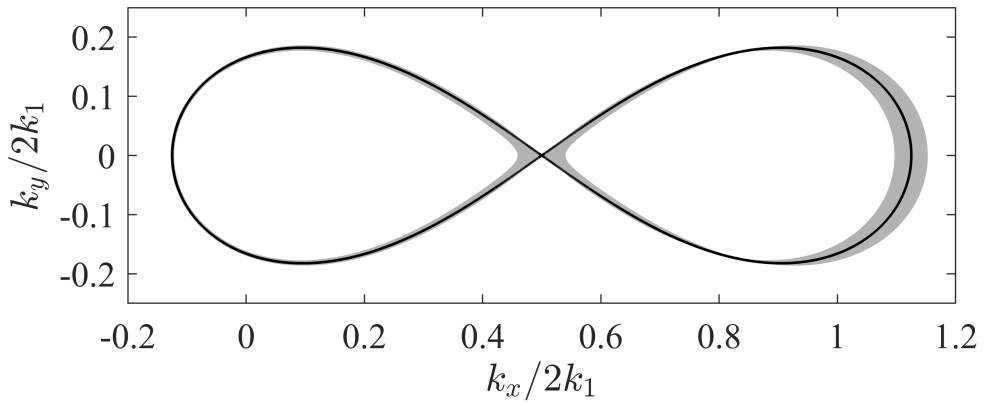

Figure 2.4: Phillips (1960) resonance loop (——) with shaded regions that show the deviations to the loop which arise for δk_x in the range $\pm 5\%$ of k_1.

For simplicity, we take $\boldsymbol{k}_1 = (k_1, 0)$, $\boldsymbol{k}_2 = (k_2, 0)$ and $\delta\boldsymbol{k} = (\delta k_x, 0)$. Thus, the frequency resonance condition in (2.29) becomes:

$$\omega_3 = 2\omega_1 \left[\frac{1}{2} + \frac{1}{2} \left(1 + 2\frac{\delta k_x}{k_1} \right)^{\frac{1}{4}} \right] - \omega_4, \tag{2.33}$$

and ω_4 follows from the linear dispersion relationship and the expression for $\boldsymbol{k}_4$ in (2.32). The linear dispersion relationship $\omega_3 = \sqrt{g|\boldsymbol{k}_3|}$ and the expression in (2.33) yield a variety of resonance loops for $\boldsymbol{k}_3 = (k_x, k_y)$, based on the value of δk_x. The Phillips (1960) resonance loop is recovered for $\delta k_x = 0$, shown as a black line in figure 2.4, featuring a resonance angle of 35.26° at the intersection. The shaded regions in figure 2.4 show the deviations to the loop which arise for δk_x in the range $\pm 5\%$ of k_1. Thus, the small deviations between $\boldsymbol{k}_1$ and $\boldsymbol{k}_2$ which arise for different values of δk_x do alter the resonance loop but the directional energy transfers still resemble the classic resonance loop of a strictly degenerate quartet ($\boldsymbol{k}_1 = \boldsymbol{k}_2$).

2.9 Removal of Bound Harmonics with Phase Separation

The bound harmonics described in the previous sections can obscure the spectral changes to the first-order components, which occur as a result of third-order interactions. We remove the bound harmonics, using a technique known as phase separation (see Fitzgerald *et al.* (2014)) to assist our investigation of the spectral changes. Appendix A of this thesis includes a detailed comparison between the method of phase separation and another method for removing bound harmonics,

based on a three-dimensional Fourier transform. A brief summary is included here.

Figure 2.5 shows amplitude spectra of surface elevation for a steep focused wave group with $A_L k_p = 0.30$ in deep water $k_p d = 5.592$. Here, A_L represents the envelope amplitude at linear focus, k_p represents the wavenumber of the spectral peak and d denotes the water depth. Panels $(a - d)$ show the spectrum including bound harmonics. Panels $(e - f)$ show the same spectra with bound harmonics removed by phase separation. The time corresponding to each spectrum is shown in the panel. As can be seen in panels $(a - d)$, the bound harmonics obscure changes to the free-wave components. The second-order superharmonics, in particular, alter the shape of the spectrum as the steepness of the wave group varies across one characteristic period. In contrast, removal of the bound harmonics in panels $(e - f)$ clarifies changes to the free-wave components. Thus, we remove the bound harmonics to perform our analyses of the wave spectra.

The technique of phase separation can be illustrated with a Stokes' expansion, shown here to the fourth-order in steepness for a single component a_i with phase $\vartheta_i(t)$:

$$\begin{aligned}\eta_i(t) = &+ a_i \cos\vartheta_i(t) \\ &+ C_{22} a_i^2 \cos 2\vartheta_i(t) + C_{20} a_i^2 \\ &+ C_{31} a_i^3 \cos\vartheta_i(t) + C_{33} a_i^3 \cos 3\vartheta_i(t) \\ &+ C_{42} a_i^4 \cos 2\vartheta_i(t) + C_{44} a_i^4 \cos 4\vartheta_i(t),\end{aligned} \tag{2.34}$$

where $\vartheta_i(t) = k_i\, x \cos\theta_i + k_i\, y \sin\theta_i - \omega_i\, t + \varphi_0$. The method allows particular terms of the Stokes expansion to be isolated by performing simulations with an offset in the initial phase, φ_0, followed by addition/subtraction of the resultant wave fields. A phase offset of 180°, for example, reverses the sign of the first-order and third-order terms in (2.34) but does not change the sign of the second-order and fourth-order terms. Addition of the surface elevation for the 0° and 180° cases, thus, allows the second-order and fourth-order bound harmonics to be isolated and removed from the surface elevation. Fitzgerald *et al.* (2014) introduced the four-phase approach, performing simulations with 0°, 90°, 180° and 270° phase offsets to

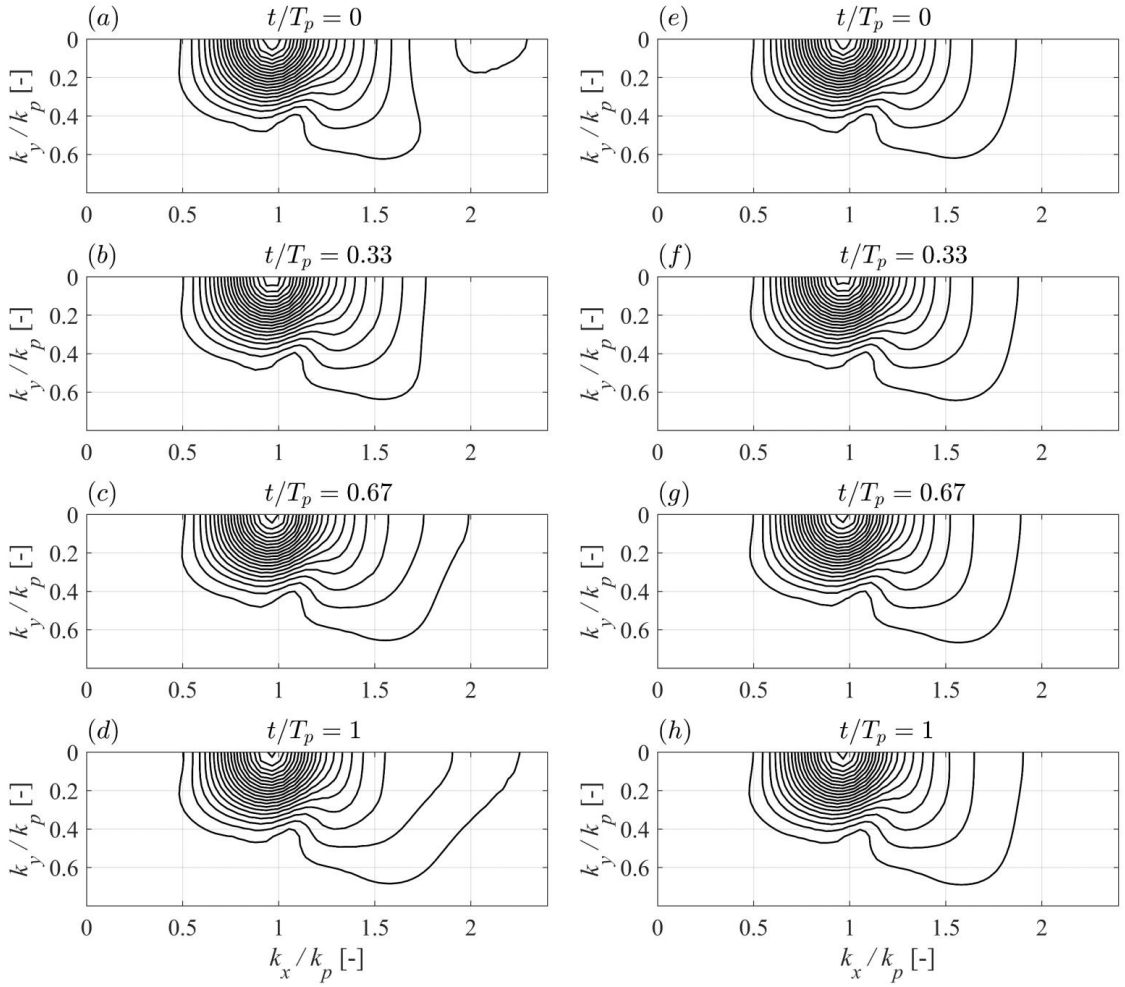

Figure 2.5: Amplitude spectra of surface elevation for a steep wave group with a steepness of $A_L k_p = 0.30$ and a dimensionless depth of $k_p d = 5.592$: (a–d) spectra including bound harmonics; (e–h) spectra after removal of bound harmonics. Contour levels are evenly distributed between 0.005m and 0.105m in intervals of 0.005m. The corresponding times for each plot are shown at the top of the panel.

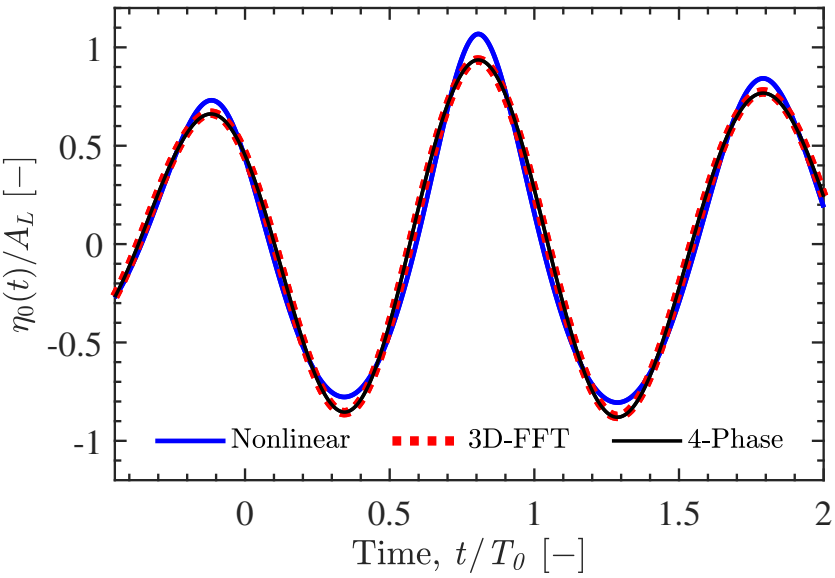

Figure 2.6: Time history of surface elevation, $\eta_0(t)$, at the location of nonlinear focus for a wave group of steepness $A_L k_p = 0.24$. Normalisation has been performed with the linear focus amplitude (A_L). The nonlinear surface elevation, including all bound harmonics, is shown (——) together with the linearized results based on filtering of the 3D-FFT (- - - -) and phase separation (——).

isolate the first-order free harmonic and the third-order principal harmonic (usually considered negligible), yielding from the Stokes expansion in (2.34):

$$\eta_L(t) = a_i \cos\vartheta_i(t) + C_{31} a_i^3 \cos\vartheta_i(t). \tag{2.35}$$

The same principle can be demonstrated for a second-order Stokes expansion consisting of two interacting components, following the formulation of Dalzell (1999):

$$\eta = \sum_{j=1}^{2} a_j \cos\vartheta_j + \sum_{j=1}^{2} a_j^2 B_s \cos 2\vartheta_j + \sum_{j=1}^{2} a_1 a_2 B_p \cos(\vartheta_1 + \vartheta_2) + a_1 a_2 B_m \cos(\vartheta_1 - \vartheta_2), \tag{2.36}$$

where $\vartheta_i(t) = k_i\, x \cos\theta_i + k_i\, y \sin\theta_i - \omega_i\, t + \varphi_0$. As before, the sign of the first-order terms will reverse for an offset of 180° in the initial phase, φ_0. However, the sign of the second-order terms will not reverse for a phase offset of 180°, allowing the second order terms to be isolated.

We have applied the phase separation technique to our simulations and compared the results with the 3D-FFT technique of Slunyaev & Kokorina (2019). Figure (2.6) shows the time history of surface elevation at the location of focus for a steep

wave group with $Ak_p = 0.24$ and a depth of $k_p d = 3.142$. The nonlinear surface elevation (including all bound harmonics) is shown together with the results of the two methods for removing the bound harmonics, indicating good agreement between the methods for removing bound harmonics.

2.10 Modified Nonlinear Schrödinger Equation

Assuming a solution to the governing equations of potential flow in the form of a modulated carrier-wave offers a means of simplifying the expressions. The Modified Nonlinear Schrödinger (MNLS) equation combines with carrier-wave approach with perturbation expansions in terms of bandwidth and steepness, providing a less computationally expensive method of modelling waves. However, bandwidth-constraints, steepness-constraints and, in the classical formulations, a truncated linear dispersion relationship may limit the applicability of the MNLS.

2.10.1 Linear Dispersion of a Wave Envelope

Superimposed propagating harmonics exactly satisfy the continuity condition for potential flow, (2.5), and approximately satisfy the free-surface boundary conditions, (2.6) and (2.7), to the first order. Therefore, any surface elevation of the form:

$$\eta(\boldsymbol{x}, t) = \frac{1}{2} \int_{-\infty}^{\infty} b(\mathbf{k}) \exp\left[i(\boldsymbol{k} \cdot \boldsymbol{x} - \omega(\boldsymbol{k})t)\right] d\boldsymbol{k} + c.c., \tag{2.37}$$

represents a valid solution according to linear theory, provided the frequency ω and wavenumber $\boldsymbol{k}$ of all components adhere to the linear dispersion relationship,

$$\omega(\boldsymbol{k}) = \sqrt{g|\boldsymbol{k}|}, \tag{2.38}$$

where $b(\mathbf{k})$ denotes the amplitude spectrum and $\boldsymbol{k} \cdot \boldsymbol{x} - \omega(\boldsymbol{k})t$ yields the phases of the superimposed propagating harmonics.

The Modified Nonlinear Schrödinger equation treats the surface elevation $\eta(\boldsymbol{x}, t)$ in (2.37) as a modulated carrier wave with a characteristic wave vector $\boldsymbol{k_0} = (k_0, 0)$

and frequency $\omega_0 = \omega(\boldsymbol{k_0})$:

$$\eta(\boldsymbol{x}, t) = \frac{1}{2} B(\boldsymbol{x}, t) \exp\left[i(\boldsymbol{k_0} \cdot \boldsymbol{x} - \omega_0 t)\right] + c.c., \tag{2.39}$$

where the 'wave envelope' $B(\boldsymbol{x}, t)$ is related to the linear surface elevation $\eta(\boldsymbol{x}, t)$ by:

$$|B| = \sqrt{\eta^2 + [\mathcal{H}\{\eta\}]^2}. \tag{2.40}$$

Equating the assumed form of a modulated carrier wave, (2.39), with the general solution form of linear theory, (2.37), an expression for the wave envelope can be obtained:

$$\begin{aligned} B(\boldsymbol{x}, t) &= \int_{-\infty}^{\infty} b(\boldsymbol{k_0} + \boldsymbol{\lambda}) \exp\left[i(\boldsymbol{\lambda} \cdot \boldsymbol{x} - (\omega(\boldsymbol{k_0} + \boldsymbol{\lambda}) - \omega_0)t)\right] d\boldsymbol{\lambda} \\ &= \int_{-\infty}^{\infty} \hat{B}(\boldsymbol{\lambda}, t) \exp\left[i\boldsymbol{\lambda} \cdot \boldsymbol{x}\right] d\boldsymbol{\lambda}, \end{aligned} \tag{2.41}$$

in terms of a modulation wave vector $\boldsymbol{\lambda}(\lambda, \mu) = \boldsymbol{k}(k_x, k_y) - \boldsymbol{k_0}(k_0, 0)$ and the Fourier components of the wave envelope:

$$\hat{B}(\boldsymbol{\lambda}, t) = b(\boldsymbol{k_0} + \boldsymbol{\lambda}) \exp\left[-i(\omega(\boldsymbol{k_0} + \boldsymbol{\lambda}) - \omega_0)t)\right]. \tag{2.42}$$

Differentiation of (2.42) with regard to time yields the temporal evolution equation:

$$\frac{\partial \hat{B}}{\partial t} + i[\omega(\boldsymbol{k_0} + \boldsymbol{\lambda}) - \omega_0]\hat{B} = 0. \tag{2.43}$$

The frequency vector $\omega(\boldsymbol{k_0} + \boldsymbol{\lambda})$ is thereafter expanded in terms of the modulation vector $\boldsymbol{\lambda}(\lambda, \mu)$ using the linear dispersion relationship, $\omega(\boldsymbol{k_0} + \boldsymbol{\lambda}) = \sqrt{g|\boldsymbol{k_0} + \boldsymbol{\lambda}|}$, and a truncated Taylor series,

$$\omega(\boldsymbol{k_0} + \boldsymbol{\lambda}) \approx \omega_0 + \lambda \left[\frac{\partial \omega}{\partial \lambda}\right]\Bigg|_{\boldsymbol{\lambda}=0} + \mu \left[\frac{\partial \omega}{\partial \mu}\right]\Bigg|_{\boldsymbol{\lambda}=0} \tag{2.44}$$

$$\approx \omega_0 + \lambda \left[\frac{\omega_0}{2k_0}\right], \tag{2.45}$$

shown here to first order. Substitution of the truncated linear dispersion relation-

ship, (2.45), into the temporal evolution equation, (2.43), followed by an inverse Fourier transform, $\mathcal{F}_{\boldsymbol{\lambda}}^{-1}$, yields:

$$\frac{\partial B}{\partial t} + \frac{\omega_0}{2k_0}\mathcal{F}_{\boldsymbol{\lambda}}^{-1}\{i\lambda\hat{B}\} = 0, \tag{2.46}$$

which can be further simplified by noting:

$$\mathcal{F}_{\boldsymbol{\lambda}}^{-1}\{i\lambda\,\mathcal{F}_{\boldsymbol{\lambda}}\{B\}\} = \frac{\partial B}{\partial x}. \tag{2.47}$$

Thus, a first-order approximation for the linear dispersion of a modulated wave envelope is:

$$\frac{\partial B}{\partial t} + \frac{\omega_0}{2k_0}\frac{\partial B}{\partial x} = 0. \tag{2.48}$$

Trulsen & Dysthe (1996) increased the order of accuracy of the truncated Taylor series in (2.44) to fifth-order and normalised with the characteristic wavenumber k_0 and frequency ω_0 to obtain:

$$\begin{aligned}\frac{\partial B}{\partial t} + \frac{1}{2}\frac{\partial B}{\partial x} + \frac{i}{8}\frac{\partial^2 B}{\partial x^2} - \frac{i}{4}\frac{\partial^2 B}{\partial y^2} - \frac{1}{16}\frac{\partial^3 B}{\partial x^3} + \frac{3}{8}\frac{\partial^3 B}{\partial x \partial y^2} - \frac{5i}{128}\frac{\partial^4 B}{\partial x^4} \\ + \frac{15i}{32}\frac{\partial^4 B}{\partial x^2 \partial y^2} - \frac{3i}{32}\frac{\partial^4 B}{\partial y^4} + \frac{7}{256}\frac{\partial^5 B}{\partial x^5} - \frac{35}{64}\frac{\partial^5 B}{\partial x^3 \partial y^2} + \frac{21}{64}\frac{\partial^5 B}{\partial x \partial y^4} = 0,\end{aligned} \tag{2.49}$$

which represents a fifth-order approximation to the linear dispersion of a modulated envelope. Since the linear dispersion relationship is infinitely differentiable, progressively higher-order expansions can be performed to improve accuracy. However, some measure of truncation error shall always exist. Trulsen *et al.* (2000) have, thus, proposed to eliminate the truncation error by direct application of the inverse Fourier transform $\mathcal{F}_{\boldsymbol{\lambda}}^{-1}$ to (2.43):

$$\frac{\partial B}{\partial t} + \frac{1}{4\pi^2}\int_{-\infty}^{\infty} i(\omega(\boldsymbol{k_0}+\boldsymbol{\lambda})-\omega_0)\exp\left[i\boldsymbol{\lambda}\cdot(\boldsymbol{x}-\boldsymbol{y})\right]B(\boldsymbol{y},t)\,d\boldsymbol{y}\,d\boldsymbol{\lambda} = 0. \tag{2.50}$$

followed by numerical integration with a split-step method, akin to Lo & Mei (1985). Thus, the linear dispersion of a modulated envelope can be calculated. However, the general solution form of (2.37) only satisfies the free-surface boundary conditions to

first order, neglecting the nonlinear terms in (2.6) and (2.7).

2.10.2 Nonlinear Evolution of a Wave Envelope

A higher-order solution to the free-surface boundary conditions, (2.6) and (2.7), can be achieved by expanding the form of the modulated carrier wave in (2.39) to include additional harmonics:

$$\eta(\boldsymbol{x},t) = \overline{\eta} + \frac{1}{2}B_1 e^{i(\boldsymbol{k_0}\cdot\boldsymbol{x}-\omega_0 t)} + \frac{1}{2}B_2 e^{2i(\boldsymbol{k_0}\cdot\boldsymbol{x}-\omega_0 t)} + c.c.\ , \tag{2.51}$$

$$\phi(\boldsymbol{x},t) = \overline{\phi} + \frac{1}{2}A_1 e^{i(\boldsymbol{k_0}\cdot\boldsymbol{x}-\omega_0 t)+k_0 z} + \frac{1}{2}A_2 e^{2i(\boldsymbol{k_0}\cdot\boldsymbol{x}-\omega_0 t)+2k_0 z} + c.c.\ , \tag{2.52}$$

The harmonic expansions for η and ϕ, (2.51) and (2.52), can be directly substituted into the governing equations of potential flow, (2.5) to (2.8), without relying upon the general linear solution form in (2.37), to obtain the nonlinear interaction terms of the Modified Nonlinear Schrödinger equation as well as the same linear dispersion term(s) as shown in truncated form in (2.49) and in exact form in (2.50). Denoting the integral in (2.50) as a pseudo-differential operator $\mathcal{L}$, the broader-banded Modified Nonlinear Schrödinger equation of Trulsen *et al.* (2000) with exact (untruncated) linear dispersion is:

$$\frac{\partial B}{\partial t} + \mathcal{L}\{B\} = -\frac{i\omega_0 k_0^2}{2}|B|^2 B - \frac{3\omega_0 k_0}{2}|B|^2\frac{\partial B}{\partial x} - \frac{\omega_0 k_0}{4}B^2\frac{\partial B^*}{\partial x} - ik_0\frac{\partial\overline{\phi}}{\partial x}B, \tag{2.53}$$

where the nonlinear terms on the right-hand-side of (2.53) account for wave-wave interactions. The accompanying boundary conditions, in terms of the wave envelope B, include a combined free-surface condition, to be applied at the mean water level ($z = 0$):

$$\frac{\partial\overline{\phi}}{\partial z} = \frac{\omega_0}{2}\frac{\partial}{\partial x}|B|^2 \quad \text{at } z = 0, \tag{2.54}$$

as well as a continuity condition for the mean flow, applied throughout the domain:

$$\nabla^2\overline{\phi} = 0 \quad \text{for } -\infty < z < 0, \tag{2.55}$$

and an asymptotic, kinematic condition for the mean flow, applied at the bottom:

$$\frac{\partial \overline{\phi}}{\partial z} = 0 \quad \text{at } z \to -\infty. \tag{2.56}$$

Equations (2.53) to (2.56) form a system of simultaneous equations which can be solved numerically by application of a two-dimensional Fourier transform, $\mathcal{F}_{\boldsymbol{xy}}$, to the continuity condition in (2.55):

$$\mathcal{F}_{\boldsymbol{xy}}\left\{\frac{\partial^2 \overline{\phi}}{\partial x^2}\right\} + \mathcal{F}_{\boldsymbol{xy}}\left\{\frac{\partial^2 \overline{\phi}}{\partial y^2}\right\} + \frac{\partial^2 \widehat{\overline{\phi}}}{\partial z^2} = 0, \tag{2.57}$$

which includes the Fourier components of the mean flow, $\widehat{\overline{\phi}}$. Here, the multiplier-operator properties of the Fourier transform (2.47) can be exploited to show that (2.57) is a second-order homogeneous ordinary-differential-equation with the solution form:

$$\widehat{\overline{\phi}} = C_1(\boldsymbol{x})e^{|\boldsymbol{k}|z} + C_2(\boldsymbol{x})e^{-|\boldsymbol{k}|z}. \tag{2.58}$$

For infinitely deep water, $k_0 d >> 1$ and $d/\sigma >> 1$ (where σ is the spatial bandwidth of the wave-group), application of the kinematic bottom condition, (2.56), requires that $C_2(\boldsymbol{x}) = 0$. Utilising the solution form of (2.58) with the combined free-surface boundary condition, (2.54), an explicit expression for the Fourier components is obtained:

$$\widehat{\overline{\phi}} = \frac{1}{|\boldsymbol{k}|}\mathcal{F}_{\boldsymbol{xy}}\left\{\frac{\omega_0}{2}\frac{\partial}{\partial x}|B|^2\right\}. \tag{2.59}$$

Similarly, an explicit expression can be obtained for the 'mean flow':

$$\widehat{\overline{\phi}} = \frac{1}{ik_x}\mathcal{F}_{\boldsymbol{xy}}\left\{\frac{\partial \overline{\phi}}{\partial x}\right\}. \tag{2.60}$$

Equating (2.59) and (2.60) to eliminate the Fourier components and substituting into (2.53),

$$\begin{aligned}\frac{\partial B}{\partial t} + \mathcal{L}\{B\} = &-\frac{i\omega_0 k_0^2}{2}|B|^2 B - \frac{3\omega_0 k_0}{2}|B|^2\frac{\partial B}{\partial x} - \frac{\omega_0 k_0}{4}B^2\frac{\partial B^*}{\partial x} \\ &- ik_0 B\mathcal{F}_{\boldsymbol{xy}}{}^{-1}\left\{\frac{ik_x}{|\boldsymbol{k}|}\mathcal{F}_{\boldsymbol{xy}}\left\{\frac{\omega_0}{2}\frac{\partial}{\partial x}|B|^2\right\}\right\},\end{aligned} \tag{2.61}$$

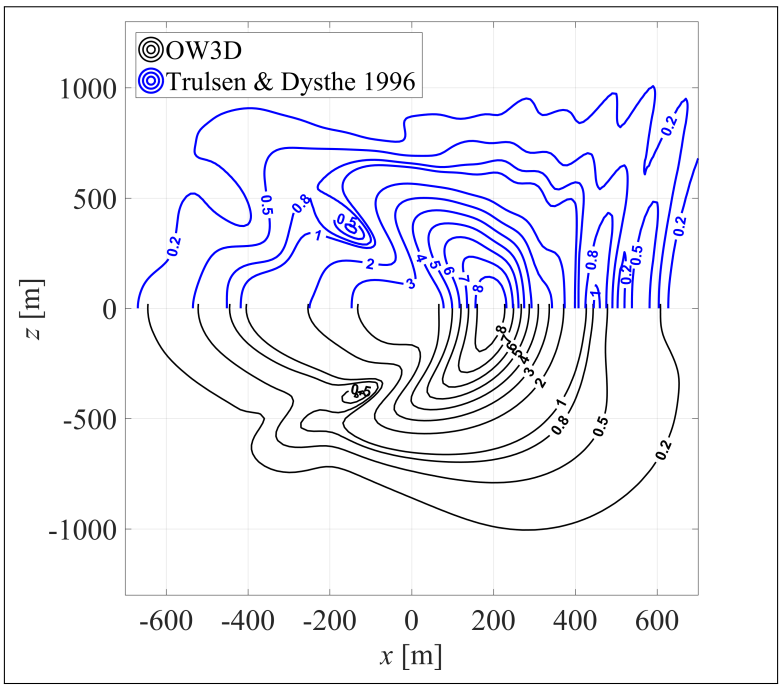

Figure 2.7: Contours plots of the wave envelope height (in meters) for a focused wave group after 28 periods of evolution, compared between *OceanWave3D* and the MNLS expression in (2.61) with 5^{th}-order truncation of the $\mathcal{L}$-operator.

produces a single expression encompassing all of the governing equations. Equation (2.61) has been simulated numerically with fifth-order truncation of the $\mathcal{L}$-operator, finite-difference discretisation in space and Runge-Kutta time-marching. As a demonstration, a focused wave group has been simulated using (2.61). A contour plot of the envelope, after 28 wave periods of evolution, is shown in figure 2.7 compared with a result from the potential flow solver *OceanWave3D*. Excellent agreement in group-shape can be seen. However, small-amplitude distortions due to energy leakage to high wavenumbers seem to have arisen as a result of truncating the linear dispersion relationship, supporting the proposition of Trulsen *et al.* (2000) to perform direct integration. In this thesis, we compare the performance of the truncated and exact versions of the dispersion operator, based on the formulations of Trulsen & Dysthe (1996) and Trulsen *et al.* (2000) respectively.

2.11 Development of Frequency-Independent Spreading

A wave spectrum with directional spreading can be expressed as the product of a unidirectional spectrum, $F(f)$, a directional spreading function, $G(f,\theta)$, and a

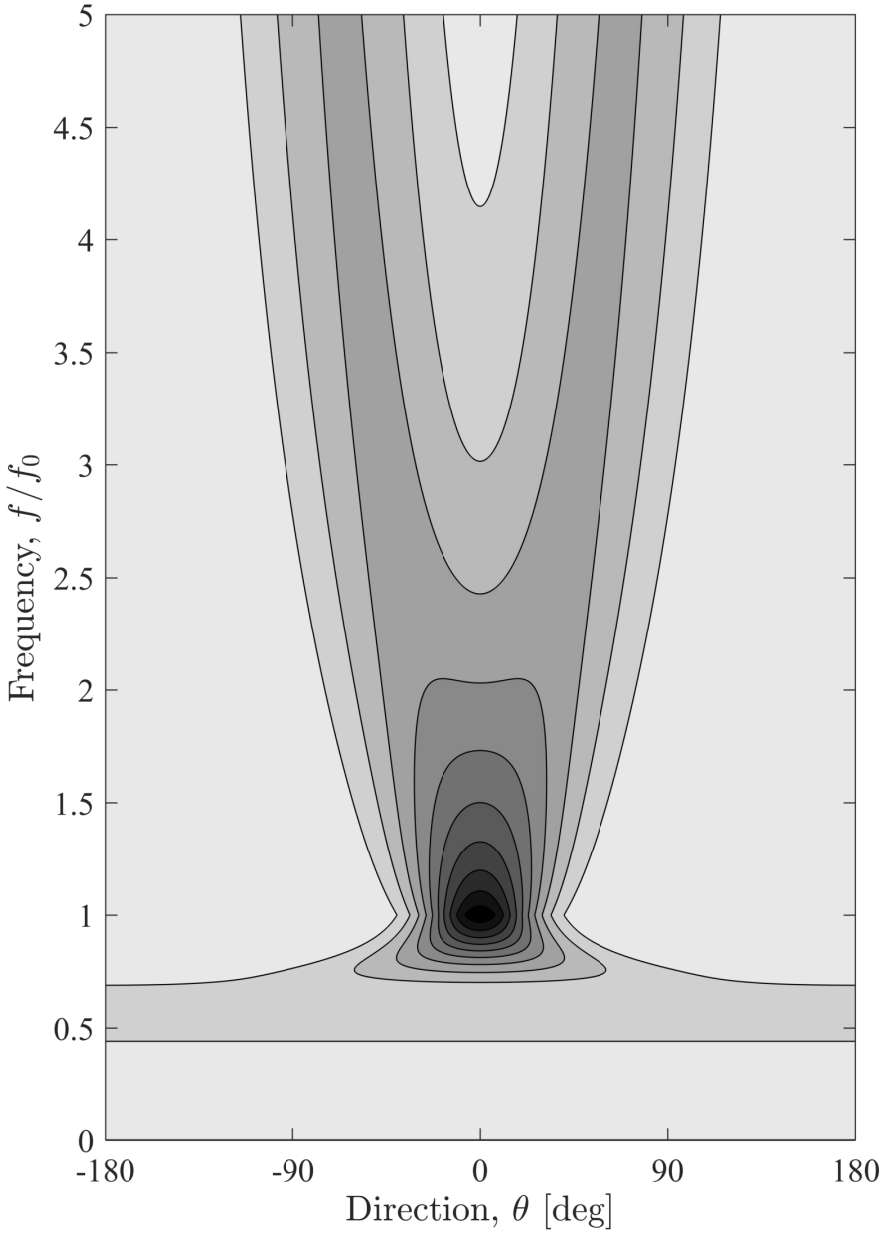

Figure 2.8: Contour plot of parametric 'double Gaussian' model for frequency independent spreading proposed by Ewans (1998). Contour levels have been normalised between zero and unity with dark corresponding to high levels and light to low levels.

normalisation function, $N(f)$:

$$E(f,\theta) = N(f)G(f,\theta)F(f), \tag{2.62}$$

where f is the frequency and θ the direction of the wave component. Energy transfer between wave components in a random-sea exhibits a directional-bias which accumulates energy amongst particular frequencies and directions in the wave spectrum, as observed by Young *et al.* (1995) with a spatial-array of gauges in Lake George, Australia. Measurements performed with a heave-pitch-roll buoy off the west coast of New Zealand, reported by Ewans (1998), confirmed the occurrence of frequency independent spreading in the ocean. Further ocean-data acquired with an airborne scanning device by Hwang *et al.* (2000) off the coast of North Carolina also revealed a clear prevalence of bimodality and stereo-video measurements completed by Leckler *et al.* (2015) and Peureux *et al.* (2018) have yielded similar results in the Black Sea and Adriatic sea, respectively. A variety of technologies have, thus, provided experimental evidence of frequency independent spreading based on field-data from a range of geographic locations. A model of frequency independent spreading has been proposed by Ewans (1998) using a parametric approach for the directional spreading function, $G(f,\theta)$, based on a 'double Gaussian' distribution:

$$G(f,\theta) = \frac{1}{\sqrt{8\pi}\sigma(f)} \sum_{k=-\infty}^{\infty} \left\{ \exp\left[-\frac{1}{2}\left(\frac{\theta-\alpha(f)-2\pi k}{\sigma(f)}\right)^2\right] + \exp\left[-\frac{1}{2}\left(\frac{\theta-\beta(f)-2\pi k}{\sigma(f)}\right)^2\right]\right\}, \tag{2.63}$$

where $\sigma(f)$ is a measure of the angular width indicating the spread of each frequency component and $\alpha(f)$ and $\beta(f)$ represent the locations of the bimodal peaks at each frequency. Tuning of parameters $\alpha(f)$, $\beta(f)$ and $\sigma(f)$ with least-square regression leads to the Ewans (1998) spectrum depicted in figure 2.8. The direction of component propagation (θ) is plotted on the abscissa with the mean direction of propagation placed in the centre of each plot. The corresponding frequency (f) of each component is shown on the ordinate normalised by the frequency of the spectral peak (f_0). Contours are shown for the directional spreading function, $G(f,\theta)$, which varies between zero and unity by definition. Figure 2.8 depicts narrow, uni-

modal, directional spreading around the spectral peak with pronounced frequency independent spreading at frequencies above f_0; at the high-frequency limit of the spatial-array ($f/f_0 = 4$) components travel approximately perpendicular.

2.12 Kurtosis Evolution Equations

The kurtosis of the free surface, Kur=$\langle\eta^4\rangle/\langle\eta^2\rangle^2$, has received particular attention, as an indicator of nonlinear wave-wave interactions and rogue wave occurrence (see, e.g., Mori & Janssen (2006)). Here, η denotes the free-surface elevation and the angled brackets denote a statistical average. The evolution in kurtosis for a sea with initially Gaussian statistics, Kur($\eta(x, y, t_0)$)=3, has originally been studied by Janssen (2003). In his model, the wave field is assumed to be sufficiently weakly nonlinear that the sea surface is near to a Gaussian state, meaning that the kurtosis can be expressed in terms of lower-order moments, following the approach of Hasselmann (1962). An initially uniform phase distribution is assumed. Thus, the wave field is treated as homogeneous in space, and the fourth cumulant can be approximated to form a closed system of equations based on the Zakharov equation (see Eq. (20) and Eq. (28) of Janssen (2003)). Mori & Janssen (2006) invoked the assumption of narrow bandwidth to obtain an evolution equation for kurtosis, which is consistent with the cubic Non-linear Schrödinger equation (NLS) and assumes an underlying one-dimensional Gaussian spectrum. Janssen & Bidlot (2009) and Mori *et al.* (2011) extended the work of Mori & Janssen (2006) by considering the role of directional effects. A theoretical model describing the evolution of kurtosis was derived by Fedele (2015) building on this previous work. This used the cubic NLS to derive how the kurtosis of a random wave train would evolve. He found that the excess kurtosis increased with a timescale dependent on the bandwidth of the initial spectrum and the dominant wave period. The dynamic excess kurtosis then levels off tending to a value of $\pi/(3\sqrt{3})$ divided by the Benjamin-Feir Index (BFI) squared, where the BFI is a measure of the ratio of the significant wave height to the bandwidth of the starting waves. In this thesis, we perform random sea simulations using the MNLS equation and compare the evolution in kurtosis observed in our simulations with the theoretical results of Fedele (2015).

3 Nonlinear Evolution of a Steep, Focusing Wave Group in Deep Water Simulated with *OceanWave3D*

Abstract

Steep, focusing waves can experience fast and local nonlinear evolution of the spectrum due to wave-wave interactions resulting in energy transfer to both higher and lower wavenumber components. The shape and kinematics of a steep wave may, thus, differ substantially from the predictions of linear theory. We have investigated the role of nonlinear interactions on group shape for a steep, narrow-banded, directionally-spread wave group focusing in deep water using the fully-nonlinear potential flow solver, OceanWave3D. Exact second-order correction of the initial conditions has been implemented together with a novel third-order approximate correction based on a Stokes-type formulation for surface elevation combined with a scaling argument for the third-order velocity potential. Four-phase separation reveals that the third-order scheme provides a good estimate for the third-order superharmonics. A quantitative assessment of numerical error has also been performed for the spatial and temporal discretization, including energy conservation, a reversibility check and validation against previous simulations performed with a higher-order spectral (HOS) code. The initially narrow-banded amplitude spectrum exhibits the formation of 'sidelobes' at angles of approximately $\pm 35^\circ$ to the spectral peak during the simulated extreme wave event, occurring in approximately 10 wave periods, with a preferential energy transfer to high-wavenumber components. The directional energy transfer is attributed to resonant third-order interactions with a discussion of the engineering implications.

3.1 Introduction

The shape and kinematics of extreme waves remains a topic of interest for research and a relevant consideration for offshore engineering design. Extreme wave formation can arise from dispersive focusing, characterised by the superposition of Fourier modes, as well as various nonlinear focusing mechanisms such as the modulational instability; wave interactions with current, wind and bathymetry; crossing seas and shallow water effects with extensive reviews by Kharif & Pelinovsky (2003), Dysthe *et al.* (2008) and Adcock & Taylor (2014). Extreme waves are characterised by excessive *steepness* ($\epsilon = \pi H_0/\lambda_0$), defined in terms of the characteristic height (H_0) and characteristic length (λ_0) of the waves. Linear theory approximately describes the evolution of a wave group if $\epsilon << 1$ but nonlinearity becomes significant for steeper waves due to the presence of higher-order nonlinear terms in the dynamic and kinematic free surface boundary conditions. Rogue waves are typically expected to be steep and consequently exhibit a greater prevalence of nonlinearity. The shape of an extreme wave has been previously investigated for 'weakly nonlinear' random seas featuring waves of moderate steepness with a uniform distribution of phase (see, e.g., Adcock *et al.* (2015), Latheef *et al.* (2017) and Fujimoto *et al.* (2019)). Random-sea investigations of extreme waves represent the most realistic approach and account for the natural variability of focused events as well as the interaction of focused events with surrounding wave groups and the background sea state. However, the random-sea approach is also innately computationally inefficient because, for much of the space and time, the simulation is resolving wave events which are not particularly extreme. Thus, an alternate approach has been used, based on isolated wave groups featuring a coherent phase distribution designed to focus components in time and space; this approach has also been suggested as a design method for the assessment of loads on offshore structures (see Bateman *et al.* (2012)) since a focusing wave group encompasses all forms of wave-wave interaction present in a random sea but remains less computationally expensive to simulate, less vulnerable to error wave contamination (since the error waves separate out from the wave group during the simulation) and changes in group shape can be more easily identified. Gibbs &

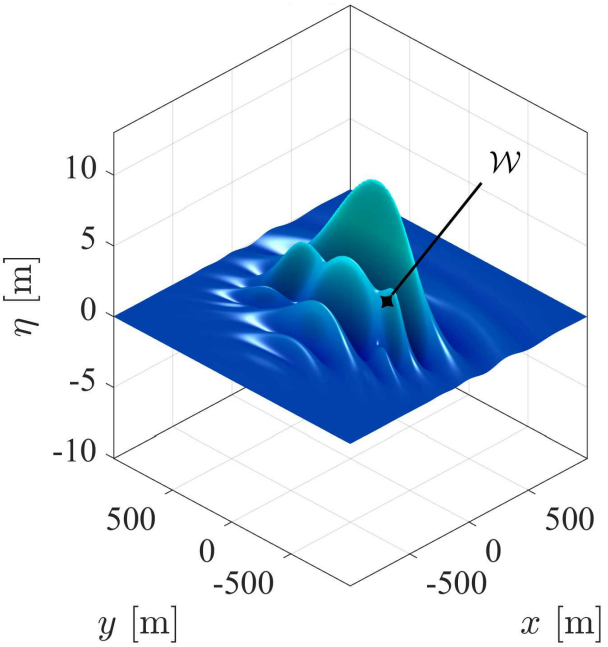

Figure 3.1: Constructive interference between wing waves and central crests as observed by Gibbs & Taylor (2005).

Taylor (2005) simulated extreme waves of the *NewWave* form (see Tromans *et al.* (1991)), with directional spreading, using the 'BST' code of Bateman *et al.* (2001), with a 5^{th}-order Dirichlet-Neumann operator, and identified third-order nonlinear wave-wave interactions as the cause of group contraction in the direction of propagation and group expansion in the lateral direction as well as the movement of the largest crest to the front of the group. The lateral group expansion has been linked to the formation of 'wing waves' (labeled $\mathcal{W}$ in figure 3.1) which manifest as localised protrusions at the periphery of the group and interfere constructively with the central crests to form notably broader crests. An intriguing feature of the wing waves is the observed direction of travel, at approximately $\pm 35°$ to the propagating wave group, leading Adcock & Taylor (2016) to suggest that the wing waves are a direct result of third-order interactions along the $\arctan(1/\sqrt{2})$ resonance angle identified by Longuet-Higgins (1976) for the spectral peak of a three-dimensional wave packet. The present study investigates the spectral evolution of a steep, focusing wave group, of the same form as Gibbs & Taylor (2005), using the fully-nonlinear potential flow solver *OceanWave3D* (see Engsig-Karup *et al.* (2009)) and performs a detailed assessment of the simulation fidelity.

3.2 Numerical Method

OceanWave3D numerically solves the governing equations of potential flow for surface gravity waves (see Currie (1993)) in a three-dimensional Eulerian frame of reference using a Cartesian coordinate system (x, y, z) with the origin of the vertical coordinate ($z = 0$) at the mean-water-level. The code is, thus, restricted to free-surface shapes which can be expressed as a single-valued function of the horizontal coordinates and cannot capture overturning waves.

3.2.1 Code Description

The governing equations require nonlinear boundary conditions to be applied at the free surface and, as a 'fully nonlinear' code, *OceanWave3D* applies the prescribed boundary conditions without simplification. However, the location of the free surface, $\eta(x, y, t)$, is unknown *a priori*. Thus, a non-conformal transform maps the solution to a time-invariant domain:

$$\sigma \equiv \frac{z + d(x, y)}{\eta(x, y, t) + d(x, y)}, \tag{3.1}$$

compatible with a variable depth domain, $d(x, y)$, but restricted to constant depth, $d(x, y) = d$, for the present study. Discretization of the governing equations is performed with a method of lines approach, based on time integration with the classical explicit four-stage, fourth-order Runge-Kutta scheme and finite-difference discretization of the spatial derivatives with direct product approximation of the nonlinear terms. A grid (N_x, N_y) of uniformly distributed points is defined along the horizontal xy-axes for evolution of the free-surface variables $\eta(x, y, t)$ and $\tilde{\phi} = \phi(x, y, \eta, t)$. In the σ-transformed domain, N_σ points are defined in the vertical direction below each horizontal free-surface grid point, in the restricted range $0 \leq \sigma \leq 1$. Thus, h-adaptivity is implemented by adjusting the number of grid points in the horizontal and vertical directions, for a given size of domain, to refine or coarsen the spatial resolution. In the interior of the domain, all derivatives are centrally discretized with a flexible-order finite-difference scheme that allows for p-adaptivity. Near the structural boundaries (i.e., the bottom and sidewalls of the

domain) stencils become off-centered but the order of the scheme is the same as the interior domain. Simultaneous application of the Laplace equation and no-normal-flow condition is accomplished at the structural boundaries using a single layer of ghost nodes outside the physical domain of interest, as explained by Engsig-Karup *et al.* (2009). Discretization, thus, yields a rank $n = N_x N_y N_z$ linear system of equations of the form:

$$A\Phi = b, \tag{3.2}$$

comprised of the coefficient matrix A, the unknown vector of velocity potential (Φ) corresponding to each grid point at an instant in time and the vector b holding zeros and the inhomogeneous boundary conditions. Numerical solution of (3.2) is performed with the Generalized Minimum Residual (GMRES) method with left-preconditioning by the linearised version of the coefficient matrix A, constructed with a second-order finite difference scheme and denoted as A_2:

$$A_2{}^{-1}\{A\Phi = b\} \tag{3.3}$$

The preconditioner A_2 is not time dependent and, thus, needs only to be generated once at the beginning of the simulation. Based on an initial guess for Φ_0, the initial residual is computed, $r_0 = A\Phi_0 - b$, and preconditioned by solving $A_2 u_0 = r_0$ followed by one iteration of the GMRES algorithm in the Krylov subspace. Preconditioning is, thus, repeated once every iteration solving a system of the form $A_2 u_m = r_m$ where m indicates the iteration number. Optimal linear scaling of the solution effort is ensured by multi-grid solution of the preconditioning step using Gauss-Seidel smoothing. The preconditioner A_2 is thus generated for every grid level using Direct Coarse grid Approximation (DCA) and a V-cycle with one pre-smoothing step and one post-smoothing step employed. The number of GMRES iterations required for convergence at a particular time step has been found to be independent of grid size using the multi-grid preconditioning scheme (see Engsig-Karup *et al.* (2009)). Notably, the inclusion of ghost nodes has also been shown to improve the numerical stability of the preconditioning relaxation scheme, especially in the

presence of the Neumann boundary conditions applied at the structural boundaries (see Engsig-Karup *et al.* (2009)), allowing for an anisotropic grid distribution in the vertical direction. Clustering of points near the free surface using Chebyshev-Gauss-Lobatto (CGL) points has, thus, been implemented to minimise dispersion error, anticipated to be the dominant form of error in *OceanWave3D* (see Bingham & Zhang (2007)).

3.2.2 Numerical Domain

A numerical wave tank 7680 m in length (L), 2560 m in width (W) and 200 m in depth (d) has been employed. The simulated extreme wave event follows the dimensions and timescales of Gibbs & Taylor (2005) with a characteristic wavelength (λ_p) of 225 m and characteristic period (T_p) of 12 s – both corresponding to the initial peak of the wavenumber spectrum, $k_p = 0.02796$ m^{-1}. The water is consequently approximated as 'deep' with $k_p d = 5.6$. A symmetry plane has been implemented in the transverse (y) direction along the center plane of the group to exploit the symmetry property of the wave event (see figure 3.1).

3.3 Initial Conditions

The *NewWave* model describes the average shape of an extreme wave in a linear sea using the scaled autocorrelation function, as detailed by Tromans *et al.* (1991). In the present study, initial conditions for the simulations have been prescribed as an approximation for a *NewWave* group calculated at 20 wave periods before the linear focus time, using the linear dispersion relationship. The low steepness of the dispersed initial conditions minimises the contribution of higher-order bound harmonics. However, exact second-order correction of the surface elevation and velocity potential has been performed with the expressions of Dalzell (1999) for finite-depth wave-wave interactions—the second order terms have been evaluated at the mean-water-level ($z = 0$) but the first-order terms have been evaluated at the free surface ($z = \eta$) to avoid pseudo-second-order error waves, as detailed in Appendix 3.7 at the end of this chapter. Time marching of the initial conditions has been performed for a total of 40 wave periods, terminating the simulation at 20

Table 3.1: Initial Condition Parameters.

Ak_p	k_p	k_w	ς
0.3	0.02796 m^{-1}	0.004606 m^{-1}	15°

wave periods after the linear focus time. The parameters for the initial conditions of the wave group match those of Gibbs & Taylor (2005) and are listed in table 3.1.

Conventionally, directional spreading of the frequency spectrum is implemented as the product of a unidirectional spectrum, $S(\omega)$, and a spreading function, $D(\theta)$, where ω is the angular frequency and θ the direction of wave propagation: $F(\omega, \theta) = S(\omega)D(\theta)$.

A Gaussian unidirectional spectrum has been implemented in terms of wavenumber, $\hat{S}(k)$, by this study:

$$\hat{S}(k) = \exp\left(\frac{-(k-k_p)^2}{2k_w^2}\right), \tag{3.4}$$

where k is the wavenumber, k_p is the wavenumber corresponding to the initial spectral peak and k_w is the spectral width, which yields a close approximation to a JONSWAP spectrum with a peak enhancement of $\gamma = 3.3$. A Gaussian distribution has also been used for the spreading function:

$$D(\theta) = \frac{1}{\sqrt{2\pi}\varsigma}\exp\left(-\left(\frac{\theta^2}{2\varsigma^2}\right)\right), \tag{3.5}$$

with a constant rms spreading parameter (ς) of 15°. The directional frequency spectrum, $F(\omega, \theta)$, has thus been defined as the product of two Gaussian functions so the surface elevation of the focused linear event assumes an approximate form expressed in terms of the spatial bandwidths S_x and S_y:

$$\eta(x, y) = Ae^{-\frac{1}{2}S_x^2x^2}e^{-\frac{1}{2}S_y^2y^2}\cos(k_px), \tag{3.6}$$

which represents a close approximation to the form of a linearly-focused *NewWave* group.

3.3.1 Phase Separation Technique

A system of bound harmonics associated with each free harmonic can be described with a Stokes regular wave expansion, shown here to the fourth-order for a single amplitude component, a_i, with phase $\vartheta_i(t)$:

$$\begin{aligned}\eta_i(t) = &+ a_i \cos\vartheta_i(t) \\ &+ C_{22}a_i^2 \cos 2\vartheta_i(t) + C_{20}a_i^2 \\ &+ C_{31}a_i^3 \cos\vartheta_i(t) + C_{33}a_i^3 \cos 3\vartheta_i(t) \\ &+ C_{42}a_i^4 \cos 2\vartheta_i(t) + C_{44}a_i^4 \cos 4\vartheta_i(t),\end{aligned} \tag{3.7}$$

where $\vartheta_i(t) = k_i\, x \cos\theta_i + k_i\, y \sin\theta_i - \omega_i\, t + \varphi_0$. The initial phase φ_0 is defined relative to a 0° baseline and the coefficients, C, determine depth sensitivity, as listed by Walker *et al.* (2004). The method of phase separation, see Fitzgerald *et al.* (2014), allows particular terms of the Stokes expansion to be isolated by performing simulations with an offset in the initial phase, φ_0, followed by addition/subtraction of the results. Performing simulations with 0°, 90°, 180° and 270° phase shifts for the initial phase allows for isolation of the first-order free harmonic and the third-order principal harmonic (generally considered negligible) to obtain the linearised surface elevation (η_L):

$$\eta_L(t) = a_i \cos\vartheta_i(t) + C_{31}a_i^3 \cos\vartheta_i(t), \tag{3.8}$$

Linearisation of the wave spectrum has, thus, been performed with the *four-phase separation technique* in this study.

3.3.2 Approximate Third-Order Correction

An exact description of the third-order bound harmonics has been presented by Madsen & Fuhrman (2012). However, an approximate description may be sufficient for the present study since the third-order harmonics are small for the initially dispersed group. An approximation has been proposed by Walker *et al.* (2004) based on the Stokes-type expansion in (3.7) with use of the *Hilbert transform*, denoted by

$\mathcal{H}$, which introduces a 90° phase shift into the operand. The third-order *principal harmonic* of surface elevation (η_{31}) can, thus, be approximated as:

$$\eta_{31} = \frac{-3(1+3B+3B^2+2B^3)}{8(1-B)^3} k_0^2 \eta_L (\eta_L^2 + [\mathcal{H}\{\eta_L\}]^2), \tag{3.9}$$

and the third-order *superharmonic* of surface elevation (η_{33}) as:

$$\eta_{33} = \frac{3(1+3B+3B^2+2B^3)}{8(1-B)^3} k_0^2 \eta_L (\eta_L^2 - 3[\mathcal{H}\{\eta_L\}]^2), \tag{3.10}$$

where $B = \mathrm{sech}(2k_0 d)$ and k_0 is the characteristic wavenumber.

The corresponding velocity potential associated with the third-order surface elevation has been approximated in this study with a scaling argument. Noting the scaling relation between velocity potential and surface elevation $\phi \sim g\eta/\omega$ (described by Lannes (2013)) and the 90° phase shift expected between surface elevation and velocity potential, an approximation can, thus, be obtained for the third-order superharmonic:

$$\phi_{33} = K_{33} \frac{g}{\omega_0} \mathcal{H}\{\eta_{33}\}, \tag{3.11}$$

where ω_0 is the characteristic frequency and the coefficient K_{33} is a proportionality constant. A similar expression can be obtained for the third-order principal harmonic and both sets of third-order terms have been assessed in this study as a proposed method for correction of the initial conditions, with the proportionality constants set to unity. Simplified expressions for the bound harmonics can also be found in Adcock & Taylor (2016) with detailed comparisons against fully-nonlinear simulation results.

3.4 Simulation Fidelity

A convergence study based upon grid resolution (h-adaptivity) has been performed with the use of grid-halving in all three dimensions to assess grid independence across two resolution levels, termed 'intermediate' and 'fine', both listed in table 3.2 with the height of the first grid at the free surface (Δz^*) and the grid resolution of Gibbs & Taylor (2005), denoted as G&T'05, also listed. A convergence study based upon

Table 3.2: Discretization Parameters.

Grid	N_x	N_y	N_z	Δx	Δy	Δz^*
Fine	1025	257	17	7.5m	10m	0.25m
Inter.	513	129	9	15m	20m	1m
G&T'05	255	127	-	14.1m	22.7m	-

p-adaptivity has also been performed by altering the order of the finite difference scheme used for the spatial derivatives in the governing equations. Time integration of the governing equations is performed with the classic fourth-order Runge–Kutta scheme and sensitivity to time step size (Δt) has been assessed with the Courant-Friedrichs-Lewy (CFL) condition calculated from the phase speed associated with the initial peak of the wavenumber spectrum. All simulations have been performed with exact second-order correction of the initial conditions; approximate third-order correction has been implemented where stated. The validity of the 'deep' water assumption has also been assessed together with the modelling error of the proposed third-order correction scheme for the initial conditions.

3.4.1 Order of Finite Differencing

OceanWave3D utilises centered stencils for the finite difference discretization of spatial derivatives in the governing equation, except near the structural boundaries where off-center stencils must be used. Thus, only even-numbered orders can be implemented and the current study has performed simulations with fourth, sixth and eighth-order finite difference schemes on both the intermediate and fine grids. The maximum number of multi-grid levels (N_{MG}) has been used for preconditioning on both the fine grid, $N_{MG} = 10$, and the intermediate grid, $N_{MG} = 9$. A CFL of 0.5 has previously been shown to be adequate for steep waves (see Engsig-Karup *et al.* (2009)) and has also been used here. Increasing the order of the finite difference scheme has also been shown to improve dispersion error without significantly influencing diffusion error (see Bingham & Zhang (2007)). Since *OceanWave3D* is anticipated to be dispersion-error dominant, p-adaptivity is, thus, a particularly effective method of improving simulation fidelity. A key feature of *OceanWave3D*

Table 3.3: Average Number of GMRES Iterations.

Grid	CFL_x	n_x	n_y	FD4	FD6	FD8
Fine	0.5	30	22.5	19.34	21.10	23.19
Inter.	0.5	15	11.3	13.69	15.64	23.15

is the grid-independent iteration count for the GMRES algorithm, with multi-grid preconditioning, which ensures optimal scaling of the solution effort. The average number of GMRES iterations required for convergence at each time step, with a tolerance of 10^{-6} (see table I of Ducrozet *et al.* (2012)), has been recorded over the entirety of each simulation, from $-20T_p$ to $+20T_p$, and listed in table 3.3 for both the intermediate and fine grid resolutions. The number of grid points per characteristic wavelength in the direction of wave group propagation, $n_x = \lambda_p/\Delta x$, and the direction transverse to propagation, $n_y = \lambda_p/\Delta y$, has also been listed for both grid resolutions. As can be seen, a grid-independent iteration count arises for eighth-order finite differencing but not for the sixth-order and fourth-order schemes. Simulations of steep waves with *OceanWave3D* have been previously shown to require a grid resolution of at least $n_x \approx 32$ with sixth-order finite differencing (see Engsig-Karup *et al.* (2009)). The low number of GMRES iterations on the intermediate grid with sixth and fourth-order schemes may, thus, be a result of inadequate spatial resolution for the given discretization schemes. Eighth-order finite difference schemes have, thus, been used for the present study on both the intermediate and fine grids.

3.4.2 Grid Convergence and CFL

The peak surface elevation (η_{peak}) occurring at any point in the simulation has been recorded for both grid levels, intermediate and fine, for CFL conditions of 0.5 and 1.0. Similarly, the peak vertical velocity ($\tilde{w}_{peak}$) and the peak horizontal velocity ($\tilde{u}_{peak}$) have also been recorded to assess convergence of the kinematics. Refinement of the grid resolution has been shown to suppress both diffusion and dispersion errors (see Bingham & Zhang (2007)); thus, h-adaptivity offers an effective convergence strategy for *OceanWave3D*. Refinement of the time step to reduce the CFL condition, for a

Table 3.4: Convergence study based on grid resolution (h-adaptivity) and CFL with eighth-order finite differencing (FD8).

Grid	$\mathrm{CFL_x}$ [-]	n_x [-]	n_y [-]	η_{peak} [m]	$\tilde{w}_{peak}$ [m/s]	$\tilde{u}_{peak}$ [m/s]
Inter.	1.0	15	11.3	11.725	5.435	7.405
Inter.	0.5	15	11.3	12.466	5.689	8.075
Fine	1.0	30	22.5	12.702	5.767	8.837
Fine	0.5	30	22.5	12.801	5.820	8.980
Fine, $N_z=9$	0.5	30	22.5	12.786	5.810	8.954
G&T'05	0.13	16	9.9	12.840	-	-

given grid resolution, has been shown to suppress diffusion error but not dispersion error. Since, by definition, kinematics are expressed in terms of derivatives of the velocity potential, the order of convergence for the kinematics is expected to be lower than that of the velocity potential and surface elevation. The results of the convergence study are listed in table 3.4 and compared with the results of Gibbs & Taylor (2005) for the same test case. The fine grid simulation performed with a CFL of 0.5 using *OceanWave3D* is expected to be converged since the CFL condition and the horizontal resolution of $n_x = 30$ meets the recommendation for steep, nonlinear waves (see Engsig-Karup *et al.* (2009))—this case has, thus, been compared with the results of Gibbs & Taylor (2005) using the time history of surface elevation at the location of nonlinear focus plotted in figure 3.2. Nonlinear focus occurs at $t = 1.3T_p$, relative to the linear focus time of $t = 0T_p$, indicating a slight delay in the focusing event due to nonlinear wave-wave interactions. Cubic spline interpolation has been used on both curves to improve the plotting resolution. Good agreement between the time histories can be seen, although a slight lead by *OceanWave3D* is observed before focus and a slight lead by the HOS code is observed after focus. Table 3.4 indicates a 0.3% discrepancy in η_{peak} between Gibbs & Taylor (2005) and the fine-grid result with a CFL of 0.5 which further supports the conclusion of convergence. In contrast, diffusion error seems apparent on the intermediate grid with a CFL condition of 1.0 since all the convergence parameters are substantially lower than the converged fine grid result with a CFL of 0.5. The intermediate grid with a CFL

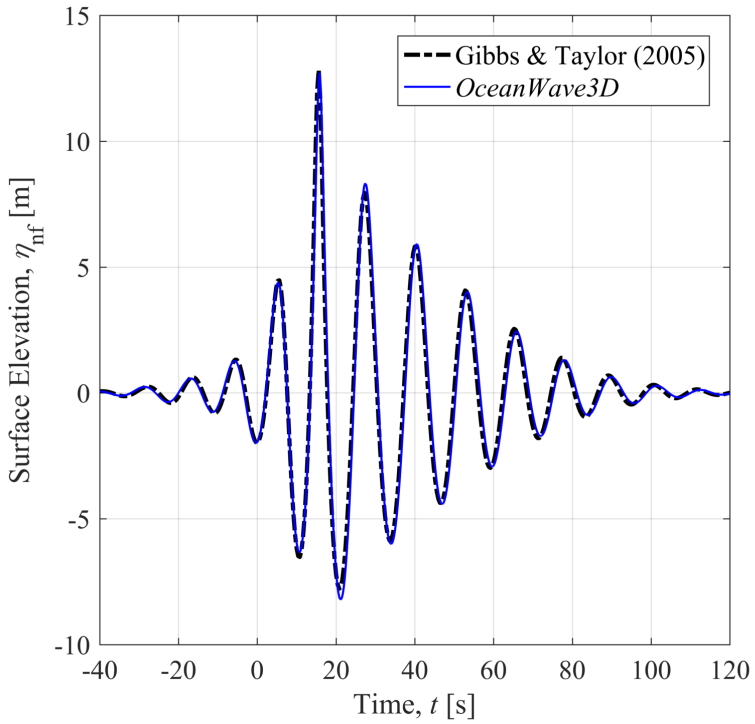

Figure 3.2: Time history of surface elevation at nonlinear focus point—comparison between *OceanWave3D* and Higher-Order Spectral (HOS) results of Gibbs & Taylor (2005)

of 0.5, however, indicates an deviation of -2.6% for η_{peak}, -2.3% for $\tilde{w}_{peak}$ and -10.1% for $\tilde{u}_{peak}$ which may be seen as an unexpectedly good result since the total grid size has been reduced by a factor of 8. The fine grid resolution with a CFL of 1.0 exhibits deviations of -0.8% for η_{peak}, -0.9% for $\tilde{w}_{peak}$ and -1.6% for $\tilde{u}_{peak}$ which suggests that the physical parameters are reasonably well resolved on the fine grid with a CFL of 1.0. However, the diffusivity of the solution can be assessed with the total energy of the solution (E) at every time step, including kinetic energy and potential energy contributions. Potential flow is inherently non-diffusive since the combination of the incompressibility condition, $\nabla \cdot u = 0$, and the irrotationality condition, $\nabla \times u = 0$, identically satisfies $\nabla^2 u = 0$ while the assumption of an inviscid fluid theoretically eliminates viscous dissipation. However, discretization of the governing equations with finite differencing results in numerical diffusion, due to truncation error, which can also mimic the effects of dissipation and reduce the total energy of the wave field. The change in total energy relative to the initial condition is shown in normalised form in figure 3.3 for the cases in table 3.4. As can be seen, the fine grid resolution with a CFL of 0.5 exhibits a change in total energy of -0.024% over the complete

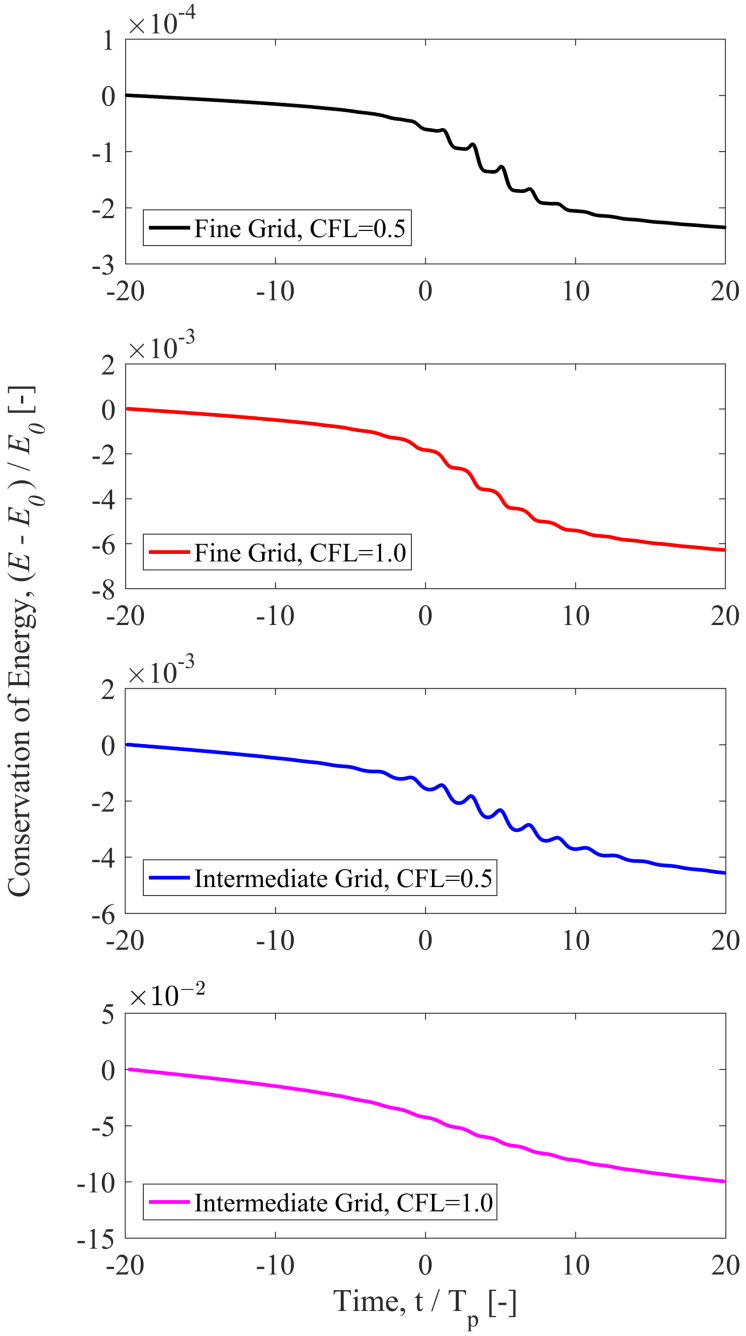

Figure 3.3: Change in total energy during simulation for various grid resolutions and CFL conditions.

simulation. The change in total energy occurs predominantly during the nonlinear focus event, from $0T_p$ to $10T_p$, when the wave group is steepest and numerical diffusion likely to be most severe. A decline in total energy is also expected as a result of the Savitzky-Golay filters which prevent the accumulation of high-frequency aliasing errors in *OceanWave3D*. In contrast, the fine grid solution with a CFL of 1.0 exhibits a total energy change of -0.63% which is more than an order of magnitude greater and even exceeds the -0.46% change in total energy for the intermediate grid with a CFL of 0.5. Combining the intermediate grid with a CFL condition of 1.0 further exacerbates diffusivity with a change in total energy of -9.96% over the course of the simulation. The sensitivity of diffusion error to the CFL condition is, thus, apparent and a CFL of 0.5 has been selected for all further simulations and the results which form the basis of the discussion. A further assessment of the necessary grid resolution in the vertical (z) direction has also been performed by retaining the 'fine' grid resolution in the horizontal directions ($N_x = 1025$, $N_y = 257$) while reducing the number of grid points in the vertical direction to $N_z = 9$, with the results listed in table 3.4. As can be seen, halving the number of vertical grid points has negligibly influenced the results of the fine grid resolution with discrepancies of -0.12%, -0.17%, and -0.29% in η_{peak}, $\tilde{w}_{peak}$ and $\tilde{u}_{peak}$, respectively, compared against the fine grid resolution with $N_z = 17$. Thus, the reduced vertical resolution offers an attractive alternative and the implications for dispersion error are considered in the next section.

3.4.3 Linear Dispersion Error

Grid points have been clustered near the free surface using the symmetric half of a Chebyshev-Gauss-Lobatto distribution: $\sigma_j = \sin((\pi[j-1])/(2[N_z-1]))$, which offers a compromise between the accuracy of dispersion and the accuracy of internal kinematics (see Engsig-Karup *et al.* (2009)). Here, j denotes the index of the grid point with $j = 1$ at the bottom and $j = N_z$ at the free surface. A linear analysis of dispersion error has been performed for the fine grid resolution in the horizontal directions ($N_x = 1025$, $N_y = 257$) while varying the number of grid points in the vertical direction, following the method of Engsig-Karup *et al.* (2009) and Bingham

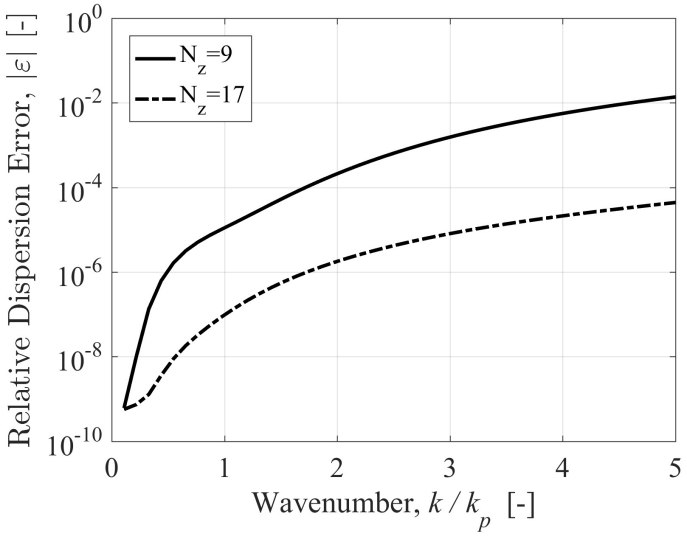

Figure 3.4: Linear analysis of dispersion error due to discretization of governing equations.

& Zhang (2007), for $N_z = 9$ and $N_z = 17$ with a depth (d) of 200 m. The dispersion error is estimated with the unidirectional travelling wave solution, formulated in a periodic domain in x with uniform transverse grid spacing Δx. The known non-dimensional dispersion operator for this solution:

$$\frac{\tilde{w}}{k\tilde{\phi}} = \tanh kh, \tag{3.12}$$

can be evaluated numerically on the left-hand side by applying the prescribed velocity potential at the free surface ($\tilde{\phi}$) followed by numerical solution for the vertical velocity at the free surface ($\tilde{w}$) using the eighth-order numerical scheme of *OceanWave3D* with linearised free surface boundary conditions. The difference between the numerically-evaluated left-hand side of (3.12) and the exact right-hand side of (3.12) yields the relative dispersion error (ε), with the results shown in figure 3.4. As can be seen, both vertical resolutions exhibit negligible dispersion error for the spectral peak ($k/k_p = 1$). Comparatively larger errors are observed for higher wavenumbers with an error of 1% for $N_z = 9$ at $k/k_p = 5$. However, for the narrow-banded simulations in this study, negligible energy is associated with wavenumbers higher than $k/k_p = 3$ suggesting that the vertical resolutions of $N_z = 9$ and $N_z = 17$ result in maximum dispersion errors of 0.15% and 0.001%, respectively. A vertical resolution of $N_z = 17$ has been used for the fine grid in this study, but the resolution

of $N_z = 9$ is also likely to be adequate for many engineering applications.

3.4.4 Symmetry Plane

A symmetry plane has been utilised along the center plane of the focusing wave group to reduce the size of the numerical domain. The boundary conditions of the symmetry plane are the same as all other sidewalls: no flow normal to the boundary enforced with a Neumann-type boundary condition in terms of the velocity potential. *OceanWave3D* incorporates a single layer of ghost nodes, outside the domain of interest, along all sidewalls and the bottom of the domain. Consequently, the stencils used at the sidewalls and bottom must be asymmetric for any finite-difference scheme higher than second-order. The current study utilises fourth, sixth and eighth-order finite difference schemes. Thus, asymmetric stencils are required along all boundaries (with the exception of the free surface) including the symmetry plane. Since asymmetric stencils are known to aggravate numerical diffusion, we have analysed the influence of the symmetry plane using the resolution of the intermediate grid with an eighth-order finite-difference scheme—stencil asymmetry is most severe for the case of an eighth-order finite difference scheme and the lower spatial resolution of the intermediate grid is anticipated to further exacerbate numerical diffusion. Simulations have been completed with and without a symmetry plane followed by a comparison of the surface elevation across the entire numerical domain at every time step. A maximum discrepancy of $0.13(10^{-3})$ m has been observed at a node on the symmetry plane coinciding with a crest of height 11.79 m—the percentage error of 0.001%, thus, confirms the negligible influence of the symmetry plane.

3.4.5 Reversibility Check

Aliasing error due to discretization is known to accumulate amongst high frequency components. To ensure that the evolution of the amplitude spectrum (see figure 3.5) is solely the result of physical processes, a *reversibility check* has been performed with the enumerated steps:

1 Prescribe initial conditions at $t = -20T_p$

2 Run simulation forwards in time for $32T_p$

3 Halt simulation at $t = 12T_p$

4 Reverse sign of time step

5 Run simulation backwards in time for $32T_p$

6 Halt simulation at $t = -20T_p$

7 Compare forwards & backwards simulation results

The amplitude spectrum has been calculated with a Discrete Fourier Transform (DFT) of the surface elevation, extracted from the simulation at every time step and linearised using four-phase separation. The linearised wavenumber amplitude spectrum is shown in figure 3.5 for the initial condition, $t = -20T_p$, as well as the time of nonlinear focus, $t = 1.3T_p$, and the final condition, $t = 12T_p$. The initial amplitude spectrum, figure 3.5(a), depicts the prescribed Gaussian unidirectional spectrum with Gaussian directional spreading (ς) of 15°. At nonlinear focus, figure 3.5(b), the amplitude spectrum exhibits minor sidelobes—symmetrically located about the spectral peak with a discernible preferential excitation of higher wavenumbers. After nonlinear focus, figure 3.5(c), the spectral sidelobes have become markedly more pronounced, with an obvious bias towards high-wavenumber components. An appreciable downshift in wavenumber for the spectral peak can also be seen. The spectral evolution of the amplitude spectrum, thus, closely matches the observations of Gibbs & Taylor (2005) for the forwards run, indicating consistent results between the code of Bateman *et al.* (2001) and *OceanWave3D*. The backwards simulation depicts close agreement at nonlinear focus, figure 3.5(d), with the forwards simulation and eventually recovers the initial condition, figure 3.5(e), with a complete reversal of the spectral changes observed in the forwards simulation. Thus, the spectral changes are attributed entirely to physical processes of wave-wave interaction rather than the accumulation of high-frequency aliasing errors.

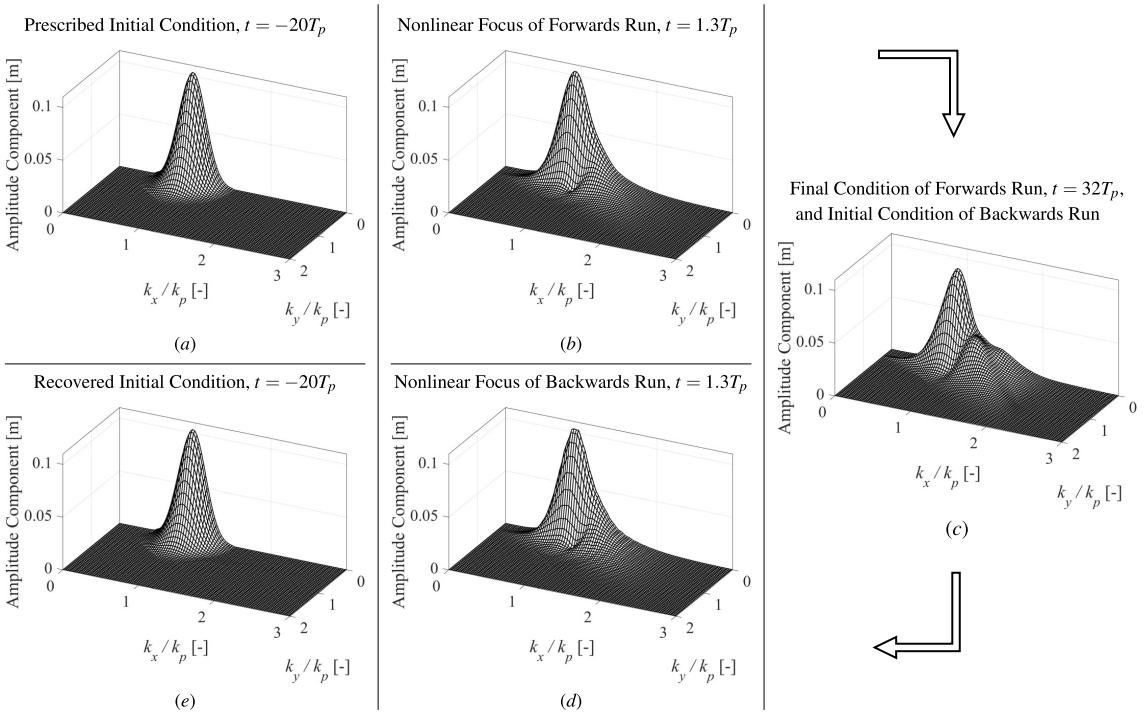

Figure 3.5: Amplitude spectra of surface elevation: (*a*–*c*) forwards run with positive time step; (*c*–*e*) subsequent backwards run with negative time step to recover initial condition.

3.4.6 Deep Water Assumption

The potential flow solver *OceanWave3D* requires a numerical domain of finite extent and, thus, cannot simulate surface waves in infinitely deep water. Dalzell (1999) provides a finite-depth version of second-order theory that considers two intersecting wave trains (denoted with subscripts 1 and 2) and provides expressions for both surface elevation and velocity potential. The expressions of Dalzell (1999) include second-order *superharmonics* and *subharmonics* neither of which adhere to the linear dispersion relation and both of which propagate with a dynamic slaved to the free wave components. The *superharmonics* manifest with an effective wavenumber of $k_1 + k_2$ and, thus, appear as a short-wavelength modification to the free harmonics. Conversely, the *subharmonics* manifest with an effective wavenumber of $k_1 - k_2$ and, thus, appear as a long-wavelength modification to the free harmonics. The larger length scale of the subharmonics results in greater depth sensitivity than observed for the superharmonics or free harmonics influencing the evolution of the wave group (figure 3.6). The second-order subharmonics are also associated with the formation of a *return current*, depicted in figure 3.7, beneath the wave group which counteracts

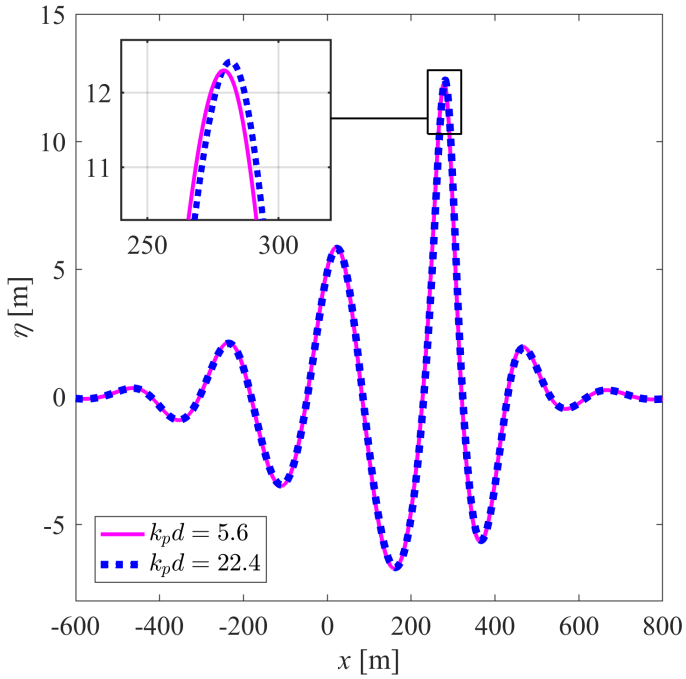

Figure 3.6: Surface elevation along center plane of wave group at a time ($t = 1T_p$) soon before nonlinear focus for domain depths of 200 m ($k_pd = 5.6$) and 800 m ($k_pd = 22.4$).

the Stokes transport occurring at the free surface and forms a localised depression in surface elevation known as a *set down* (see van den Bremer & Taylor (2015)). The return current and set down scale with the dimensions of the wave group and, thus, may be influenced by finite-depth effects even in water typically approximated to be 'deep' (see van den Bremer & Taylor (2015)). The current study has utilised a domain depth of 200 m which corresponds to a dimensionless depth of $k_pd = 5.6$. To assess the significance of the finite-depth effect, a simulation has also been performed with a domain depth of 800 m, corresponding to a dimensionless depth of $k_pd = 22.4$, with a comparison of surface elevation along the center plane of the wave group at a time, $t = 1T_p$, soon before nonlinear focus. Cubic-spline interpolation of the curves in figure 3.6 has been implemented for clarity. The amplitude of the largest crest is 0.9% smaller for $k_pd = 5.6$ which is expected because the set down should be more prevalent for $k_pd = 5.6$. The largest crest in the $k_pd = 5.6$ solution also appears to lag behind the largest crest in the $k_pd = 22.4$ solution which is the net result of counteracting effects influencing the group velocity and return current. The group velocity is expected to be greater for $k_pd = 5.6$, however, the velocity of the return current is also expected to be greater for $k_pd = 5.6$ and serves to retard

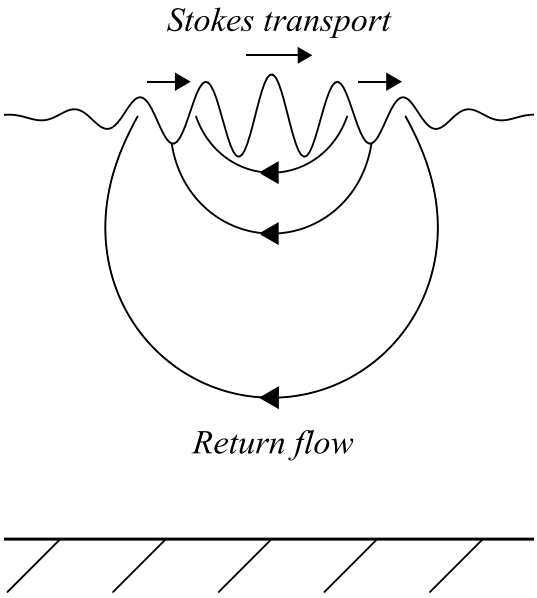

Figure 3.7: Stokes transport at free surface counteracted by return current underneath wave group (see van den Bremer & Taylor (2015))

the propagation of the group since the direction of the return current opposes the direction of wave group propagation. Figure 3.6 confirms that the effect of the return current prevails causing the wave group to lag behind in the $k_p d = 5.6$ solution. Based on figure 3.6, the depth effect is, however, considered to be negligible and $k_p d = 5.6$ a reasonable approximation for deep water.

3.4.7 Second-Order Error Waves

An exact formulation of the second-order bound harmonics at finite depths has been provided by Dalzell (1999), including expressions for both the linear and second-order terms. We evaluate the second-order terms at the mean-water-level ($z = 0$). However, we find that the linear terms must be evaluated at the free-surface ($z = \eta$) to avoid the formation of second-order error waves. Consider the expression provided by Dalzell (1999) for the first-order velocity potential, $\phi^{(1)}$, resulting from two interacting wave trains ($j = 1$ and $j = 2$):

$$\phi^{(1)} = \sum_{j=1}^{2} a_j \frac{g}{\omega_j} \frac{\cosh\{|k_j|(z+d)\}}{\cosh\{|k_j|d\}} \sin\psi_j, \tag{3.13}$$

where a_j, ω_j, k_j and ψ_j denote the component amplitude, angular frequency, wavenumber and phase respectively. Reformulation of the hyperbolic functions followed by a

first order Taylor series expansion about $z = 0$ and invocation of the linear dispersion relation, $\omega_j^2 = g|k_j| \tanh\{|k_j|d\}$, yields:

$$\begin{aligned}\phi^{(1)}\Big|_{z=\eta} &= \phi^{(1)}\Big|_{z=0} \\ &+ \sum_{j=1}^{2}\sum_{k=1}^{2}\frac{1}{2}a_j a_k \omega_j \sin\{\psi_j + \psi_k\} \\ &+ \sum_{j=1}^{2}\sum_{k=1}^{2}\frac{1}{2}a_j a_k \omega_j \sin\{\psi_j - \psi_k\}\end{aligned} \tag{3.14}$$

As can be seen, calculation of the first order initial conditions at the mean-water-level ($z = 0$) rather than the free surface ($z = \eta$) results in spurious terms which resemble second-order *superharmonics* and *subharmonics* in form—manifesting as pseudo-second-order error waves in the *OceanWave3D* simulations. Thus, we evaluate the linear terms at the free surface ($z = \eta$) for all our simulations.

3.4.8 Third-Order Error Waves

An approximation for the third-order bound harmonics has been proposed for correction of the initial conditions, based on a Stokes-type expansion for surface elevation and a scaling argument for velocity potential. Third-order correction of the initial conditions may improve the accuracy of the solution and eliminate third-order error waves which manifest as superharmonics and principal harmonics, described by the Stokes expansion in (3.7). The efficacy of the third-order correction has been analysed with the third-order superharmonic error waves. If no third-order correction is performed, the third-order bound harmonics will be generated during the course of the simulation accompanied by the generation of third-order free harmonics, known as *error waves*, required to satisfy the governing equations. The third-order superharmonic error waves possess a wavenumber substantially higher than the free harmonics comprising the wave group. Thus, the third-order superharmonic error waves will eventually lag behind and separate out from the main group as a result of the lower phase velocity. Figure 3.8 depicts the surface elevation along the center plane of the wave group after nonlinear focus, $t = 12T_p$, for a solution with exact second-order correction of the initial conditions and another solution with exact

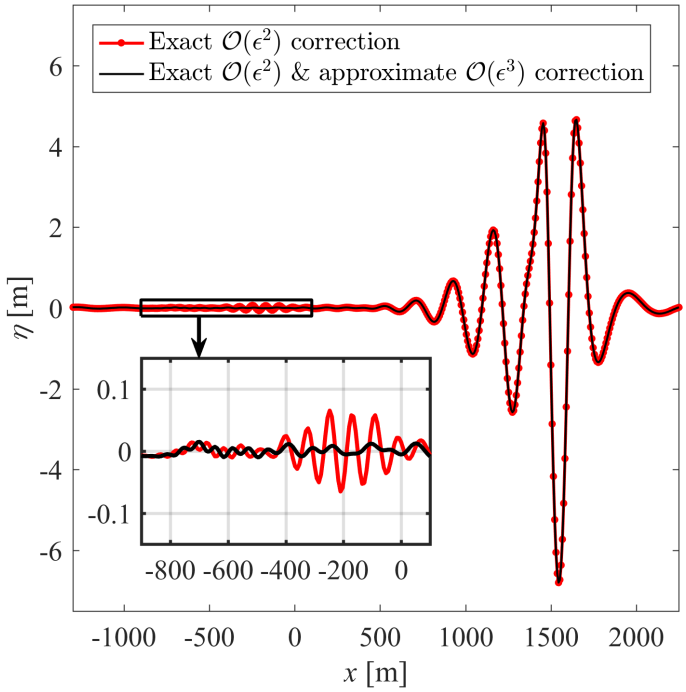

Figure 3.8: Surface elevation along center plane of wave group at time $t = 12T_p$ confirms that third-order superharmonic error waves have been eliminated.

second-order correction and approximate third-order correction of the initial conditions using the proposed scheme. As can be seen, the third-order superharmonic error waves have separated out from the main group for the case of second-order initial conditions. In contrast, the solution with approximately third-order initial conditions exhibits no discernible third-order superharmonic error waves confirming the efficacy of the proposed correction. Note, however, that a similar assessment of the third-order principal harmonic error waves cannot be performed since these error waves propagate with the wave group and do not separate out during the course of the simulation.

3.5 Discussion

The spectral evolution depicted in figure 3.5 has been attributed to resonant third-order interactions, based on the simulations of Gibbs & Taylor (2005) which utilised an expanded form of Dirichlet-Neumann operator (the G-operator) to capture various orders of nonlinear wave-wave interactions. The third-order version of the G-operator produced results similar to figure 3.5 confirming resonant third-order wave-wave interactions as the cause of the spectral evolution. A notable feature

of the spectral evolution in figure 3.5 is the development of low-wavenumber and high-wavenumber sidelobes in the initially narrow-banded wavenumber spectrum, with an obvious bias in energy transfer to high-wavenumber components. The high-wavenumber sidelobe initially develops at an angle of $\pm 35^{\circ}$ to the spectral peak up until the time of nonlinear focus, corresponding to the $\arctan(1/\sqrt{2})$ resonance angle identified by Longuet-Higgins (1976) for the spectral peak of a narrow-banded three-dimensional wave packet and the resonance angle predicted by the Phillips 'figure-of-eight' loop (see Phillips (1960)) for the narrow-banded interactions of a degenerate quartet. Agreement with the narrow-banded results of Longuet-Higgins (1976) and Phillips (1960) may be expected in the pre-focus regime since the wavenumber spectrum remains narrow-banded up until nonlinear focus (figure 3.5(b)). However, after focus, the wavenumber spectrum broadens and the high-wavenumber sidelobe shifts, ultimately forming an angle of $\pm 55^{\circ}$ with the spectral peak. Energy transfer to high-wavenumber components propagating at an oblique angle to the spectral peak has, thus, been confirmed by the present study and may be responsible for the formation of obliquely propagating wing waves observed during the simulated extreme wave event. Contour plots of surface elevation are shown in figure 3.9 in the post focus regime ($t > 1.3T_p$); only crests are shown since the contour levels are evenly distributed between 1 m and 11 m in intervals of 1 m. The surface elevation is shown on both sides of the symmetry plane for clarity and the results are plotted in a reference frame that moves with the group velocity in the direction of group propagation. Crest $\mathcal{C}0$ leads the group at $t = 5.1T_p$, shown in figure 3.9(a), and exhibits the highest surface elevation of all the crests—the position of the largest crest at the front of the wave group is consistent with the observations of Adcock & Taylor (2016) as well as Gibbs & Taylor (2005). Figure 3.9(a) also depicts crest $\mathcal{C}1$ trailing behind the leading crest and a wing wave $\mathcal{W}1$ appears at the periphery of the wave group. A gradual merger of the trailing crest $\mathcal{C}1$ with the wing wave $\mathcal{W}1$ is depicted at $t = 5.5T_p$ in figure 3.9(b) and at $t = 5.9T_p$ in figure 3.9(c). The merger process occurs as crest $\mathcal{C}1$ moves towards the front of the wave group, gradually overtaking the wing wave $\mathcal{W}1$, while the the leading crest $\mathcal{C}0$ diminishes

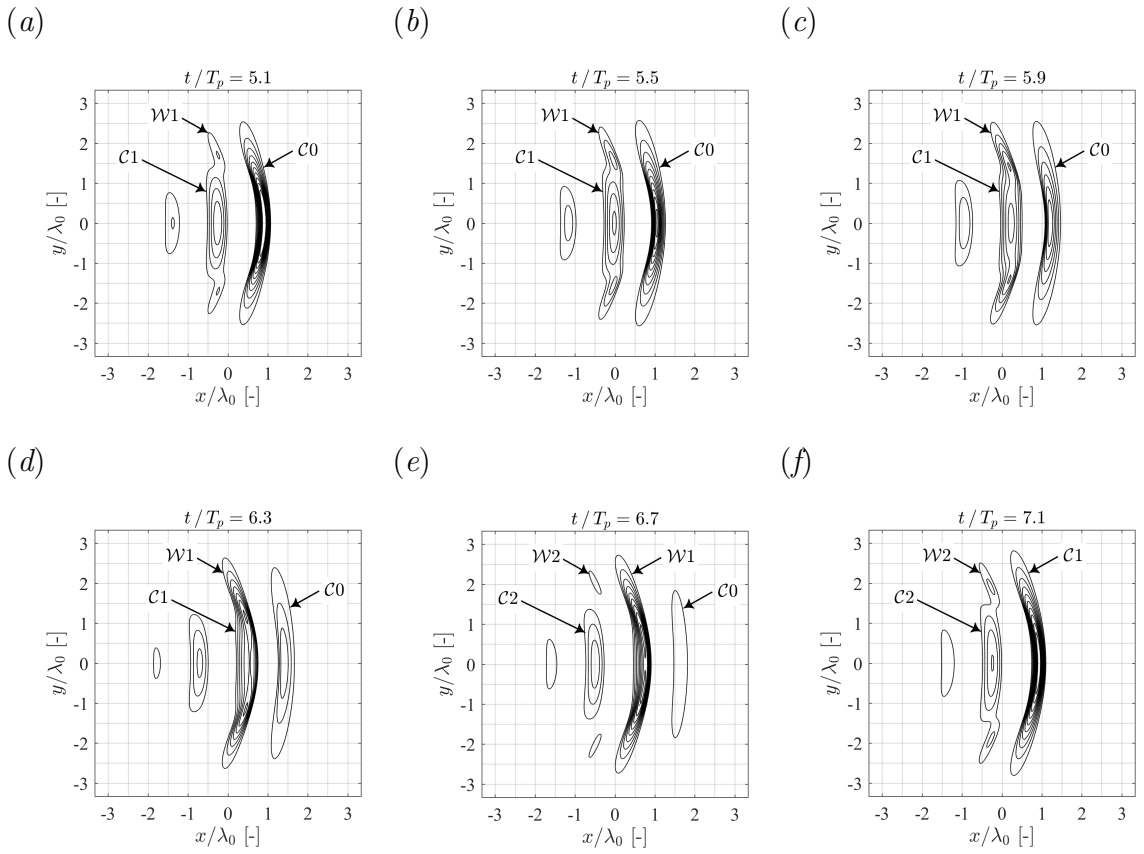

Figure 3.9: Contour plots of surface elevation evenly distributed between 1 m and 11 m in intervals of 1 m—only crests are shown: (*a*) $t\,/\,T_p = 5.1$; (*b*) $t\,/\,T_p = 5.5$; (*c*) $t\,/\,T_p = 5.9$; (*d*) $t\,/\,T_p = 6.3$; (*e*) $t\,/\,T_p = 6.7$; (*f*) $t\,/\,T_p = 7.1$.

in amplitude. The wing wave $\mathcal{W}1$ can, thus, be seen to propagate slower than the crest $\mathcal{C}1$ in the mean direction of wave group propagation—an expected result since the formation of wing waves is associated with energy transfer to high-wavenumber components propagating at an oblique angle to the spectral peak. Crest $\mathcal{C}1$ has overtaken the wing wave $\mathcal{W}1$ at $t = 6.3T_p$, shown in figure 3.9(d), and another wing wave $\mathcal{W}2$ appears at the periphery of the wave group at $t = 6.7T_p$, shown in figure 3.9(e). The distance between the wing waves $\mathcal{W}1$ and $\mathcal{W}2$ is smaller than the distance between the central crests, consistent with the high-wavenumber components thought to comprise the wing waves. Complete merger of the wing wave $\mathcal{W}1$ with the central crest $\mathcal{C}1$ can be seen at $t = 7.1T_p$ in figure 3.9(f) forming a single, crescent-shaped, broad crest at the front of the wave group while crest $\mathcal{C}0$, which initially led the group, has completely receded and no longer appears in the plot. Consistent with our results, Fujimoto *et al.* (2019) noted front-to-rear asymmetry and crescent-shape deformation as characteristic features of extreme wave events. The present study has, thus, numerically simulated a narrow-banded extreme wave event and observed energy transfer to high-wavenumber components propagating at an oblique angle to the spectral peak. The preferential energy transfers have been attributed to third-order resonant interactions and associated with the formation of wing waves at the edge of the wave group. Constructive interference between the wing waves and central crests contributes to the formation of broad, crescent-shaped crests at the front of the wave group—termed 'walls of water' Gibbs & Taylor (2005). Thus, directional energy transfer due to third-order interactions has influenced the shape of the narrow-banded extreme wave event.

3.6 Conclusion

The current study has investigated the spectral evolution of a steep, focusing wave group using the fully-nonlinear potential flow solver *OceanWave3D* with a detailed assessment of simulation fidelity. A combination of eighth-order finite differencing with a spatial resolution of 30 grid points per characteristic wavelength, in the the direction of group propagation, and a Courant-Friedrichs-Lewy (CFL) condition of 0.5 has been used to validate the simulations against a Higher-Order Spectral (HOS)

code and achieve energy conservation within 0.024%. A symmetry plane located along the center plane of the wave group has proved effective in reducing the size of the numerical domain, with negligible aggravation of the numerical diffusion, and the finite-depth domain with $k_p d = 5.6$ has been found to be a reasonable approximation for infinitely deep water. A novel approximate third-order correction scheme for the initial conditions has been proposed and shown to eliminate the third-order superharmonic error waves. Negligible aliasing error has also been confirmed by running simulations forwards in time, with a positive time step, and backwards in time, with a negative time step, to recover the initial condition and ensure that all spectral evolution is the result of physical processes. Energy transfer to high-wavenumber components propagating at an angle of approximately $\pm 35^\circ$ to the spectral peak has been confirmed, up until the time of nonlinear focus, which may be responsible for the obliquely propagating 'wing waves' observed in the simulated extreme wave event.

4 Rapid Spectral Evolution of Steep Surface Wave Groups with Directional Spreading

Abstract

We have investigated steep three-dimensional surface gravity wave groups formed by dispersive focusing using a fully-nonlinear potential flow solver. We find that third-order resonant interactions result in rapid energy transfers to higher wavenumbers and reduced directional spreading during focusing, followed by spectral broadening during defocusing, forming steep wave groups with augmented kinematics and a prolonged lifespan. If the wave group is initially narrow-banded, quasi-degenerate interactions arise, characterised by energy transfers along the resonance angle, $\pm 35.26°$, of the Phillips 'figure-of-eight' loop. Spectral broadening due to the quasi-degenerate interactions facilitates non-degenerate interactions, characterised by oblique energy transfers at approximately $\pm 55°$ to the spectral peak. We consider the influence of steepness, finite depth, directional spreading and the high-wavenumber tail on spectral evolution. Steepness is found to augment both the quasi-degenerate and non-degenerate interactions similarly. However, a reduction in depth is found to weaken the quasi-degenerate interactions more severely than the non-degenerate interactions. We observe that increased directional spreading reduces spectral evolution, partially because wave groups with more spreading focus for a shorter duration due to linear dispersion. However, we also find that directional spreading reduces the peak rates of energy transfer. Inclusion of the high-wavenumber tail of the JONSWAP spectrum further reduces rates of energy transfer compared with a Gaussian wavenumber spectrum. Thus, directional spreading and the high-wavenumber tail may be integral to a form of spectral equilibrium that reduces rapid energy transfers during a steep wave event.

4.1 Introduction

Steep groups of surface gravity waves can arise from a variety of mechanisms, both linear and nonlinear. Frequency and directional dispersion can facilitate constructive interference between wave components (see for example Fedele *et al.* (2016)) while nonlinear wave-wave interactions alter the dispersive characteristics of a wave field allowing for self focusing(see Janssen (2003)). Interactions with wind, current and bathymetry have been identified as further focusing mechanisms. Reviews by Kharif & Pelinovsky (2003), Kharif *et al.* (2008*b*), Dysthe *et al.* (2008), and Adcock & Taylor (2014) provide an extensive overview of steep wave formation and 'rogue waves'. The characteristics of steep wave groups have been investigated in numerous previous studies, both in the context of random seas and isolated wave groups.

The random sea approach, characterised by an initially-uniform phase distribution, captures the natural variability of wave focusing as well as interactions between neighbouring focused events and the global evolution of the background sea state. Steep wave events in a random sea have been found to exhibit front-rear asymmetry (Xiao *et al.* (2013), Adcock *et al.* (2015), Fujimoto *et al.* (2019)), contraction in the direction of propagation (Adcock *et al.* (2015)) and a localised reduction in spreading at focus (Adcock *et al.* (2015), Latheef *et al.* (2017)). Steep wave groups in a random sea have also been observed to exhibit a prolonged 'lifetime' due to nonlinear interactions (Fujimoto *et al.* (2019)). Random sea simulations and experiments are, however, innately inefficient because the vast majority of the observed wave events are not particularly steep. An alternative approach based on isolated wave groups has thus been pursued by previous studies, characterised by a coherent phase distribution designed to focus wave components in time and space. This is less computationally expensive, allows error waves associated with low-order numerical wave paddles or initial conditions to be easily identified and discounted (since the error waves separate out from the main group) and highlights changes in group shape. The wave-wave interactions which arise for an isolated wave group are driven by the same physical processes as those of a random sea, and we use the isolated wave group approach in this study. Numerical simulations of isolated wave groups

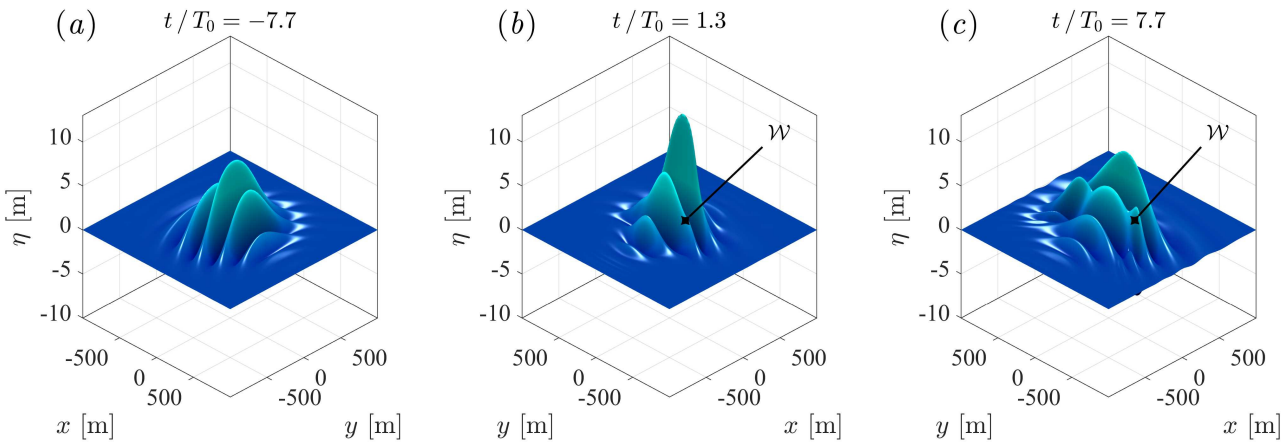

Figure 4.1: Surface elevation (η) of a steep wave group formed by dispersive focusing, simulated by Barratt *et al.* (2020) with *OceanWave3D*: (a) pre-focus, $t/T_0 = -7.5$; (b) nonlinear focus, $t/T_0 = 1.3$; (c) post-focus, $t/T_0 = 7.5$. Times are defined relative to the linear focus time, normalised by the characteristic period (T_0). The formation of 'wing waves', localised regions of elevation due to energised oblique components, is demarcated with $\mathcal{W}$. These results have been compared against the HOS simulations of Gibbs & Taylor (2005); the maximum surface elevation agrees within 0.3% with total energy conservation within 0.024% over 40 wave periods.

performed by Gibbs & Taylor (2005) and Gibson & Swan (2007) reported 'rapid' changes to the underlying wave spectrum, altering the amplitude and phase speed of the resonant components, and attributed the spectral changes to third-order resonant interactions. Barratt *et al.* (2020) used the potential flow code *OceanWave3D* to simulate focusing wave groups, depicted before focus in figure 4.1(a), at nonlinear focus in figure 4.1(b), and after focus in figure 4.1(c). Directional energy transfers were found to cause the formation of 'wing waves', localised oblique protrusions at the periphery of the wave group marked with $\mathcal{W}$ in figure 4.1. The formation of wing waves has been attributed by Barratt *et al.* (2020) to third-order resonant interactions. Thus, previous studies indicate that third-order resonant interactions influence the characteristics of steep wave groups formed by dispersive focusing.

Third-order resonance for deep-water waves has been shown by Phillips (1960) to occur between four wave components that satisfy the conditions:

$$\boldsymbol{k}_1 \pm \boldsymbol{k}_2 \pm \boldsymbol{k}_3 \pm \boldsymbol{k}_4 = 0, \tag{4.1}$$

and with the same combination of signs,

$$\omega_1 \pm \omega_2 \pm \omega_3 \pm \omega_4 = \delta\omega, \tag{4.2}$$

consistent with the deep-water linear dispersion relationship,

$$\omega_i{}^2 = gk_i. \tag{4.3}$$

Here, the wavenumber and angular frequency of each component are denoted with $\boldsymbol{k}_i$ and ω_i, respectively. The gravitational constant is denoted with g, and $\delta\omega$ represents an angular frequency mismatch which detunes the interaction. Resonant interactions can be categorised as either exactly resonant, if $\delta\omega$ is strictly zero, or nearly resonant, if $\delta\omega$ is $O(\epsilon^2\omega_0)$, based on a characteristic frequency (ω_0). As discussed by Stiassnie (2017), the Zakharov equation accounts for exactly and nearly-resonant quartets, with an associated dynamic timescale of $O(\epsilon^{-2}T_0)$, based on the characteristic time scale of the wave field (T_0). In contrast, the Hasselmann (1962) equation only accounts for exactly resonant quartets, with an associated kinetic timescale of $O(\epsilon^{-4}T_0)$. A quartet of interacting wave components is termed 'degenerate' if only three unique wave components are involved—one of the components participates twice in the interaction (e.g., $\boldsymbol{k}_1 = \boldsymbol{k}_2$). Degenerate quartet interactions form the basis of stability analyses for a regular/monochromatic wave. In this study, we consider the role of degenerate interactions in the spectral evolution of narrow-banded focusing wave groups. Previous studies indicate that quartet interactions are particularly prevalent for narrow-banded wave fields and wave fields which are 'out of equilibrium', both of which are considered in this study.

Narrow-banded wave fields have been a particular focus of previous studies due to their large third-order interactions. Longuet-Higgins (1976) investigated the resonant interactions of a narrow-banded wave spectrum, using the Davey & Stewartson (1974) equation, and calculated a resonance angle of $\arctan(\pm 1/\sqrt{2}) = \pm 35.26°$ relative to the spectral peak. Notably, the angle calculated by Longuet-Higgins (1976) matches the resonance angle of the Phillips (1960) 'figure-of-eight' loop for a degen-

erate quartet and the instability region of the 2+1 NLS equation, as calculated by Zakharov (1968), Benney & Roskes (1969) and Davey & Stewartson (1974). Crawford *et al.* (1981) used the Zakharov equation to investigate the stability of a wave train to three-dimensional modulations and observed instability bands contained within the Phillips resonance loop. The eigenvalue stability analysis of McLean (1982*b*) also revealed quartet instability bands within the Phillips resonance loop for a finite-amplitude regular wave and showed that the dominant quartet instabilities are unidirectional in deep water. Alber (1978) performed a stability analysis, based on the Davey & Stewartson (1974) equation, and found that a homogeneous spectrum of random waves is unstable to oblique inhomogeneous disturbances at angles less than $\pm 35.26^\circ$ if the bandwidth is sufficiently narrow but becomes stable for broader bandwidths. Conversely, Stuhlmeier & Stiassnie (2017) observed evidence of instability for broad-banded spectra subject to small inhomogeneous disturbances, using a discretized version of the Zakharov equation without bandwidth limits. In this study, our simulations of narrow-banded wave groups exhibit directional energy transfers which resemble the Philips resonance loop for a degenerate quartet. However, as the wave group becomes more broad-banded we observe other directional energy transfers not encompassed by the Phillips resonance loop. We discuss the impact of the spectral evolution on the shape, kinematics and lifespan of the wave groups and assess the effects of steepness, finite depth, directional spreading and the high-wavenumber tail.

Spectral equilibrium is another factor which has been linked by previous studies to the importance of third-order interactions. The role of wave-field equilibrium in the formation of extreme waves has been highlighted by Trulsen (2018); sudden changes in water depth and meteorological conditions were identified as possible causes for non-equilibrium. Random wave fields which are 'out of equilibrium' are expected to evolve on the dynamic $O(\epsilon^{-2}T_0)$ timescale, as discussed by Annenkov & Shrira (2006) and Annenkov & Shrira (2018). Onorato & Suret (2016) identified wind, current and topography as factors which can bring a wave field out of equilibrium. As noted by Trulsen (2018), random wave-field simulations initialised with

artificial spectra exhibit rapid spectral evolution during the early-stages of the simulation (see, e.g., Dysthe *et al.* (2003), Socquet-Juglard *et al.* (2005), Toffoli *et al.* (2010*b*) and Xiao *et al.* (2013)). A similar effect has been observed experimentally by Shemer *et al.* (2010) for waves generated from an artificial spectrum in a laboratory tank. Gramstad & Trulsen (2007) performed MNLS simulations based on the equation of Trulsen & Dysthe (1996) and found that the occurrence of freak waves relates to crest and group length, highlighting the role of spectral bandwidth and spreading. The theory of wave turbulence associates nonlinear interactions (and non-Gaussian properties) with intermittency and Fadaeiazar *et al.* (2018) found that directional spreading reduces intermittency also indicating that spreading may be an important feature of spectral equilibrium. Various early studies have furthered the discussion of wave-field equilibrium, including: the wind speed investigation of Waseda *et al.* (2001), the NLS simulations of Onorato *et al.* (2001), the wave turbulence study of Onorato *et al.* (2002), the kurtosis evolution analysis of Janssen (2003) and the phase-resolved stochastic analysis of Stiassnie & Shemer (2005). In this study, we perform simulations based on Gaussian as well as JONSWAP spectra, with different spreading functions, and consider the role of directional spreading and the high-wavenumber tail in spectral equilibrium for steep wave groups formed by dispersive focusing.

In summary, we perform numerical simulations of narrow-banded wave groups, formed by dispersive focusing, using a fully-nonlinear potential flow code. We investigate the rapid spectral evolution due to third-order interactions and assess the effects of steepness, finite depth, directional spreading and the tail of the spectrum. We also consider the implications of third-order interactions for the shape, lifetime and kinematics of the wave groups, as well as the implications for wave loads acting on a column. Our simulations indicate that the directional energy transfers of a narrow-banded wave group initially resemble the Phillips resonance loop but agreement deteriorates as the wave group becomes more broad-banded. We also observe that the localised nonlinear features of an individual steep wave event may depend on the spectral equilibrium of the underlying sea state.

4.2 Details of the numerical simulations

We perform numerical simulations with the fully-nonlinear potential flow code *OceanWave3D*, described in Engsig-Karup *et al.* (2009). Time marching of the initial conditions has been performed both excluding and including the nonlinear terms in the free-surface boundary conditions. The linear and nonlinear simulations begin with identical amplitudes and phases for the wave components, highlighting the influence of wave-wave interactions. We use the method of phase separation (Fitzgerald *et al.* (2014)) to remove the bound harmonics from the nonlinear simulations, isolating the free wave components.

4.2.1 Initial conditions

We prescribe the initial conditions in terms of surface elevation, $\eta(x, y, t)$, and velocity potential at the free surface, $\tilde{\phi}(x, y, t)$, calculated 15 characteristic wave periods before the time of linear focus. Time is thus defined relative to the linear focus time ($t/T_0 = 0$), and the free-surface quantities time marched for 30 wave periods, terminating the simulation 15 wave periods after the linear focus time. Typical of the North Sea, the initial peak of the wavenumber spectrum for all simulations is located at $k_p = 0.02796$ m^{-1}, which corresponds to a characteristic wavelength (λ_0) of 225 m and characteristic wave period (T_0) of 12.0–12.8 s for depths in the range of 48.7–200 m.

The variance density spectrum $F(k, \theta)$ of the initial conditions has been defined as the product of a wavenumber magnitude spectrum $S(k)$ and a spreading function $D(\theta)$. Two types of wavenumber magnitude spectra are considered in this study, a Gaussian spectrum:

$$S(k) = S_0 \exp\left(\frac{-(k - k_p)^2}{2{k_w}^2}\right), \tag{4.4}$$

and a JONSWAP spectrum with $\gamma = 3.3$ (Hasselmann *et al.* (1973)). The coefficient S_0 of (4.4) is taken to be unity since the focused amplitude of the wave event is determined by A_L in (4.6). The JONSWAP spectrum represents a realistic spectrum for fetch-limited seas. Here, k_p denotes the wavenumber corresponding to the initial peak of the wavenumber spectrum and k_w represents the bandwidth of the Gaussian

Wavenumber spectrum, $S(k)$	Gaussian, JONSWAP ($\gamma = 3.3$), $k_p = 0.02796$ m^{-1}, $k_w = 0.004606$ m^{-1}
Spreading function, $D(\theta)$	Gaussian, Ewans (1998)
Spreading parameter, ς_0	5°, 10°, 15°, 20°, 25°
Steepness, $A_L k_p$	0.12, 0.15, 0.18, 0.21, 0.24, 0.27, 0.30
Depth, $k_p d$	1.363, 1.600, 2.000, 2.600, 3.142, 5.592

Table 4.1: Parameter space of initial conditions.

spectra. A value of $k_p = 0.02796$ m^{-1} has been used for both the Gaussian and JONSWAP spectra and a bandwidth of $k_w = 0.004606$ m^{-1} has been used for all the Gaussian cases. The Gaussian spectra have been calculated from three bandwidths below the spectral peak ($k = k_p - 3k_w$) to three bandwidths above the spectral peak ($k = k_p + 3k_w$) and the JONSWAP spectrum has been calculated up to $k/k_p = 10$ based on the resolution of the grid in the *OceanWave3D* simulations. Note that the Gaussian wavenumber magnitude spectrum used in the study closely approximates the shape of the spectral peak for a JONSWAP spectrum with $\gamma = 3.3$.

Two different spreading functions have been implemented in this study: a frequency-independent Gaussian spreading function:

$$D(\theta) = \frac{1}{\varsigma_0\sqrt{2\pi}} \exp\left(\frac{-\theta^2}{2\varsigma_0^2}\right), \tag{4.5}$$

and the frequency-dependent spreading function of Ewans (1998). The Gaussian spreading function includes an initial spreading parameter (ς_0) listed in table 4.1 for the various test cases. The Ewans (1998) spreading function has been selected to account for the oblique angle of high-wavenumber components in the tail of the spectrum frequently observed in the field measurements of fetch-limited seas as described by Banner & Young (1994), Hwang *et al.* (2000), Leckler *et al.* (2015) and Peureux *et al.* (2018).

Quasi-determinism (QD) theory, based on Boccotti (1983) and Lindgren (1970) (see Boccotti (2000) for a comprehensive review), indicates that the average shape of a an extreme event in a random, linear Gaussian field is the scaled auto-correlation function, used in this study to calculate the initial conditions of the extreme wave

groups. The wave field is, thus, spatially inhomogeneous, and the linear surface elevation of the wave group, $\eta(x, y, t)$, is given by:

$$\eta(x, y, t) = A_L \frac{\sum_{i,j} F(k_i, \theta_j) \cos\left(k_i \cos\theta_j \, x + k_i \sin\theta_j \, y - \omega_i t + \varphi_0\right)}{\sum_{i,j} F(k_i, \theta_j)}. \tag{4.6}$$

Here, k_i is the magnitude of the wavenumber for each component, θ_i is the direction of propagation, A_L is the linear amplitude of the wave group at focus ($t/T_0 = 0$) and the angular frequency of each component (ω_i) is calculated from the arbitrary-depth linear dispersion relationship, $\omega_i = \sqrt{g k_i \tanh\left(k_i d\right)}$. Table 4.1 lists the linear steepnesses of the simulated wave groups as well as the dimensionless depths, both based on the initial peak of the wavenumber spectrum k_p. The phase offset (φ_0) is required for the four-phase separation technique (Fitzgerald *et al.*, 2014) used to remove bound harmonics from the wave spectrum; we have performed the simulations with phase offsets of 0°, 90°, 180°, 270° for every case, which allows the free harmonics to be approximately separated from the bound harmonics. We apply exact second-order corrections to the initial conditions based on the formulation of Dalzell (1999) together with an approximate form of third-order correction based on Barratt *et al.* (2020). Note that we evaluate the second-order terms of Dalzell (1999) at the mean water level but we evaluate the linear terms at the free surface to minimise the formation of second-order error waves.

4.2.2 Code description and simulation fidelity

OceanWave3D discretizes the potential flow equations for surface gravity waves in a three-dimensional spatial domain using Cartesian coordinates (x, y, z). The code is based upon an Eulerian frame of reference and cannot capture overturning waves. A non-conformal transform is used to map the solution to a time-invariant domain comprised of structured rectilinear grids:

$$\sigma \equiv \frac{z + d(x, y)}{\eta(x, y, t) + d(x, y)}, \tag{4.7}$$

and uniform depth, $d(x, y) = d$, in this study. Classic fourth-order Runge-Kutta (RK4) time marching combined with finite differencing of the spatial derivatives

Characteristic time and length scales	Wavelength (λ_0) 225 m Wave period* (T_0) 12.0–12.8 s
Numerical domain	Length (L) 7680 m Width† (W) 2560 m Depth (d) 48.7–200 m †Out from symmetry plane at $y = 0$
Discretization of Gaussian cases	$N_x = 1024$, $\Delta x = 7.5$ m $N_y = 256$, $\Delta y = 10.0$ m $N_z = 8$, CGL-distribution in z $N_{MG} = 10$ $N_t = 1801$, $\Delta t = 0.2$ s, CFL = 0.5
Discretization of JONSWAP cases	$N_x = 2048$, $\Delta x = 3.75$ m $N_y = 512$, $\Delta y = 5.0$ m $N_z = 8$, CGL-distribution in z $N_{MG} = 11$ $N_t = 1801$, $\Delta t = 0.2$ s, CFL = 1.0
Finite differencing	Eighth-order (FD8) in space
Time marching	Fourth-order Runge-Kutta (RK4)

Table 4.2: Numerical details of *OceanWave3D* simulations.

yields a linear system of equations, solved with the Generalised Minimum Residual (GMRES) algorithm. Left preconditioning is performed once every iteration with multi-grid Gauss-Seidel relaxation. The multi-grid scheme is based on direct coarse grid approximation and follows a 'V-cycle', descending from the finest grid resolution down to the coarsest grid resolution before ascending again from the coarsest grid resolution to the finest grid resolution, with one pre-smoothing and one post-smoothing step. We apply a relative tolerance of 10^{-6} for convergence of the GMRES algorithm at each time step.

The grid-convergence study of Barratt *et al.* (2020), based on grid halving in all three spatial dimensions, informs our selection of the grid resolution. The size of the numerical domain is listed in table 4.2, indicating the length (L) in the x-direction, width (W) in the y-direction, and depth (d) in the vertical, z-direction. The length and width of the domain are fixed for all simulations. However, we vary the depth of the domain. The horizontal grid distribution (Δx, Δy) is uniform throughout the domain. We utilise a symmetry plane along the centreline of the wave group ($y = 0$). Thus, the width of the domain listed in table 4.2 only represents half of the

effective domain width. The position of the symmetry plane results in asymmetric stencils along the center of the wave group. However, by performing simulations with and without a symmetry plane, Barratt *et al.* (2020) confirmed that the additional numerical diffusion due to the asymmetric stencils is negligible. We use powers of two for the number of grids (N_x, N_y, N_z) in all three spatial dimensions, to ensure the maximum number of multi-grid levels (N_{MG}) for the preconditioning scheme. The number of grids in the horizontal directions (N_x, N_y) has been doubled for the JONSWAP cases, compared with the Gaussian cases, to better resolve the smaller-wavelength components in the tail of the JONSWAP spectrum.

We use eighth-order finite differencing, confirmed by Barratt *et al.* (2020) to exhibit a grid-independent iteration count for simulations similar to those of this study. Central-differencing schemes have been used, except at the boundaries, and the order of finite differencing is consistent throughout. We include a single layer of ghost nodes, outside the domain of interest, for all surfaces except the free surface. The presence of ghost nodes at the bottom boundary allows both continuity and the Neumann boundary condition to be simultaneously satisfied while improving the numerical stability of the preconditioning scheme, even for anisotropic grid distributions in the vertical direction. Thus, we use the symmetric half of a Chebyshev-Gauss-Lobatto (CGL) distribution in the vertical direction: $\sigma_j = \sin\left((\pi[j-1])/(2[N_z-1])\right)$, where j denotes the index of the grid point with $j = 1$ at the bottom and $j = N_z$ at the free surface. The time step size, based on the Courant-Friedrichs-Lewy (CFL) condition, influences diffusion error but not dispersion error. Thus, we use the same time step for the JONSWAP and Gaussian cases based upon the permissible levels of diffusivity, resulting in CFL values of 1.0 and 0.5 respectively.

4.2.3 Spectral parameters

We analyse the spectral evolution of the various simulations performed in this study in terms of moments of the wavenumber-amplitude spectrum as well as spreading bandwidth. We also consider the wave action density spectrum to determine the timescales of energy transfer between wave components. The zeroth moment of the

discrete wavenumber-amplitude spectrum ($\mathcal{M}_0$):

$$\mathcal{M}_0 = \sum_i |\hat{\eta}(k_i, \theta_i)|, \tag{4.8}$$

represents a summation of amplitudes for the Fourier components of surface elevation in the discrete wavenumber spectrum, $\hat{\eta}(k_i, \theta_i)$, and thus represents the amplitude of the wave which would be formed by perfect constructive interference between all wave components. For linear evolution, $\mathcal{M}_0$ in (4.8) equals A_L as defined in (4.6) for the entirety of the simulation. The zeroth spectral moment $\mathcal{M}_0$ can be expected to increase as energy transfers in a narrow-banded spectrum lead to broadening of the spectrum. We use the first moment of the wavenumber-amplitude spectrum

$$\mathcal{M}_1 = \sum_i k_i |\hat{\eta}(k_i, \theta_i)|, \tag{4.9}$$

normalised by the zeroth spectral moment ($\mathcal{M}_0$) to define a mean wavenumber ($\mathcal{K}$):

$$\mathcal{K} = \mathcal{M}_1 / \mathcal{M}_0. \tag{4.10}$$

The mean wavenumber $\mathcal{K}$ increases if high-wavenumber components grow in amplitude while low-wavenumber components diminish in amplitude. Thus, $\mathcal{K}$ increases if energy transfer from low-wavenumber components to high-wavenumber components prevails and decreases in the opposite scenario. We also consider the root-mean-square (RMS) spreading (ς):

$$\varsigma = \sqrt{\frac{\sum_i {\theta_i}^2 |\hat{\eta}(k_i, \theta_i)|}{\mathcal{M}_0}}, \tag{4.11}$$

which quantifies the bandwidth of directional spreading. Note that the initial value of (4.11) matches the parameter ς_0 in (4.5) if the frequency-independent Gaussian spreading function is used. The spectral parameters defined in (4.10) and (4.11) have been evaluated for both the Gaussian and JONSWAP cases based on wavenumber components in the range: $0 < k_x/k_p \leq 2$ and $-2 \leq k_y/k_p \leq 2$. We restrict the calculation to the vicinity of the spectral peak to assess the Gaussian spectrum as a

model for the peak of a JONSWAP spectrum. Thus, we do not include the full tail of the JONSWAP spectrum in the calculation of the spectral parameters. However, we note that the considered range of wavenumbers accounts for 96–98% of the total energy for the JONSWAP cases, calculated at every time step for each simulation.

The total wave action of a wave group is a conserved quantity (see Komen *et al.* (1994)), and the spectrum of wave action density has been calculated from the amplitude spectrum to quantify the component growth rates. The energy density spectrum $E(k_i, \theta_i)$, associated with the amplitude spectrum of surface elevation in wavenumber space, has been calculated based upon the amplitude of each Fourier component, a_i, and the discrete wave number intervals $(\Delta k_x, \Delta k_y)$ together with the density of water (ρ):

$$E(k_i) = \frac{\frac{1}{2}\rho g a_i^2}{\Delta k_x \Delta k_y}. \tag{4.12}$$

Using the linear dispersion relation, the wave action density spectrum is given by:

$$A(k_i) = \frac{E(k_i)}{\omega_i}, \tag{4.13}$$

In this study, we consider the growth rate of specific wave components. For context, Stiassnie (2001) notes that the growth rate associated with the Hasselmann equation is:

$$\big[\partial \mathcal{A}(k_i, \theta_i)/\partial t\big] T_0 \big/ \mathcal{A}(k_i, \theta_i) = O(\epsilon^4 \omega_0 T_0), \tag{4.14}$$

where ω_0 represents the characteristic wave period, and the growth rate associated with the Zakharov equation is:

$$\big[\partial \mathcal{A}(k_i, \theta_i)/\partial t\big] T_0 \big/ \mathcal{A}(k_i, \theta_i) = O(\epsilon^2 \omega_0 T_0). \tag{4.15}$$

4.3 Results and discussion

We begin our analysis with a base case, followed by an investigation of steepness, finite depth, directional spreading and the high-wavenumber tail of the spectrum.

4.3.1 Directional energy transfers due to third-order interactions

The selected base case features a Gaussian wavenumber spectrum with a Gaussian spreading function and a spreading parameter (ς) of 15°, denoted as case 'GG15'. We prescribe a linear steepness ($A_L k_p$) of 0.3 for the base case at the linear focus time ($t/T_0 = 0$), from (4.6), together with a dimensionless depth ($k_p d$) of 3.142. Results are shown for the linear version of the base case, in which the nonlinear terms of the free surface boundary conditions are neglected, and the fully nonlinear version of the base case which includes all terms in the free-surface boundary conditions. Figure 4.1 shows the surface elevation corresponding to the nonlinear version of the base case, including the wing waves (demarcated with $\mathcal{W}$) which form as a result of directional energy transfers.

The steepness of the wave envelope over time ($A(t)k_p$) is shown in figure 4.2(a) for both the linear and nonlinear version of the base case. As expected, the linear envelope is symmetric about the focal time. However, the nonlinear envelope exhibits asymmetry about $t/T_p = 0$ due to nonlinear wave-wave interactions which modify the amplitude and dispersion of the wave components, extending the life span of this focused wave event, as observed by Fujimoto *et al.* (2019). Nonlinear interactions are known to alter the phase speed of the participating wave components, which can counteract dispersion and preserve the form of a focused wave event—the competing effects of nonlinearity and dispersion is a central idea to the Benjamin-Feir index (see Janssen (2003)). Figure 4.2(b) shows the zeroth spectral moment of the amplitude spectrum ($\mathcal{M}_0$), normalised by the linear focus amplitude (A_L). For linear evolution, the ratio equals unity at all times. However, for nonlinear evolution the zeroth moment can be seen to increase during the focusing of the wave group reaching a maximum value of $\mathcal{M}_0/A_L = 1.7$ at $t/T_0 = 8.0$ in figure 4.2(b). Although the zeroth moment increases continuously during the wave focusing event, the amplitude of the nonlinear event at focus is smaller than the amplitude of the linear event due to modifications in phase speed. For the linear simulation, the phase of each component has been selected to ensure perfect constructive interference at $t/T_0 = 0$. For the nonlinear simulation, nonlinear dispersion prevents perfect constructive interference

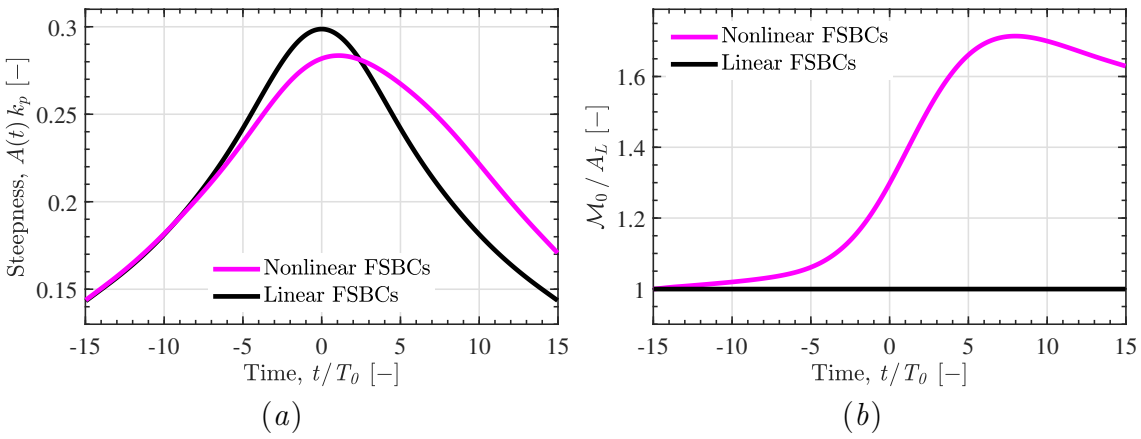

(a) (b)

Figure 4.2: Comparison for case GG15 with linear and nonlinear free-surface boundary conditions (FSBCs), a steepness of $A_L k_p = 0.3$ and a dimensionless depth of $k_p d = 3.142$: (a) Steepness of the wave envelope over time. The amplitude $A(t)$ is based on the maximum elevation of the wave envelope at time t. The linear case is represented by the black line (——) and the nonlinear case is represented by the magenta line (——). (b) The zeroth moment of the wavenumber-amplitude spectrum ($\mathcal{M}_0$) normalised by the linear focus amplitude (A_L). The dimensionless ratio is plotted over time for the nonlinear case (——) and the linear case (——). For the linear case, the ratio $\mathcal{M}_0/A_L$ equals unity at all instances in time.

at focus. Thus, the steepness of the focused event is reduced, despite the increase in zeroth moment shown in figure 4.2(b). Although the spectral evolution of the nonlinear event does not increase the amplitude of the wave envelope in this case, the wave-wave interactions significantly alter the shape of the wave group and the magnitude of the wave kinematics, discussed in section 4.3.2. Adjusting the initial phase of the wave components could evidently result in a nonlinear event which is locally larger than the linear version of the event.

For the base case, we also consider the evolution of the wave spectrum due to nonlinear wave-wave interactions, calculated with a Discrete Fourier Transform (DFT) of the wave group surface elevation. Figure 4.3 depicts contour plots of the amplitude spectrum in wavenumber space for: the initial condition, $t/T_0 = -15$; the time of nonlinear focus, $t/T_0 = 1.3$; and the end of the simulation, $t/T_0 = 15$. Segments of the Phillips 'figure-of-eight' resonance loop are also shown. The initial condition in figure 4.3(a) is narrow-banded and remains narrow-banded during the early stages of focusing due to the low steepness of the initially dispersed wave group. However, evolution of the amplitude spectrum occurs as the wave group steepens and approaches focus, see figure 4.2. In particular, energy transfer to

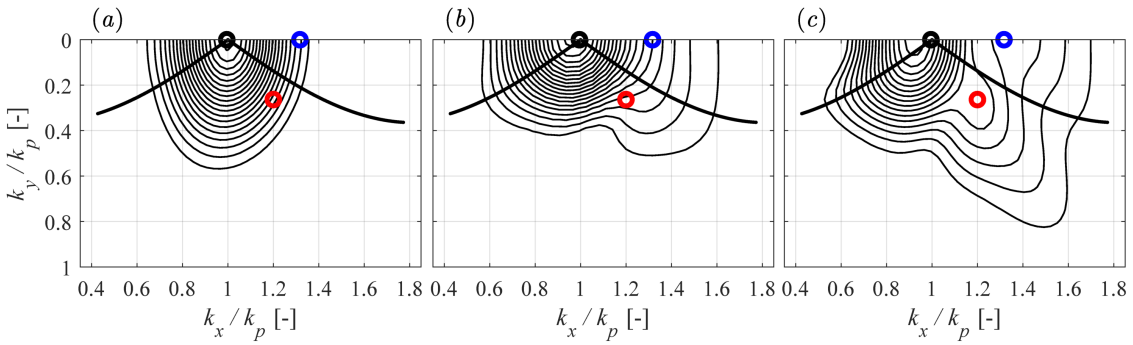

Figure 4.3: Discrete amplitude spectra of surface elevation corresponding to case GG15 with a steepness of $A_L k_p = 0.3$ and a dimensionless depth of $k_p d = 3.142$: (a) initial condition, $t/T_0 = -15$; (b) nonlinear focus, $t/T_0 = 1.3$; (c) post-focus, $t/T_0 = 15$. Contour levels (——) are evenly distributed between 0.01 m and 0.105 m in intervals of 0.005 m. The thick black line (▬) represents a segment of the Phillips 'figure-of-eight' resonance loop and the open circles specify particular wavenumber components for further analysis: $\mathcal{Q}$ (o) $k_x/k_p = 0.995$, $k_y/k_p = 0.000$; $\mathcal{R}$ (o) $k_x/k_p = 1.200$, $k_y/k_p = 0.263$; $\mathcal{S}$ (o) $k_x/k_p = 1.317$, $k_y/k_p = 0.000$.

high-wavenumber components is evident in figure 4.3(b), with a directional bias qualitatively consistent with the Phillips resonance loop, at angles of $\pm 35.26°$ to the spectral peak, accompanied by unidirectional energy transfers along the k_x-axis. A low-wavenumber sidelobe can be seen at nonlinear focus in figure 4.3(b), although the footprint is considerably smaller than the high-wavenumber sidelobe. The spectral changes observed in figure 4.3(b) are, thus, reminiscent of the Class I instability band for a regular wave train of finite amplitude, described by McLean (1982*b*), and we attribute the spectral changes to 'quasi-degenerate' interactions. A degenerate quartet is comprised of only three unique wave components (since one component participates twice, $\boldsymbol{k}_1 = \boldsymbol{k}_2$) and forms the basis of stability analyses for a regular/monochromatic wave, assuming that $\boldsymbol{k}_1$ and $\boldsymbol{k}_2$ both equate to the characteristic wavenumber $\boldsymbol{k}_0$ of the regular wave. Phillips (1960) showed that the interacting components of a degenerate quartet form the 'figure-of-eight' resonance loop, and the eigenvalue stability analysis of McLean (1982*b*) indicates that the instability band of a finite-amplitude regular wave includes components on the k_x-axis if the water is deep. In this study, we consider narrow-banded wave spectra which form focused wave groups. The concentration of energy around the spectral peak means that we anticipate interactions in which $\boldsymbol{k}_1$ and $\boldsymbol{k}_2$ resemble the characteristic wavenumber $\boldsymbol{k}_0$ (wavenumber of the initial spectral peak) but may not strictly equate. Thus, we

expect $\boldsymbol{k}_1 \approx \boldsymbol{k}_2 \approx \boldsymbol{k}_0$ for our narrow-banded wave groups, rather than $\boldsymbol{k}_1 = \boldsymbol{k}_2 = \boldsymbol{k}_0$ as expected for a regular/monochromatic wave. Interactions of the form $\boldsymbol{k}_1 \approx \boldsymbol{k}_2$ are not strictly degenerate. Thus, we use the term 'quasi-degenerate' to describe quartet interactions with $\boldsymbol{k}_1 \approx \boldsymbol{k}_2$. Despite the resemblance of the directional energy transfers figure 4.3(b) to the Phillips resonance loop, it seems improbable that all the directional energy transfers in figure 4.3(b) are the result of exactly degenerate quartets, due to the strict definition. Thus, we attribute the directional energy transfers evident in 4.3(b) to quasi-degenerate interactions since the definition of quasi-degenerate interactions is more relaxed and encompasses a large number of interactions with resonance loops that resemble the classic Phillips resonance loop. After nonlinear focus, figure 4.3(c), the amplitude spectrum continues to broaden with directional energy transfer to high-wavenumber components not encompassed by the Phillips resonance loop. Divergence from the figure-of-eight is likely due to the degenerate nature of the resonance loop. Broadening of the spectrum during focusing, thus, appears to facilitate non-degenerate interactions ($\boldsymbol{k}_1 \neq \boldsymbol{k}_2$) after focus, resulting in high-angle oblique energy transfers along a $\pm 55°$ angle. Notably, there are spectral changes which arise during focus that do not reverse after focus indicating permanent changes to the spectrum. We note that suppressed linear dispersion has been observed by Steer *et al.* (2019) for modulations which propagate at $\pm 35.26°$ to the wave group, which can increase the lifetime of a focused wave event. Thus, the $\pm 35.26°$ energy transfers apparent in figure 4.3(b) may contribute to the lifetime extension depicted in figure 4.2(a). The formation of a high-wavenumber sidelobe has also been associated by Adcock & Taylor (2016) with contraction of the wave group in the direction of propagation. The amplitude spectrum at nonlinear focus also exhibits a contraction of the spectrum along the k_y-direction, which implies lateral expansion of the wave group and a focused wave event which is less directionally spread than the initial wave spectrum.

Three specific components in the wavenumber spectrum ($\mathcal{Q}$, $\mathcal{R}$, $\mathcal{S}$) have been selected for further analysis of the growth rate—the components are shown in figure 4.3 and listed in table 4.3. Component $\mathcal{Q}$ coincides with the initial peak of the

	$\mathcal{Q}$	$\mathcal{R}$	$\mathcal{S}$
k_x/k_p	0.995	1.200	1.317
k_y/k_p	0.000	0.263	0.000
$\lvert\boldsymbol{k}\rvert/k_p$	0.995	1.228	1.317

Table 4.3: Wavenumber components selected for growth analysis shown in figure 4.3.

wavenumber spectrum, component $\mathcal{S}$ denotes a component on the k_x-axis, in the instability band of a finite-amplitude regular wave train, and component $\mathcal{R}$ coincides with the local maximum of the oblique ridge at $\pm 55^\circ$ formed by non-degenerate interactions. Figure 4.4(a) shows the wave action density of the three components. Before focus, the wave action density of component $\mathcal{Q}$ grows, indicating energy transfer to the spectral peak, while the wave action density of component $\mathcal{R}$ declines, due to contraction of the spectrum in the k_y-direction, and component $\mathcal{S}$ grows, due to energy transfers to higher wavenumbers. Before nonlinear focus occurs at $t/T_0 = 1.3$, the wave action density of component $\mathcal{Q}$ begins to decline, signalling the onset of a downshift in the spectral peak, and component $\mathcal{R}$ begins to grow, continuing to grow for the remainder of the simulation. Component $\mathcal{S}$ reaches a maximum in wave action density before nonlinear focus and thereafter begins to decline, which is likely a result of spectral broadening inhibiting quasi-degenerate interactions. Previous work by Longuet-Higgins (1978), McLean (1982*b*), Francius & Kharif (2003) and Fedele (2014) has also demonstrated the suppression of unidirectional instabilities at high wave steepnesses, which may also constrain the growth in wave action density for component $\mathcal{S}$ during focus. The corresponding dimensionless growth rates for the three components ($\mathcal{Q}$, $\mathcal{R}$, $\mathcal{S}$) are shown in figure 4.4(b) in terms of wave action density. For context, the dynamic timescale associated with near-resonance and the Zakharov equation, $O(\epsilon^2\omega_0 T_0)$, is shown together with the kinetic timescale associated with exact resonance and the Hasselmann equation, $O(\epsilon^4\omega_0 T_0)$.

Similar results to figure 4.3 have been observed by Adcock & Taylor (2016) using the MNLS equation of Trulsen & Dysthe (1996). Thus, these spectral changes can be attributed to resonant third-order interactions, since the MNLS equation is only capable of resolving third-order/four-wave interactions, as demonstrated by

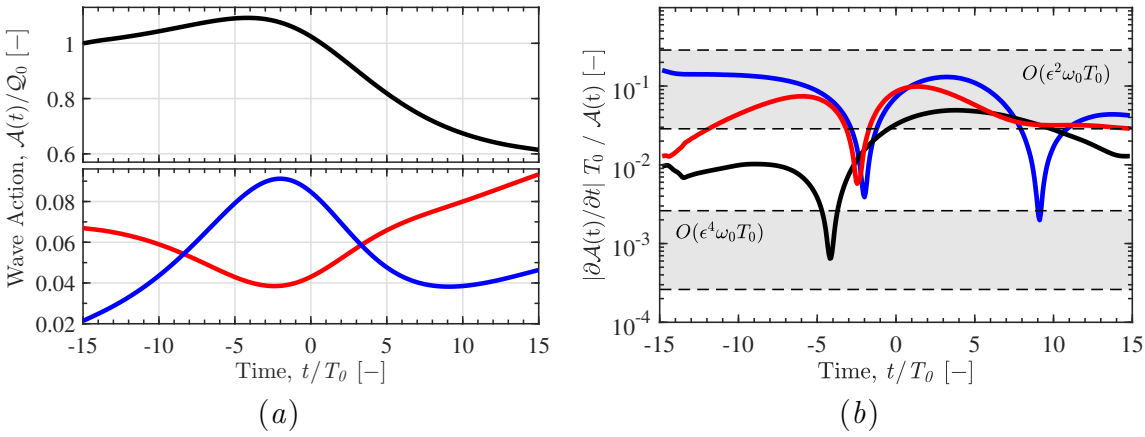

(a) (b)

Figure 4.4: Component-wise analysis of the wave action density spectrum for case GG15 with a steepness of $A_L k_p = 0.3$ and a dimensionless depth of $k_p d = 3.142$: (a) the wave action density of each component over time, normalised by the initial wave action density of the spectral peak ($\mathcal{Q}_0$); (b) the nondimensional growth rate of each component over time, plotted on a logarithmic ordinate. The components correspond to those indicated in figure 4.3: $\mathcal{Q}$ (——) $k_x/k_p = 0.995$, $k_y/k_p = 0.000$; $\mathcal{R}$ (——) $k_x/k_p = 1.200$, $k_y/k_p = 0.263$; $\mathcal{S}$ (——) $k_x/k_p = 1.317$, $k_y/k_p = 0.000$. The dynamic growth rate $O(\epsilon^2\omega_0 T_0)$ and the kinetic growth rate $O(\epsilon^4\omega_0 T_0)$ are indicated by bounded (– – –) grey bands. The value of ϵ equates to $A_L k_p/\pi$ in the growth rate calculations.

Stiassnie (1984). Furthermore, the HOS simulations of Gibbs & Taylor (2005) were performed with a truncated form of Dirichlet-Neumann operator and yielded results similar to figure 4.3; the authors indicated that a comparison of third-order and fifth-order simulations produced no significant variations. Thus, the fourth-order Class II instabilities observed by McLean (1982*b*) do not appear to be significant for the simulated wave groups in this study, consistent with the results of Fujimoto & Waseda (2016). Although the present study is focused on isolated wave groups, the oblique energy transfers and consequent spectral evolution shown in figure 4.3 qualitatively resemble previous random sea results (e.g., Dysthe *et al.* (2003), Socquet-Juglard *et al.* (2005), Toffoli *et al.* (2010*b*), Xiao *et al.* (2013), Simanesew *et al.* (2016) and Simanesew *et al.* (2018)). Toffoli *et al.* (2010*b*), for example, used Higher Order Spectral (HOS) simulations to demonstrate that a random wave field initialised with frequency-independent spreading develops frequency-dependent spreading resembling figure 4.3. The simulations of Toffoli *et al.* (2010*b*) did not include external forcing, such as wind and breaking, and the spectral evolution can thus be attributed to nonlinear wave-wave interactions. Simanesew *et al.* (2016) performed

laboratory experiments and Modified Nonlinear Schrödinger (MNLS) simulations initialised with frequency-independent spreading and also observed the development of frequency-dependent spreading. Dynamic nonlinear contributions to the development of frequency-dependent spreading, above and below the spectral peak, were identified, consistent with our observations. Simanesew *et al.* (2018) investigated wave spectra based on field measurements from the North Sea and MNLS simulations, using different data-adaptive methods and indicate that frequency-dependent spreading can be a numerical artefact of 'peak-splitting' by maximum entropy methods. However, Simanesew *et al.* (2018) conclude that the development of frequency-dependent spreading in the spectral tail does also result from nonlinear wave-wave interactions, consistent with our results. Thus, the local spectral evolution surrounding steep wave events, featuring oblique energy transfers away from the spectral peak, may contribute to the global evolution of the underlying sea-state. The development of frequency-dependent spreading does, however, occur slower for the background sea-state of a random sea requiring hundreds of wave periods to fully develop. In contrast, significant frequency-dependent spreading develops within 30 wave periods in the present study of steep wave groups.

4.3.2 Implications of spectral changes for kinematics and loads

The spectral changes observed in figure 4.3 are relevant to the kinematics of the wave group. The wave loads acting upon a vertical cylinder can be calculated with the Morison equation, see for example Paulsen *et al.* (2014), yielding the horizontal force:

$$F = \int_{-d}^{\eta} \frac{1}{2} C_D \rho A \, u(z)|u(z)| \, dz + \int_{-d}^{\eta} C_M \rho V \frac{Du(z)}{Dt} \, dz, \tag{4.16}$$

featuring a drag term with a quadratic dependency on the horizontal velocity, $u|u|$, and an inertial term proportional to the Lagrangian acceleration of the horizontal velocity, Du/Dt, defined in terms of the material derivative. Here, $u(z)$ represents the characteristic horizontal velocity which may vary in the vertical, z-direction. Constants C_D and C_M depend on geometry and Reynolds number. The frontal area of the body (A) as well as the volume (V) are required for the calculation, together with the density of the fluid (ρ). Energy transfers to higher wavenumbers augments

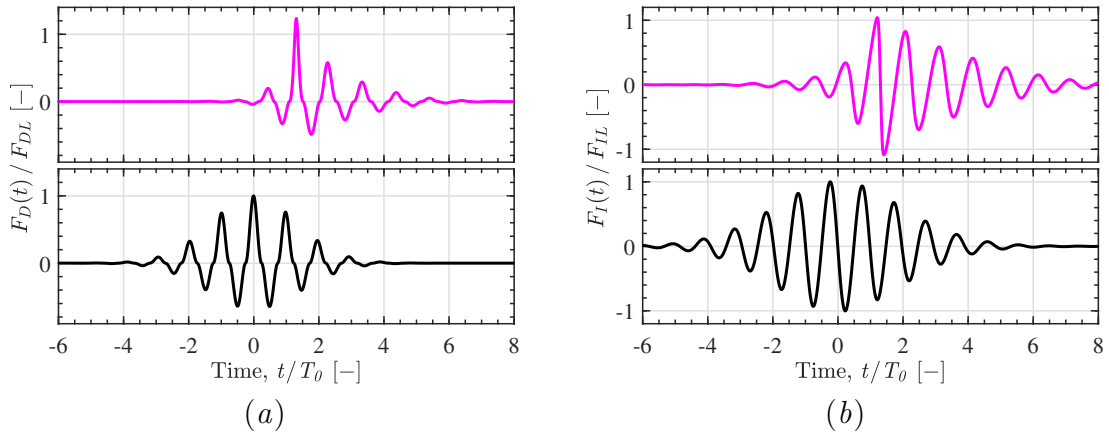

Figure 4.5: Time-history of force calculated from the terms of the Morison equation for case GG15 with a steepness of $A_L k_p = 0.3$ and a dimensionless depth of $k_p d = 3.142$: (a) drag force corresponding to the $u|u|$ term of the Morison equation—the force has been normalised by the maximum drag force of the linear case F_{DL}; (b) inertial force corresponding to the $\partial u/\partial t$ term of the Morison equation—the force has been normalised by the maximum inertial force of the linear case F_{IL}. The linear case is depicted by the black line (——) and the nonlinear case is depicted by the magenta line (——). The time-history of force is calculated at the spatial location where focus of the wave group occurs: $x/\lambda_0 = 0$, $y/\lambda_0 = 0$ for the linear case and $x/\lambda_0 = 1.535$, $y/\lambda_0 = 0$ for the nonlinear case, by integrating from the bottom of the domain ($z = -d$) to the surface elevation ($z = \eta$).

both the velocities and accelerations of the wave field, increasing both the drag and inertial loads as estimated by the Morison equation. Furthermore, the reduction in directional spreading shown in 4.3(b), which occurs during focusing, increases the in-line velocity component and thus increases the horizontal velocity component used in (4.16). We have calculated (4.16) for both the linear and nonlinear versions of the base case. A time history of the force, at the spatial location where focus occurs, is plotted for both the linear and nonlinear cases—the drag term is shown in figure 4.5(a) and the inertial term is shown in figure 4.5(b). Separate axes are used in figure 4.5 for the linear and nonlinear cases for clarity. The nonlinear case exhibits higher drag and inertial forces at focus than the linear case as a result of energy transfers to higher wavenumbers and the reduced spreading of the nonlinear focused event. The maximum drag and inertial forces are, respectively, 24% and 4% higher for the nonlinear case, compared with the linear case. The shape of the linear and nonlinear focused events is shown in figure 4.6 with contours of the in-line velocity component (u), aligned to the x-direction, and normalised by the phase speed associated with the spectral peak (c_0). The linear event depicted in figure

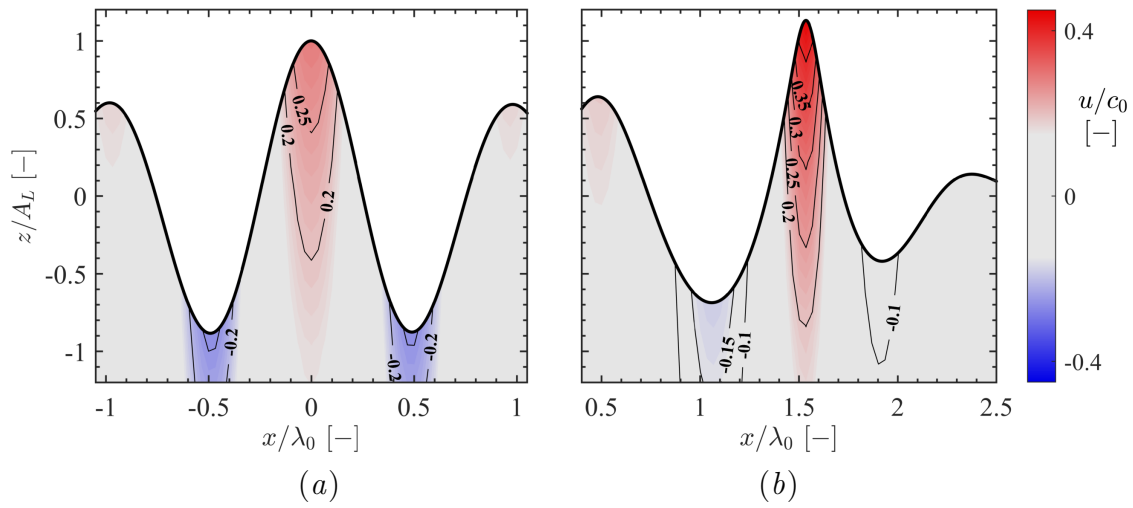

Figure 4.6: Internal kinematics at the time of focus for case GG15 with a steepness of $A_L k_p = 0.3$ and a dimensionless depth of $k_p d = 3.142$: (a) Linear evolution, focus occurs at $t/T_0 = 0$; (b) Nonlinear evolution, focus occurs at $t/T_0 = 1.3$. The spatial coordinate in the direction of propagation (x-direction) is shown on the horizontal axis and the vertical spatial coordinate (z-direction) is shown on the vertical axis. The horizontal velocity in the direction of wave group propagation (u-velocity) is shown beneath the surface elevation (——) of the wave group, normalised by the phase speed associated with the initial peak of the wavenumber spectrum (c_0). Labelled contour lines of the dimensionless velocity ratio u/c_0 are shown in the figures together with a colour bar of the same parameter.

4.6(a) exhibits front-rear symmetry, and the height of the crest is comparable to the depth of the preceding and trailing troughs; a peak inline velocity of $u/c_0 = 0.294$ arises in the crest of the linear focused event. For the nonlinear event depicted in figure 4.6(b), front-rear asymmetry is apparent as the preceding trough is shallower than the trailing trough. The surface elevation includes bound harmonics which result in a higher crest and shallower troughs than observed for the linear event; a peak inline velocity of $u/c_0 = 0.449$ arises in the crest of the nonlinear focused event, 53% higher than the linear case. The Particle Image Velocimetry (PIV) experiments of Alberello *et al.* (2018) are consistent with the numerical simulation results shown in figure 4.6. Alberello *et al.* (2018) observed that unidirectional wave groups, formed by dispersive focusing, contract in the direction of propagation and exhibit asymmetric features consistent with figure 4.6: a preceding trough that is shallower than the trailing trough and a focused crest that is sharper than both the preceding and trailing trough. The consequent kinematics measured by Alberello *et al.* (2018) featured concentrated high-velocity regions in the crest, similar to figure

4.6, associated with the onset of breaking. Note that a variety of breaking criteria have been proposed based on crest kinematics/energy-fluxes (see, e.g., Barthelemy *et al.* (2018)) and neither of the focused events shown in figure 4.6 are expected to break (see Perlin *et al.* (2013) for a review of breaking criteria). In summary, the spectral evolution observed in the base case GG15 results in augmented kinematics and loads, demonstrating the significance of nonlinear interactions.

4.3.3 Steepness, finite depth and directional spreading effects

Following our analysis of the base case, we investigate the effects of steepness, finite depth and directional spreading on spectral evolution on the mean wavenumber ($\mathcal{K}$) and the spreading parameter (ς).

Steepness We assess the effect of amplitude for wave groups based on a Gaussian wavenumber spectrum and a Gaussian spreading function with an initial spreading parameter (ς_0) of 15° and a dimensionless depth of $k_p d = 3.142$. The linear steepness at focus is varied between 0.12 and 0.30 in intervals of 0.03. The mean wavenumber, defined in (4.10), and spreading parameter, defined in (4.11), are shown in figure 4.7. The vertical axis of both plots is normalised by the initial value of the parameter. The evolution in mean wavenumber, shown in figure 4.7(a), depicts an increase during focus with a rate dependent upon steepness. The increase during focus is predominantly due to the quasi-degenerate interactions, discussed in section 3.1, which result in energy transfers to higher wavenumbers. After focus, the mean wavenumber peaks and thereafter declines for all cases. The post-focus decline in mean wavenumber is due to the post-focus dominance of the non-degenerate interactions discussed in section 3.1—the high oblique angle components possess a smaller absolute wavenumber than those along the unidirectional k_x-axis, thereby decreasing the mean wavenumber. Figure 4.7(b) shows the corresponding evolution of the spreading parameter (ς), which exhibits a qualitatively similar trend for all steepnesses. The spreading parameter initially declines during focusing, indicating a more unidirectional wave group resembling the 'wall of water' effect described by Gibbs & Taylor (2005) and observed experimentally by Steer *et al.* (2019), followed

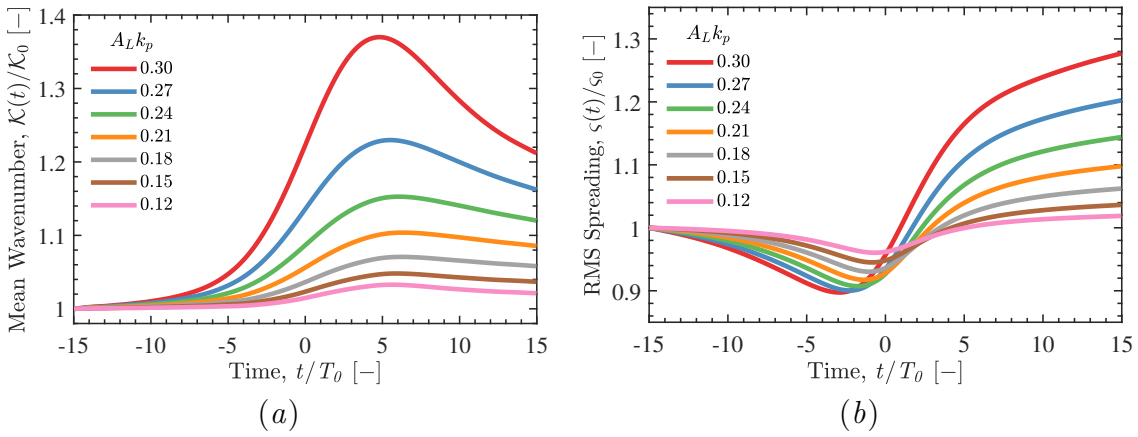

Figure 4.7: Spectral evolution over time for case GG15 with different linear steepnesses ($A_L k_p$) and a dimensionless depth of $k_p d = 3.142$: (a) mean wavenumber $\mathcal{K}(t)$ normalised by the initial value $\mathcal{K}_0$; (b) RMS spreading parameter $\varsigma(t)$ normalised by the initial value ς_0. The various steepnesses are indicated by colour: $A_L k_p = 0.30$, ; 0.27, ; 0.24, ; 0.21, ; 0.18, ; 0.15, ; 0.12, .

by a rapid increase in directional spreading due to the oblique non-degenerate energy transfers shown in figure 4.3(c). The increase in directional spreading occurs earlier for the steeper wave groups indicating an earlier onset of the non-degenerate interactions.

Finite depth The effect of finite depth has also been assessed for wave groups based on a Gaussian wavenumber spectrum and a Gaussian spreading function with an initial spreading parameter (ς_0) of 15° and a linear steepness ($A_L k_p$) of 0.30, with the results shown in figure 4.8. The considered range of depths spans from $k_p d = 5.592$ to $k_p d = 1.363$; a depth of $k_p d = 3.142$ is frequently considered to be 'deep water', and the lower bound of $k_p d = 1.363$ is significant as the critical depth of vanishing modulational instability for unidirectional waves (see Benjamin (1967); Whitham (1967)). However, Benney & Roskes (1969) and McLean (1982*a*) showed that unstable three-dimensional perturbations remain for depths less than $k_p d = 1.363$, consistent with our findings—we observe suppressed nonlinear evolution of the wave spectrum for a depth of $k_p d = 1.363$ but rapid energy transfers evidently do still occur.

Figure 4.8(a) depicts the evolution of the mean wavenumber, normalised by the initial value, for various finite depths. A reduction in depth suppresses the increase in mean wavenumber observed during focus but a discernible increase remains apparent

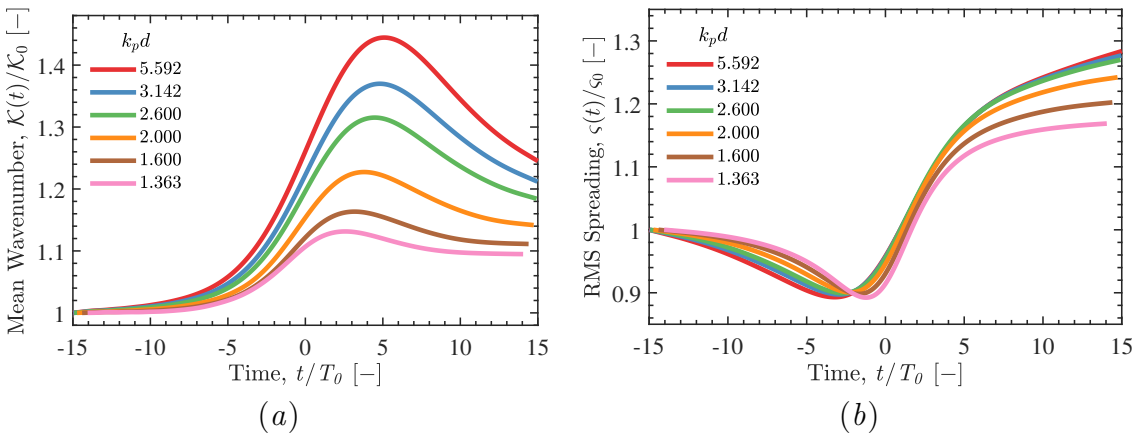

Figure 4.8: Spectral evolution over time for case GG15 with different dimensionless depths (k_pd) and a steepness of $A_Lk_p = 0.3$: (a) mean wavenumber $\mathcal{K}(t)$ normalised by the initial value $\mathcal{K}_0$; (b) RMS spreading parameter $\varsigma(t)$ normalised by the initial value ς_0. The various depths are indicated by colour: $k_pd = 5.592$, ——; $k_pd = 3.142$, ——; $k_pd = 2.600$, ——; $k_pd = 2.000$, ——; $k_pd = 1.600$, ——; $k_pd = 1.363$, ——.

for $k_pd = 1.363$. We also observe sensitivity to depth between k_pd values typically considered to represent 'deep water'. Depths of $k_pd = 5.592$ and $k_pd = 3.142$ result in peak $\mathcal{K}(t)/\mathcal{K}_0$ values of 1.44 and 1.37, respectively. Figure 4.9 shows the amplitude spectrum of surface elevation at the end of the simulation ($t/T_0 = 15$) for the various finite-depth cases. The case of $k_pd = 5.592$ depicted in figure 4.9(a) exhibits greater energy transfers along the unidirectional k_x-axis and the Phillips resonance loop than observed for the $k_pd = 3.142$ case shown in figure 4.9(b). Thus, the quasi-degenerate interactions appear to be depth sensitive even in water typically considered to be deep; the observation can be explained by the interplay between the modulation instability and the return current as found by Benjamin (1967) and Whitham (1974) and discussed by Dysthe (1979) and Janssen & Onorato (2007). The return current develops beneath the wave group with a length scale comparable to the wave group as a whole. Thus, the return current is more sensitive to depth than any individual wave component and, as observed in this study, can be altered by depths greater than $k_pd = 3.142$. The return current is also capable of 'detuning' the modulational instability. Thus, the sensitivity of the return current to depth appears to influence the quasi-degenerate interactions observed in this study, altering the nonlinear wave-wave interactions of cases $k_pd = 5.592$ and $k_pd = 3.142$.

In contrast, the spreading parameter shown in figure 4.8(b) is less significantly

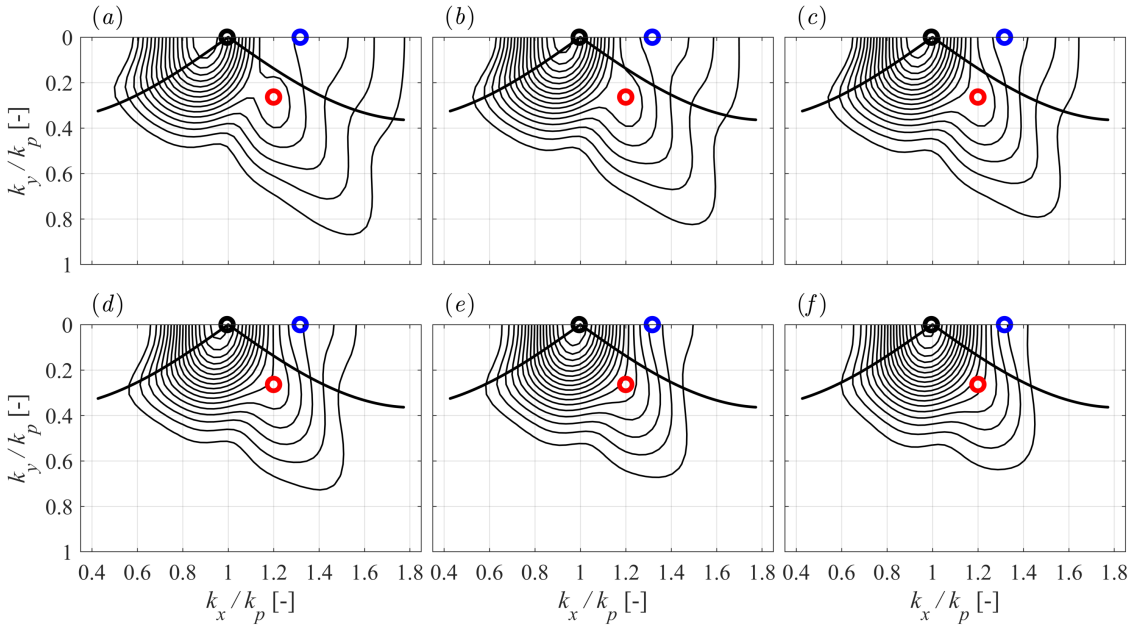

Figure 4.9: Amplitude spectra of surface elevation at the end of the simulation, $t/T_0 = 15$, corresponding to case GG15 with a steepness of $A_L k_p = 0.3$ and various dimensionless depths: (a) $k_p d = 5.592$; (b) $k_p d = 3.142$; (c) $k_p d = 2.600$; (d) $k_p d = 2.000$; (e) $k_p d = 1.600$; (f) $k_p d = 1.363$. Contour levels (——) are evenly distributed between 0.01 m and 0.105 m in intervals of 0.005 m. The thick black line (▬) represents segments of the Phillips 'figure-of-eight' resonance loop and the open circles specify particular wavenumber components: $\mathcal{Q}$ (o) $k_x/k_p = 0.995$, $k_y/k_p = 0.000$; $\mathcal{R}$ (o) $k_x/k_p = 1.200$, $k_y/k_p = 0.263$; $\mathcal{S}$ (o) $k_x/k_p = 1.317$, $k_y/k_p = 0.000$.

affected by depth. The reduction in directional spreading, observed during focus, achieves a similar minimum value for all the finite-depth cases, although the less deep cases exhibit a delay compared with the deeper cases. The delay is expected because the increase in directional spreading is associated with spectral broadening due to quasi-degenerate interactions. Thus, suppression of the quasi-degenerate interactions by depth delays the onset of non-degenerate interactions. The increase in directional spreading, which dominates the wavenumber spectrum after focus, exhibits only a weak sensitivity to depth with an almost identical spreading parameter at the end of the simulation for finite depths ($k_p d$) of 5.592, 3.142 and 2.600. The relative insensitivity of the spreading parameter to depth, compared with the mean wavenumber, appears to result from differing depth sensitivity for the quasi-degenerate and non-degenerate interactions discussed in section 4.3.1. As demonstrated by figure 4.9, the quasi-degenerate interactions which transfer energy along the unidirectional k_x-axis and the Phillips resonance loop exhibit a clear sensitivity to depth and continuously weaken for less deep cases, almost disappearing for the case of $k_p d = 1.363$. In contrast, the non-degenerate interactions, which develop once the wave spectrum is sufficiently broad-banded and transfer energy at an angle of $\pm 55^\circ$ to the spectral peak, are significantly less affected by depth. The oblique energy transfers at $\pm 55^\circ$ are suppressed by depth but continue to dominate the spectral evolution even for $k_p d = 1.363$. Consequently, the mean wavenumber is sensitive to energy transfers to higher wavenumbers by the quasi-degenerate interactions and, thus, exhibits depth sensitivity. The spreading parameter is principally governed by the oblique energy transfers of the non-degenerate interactions and, thus, exhibits less sensitivity to depth.

We have also analysed the change in wave action density for components $\mathcal{R}$ and $\mathcal{S}$ with the results shown in figure 4.10. Normalisation is performed with the initial wave action density of the spectral peak ($\mathcal{Q}_0$). The wave action density of component $\mathcal{S}$, shown in figure 4.10(a), depicts a qualitatively similar trend for all the depth cases but demonstrates suppressed energy transfers at reduced depths. In contrast, component $\mathcal{R}$ depicts a similar quantitative trend in wave action density

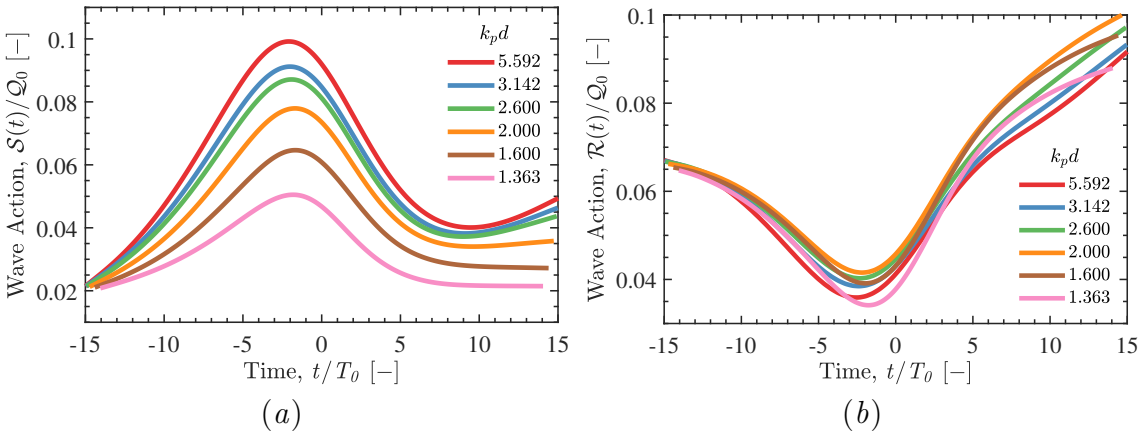

Figure 4.10: Change in wave action density corresponding to case GG15 with a steepness of $A_Lk_p = 0.3$ and various dimensionless depths: $k_pd = 5.592$, ——; $k_pd = 3.142$, ——; $k_pd = 2.600$, ——; $k_pd = 2.000$, ——; $k_pd = 1.600$, ——; $k_pd = 1.363$, ——. The analysis has been performed for specific wavenumber components: (a) component $\mathcal{S}$ ($k_x/k_p = 1.317$, $k_y/k_p = 0.000$); (b) component $\mathcal{R}$ ($k_x/k_p = 1.200$, $k_y/k_p = 0.263$); both components are normalised by the initial wave action density of the spectral peak ($\mathcal{Q}_0$), and the location of the components in the wavenumber spectrum is shown in figure 4.9.

for all depths and even exhibits faster growth for finite depth cases $k_pd = 2.000$ and $k_pd = 1.600$ than the deep water cases. Benney & Roskes (1969) and McLean (1982*a*) showed that the peak instability of a regular wave train becomes oblique, rather than unidirectional, at intermediate depths. Thus, the faster growth rate for component $\mathcal{R}$ observed for cases $k_pd = 2.000$ and $k_pd = 1.600$ may be a result of the quasi-degenerate interactions biasing towards oblique rather than unidirectional components. Ultimately, depth suppresses all forms of spectral evolution in the intermediate range of depths ($5.592 > k_pd > 1.363$) considered by this study, consistent with the finite-depth random sea simulations of Toffoli *et al.* (2009). However, unidirectional energy transfers appear to be particularly suppressed relative to the oblique energy transfers. Thus, the increase in mean wavenumber is suppressed, which suggests less severe wave kinematics. However, the reduction in directional spreading, observed during focus, appears to occur for all the finite-depth cases suggesting that the 'wall of water' effect may also be observed in waters of intermediate depth, consistent with the experiments of Latheef *et al.* (2017). The interplay between the return current and modulation instability also results in depth sensitivity within the range of depths commonly considered to be 'deep', suggesting that the

length scale of the return current and wave group are of greater significance than the length scale of individual wave components when categorising water as 'deep'.

Directional spreading We consider the effects of directional spreading for wave groups with a linear steepness ($A_L k_p$) of 0.24 based on a Gaussian wavenumber magnitude spectrum with a Gaussian spreading function and a finite depth ($k_p d$) of 3.142. Our simulations include initial spreading parameters (ς_0) in the range of 5° to 25° in intervals of 5°. Focused wave events with high values of directional spreading exhibit a reduced focal time, compared with less-spread or unidirectional events, due to linear dispersion. Figure 4.11(a) shows the steepness of the wave envelope for the various cases of directional spreading. As can be seen, the less spread cases, e.g. $\varsigma_0 = 10°$, begin with a higher steepness and steepen gradually until focus. In contrast, the cases with more directional spreading, e.g. $\varsigma_0 = 25°$, begin with a lower steepness and steepen rapidly before focus. Directional spreading, thus, reduces the focal time of the wave event, limiting the total energy transfer in an integral sense. Figure 4.11(a) also demonstrates the influence of nonlinear interactions on the life span of the focused wave events. Under linear evolution, each case should focus and defocus symmetrically, see figure 4.2. However, cases $\varsigma_0 = 5°$ and $\varsigma_0 = 10°$ exhibit deviations between focusing and defocusing due to nonlinear interactions, extending the life span of the focused events.

The spectral evolution is also demonstrated by figure 4.11(b), which shows the zeroth moment of the amplitude spectrum ($\mathcal{M}_0$), normalised by the linear amplitude at focus (A_L), for all the spreading cases. Under linear evolution, $\mathcal{M}_0 = A_L$ throughout the simulation. Under nonlinear evolution, an increase in $\mathcal{M}_0$ indicates a transition from a narrow-banded to a more broad-banded spectrum. The zeroth moment increases drastically for the $\varsigma_0 = 5°$ case due to rapid broadening of the spectrum. Consequently, the focused wave event is significantly steeper than the linear steepness, and the lifespan of the event is extended. In contrast, the $\varsigma_0 = 25°$ case depicts a nearly constant zeroth moment until shortly before focus, indicating less spectral broadening during focus, which results in a steepness and focused lifespan which resembles the linear event.

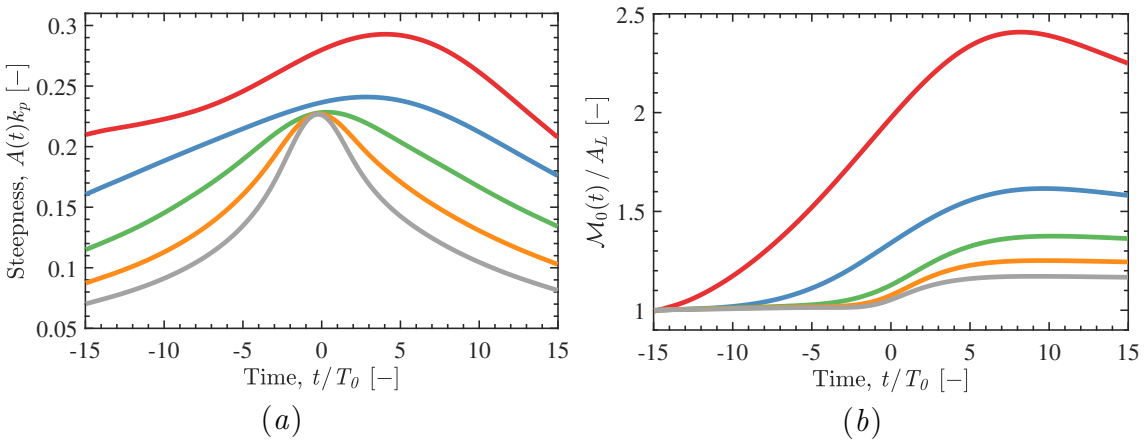

Figure 4.11: Effect of directional spreading for wave groups with a steepness of $A_L k_p = 0.24$, finite depth of $k_p d = 3.142$ and initial spreading parameters of 5° (——), 10° (——), 15° (——), 20° (——) and 25° (——): (a) Steepness of the wave envelope over time—the amplitude $A(t)$ is based on the maximum elevation of the wave envelope at time t; (b) The zeroth moment of the wavenumber-amplitude spectrum ($\mathcal{M}_0$) normalised by the linear focus amplitude (A_L). All cases are based on a Gaussian wavenumber spectrum with a Gaussian spreading function.

The associated change in mean wavenumber $\mathcal{K}(t)$ is shown in figure 4.12(a) for the various cases of directional spreading, normalised by the initial value $\mathcal{K}_0$. The increase in mean wavenumber is also delayed for cases with more directional spreading due to the comparatively late focusing of the event, but the qualitative trend is consistent. An increase in directional spreading reduces energy transfers and limits the growth in mean wavenumber. However, the change in spreading parameter shown in figure 4.12(b) depicts a qualitatively different trend for the different cases of directional spreading. Case $\varsigma_0 = 5°$ features an increase in directional spreading during focus and ultimately results in a focused event which is more spread than the initial condition—the time of nonlinear focus is indicated with a black hexagram. Case $\varsigma_0 = 10°$ features a reduction in directional spreading for a few wave periods after the start of the simulation but thereafter an increase in directional spreading follows and the focused wave event is also more spread than the initial conditions. Conversely, cases $\varsigma_0 = 15°$, 20° and 25° feature a reduction in directional spreading before focus and the focused wave event is ultimately less spread than the initial conditions.

These results suggest that a steep wave event in a sea with low directional spread-

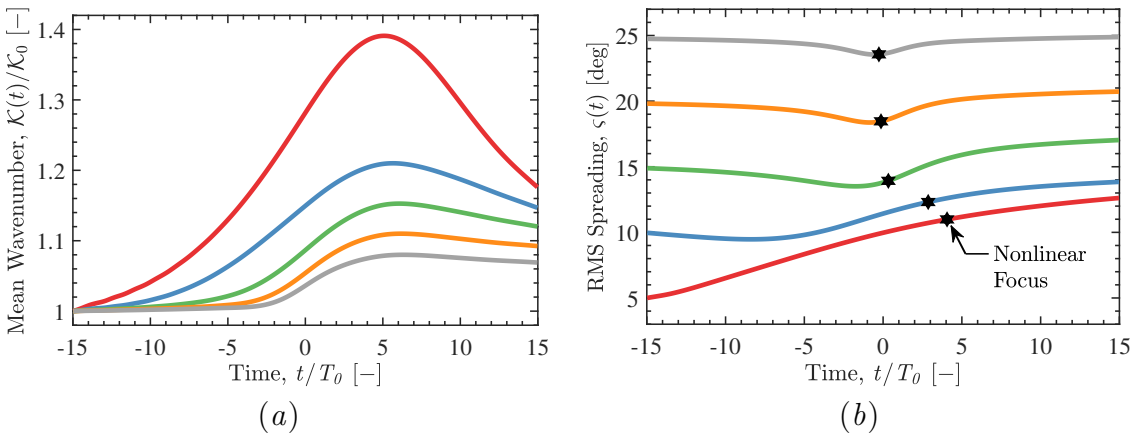

Figure 4.12: Spectral evolution over time for wave groups with a steepness of $A_L k_p = 0.24$, dimensionless depth of $k_p d = 3.142$ and and initial spreading parameters of 5° (——), 10° (——), 15° (——), 20° (——) and 25° (——). The spectral parameters include: (a) mean wavenumber $\mathcal{K}(t)$ normalised by the initial value $\mathcal{K}_0$; (b) RMS spreading parameter $\varsigma(t)$. The time of nonlinear focus is indicated with a black hexagram. All cases are based on a Gaussian wavenumber spectrum with a Gaussian spreading function.

ing, i.e., $\varsigma_0 \leq 10°$, may tend to be more spread than the background sea state, while seas with more directional spreading, i.e., $\varsigma_0 \geq 15°$, may produce steep wave events which are less directionally spread than the background sea state. Note, the cases with more directional spreading, $\varsigma_0 \geq 15°$, exhibit a reduction in spreading before focus, but the trend is largely reversed after focus so the final value of the spreading parameter nearly matches the initial value, as demonstrated by case $\varsigma_0 = 25°$. However, the cases with low spreading $\varsigma_0 \leq 10°$ do not exhibit such a reversal—the final spreading parameter is significantly larger than the initial spreading parameter.

4.3.4 Effect of the high-wavenumber tail

The peak of the JONSWAP spectrum contains most of the total energy. Thus, Gaussian wavenumber spectra are frequently used in studies of wave-wave interactions with the high-wavenumber components of the tail neglected from the analysis (see, e.g., Mori *et al.* (2011)). Certain physical processes have been found to suppress high-wavenumber components, which comprise the tail of the spectrum, more severely than low-wavenumber components. Such mechanisms can suppress the development of the high-wavenumber tail. Wave blocking due to currents (see, e.g., Ma *et al.* (2010)) can suppress the tail of the wave spectrum at a particular loca-

tion, if low-wavenumber components continue to propagate while high-wavenumber components are blocked from propagating further, as discussed by Chawla & Kirby (2002). Rapizo *et al.* (2016) found that the development of the spectral tail is disturbed for waves propagating on a coflowing current, due to detuning of the quartet resonance interactions. Similarly, Waseda *et al.* (2015) found that the spectral tail can be suppressed by detuning due to currents. Ice sheets also tend to suppress high-wavenumber components, attenuating the amplitude of high-wavenumber components more severely than low-wavenumber components (see Meylan *et al.* (2018) and Toffoli *et al.* (2015)), possibly suppressing the tail of the spectrum. Thus, a comparison between Gaussian and JONSWAP spectra serves two purposes: (1) to indicate the appropriacy of a Gaussian spectrum as a model for the peak of a JONSWAP spectrum in typical sea states and; (2) to contrast the spectral evolution of a steep wave event in seas with and without a fully-developed spectral tail.

We combine a JONSWAP wavenumber spectrum ($\gamma = 3.3$) with a frequency-independent spreading function, a Gaussian with an initial spreading parameter of $\varsigma_0 = 15°$, and denote this case as JG15. Similarly, we combine a JONSWAP spectrum ($\gamma = 3.3$) with the frequency-dependent spreading function of Ewans (1998) and denote this case as JE. The combination of a JONSWAP spectrum with an Ewans (1998) spreading function realistically captures the spectral shape of fetch-limited seas. We compare against two cases based on a Gaussian wavenumber spectrum: one with an initial spreading parameter of $\varsigma_0 = 15°$, denoted as GG15, and another with an initial spreading parameter of $\varsigma_0 = 20°$, denoted as GG20. A summary of the case acronyms is listed in table 4.4. The results are shown in figure 4.13 for both the mean wavenumber $\mathcal{K}(t)$ and spreading parameter $\varsigma_0(t)$. The mean wavenumber is normalised by the initial value for each case $\mathcal{K}_0$. Figure 4.13(a) indicates that the simulations performed with a Gaussian wavenumber spectrum produces an increase in mean wavenumber. However, the simulations performed with a JONSWAP spectrum, cases JG15 and JE, exhibit a qualitatively different trend; the mean wavenumber remains approximately constant during the early stages of focusing and reduces during the focus event. Thus, the increase in

Case	Wavenumber Spectrum, $S(k)$	Spreading Function, $D(\theta)$	Spreading Parameter, ς_0
GG5	Gaussian	Gaussian	5°
GG10	Gaussian	Gaussian	10°
GG15	Gaussian	Gaussian	15°
GG20	Gaussian	Gaussian	20°
GG25	Gaussian	Gaussian	25°
JG15	JONSWAP	Gaussian	15°
JE	JONSWAP	Ewans (1998)	—

Table 4.4: Summary of acronyms for simulation cases.

mean wavenumber observed for the Gaussian cases, GG15 and GG20, appears to be associated with redevelopment of the truncated high-wavenumber tail, and the JONSWAP cases do not show the same trend. The trend for the spreading parameter is however qualitatively similar between the Gaussian and JONSWAP cases, as shown in figure 4.13(b). All cases feature a reduction in the spreading parameter during focus, indicating focused wave events which are less directionally spread than the background sea state, i.e. the 'wall-of-water' effect.

Thus, a Gaussian wavenumber spectrum exhibits qualitatively similar trends to a JONSWAP spectrum in terms of the spreading parameter, but redevelopment of the spectral tail leads to an increase in mean wavenumber, which is not observed for the JONSWAP spectrum. Furthermore, the changes in mean wavenumber and spreading parameter for the JONSWAP cases appear to be largely temporary since the reduction in both parameters reverses after focus. In contrast, the changes in mean wavenumber and spreading parameter for the Gaussian cases appear to include more permanent changes since the trends do not entirely reverse after focus. Thus, the JONSWAP spectra exhibit a form of spectral equilibrium which inhibits changes to the spectrum. The results of the previous sections based on Gaussian wavenumber spectra may, thus, be most applicable to sea states without a fully developed spectral tail. Energy transfer to higher wavenumbers, in particular, is reduced for steep wave events based on a fully-developed JONSWAP spectrum.

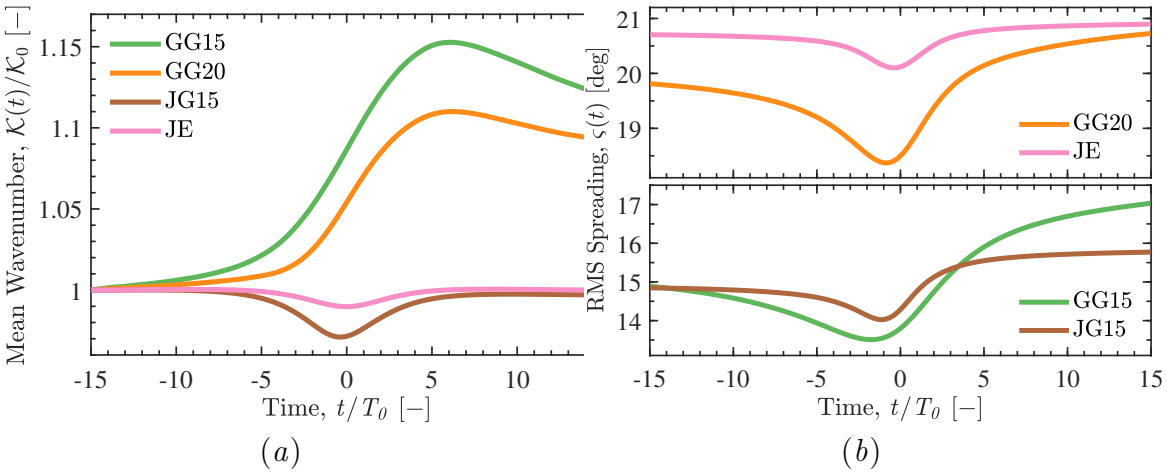

Figure 4.13: The effect of the high-wavenumber tail on the spectral evolution of wave groups with a steepness of $A_L k_p = 0.24$, dimensionless depth of $k_p d = 3.142$ and different spectral shapes: GG15, ——; GG20, ——; JG15, ——; JE, ——. The spectral parameters include: (a) mean wavenumber $\mathcal{K}(t)$ normalised by the initial value $\mathcal{K}_0$; (b) RMS spreading parameter $\varsigma(t)$ in degrees.

We conclude that the high-wavenumber tail of the spectrum influences the spectral evolution of a steep wave event. Thus, studies based solely on Gaussian spectra, e.g. Adcock *et al.* (2015), should be treated with caution.

Amplitude spectra of surface elevation, shown in figure 4.14, depict the spectral evolution of the JONSWAP cases (JG15 and JE). The top row of panels, figure 4.14(a, b, c), correspond to case JG15. The bottom row of panels, figure 4.14(d, e, f), correspond to case JE. The initial conditions $(t/T_0 = -15)$ are shown in figure 4.14(a) and figure 4.14(d). The initial conditions indicate that the Ewans (1998) spreading function of case JE features higher levels of spreading in the tail than the Gaussian spreading function of case JG15. Figure 4.13(b) confirms that the spreading parameter is consistently lower for case JG15 than case JE, due to lower levels of spreading in the tail for case JG15. The spectral evolution of both JONSWAP cases (JG15 and JE) is less noticeable than the GG cases. Thus, we show the difference in the amplitude spectrum relative to the initial condition: around the time of focus $(t/T_0 = 0)$ in figure 4.14(b, e); and at the end of the simulation $(t/T_0 = 15)$ in figure 4.14(c, f). We use a colour scale to indicate the growth (in red) and decline (in blue) of component amplitudes relative to the initial condition. As shown in figure 4.13, the spectral changes are most apparent around the time of focus $(t/T_0 = 0)$, figure 4.14(b, e), but the changes appear to be mostly temporary

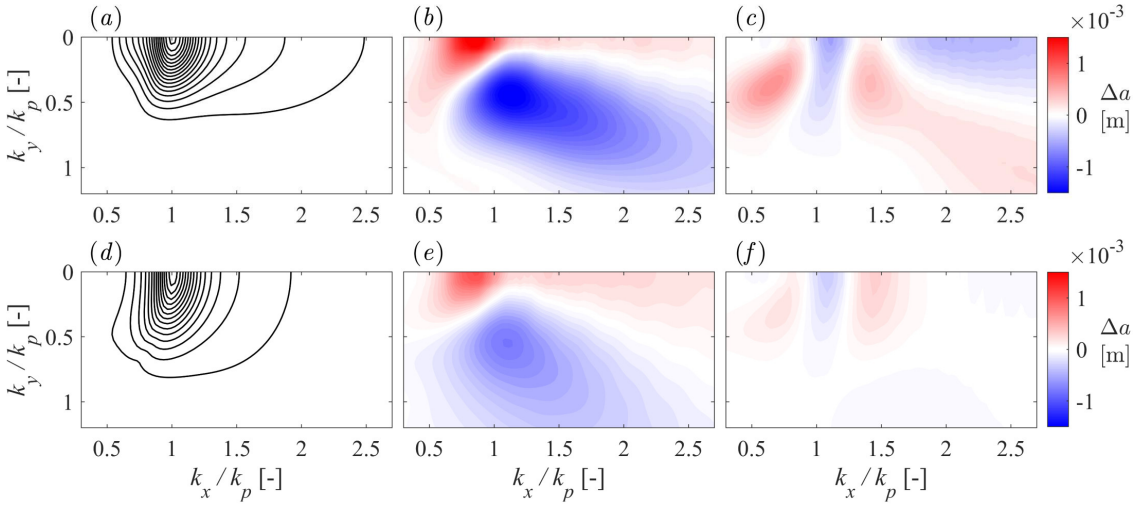

Figure 4.14: Amplitude spectra of surface elevation for JONSWAP cases: JG15 in (a), (b), (c); and JE in (d), (e), (f). Initial conditions ($t/T_0 = -15$) are shown in (a) and (d) with contour levels (——) evenly distributed between 0.002 m and 0.034 m in intervals of 0.002 m. The difference in the amplitude spectrum at time $t/T_0 = 0$, relative to the initial condition, is shown in (b) and (e) using a colour scale with levels shown in the figure. Similarly, the difference in the amplitude spectrum at the end of the simulation ($t/T_0 = 15$), relative to the initial condition, is shown in (c) and (f) using the same colour scale.

and reverse after focus, leaving few permanent changes at the end of the simulation ($t/T_0 = 15$), figure 4.14(c, f). Case JG15 does exhibit some permanent changes to the spectrum—the directional spreading of the tail increases as energy is transferred to oblique high-wavenumber components, consistent with the net increase in the spreading parameter shown in figure 4.13(b). In contrast, case JE exhibits fewer permanent changes, consistent with the results of figure 4.13. Thus, high levels of directional spreading in the tail, e.g. Ewans (1998), may also be a feature of spectral equilibrium. Case JG15 also exhibits more substantial spectral changes around the time of focus ($t/T_0 = 0$), figure 4.14(b, e). Contraction of the spectrum in the k_y-direction (the 'wall-of-water' effect) and a downshift in the spectral peak occurs for both case JG15 and case JE. However, both effects are more substantial for case JG15, providing further evidence that case JE may be a better representation of spectral equilibrium than case JG15 and directional spreading in the tail can influence spectral evolution.

4.3.5 Downshift of the spectral peak

We observe a downshift in wavenumber for the spectral peak during our simulations, see figure 4.3 as an example. First reported by Lake *et al.* (1977), the phenomenon is commonly termed a frequency/wavenumber downshift and has been observed by numerous studies (see Ma *et al.* (2010), Kharif *et al.* (2008*a*), Segur *et al.* (2005), Dysthe *et al.* (2003), Melville (1982), Su *et al.* (1982) and others). Downshifting has been related to nonlinear wave-wave interactions (e.g., Trulsen & Dysthe (1997)), breaking (e.g., Trulsen & Dysthe (1990), Tulin & Waseda (1999)) and wind (e.g., Hara & Mei (1991)). The downshift we observe in our potential flow simulations is exclusively due to nonlinear wave-wave interactions. We base our analysis on component $\mathcal{Q}$ ($k_x/k_p = 1.000$, $k_y/k_p = 0.000$), which coincides initially with the peak of the wavenumber spectrum. The rate of change in wave action density for $\mathcal{Q}$ is indicative of the rate of downshift for the spectral peak, and we consider the influences of directional spreading and the high-wavenumber tail on the downshift, with the results shown in figure 4.15. We consider Gaussian wavenumber spectra with a Gaussian spreading function and initial spreading parameters (ς_0) of 5°, 10°, 15°, 20°, 25°; the cases are denoted as GG5, GG10, GG15, GG20 and GG25, respectively. For comparison, we consider a JONSWAP spectrum ($\gamma = 3.3$) with frequency-independent spreading, based on a Gaussian spreading function with $\varsigma_0 =$ 15°, and denote this case as JG15. We also consider a JONSWAP spectrum with frequency-dependent spreading, based on the Ewans (1998) spreading function, and denote this case as JE. A linear steepness at focus ($A_L k_p$) of 0.24 has been selected for all cases together with a depth ($k_p d$) of 3.142.

The growth rate for component $\mathcal{Q}$ is shown in figure 4.15 for the various cases together with the dynamic timescale. For all cases except GG5, the wave action of component $\mathcal{Q}$ initially increases before the downshift of the peak begins (see figure 4.4(a) as an example). The growth rate is shown in absolute terms. Thus, a discontinuity is shown in the logarithmic plots, at the time of maximum wave action density, when the growth rate momentarily reaches zero before a change in sign occurs. The time of nonlinear focus for each case is indicated with a black

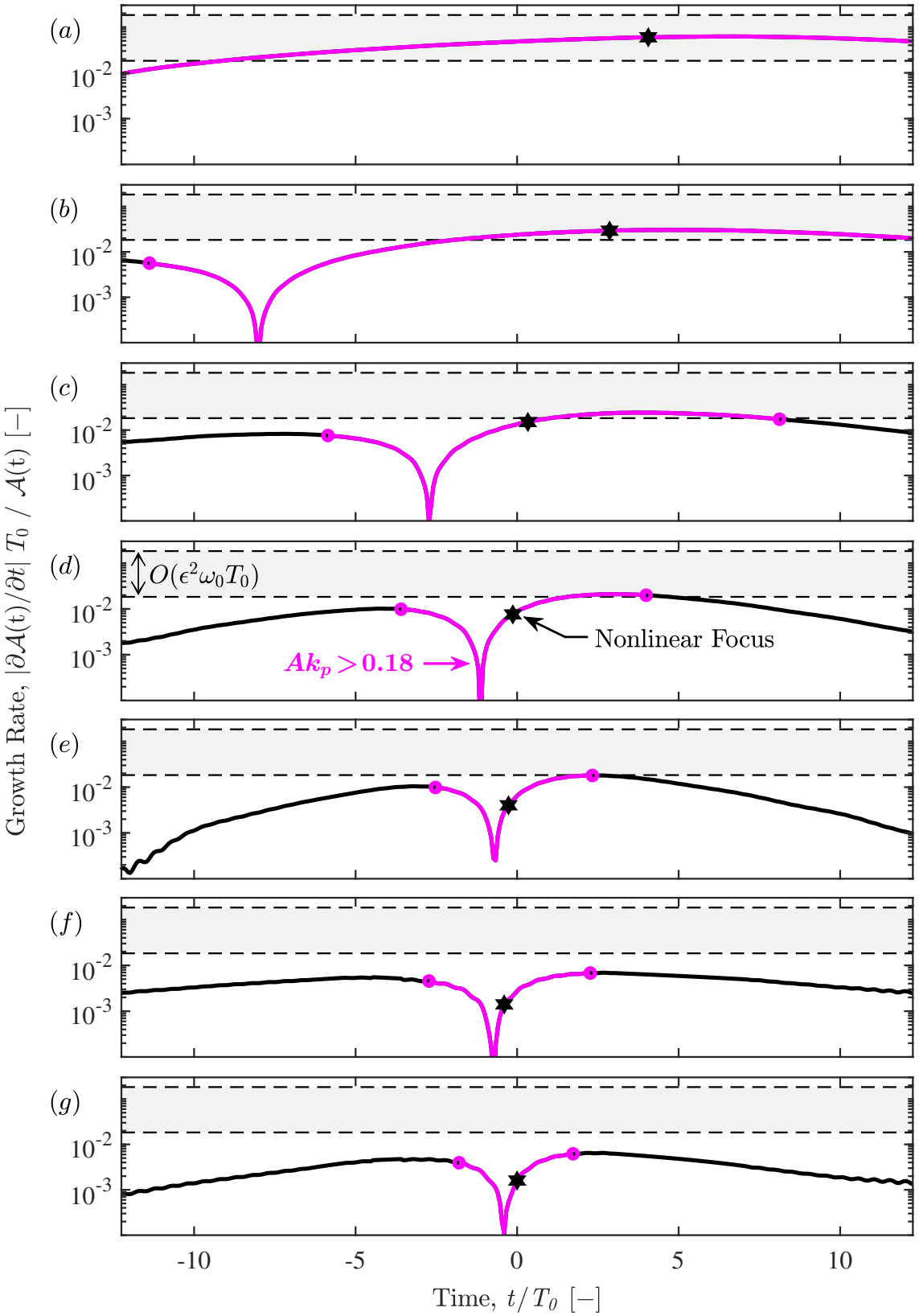

Figure 4.15: Growth rate of wave action density $\mathcal{A}$ for the spectral component $\mathcal{Q}$, which initially coincides with the peak of the amplitude spectrum: (a) GG5; (b) GG10; (c) GG15; (d) GG20; (e) GG25; (f) JG15; (g) JE. The dynamic growth rate $O(\epsilon^2\omega_0 T_0)$ is indicated by bounded $(- - -)$ grey bands. The magenta line segment (———) indicates the time interval during which $A(t)k_p$, as shown in figure 4.11, exceeds 0.18. The value of ϵ equates to $A_L k_p/\pi$ in the calculation of the growth rates. The time of nonlinear focus is indicated with a hexagram.

hexagram in figure 4.15, and the time interval for which the steepness of the wave envelope $A(t)k_p$ exceeds 0.18 is indicated by a magenta line segment. The growth rate for case GG5 is augmented because the steepness of the event exceeds the linear steepness, used to calculate the dynamic growth rate, as evidenced by figure 4.11(a). The other GG cases achieve a steepness at focus which is comparable to the linear steepness, and the post-focus growth rate for component $\mathcal{Q}$ can be seen in figure 4.15 to be consistent with the dynamic timescale. However, an increase in directional spreading for the GG cases does reduce the rate of downshift for the spectral peak and the inclusion of the high-wavenumber tail of the spectrum, featured in the JG15 and JE cases, leads to a further decrease.

The effect of the high-wavenumber tail on the downshift is summarised in figure 4.16, which shows the maximum growth rate, at any time in the simulation, on the vertical axis. The horizontal axis shows the corresponding spreading parameter ($\varsigma(t)$), at the time that the maximum growth rate occurs. Cases GG15 and JG15 exemplify the role of the high-wavenumber tail in reducing the downshift phenomenon; the two cases exhibit a similar spreading parameter but the maximum growth rate for case GG15 is a factor of three faster than case JG15. The slower growth rate for case JG15 is particularly noteworthy because the JG15 focused wave event is arguably steeper than the GG15 event. The linear steepness is calculated from $A_L k_p$, which incorporates the spectral peak, at the start of the simulation, as the characteristic wavenumber. A Gaussian wavenumber spectra is symmetric about the spectral peak which supports the use of k_p as the characteristic wavenumber, particularly if the spectrum is narrow-banded. However, a JONSWAP spectrum features a high-wavenumber tail which arguably should result in a characteristic wavenumber above k_p, suggesting cases JG15 and JE are steeper than indicated by $A_L k_p$. However, the maximum growth rate for case GG15 is significantly higher than the maximum growth rate for cases JG15 and JE. Inclusion of the high-wavenumber tail, thus, appears to reduce the downshift of the spectral peak.

In summary, all focused wave events in this study exhibit a downshift of the spectral peak. However, spreading and the inclusion of the high-wavenumber tail reduce

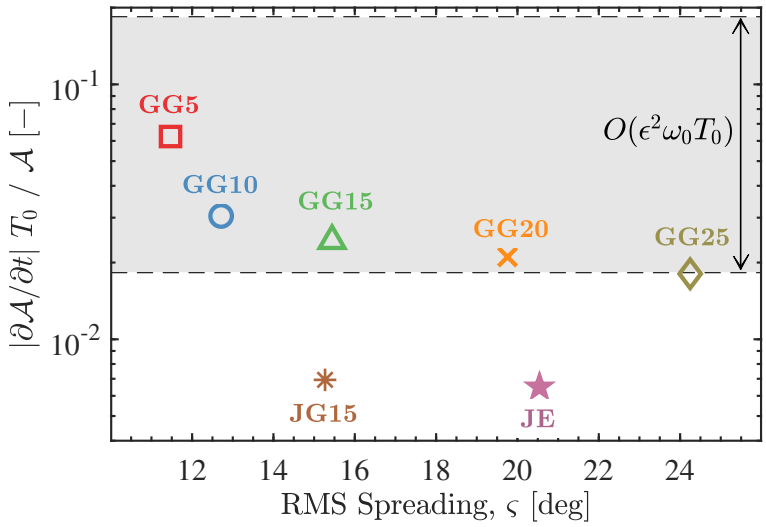

Figure 4.16: The stabilising effect of directional spreading and the high-wavenumber tail: the vertical axis indicates the maximum growth rate calculated at any point in the simulation; the horizontal axis indicates the RMS spreading parameter of the spectrum at the corresponding time. The growth rate calculation is based on component $\mathcal{Q}$ ($k_x/k_p = 0.995$, $k_y/k_p = 0.000$), which initially coincides with the peak of the wavenumber spectrum. The various cases, all with a steepness of $A_L k_p = 0.24$ and a depth of $k_p d = 3.142$, are labelled within the figure. The dynamic growth rate $O(\epsilon^2\omega_0 T_0)$ is indicated by bounded $(- - -)$ grey bands. The value of ϵ equates to $A_L k_p/\pi$ in the growth rate calculations.

the downshift, and nonlinear evolution of the wavenumber spectrum in general. The mechanism is not limited to a reduced focal time caused by linear dispersion. Rather, the rate of the downshift, even at the steepest stages of focusing, is also reduced by spreading and the high-wavenumber tail. Thus, directional spreading and the spectral tail appear to be integral features of a spectral equilibrium, which limits directional energy transfers during a steep wave event.

4.4 Conclusion

We have studied steep focusing wave groups formed by dispersive focusing in deep and intermediate waters. For narrow-banded Gaussian wavenumber spectra with a Gaussian spreading function, quasi-degenerate interactions result in directional energy transfers: (1) Along the k_x-axis, consistent with the unidirectional instabilities observed by Longuet-Higgins (1978) and McLean (1982*b*) for a regular wave; (2) At angles of $\pm 35°$ to the spectral peak with a bias towards high-wavenumber components, consistent with the $\arctan(1/\sqrt{2})$ resonance angle identified by Longuet-Higgins (1976) and the Phillips 'figure-of-eight' resonance loop.

Spectral broadening due to the quasi-degenerate interactions eventually facilitates non-degenerate interactions, which dominate the spectral evolution of the wave group after focus. The non-degenerate interactions manifest as high-wavenumber sidelobes at angles of $\pm 55^\circ$ to the spectral peak. We also observe contraction of the wavenumber spectrum in the k_y-direction during focusing and a downshift in wavenumber for the spectral peak, consistent with previous studies (see, e.g., Trulsen & Dysthe (1997)). All the spectral changes we observe can be attributed to quartet interactions. Relative to linear theory, the combination of quasi-degenerate and non-degenerate interactions results in nonlinear wave events with augmented kinematics and an extended lifespan.

Finite depth weakens all forms of spectral evolution. However, the quasi-degenerate interactions exhibit a greater sensitivity to depth, indicating suppression of the modulation instability by the return current as discussed by Dysthe (1979) and Janssen & Onorato (2007). We also observe sensitivity to depth for $k_p d$ values commonly considered to be deep, $3.142 < k_p d < 5.592$. The non-degenerate interactions appear to be significantly less suppressed by depth with persistent evidence of a $\pm 55^\circ$ spectral sidelobe at a depth of $k_p d = 1.363$. Although the quasi-degenerate interactions are significantly suppressed by depth, the interactions do not entirely disappear for $k_p d = 1.363$ and show signs of biasing towards oblique rather than unidirectional wave components at intermediate depths, consistent with McLean (1982*a*). The contraction of the wavenumber spectrum in the k_y-direction has also proved to be resilient to depth, suggesting that lateral expansion of the wave group and the 'wall-of-water' effect may persist at intermediate depths.

We contrast our analyses of Gaussian cases with simulations based on a JONSWAP spectrum, combined with frequency-independent and frequency-dependent spreading, and find that the high-wavenumber tail of the spectrum reduces the nonlinear features observed for the Gaussian cases. In particular, the energy transfers to higher wavenumbers is reduced for the JONSWAP cases, suggesting that the Gaussian simulations are influenced by the absence of a spectral tail and the nonlinear interactions bias towards redevelopment of the tail. However, the trends in the

spreading parameter show qualitative agreement between the Gaussian and JONSWAP cases. We conclude that focused wave events in sea states without a fully developed spectral tail are more likely to exhibit rapid nonlinear evolution. Physical mechanisms which can suppress the high-wavenumber components in the spectral tail, such as dissipation by ice sheets (see Meylan *et al.* (2018)) and wave blocking by currents (see Chawla & Kirby (2002)), could thus influence the characteristics of focused wave events in the immediate vicinity. We also consider the downshift of the spectral peak and find that the downshift, and the spectral evolution in general, is reduced by directional spreading and the presence of the high-wavenumber tail. Reduced spectral evolution is not only due to the reduced focal time of the more broad-banded events. Rather, the rates of energy transfer also appear to be reduced even at the steepest stages of wave group focusing. Thus, directional spreading and the high wavenumber tail appear to be integral features of a spectral equilibrium which reduces the rapid directional energy transfers of a steep wave group.

5 MNLS Simulations of Surface Wave Groups with Directional Spreading in Deep and Finite Depth Waters

Abstract

We simulate focusing surface gravity wave groups with directional spreading using the Modified Nonlinear Schrödinger (MNLS) equation and compare the results with a fully-nonlinear potential flow code, OceanWave3D. We alter the direction and characteristic wavenumber of the MNLS carrier wave, to assess the impact on the simulation results. Both a truncated (fifth-order) and exact version of the linear dispersion operator are used for the MNLS equation. The wave groups are based on the theory of quasi-determinism and a narrow-banded Gaussian spectrum. We find that the truncated and exact dispersion operators both perform well if: (1) the direction of the carrier wave aligns with the direction of wave group propagation; (2) the characteristic wavenumber of the carrier wave coincides with the initial spectral peak. However, the MNLS simulations based on the exact linear dispersion operator perform significantly better if the direction of the carrier wave does not align with the wave group direction or if the characteristic wavenumber does not coincide with the initial spectral peak. We also perform finite-depth simulations with the MNLS equation for dimensionless depths ($k_p d$) between 1.36 and 5.59, incorporating depth into the boundary conditions as well as the dispersion operator, and compare the results with those of a fully-nonlinear potential flow code to assess the finite-depth limitations of the MNLS.

5.1 Introduction

The Modified Nonlinear Schrödinger (MNLS) equation is frequently used in studies of 'rogue' or 'freak' ocean waves due to the low computational expense and high fidelity of the simulations. A comprehensive overview of rogue wave studies can be found in Kharif & Pelinovsky (2003), Kharif *et al.* (2008*b*), Dysthe *et al.* (2008) and Adcock & Taylor (2014). Schrödinger equations are also frequently used to investigate optical rogue waves (Akhmediev *et al.* (2013), Onorato *et al.* (2013), Dudley *et al.* (2014)) including the dynamics of optical solitons (see, e.g., Pinar *et al.* (2020)). In this study, we use the MNLS equation for the first harmonic of the surface elevation as presented in Trulsen *et al.* (2000), based on the work of Trulsen & Dysthe (1996):

$$\begin{aligned}\frac{\partial B}{\partial t} + \mathfrak{L}\,B + \frac{1}{2}i\omega_0 k_0^2|B|^2 B + \frac{3}{2}\omega_0 k_0 |B|^2 \frac{\partial B}{\partial x} \\ + \frac{1}{4}\omega_0 k_0 B^2 \frac{\partial B^*}{\partial x} + ik_0 \frac{\partial \overline{\phi}}{\partial x} B = 0,\end{aligned} \tag{5.1}$$

to simulate directionally-spread, steep groups of ocean waves formed by dispersive focusing. Here, B represents the complex wave envelope based on the first harmonic of the surface elevation and the characteristic wavenumber and angular frequency of the carrier wave are denoted by k_0 and ω_0. Note that the velocity potential expression corresponding to (5.1) reverses the sign of the $B^2(\partial B^*/\partial x)$ term to be negative, as listed in Trulsen & Dysthe (1996). The dispersion operator $\mathfrak{L}$ in (5.1) may be based upon a truncated version of the linear dispersion relationship (see Trulsen & Dysthe (1996)) or an alternative pseudo-differential operator that preserves the exact linear dispersion relationship (see Trulsen *et al.* (2000)). We contrast the performance of the two dispersion operators and compare the results with a fully-nonlinear potential flow solver. We also consider the effect of selecting different characteristic wavenumbers and directions for the MNLS carrier wave. Finally, we perform finite-depth simulations with (5.1) using the arbitrary-depth linear dispersion relationship, $\omega = \sqrt{gk\tanh(kd)}$ to evaluate the exact version of $\mathfrak{L}B$ with finite-depth also incorporated into the boundary conditions to assess the

finite-depth limitations of (5.1). We focus on the impact of four-wave, or 'quartet', interactions on the shape and spectral evolution of the focusing wave groups and assess the fidelity of the various MNLS formulations.

The MNLS formulation is based upon a carrier wave that requires a characteristic wavenumber and direction. In random seas, the selection of the characteristic wavenumber and direction is typically based on the background sea state. Examples of MNLS simulations of random seas include Dysthe *et al.* (2003), Socquet-Juglard *et al.* (2005), Gramstad & Trulsen (2007), Xiao *et al.* (2013) and Adcock *et al.* (2015). An appropriate value for the characteristic wavenumber may be clear if the wave spectrum is symmetric about a spectral peak. Similarly, a sea state featuring a concentration of wave components aligned to a particular direction provides a clear choice for the carrier wave direction. However, sea states without a clear spectral peak or dominant wave direction provide less clarity for the carrier wave parameters. For long simulations there may also be a change in the spectral peak due to non-linear physics and, if activated, energy input or damping. Furthermore, the characteristics of an individual steep wave event in a random sea may not be consistent with the background sea state. Waseda *et al.* (2021) investigate the formation of a steep, short-crested wave group formed at an oblique angle to the dominant wave direction, based on stereo images of the ocean. Thus, individual wave events may form at an angle to the dominant wave direction and local spectral distortions may also arise in the vicinity of a steep wave event due to nonlinear wave-wave interactions. The selection of the characteristic direction and wavenumber for the MNLS carrier wave can, therefore, present obstacles. We investigate the sensitivity of our results to the selection of the characteristic wavenumber and direction of the MNLS carrier wave. We deliberately test the MNLS equations beyond the parameter range expected in practice, to ascertain the limits of the various formulations.

We simulate isolated wave groups formed by dispersive focusing rather than random seas. An isolated wave group, based on a coherent phase distribution, features the same nonlinear wave-wave interactions observed in random seas. However, the effect of the nonlinear interactions can be more easily identified and the compu-

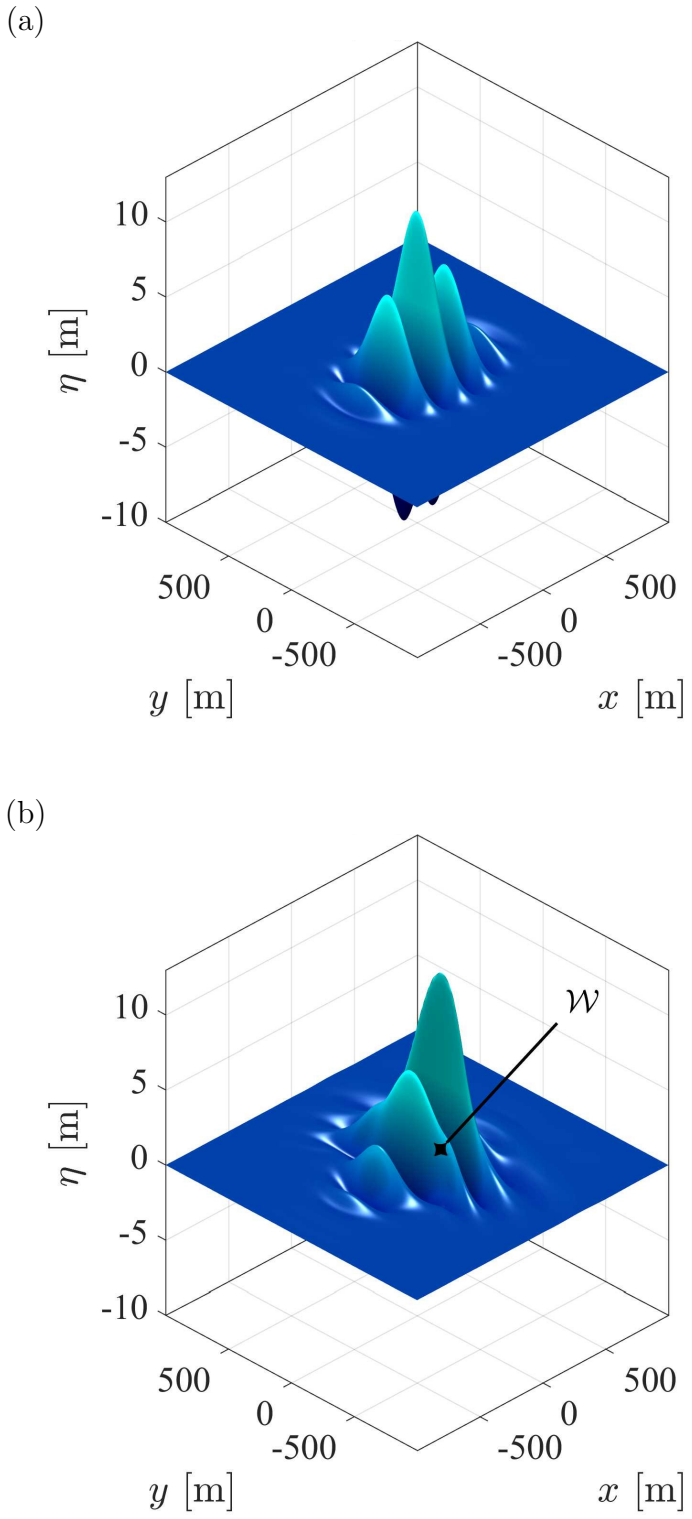

Figure 5.1: Surface elevation of wave groups at focus with a steepness (Ak_p) of 0.3, simulated with identical initial conditions using the fully-nonlinear potential flow solver OceanWave3D: (a) time marched with linear free surface boundary conditions; (b) time marched with nonlinear free surface boundary conditions. The formation of *wing waves* is indicated with $\mathcal{W}$.

tational expense is lower. Figure 5.1 shows focused wave groups simulated with a potential flow code. Identical initial conditions were used for the wave groups shown in figure 5.1(a) and figure 5.1(b). However, figure 5.1(a) shows the focused wave event with linear free-surface boundary conditions and figure 5.1(b) shows the focused wave event with the fully-nonlinear free-surface boundary conditions. As can be seen, the shape of the focused wave event in figure 5.1(b) differs from figure 5.1(a). The largest crest sits in the center of the wave group in figure 5.1(a) but has moved to the front of the wave group in figure 5.1(b). Energy transfers to oblique components also results in the formation of 'wing waves' in figure 5.1(b), denoted with $\mathcal{W}$. Thus, nonlinear wave-wave interactions can significantly influence the formation of a steep wave event, and we investigate the fidelity of various MNLS formulations in resolving the nonlinear interactions. The wing-waves are themselves propagating at approximately 12 degrees to the mean direction and are thus an example of the phenomena which may be poorly captured by an MNLS type model.

The MNLS equation accounts for linear dispersion of the wave components as well as nonlinear wave-wave interactions. The MNLS equation of Trulsen & Dysthe (1996) performs an expansion on the linear dispersion operator with truncation at the fifth order. In contrast, the MNLS equation of Trulsen *et al.* (2000) retains the exact linear dispersion relation by numerical evaluation of the linear dispersion operator. Use of the exact linear dispersion relation by Trulsen *et al.* (2000) is expected to increase the bandwidth limits of the MNLS equation while improving the resolution of four-wave 'quartet' interactions and eliminating energy leakage. In this study, we contrast the results of the two dispersion operators. We note that the MNLS equations of Trulsen & Dysthe (1996) and Trulsen *et al.* (2000) are both fourth-order in steepness, shown by Stiassnie (1984) to only resolve quartet interactions. Thus, all the spectral changes observed in this study are attributed to quartet interactions.

The impact of finite depth on quartet interactions has been previously investigated. Benney & Roskes (1969) and McLean (1982*a*) showed that the dominant directions of energy transfer for a degenerate quartet depend upon the dimensionless

water depth. A variety of MNLS formulations have been proposed to account for the impact of depth on quartet interactions. Third-order 'cubic' Nonlinear Schrödinger (NLS) equations for three-dimensional waves at finite depths have been presented by Benney & Roskes (1969) and Davey & Stewartson (1974). A fourth-order equation for water waves at finite depths has been presented by Brinch-Nielsen & Jonsson (1986). The classic MNLS equation of Trulsen & Dysthe (1996) does, however, incorporate finite-depth into the boundary conditions and the exact dispersion operator of Trulsen *et al.* (2000) allows depth effects to be included in the dispersion relationship with ease. Trulsen & Dysthe (1996) show that the classic MNLS formulation captures the bifurcation of the most unstable perturbation for a Stokes wave at finite depths, suggesting that the classic MNLS equation may be appropriate for some finite-depth simulations. Depth-sensitive coefficients for the nonlinear terms of the MNLS equation have also been proposed by Sedletsky (2003) and we use these coefficients together with the exact linear dispersion operator of Trulsen *et al.* (2000) as a potential finite-depth MNLS model. To assess the performance of our finite-depth MNLS simulations, we compare the results with those of a fully-nonlinear potential flow code.

5.2 Numerical Methodology

We perform simulations with the MNLS equation as well as the fully-nonlinear potential flow code OceanWave3D based on wave groups formed by dispersive focusing. Our simulations follow a three-step process: (1) We use the theory of quasi-determinism to determine the shape of the wave group at focus; (2) Using the linear dispersion relation, we propagate the wave components for 15 characteristic wave periods backwards in time to calculate the initial conditions at $t/T_0 = -15$; (3) We initialise the simulations at $t/T_0 = -15$ and run the simulation forwards in time for 30 characteristic wave periods until $t/T_0 = +15$. Steps 1 and 2 are identical for the OceanWave3D and MNLS simulations, i.e., we use identical initial conditions for the two types of simulations. Only step 3 differs, in terms of which code is used to do the forward propagation of the wave components in time.

5.2.1 Initial Conditions

Implementation of the theory of quasi-determinism requires the underlying wave spectrum of the sea state. We define the variance density spectrum $F(k,\theta)$ as the product of a wavenumber magnitude spectrum $S(k)$ and a spreading function $D(\theta)$. We use a Gaussian function as the wavenumber magnitude spectrum:

$$S(k) = S_0 \exp\left(\frac{-(k-k_p)^2}{2{k_w}^2}\right), \tag{5.2}$$

where k is the wavenumber, k_p is the wavenumber corresponding to the initial spectral peak, and k_w is the spectral width. A Gaussian distribution has also been used for the spreading function:

$$D(\theta) = \frac{1}{\varsigma_0\sqrt{2\pi}} \exp\left(\frac{-(\theta-\chi)^2}{2\varsigma_0^2}\right), \tag{5.3}$$

based on the initial spreading parameter (ς_0) and the direction of the wave component (θ). Here, χ represents the dominant angle of propagation for the wave components. The variance density spectrum $F(k,\theta)$ is thus defined as the product of two Gaussian functions, and table 5.1 lists the values used in this study. All the simulations considered in this investigation are based upon a fixed steepness (Ak_p) with fixed spectral parameters (k_p, k_w, ς_0). Only the parameters of the MNLS carrier wave and the dimensionless depth ($k_p d$) of the domain are varied. Barratt *et al.* (2021*a*) showed that the absence of the spectral tail can result in augmented wave-wave interactions. Thus, the spectra used in this study represent a conservative test of the MNLS equation, since more realistic spectra are likely to result in weaker wave-wave interactions than those observed in this investigation. The initial spectrum used is reasonably narrow-banded and thus one would expect the MNLS model to perform well. However, the rapid weakly nonlinear wave-wave interactions will cause a broadening of the bandwidth in the mean wave direction (Gibbs & Taylor (2005); Adcock *et al.* (2012)) which potentially invalidates the narrow-banded assumption.

Quasi-determinism (QD) theory, based on Boccotti (2000) and Lindgren (1970),

Table 5.1: Initial Condition Parameters.

Ak_p	k_p	k_w	ς
0.3	0.02796 m^{-1}	0.004606 m^{-1}	15°

indicates that the average shape of an extreme event in a random, linear Gaussian field is the scaled auto-correlation function. The linear surface elevation of the wave group is, thus, given by:

$$\eta_L(x, y, t) = A_L \frac{\sum_{i,j} F(k_i, \theta_j) \cos\left(k_i \cos\theta_j \, x + k_i \sin\theta_j \, y - \omega_i t + \varphi_0\right)}{\sum_{i,j} F(k_i, \theta_j)}. \tag{5.4}$$

Here, k_i is the magnitude of the wavenumber component, θ_j is the propagation direction and A_L is the linear amplitude of the wave group at focus. A phase offset φ_0 is included in (5.4) to implement the 'phase separation' method of removing bound harmonics (see Fitzgerald *et al.* (2014)). For the MNLS simulations, removal of the bound harmonics is not necessary and φ_0 is set to zero, causing linear focus to occur at ($x = 0$, $y = 0$, $t/T_0 = 0$). For the OceanWave3D simulations, each simulation is repeated with φ_0 values of 0°, 90°, 180° and 270° to remove the bound harmonics with four-phase separation, as used by Barratt *et al.* (2021*a*). The angular frequency of each component (ω_i) is calculated from the arbitrary-depth linear dispersion relationship, $\omega_i = \sqrt{g k_i \tanh\left(k_i d\right)}$, allowing the initial conditions to be calculated at $t/T_0 = -15$. We calculate the corresponding velocity potential and apply exact second-order correction of the initial conditions using Dalzell (1999). The surface elevation and velocity potential are prescribed as initial conditions for the potential flow simulations.

For the MNLS simulations, we calculate the initial complex envelope $B(\boldsymbol{x}, t)$ using the linear surface elevation η_L and the Hilbert transform of the linear surface elevation η_L^H following Osborne (2010):

$$B(\boldsymbol{x}, t) = \{\eta_L + i\eta_L^H\} \exp\left(-i[\boldsymbol{k}_0 \cdot \boldsymbol{x} - \omega_0 \, t]\right). \tag{5.5}$$

Here, $\boldsymbol{k}_0$ and ω_0 are the properties of the carrier wave.

Table 5.2: Grid parameters for OW3D and MNLS simulations.

Grid	N_x	N_y	N_z	Δx	Δy
OW3D	1025	257	9	7.5 m	10 m
MNLS Inter.	513	257	-	15 m	20 m
MNLS Fine	1025	513	-	7.5 m	10 m

5.2.2 Potential Flow Simulations

OceanWave3D numerically solves the governing equations of potential flow for surface gravity waves Currie (1993), including the fully-nonlinear free surface boundary conditions. Described in detail by Engsig-Karup *et al.* (2009), OceanWave3D is based on an Eulerian frame of reference and the three-dimensional spatial domain is discretized with Cartesian coordinates (x, y, z). Table 5.2 lists the horizontal grid resolution (Δx, Δy), which is uniform throughout the domain, together with the number of grid points (N_x, N_y) in the x and y-directions. We utilise a symmetry plane along the centreline of the wave group ($y = 0$) for the potential flow simulations. Thus, the domain width based on table 5.2 only represents half the effective domain width for the potential flow simulations. The vertical distribution of grid points follows the symmetric half of a Chebyshev-Gauss-Lobatto (CGL) distribution with the vertical number of grid points (N_z) listed in table 5.2. We use eighth-order finite differencing of the spatial derivatives throughout the domain combined with fourth-order Runge-Kutta time marching and a Courant-Friedrichs-Lewy (CFL) condition of 0.5, based on the phase speed (c_0) associated with the wavenumber of the spectral peak (k_p) and the horizontal grid resolution in the x direction (Δx). Our selection of the simulation parameters is informed by the numerical error assessment of Barratt *et al.* (2020) based on similar simulations. The simulations of Barratt *et al.* (2020) were found to agree well with other potential flow codes with total energy conservation within 0.04% over 40 wave periods. For comparison against the MNLS simulations, we use the four-phase separation technique (Fitzgerald *et al.* (2014)), to remove the bound harmonics from the potential flow simulations and approximate the linear surface elevation (η_L). Using the Hilbert

transform of the linear surface elevation (η_L^H), we calculate the absolute value of the complex wave envelope, $|B|$:

$$|B| = \sqrt{(\eta_L)^2 + (\eta_L^H)^2}, \tag{5.6}$$

to compare the envelope steepness between the potential flow and MNLS simulations. Note that the ability of the MNLS formulation to model bound harmonics has been considered by Adcock & Taylor (2016).

5.2.3 MNLS Simulations

We perform simulations with the MNLS equations of Trulsen & Dysthe (1996) as well as Trulsen *et al.* (2000). We repeat the MNLS simulations based upon different characteristic wavenumbers for the carrier wave. We also alter the direction of the carrier wave relative to the direction of wave group propagation using the parameter χ as included in (5.3). The carrier wave is always aligned with the x-axis, corresponding to $\theta = 0°$, while the direction of wave group propagation is determined by χ.

The MNLS formulation assumes that the surface elevation $\eta(\boldsymbol{x}, t)$ may be represented by modulation of a carrier wave with the characteristic wave vector $\boldsymbol{k}_0 = (k_0, 0)$ based upon a characteristic wavenumber magnitude k_0. In this study, we normalise k_0 by the wavenumber of the initial spectral peak k_p to define the ratio:

$$\beta = k_0/k_p. \tag{5.7}$$

We perform simulations with β values between 0.7 and 1.3 in increments of 0.1. We define the direction of the carrier wave relative to the direction of wave group propagation, following the coordinate system shown in figure 5.2. Our coordinate system aligns the carrier wave with the x-axis and the direction of wave group propagation aligns with the x^*-axis. The angle between the axes is denoted χ and we perform simulations with χ values between 0° and 30° in intervals of 5°. In the spectral domain, wavenumbers k_x and k_y correspond to the x and y-axes respectively while wavenumbers k_x^* and k_y^* correspond to the x^* and y^*-axes respectively. All

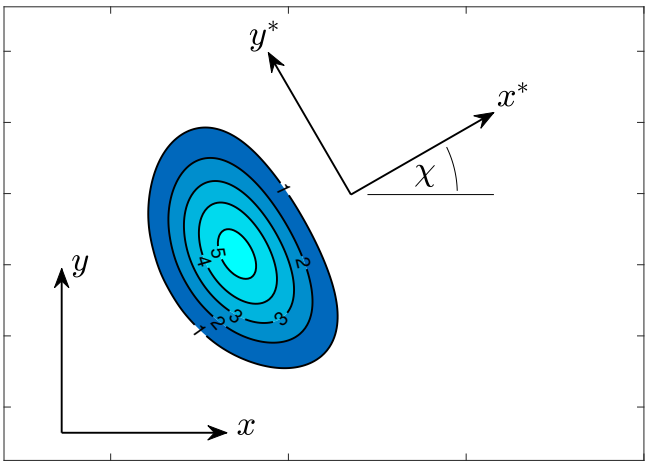

Figure 5.2: Coordinate systems for MNLS simulations. Contour levels depict the surface elevation η of the wave group, evenly distributed between 1m and 5m in intervals of 1 m. The direction of the carrier wave coincides with the x-axis and the wave group propagates in the direction of the x^*-axis. The angle between the axes is denoted as χ.

spectral evolution plots are shown in terms of k_x^* and k_y^* based on the coordinate system of the wave group.

The nonlinear evolution of the complex envelope is simulated with the MNLS equation, see (5.1), subject to the free surface and bottom boundary conditions, as well as continuity for the mean flow potential $\overline{\phi}$:

$$\frac{\partial \overline{\phi}}{\partial z} = \frac{\omega_0}{2}\frac{\partial}{\partial x}|B|^2 \quad \text{at} \quad z = 0, \tag{5.8}$$

$$\frac{\partial \overline{\phi}}{\partial z} = 0 \quad \text{at} \quad z = -d, \tag{5.9}$$

$$\nabla^2 \overline{\phi} = 0 \quad \text{for} \quad -\infty < z < 0. \tag{5.10}$$

In (5.1), $\mathfrak{L}$ represents a dispersion operator, acting upon the complex envelope B, which can be expressed as:

$$\mathfrak{L}\, B = \frac{1}{4\pi^2}\int_{-\infty}^{\infty} i[\omega(\boldsymbol{k_0}+\boldsymbol{\mu}) - \omega_0] \exp\left(i\boldsymbol{\mu}\cdot(\boldsymbol{x}-\boldsymbol{y})\right) B(\boldsymbol{y},t)\mathrm{d}\boldsymbol{y}\mathrm{d}\boldsymbol{\mu}. \tag{5.11}$$

Here, $\boldsymbol{\mu} = (\lambda, \mu)$ is the modulation wavenumber and ω_0 is the frequency corresponding to the characteristic wavenumber k_0 based on the linear dispersion relation. Expansion of $\omega(\boldsymbol{k_0}+\boldsymbol{\mu})$ in (5.11) utilising the linear dispersion relation, followed by

truncation at the fifth order, yields the linear part of the Trulsen & Dysthe (1996) equation. Direct numerical evaluation of (5.11) avoids truncation, retaining the exact linear dispersion relation, as shown by Trulsen *et al.* (2000). Retention of exact linear dispersion in (5.11) increases the bandwidth limits of the MNLS equation and improves the resolution of four-wave interactions while eliminating energy leakage (see Martin & Yuen (1980) and Yuen & Lake (1980)), with almost no additional computational cost. We use both the truncated and exact versions of (5.11) in our simulations and compare the results to assess the impact of the truncated/exact linear dispersion operators. To perform our MNLS simulations, we incorporate the boundary conditions, (5.8) and (5.9), directly into the MNLS equation, (5.1), using the continuity condition for the mean flow, (5.10), as done with the fourth-order envelope equation of Janssen (1983). A single governing equation is, thus, obtained:

$$\begin{aligned}\frac{\partial B}{\partial t} + \mathfrak{L}\,B + \frac{1}{2}i\omega_0 k_0^2|B|^2 B + \frac{3}{2}\omega_0 k_0 |B|^2\frac{\partial B}{\partial x} \\ + \frac{1}{4}\omega_0 k_0 B^2\frac{\partial B^*}{\partial x} + ik_0 B\mathcal{F}^{-1}\left\{\frac{ik_x}{|\boldsymbol{k}|}\frac{1}{\tanh(|\boldsymbol{k}|d)}\mathcal{F}\left\{\frac{\omega_0}{2}\frac{\partial}{\partial x}|B|^2\right\}\right\} = 0.\end{aligned} \tag{5.12}$$

where $\mathcal{F}$ denotes a 2D Fourier transform in x and y and $\mathcal{F}^{-1}$ denotes the inverse operation. Note that (5.12) includes a depth-dependent return current term which results from the incorporation of finite depth into the bottom boundary condition in (5.9). For our simulations based on (5.12), we use the arbitrary-depth linear dispersion relation, $\omega = \sqrt{gk\tanh(kd)}$, to evaluate the dispersion operator $\mathfrak{L}\,B$ with the exact version of (5.11). We also perform MNLS simulations based on infinite depth ($|k|d$ goes to ∞) with the corresponding expression:

$$\begin{aligned}\frac{\partial B}{\partial t} + \mathfrak{L}\,B + \frac{1}{2}i\omega_0 k_0^2|B|^2 B + \frac{3}{2}\omega_0 k_0 |B|^2\frac{\partial B}{\partial x} \\ + \frac{1}{4}\omega_0 k_0 B^2\frac{\partial B^*}{\partial x} + ik_0 B\mathcal{F}^{-1}\left\{\frac{ik_x}{|\boldsymbol{k}|}\mathcal{F}\left\{\frac{\omega_0}{2}\frac{\partial}{\partial x}|B|^2\right\}\right\} = 0.\end{aligned} \tag{5.13}$$

For our simulations based on (5.13), we use the deep-water linear dispersion relation, $\omega = \sqrt{gk}$, to evaluate the dispersion operator $\mathfrak{L}\,B$. Our comparison of the truncated and exact versions of (5.11) is based upon (5.13). We directly discretize and numerically solve (5.12) and (5.13) using a split-step algorithm. We use spectral methods

to evaluate both the exact and truncated versions of (5.11), using the Fourier transform to treat the spatial derivatives as multiplier operators for the linear dispersion terms presented in Trulsen & Dysthe (1996). We use fourth-order finite differencing with symmetric stencils for the spatial derivatives in the nonlinear terms. Time marching is performed with the classic fourth-order Runge-Kutta scheme. We perform simulations with Courant-Friedrichs-Lewy (CFL) conditions of 0.5 and 1.0 to assess the effect, based on the group speed (c_g) of the wave group (k_p) and the horizontal grid resolution in the x-direction (Δx). Note that the definition of the CFL differs between the potential flow and MNLS simulations since the group speed (c_g) is the characteristic velocity of the wave envelope in the MNLS simulations while the phase speed (c_0) is the characteristic velocity of the free surface in the potential flow simulations.

We also perform finite-depth MNLS simulations by combining the exact version of (5.11), based on the arbitrary-depth linear dispersion relation, with depth-sensitive coefficients for the nonlinear terms proposed by Sedletsky (2003):

$$\begin{aligned}\frac{\partial B}{\partial t} + \mathfrak{L}\, B + q_3 i\omega_0 k_0^2 |B|^2 B + Q_{41}\omega_0 k_0 |B|^2 \frac{\partial B}{\partial x} \\ + Q_{42}\omega_0 k_0 B^2 \frac{\partial B^*}{\partial x} = 0,\end{aligned} \tag{5.14}$$

denoted as q_3, Q_{41} and Q_{42} in (5.14) and plotted against dimensionless depth ($k_0 d$) in figure 5.3. We note that the coefficients were first derived by Sedletsky (2003) and later confirmed by Slunyaev (2005). However, Slunyaev (2005) includes one additional term in the expansion of the mean flow and we use the versions of q_3, Q_{41} and Q_{42} listed in Gandzha & Sedletsky (2017), consistent with the results of Slunyaev (2005). An expansion of the induced mean flow allows the effect of the return current term to be encompassed within the coefficients q_3, Q_{41} and Q_{42}. Thus, (5.14) does not contain a return current term. Finite-depth is known to suppress quartet interactions and figure 5.3 shows that the values of q_3, Q_{41} and Q_{42} decline as the dimensionless depth ($k_0 d$) is reduced from 5.592 to 1.363. Notably, the value of q_3 goes to zero at $k_0 d = 1.363$, the critical depth of vanishing modulational instability for unidirectional waves, and Q_{42} turns negative for $k_0 d < 1.731$. Thus,

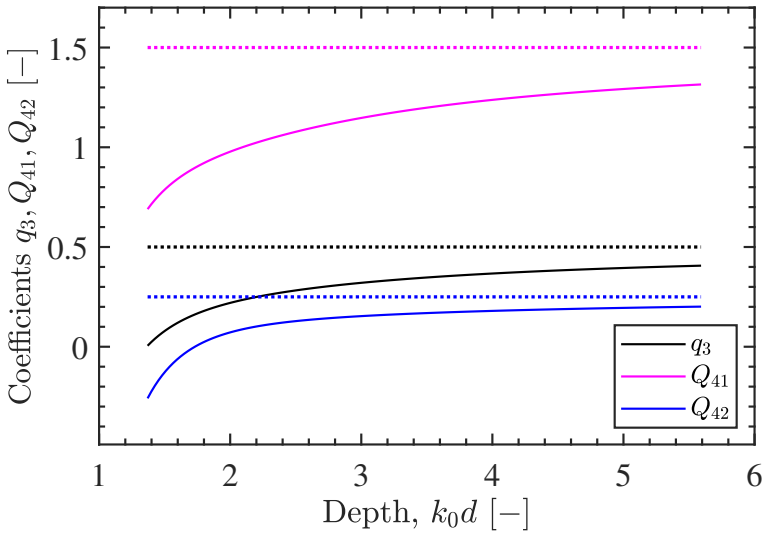

Figure 5.3: Coefficients q_3, Q_{41} and Q_{42} for dimensionless depths ($k_0 d$) between 1.363 and 5.592 based on the expressions in Gandzha & Sedletsky (2017). The solid lines represent the coefficient values, used in (5.14), and the dotted lines represent the asymptotic infinite-depth limits, used in (5.12) and (5.13).

(5.14) may present a finite-depth MNLS model that captures the suppression of quartet interactions by finite-depth and we assess its performance.

5.2.4 Grid Resolution and CFL

We have analysed the discretization error for the MNLS simulations. The OceanWave3D simulations in this study are based on the same parameters as Barratt *et al.* (2020) and a detailed assessment of the discretization errors can be found therein. The MNLS simulations have been performed with two grid levels, termed 'intermediate' and 'fine', with the parameters listed in table 5.2. Note that a symmetry plane has not been used for the MNLS simulations. We have assessed the effect of the grid resolution and CFL with the results listed in table 5.3. We consider the maximum steepness of the wave group (Ak_p^*), observed at any time in the simulation, as well as the corresponding time at which the maximum is reached (t^*/T_0). The Nonlinear Schrödinger (NLS) equation has an infinite number of conserved quantities (Zakharov & Shabat (1972)) and we consider the conserved quantity I_2.

$$I_2 = \sum_{i,j} |B(x_i, y_j)|^2, \tag{5.15}$$

Table 5.3: MNLS convergence study based on grid resolution / CFL.

Grid	CFL	n_x	n_y	Ak_p^*	t^*/T_0	$\Delta I_2^*[\%]$
Inter.	1.0	90.9	42.9	0.304	1.42	4.08e-02
Inter.	0.5	90.9	42.9	0.304	1.66	1.06e-02
Fine	1.0	181.9	85.8	0.305	1.66	1.34e-03
Fine	0.5	181.9	85.8	0.305	1.66	7.33e-04
OW3D	0.5	-	-	0.283	1.27	-

typically associated with energy conservation. We calculate I_2 at each time step and the maximum discrepancy in I_2 relative to the initial value (denoted as ΔI_2^*), has been recorded and listed in table 5.3 for the different grid resolutions and CFL conditions. Our assessment of grid resolution is based on dimensionless length scales for the wave envelope (Λ_x, Λ_y) in the x and y directions:

$$\Lambda_x = \frac{2\pi}{k_w}, \qquad \Lambda_y = \frac{2\pi}{k_p \varsigma_0}, \tag{5.16}$$

based on the spectral bandwidth (k_w), the initial peak wavenumber (k_p) and the initial spreading parameter (ς_0) in radians. Dimensionless metrics for grid resolution, in the x and y-directions can, thus, be defined as:

$$n_x = \frac{\Lambda_x}{\Delta x}, \qquad n_y = \frac{\Lambda_y}{\Delta y}, \tag{5.17}$$

which approximately represent the number of grids spanning the wave envelope in the x and y-directions. Table 5.3 lists the values of n_x and n_y for the different MNLS grid resolutions.

Table 5.3 indicates that the maximum steepness of the wave group does not differ significantly between the different grid resolutions and CFL conditions for the MNLS simulations. An Ak_p^* value of 0.304–0.305 occurs in all the cases. However, the time at which the max steepness occurs does show a dependency on the CFL condition. A combination of the intermediate grid resolution with a CFL value of 1.0 results in premature focusing of the wave group. Thus, we use the intermediate grid resolution with a CFL value of 0.5 which shows close agreement in focal time

with the fine grid cases. We note that the ΔI_2^* value of 0.0106% indicates negligible changes to the conserved quantity I_2, associated with energy conservation. The maximum steepness Ak_p^* and focal time t^*/T_0 of the MNLS simulations do differ from the potential flow results. We attribute the differences to an overestimation of nonlinear interactions by the MNLS equation, as discussed in the results section.

5.3 Results and Discussion

We investigate focusing wave groups, in deep and finite depths, and compare the results of MNLS simulations, based on exact and truncated versions of the dispersion operator, with fully-nonlinear potential flow simulations performed with OceanWave3D. The impact of the carrier wavenumber for the MNLS simulations is assessed as well as the impact of the carrier wave direction, relative to the direction of wave group propagation. Our analysis considers the steepness of the wave envelope over the course of the simulations as well as the spectral evolution of the wave group.

5.3.1 Comparison of OceanWave3D and MNLS Results

We compare the simulation results from OceanWave3D with infinite-depth MNLS simulations based on (5.13), both in terms of envelope steepness and spectral evolution. Figure 5.4 depicts envelope steepness $A(t)k_p$ over time for the OceanWave3D and MNLS simulations. The envelope amplitude $A(t)$ is the maximum elevation of the envelope at time t. The general agreement between the potential flow and MNLS results is good, although the MNLS simulations tend to overpredict the steepness of the wave group at focus. The construction of the wave group implies that the steepness curve shown in figure 5.4 should be symmetric about the time of focus ($t = 0$) if the evolution were linear. Thus, asymmetry in the steepness curve and a delay in focus beyond $t = 0$ are the result of nonlinear wave-wave interactions. The competing effects of dispersion and nonlinear wave-wave interactions are captured by the Benjamin-Feir index, as discussed by Janssen (2003), impacting the lifespan of focused wave events. The potential flow results in figure 5.4 show evidence of suppressed dispersion causing the wave group to focus after $t = 0$ and remain steep

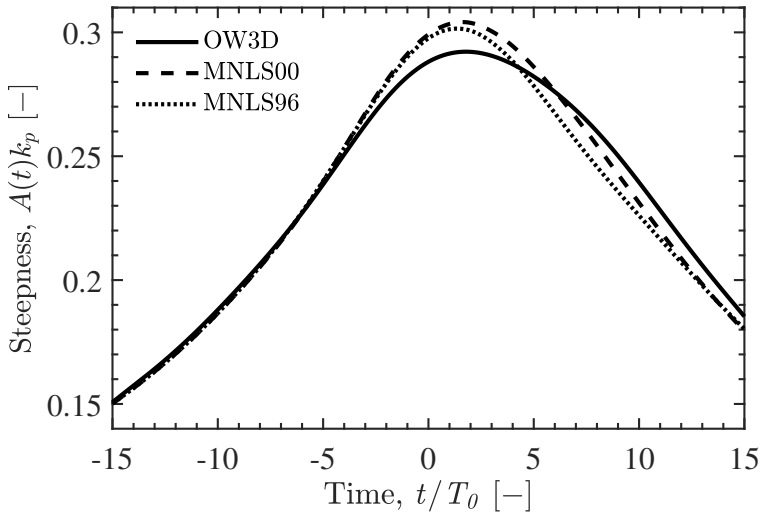

Figure 5.4: Envelope steepness over time for OceanWave3D (OW3D) and infinite-depth MNLS simulations, based on (5.13), performed with exact linear dispersion operator ('MNLS00') and truncated linear dispersion operator ('MNLS96'). The amplitude $A(t)$ is based on the maximum elevation of the wave envelope at time t.

after focus, extending the lifespan of the focused wave event. Evidence of a prolonged lifespan for steep wave events, due to nonlinear interactions, has also been presented by Fujimoto *et al.* (2019). Suppressed dispersion is also apparent for the MNLS simulations, but the effect is less noticeable than observed in the potential flow simulations, with only a small degree of asymmetry apparent for the steepness curve shown in figure 5.4. The MNLS results based on the exact and truncated dispersion operators also agree closely. The MNLS results based on the different dispersion operators are almost identical in the early stages of wave focusing but discrepancies arise during and after the nonlinear focused event.

The MNLS equation is limited in terms of bandwidth and steepness. Thus, the discrepancies may be caused by the increasing steepness of the wave group approaching focus and the oblique energy transfers which increase the spectral bandwidth. The exact dispersion operator is expected to have broader bandwidth limits and improved resolution of four-wave interactions. Thus, discrepancies between the exact and truncated dispersion operator may be expected for wave groups which are particularly steep or broad-banded, accounting for the difference observed during and after focus. Agreement between the MNLS simulations improves towards the end of the simulation, once the post focus wave group has dispersed and the steepness of the group is again reduced. Both of the MNLS results appear to overestimate non-

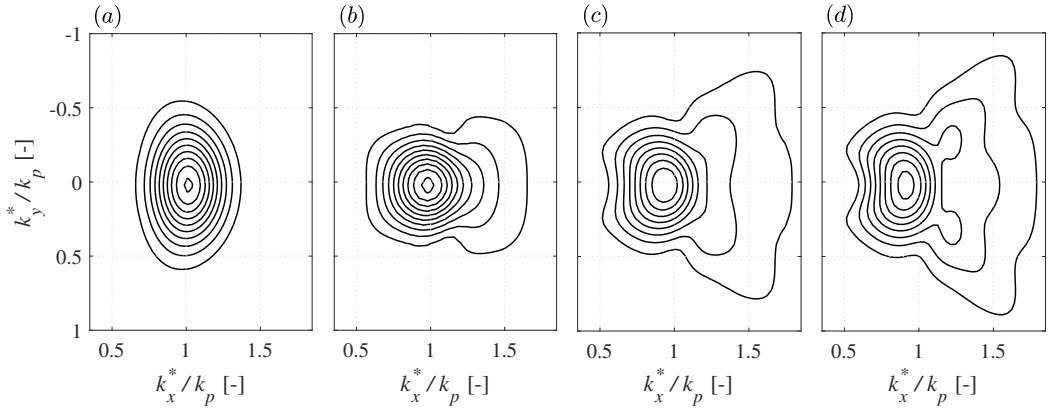

Figure 5.5: Amplitude spectra of surface elevation for a OceanWave3D simulation with dimensionless depth of $k_p d = 5.59$: (a) $t/T_0 = -15$; (b) $t/T_0 = 0.0$; (c) $t/T_0 = 7.5$; (d) $t/T_0 = 15$. Contour levels are evenly distributed between 0.005 m and 0.150 m in intervals of 0.005 m.

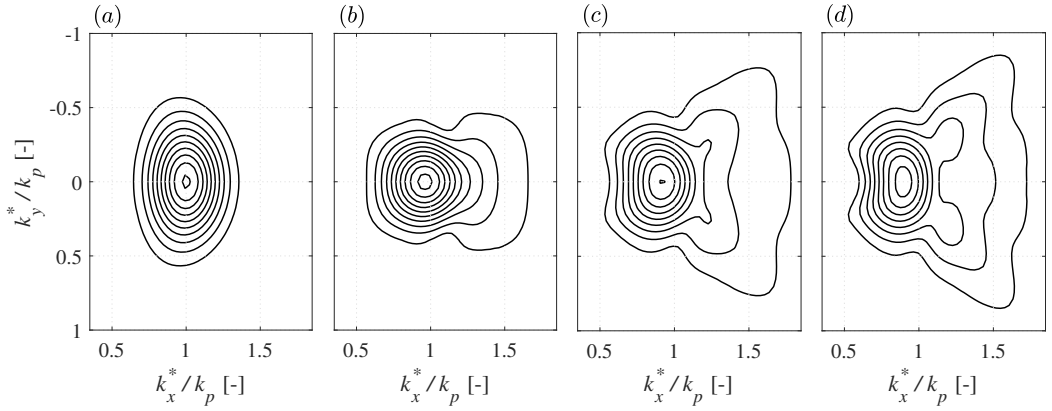

Figure 5.6: Amplitude spectra of surface elevation for an infinite-depth MNLS simulation, based on (5.13), with exact linear dispersion operator: (a) $t/T_0 = -15$; (b) $t/T_0 = 0.0$; (c) $t/T_0 = 7.5$; (d) $t/T_0 = 15$. Contour levels are evenly distributed between 0.005 m and 0.150 m in intervals of 0.005 m.

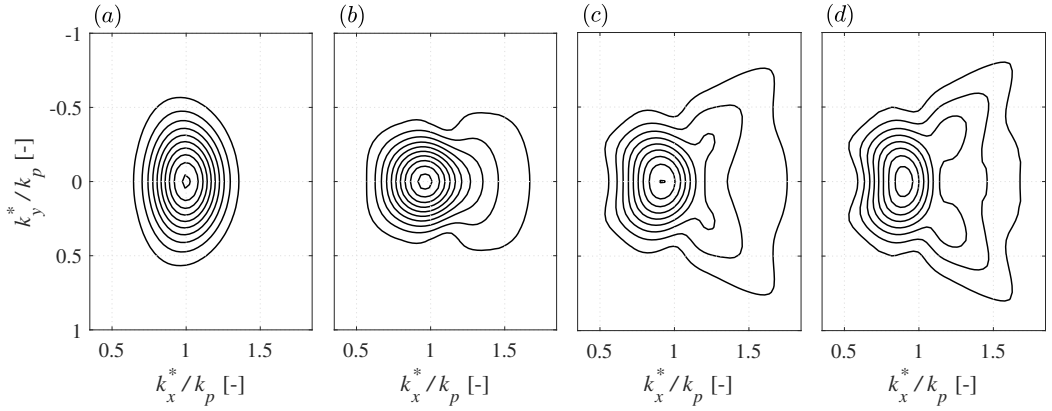

Figure 5.7: Amplitude spectra of surface elevation for an infinite-depth MNLS simulations, based on (5.13), with truncated linear dispersion operator: (a) $t/T_0 = -15$; (b) $t/T_0 = 0.0$; (c) $t/T_0 = 7.5$; (d) $t/T_0 = 15$. Contour levels are evenly distributed between 0.005 m and 0.150 m in intervals of 0.005 m.

linearity, resulting in wave groups which are steeper at focus than the OceanWave3D result. However, the discrepancy in envelope amplitude at focus is less than 4%, indicating good agreement between the fully-nonlinear potential flow simulations and the approximate MNLS results.

Figure 5.6 and 5.7 show the corresponding results from the MNLS simulations. Figure 5.6 is based on the MNLS equation of Trulsen *et al.* (2000), using the exact version of (5.11). Figure 5.7 is based on the MNLS equation of Trulsen & Dysthe (1996), using the fifth order truncated version of (5.11). As can be seen, both versions of the MNLS equation capture the spectral evolution of the wave group. The energy transfers to oblique and high-wavenumber components are captured in the MNLS wave spectra, near the time of focus and post focus, in figure 5.6 and figure 5.7.

We also compare the spectral evolution of the OceanWave3D and MNLS simulations to assess the resolution of four-wave interactions. Figure 5.5 shows the OceanWave3D result, depicting the amplitude spectrum of surface elevation for the initial condition ($t/T_0 = -15$) in figure 5.5(a) and near the time of focus ($t/T_0 = 0$) in figure 5.5(b). Post focus results are depicted at $t/T_0 = 7.5$ in figure 5.5(c) and $t/T_0 = 15$ in figure 5.5(d). The initial condition shows a concentration of wave components around the spectral peak consistent with the wave spectrum defined by (5.2) and (5.3). Approaching nonlinear focus, the wave spectrum exhibits energy transfers to higher wavenumbers and oblique wave components, as can be seen in figure 5.5(b). Post focus, the energy transfers to oblique components intensifies, as can be seen in figure 5.5(c) and 5.5(d).

5.3.2 Wavenumber of MNLS carrier wave

The effect of the carrier wavenumber on the evolution of the wave envelope is shown in figure 5.8 for infinite-depth MNLS simulations based on (5.13). The results based on the exact dispersion operator are shown in figure 5.8(a) and the results based on the truncated dispersion operator are shown in 5.8(b). Both figures depict the increasing envelope steepness during focusing followed by a post-focus decline in steepness as the wave group disperses. Figure 5.8(a) demonstrates that β values

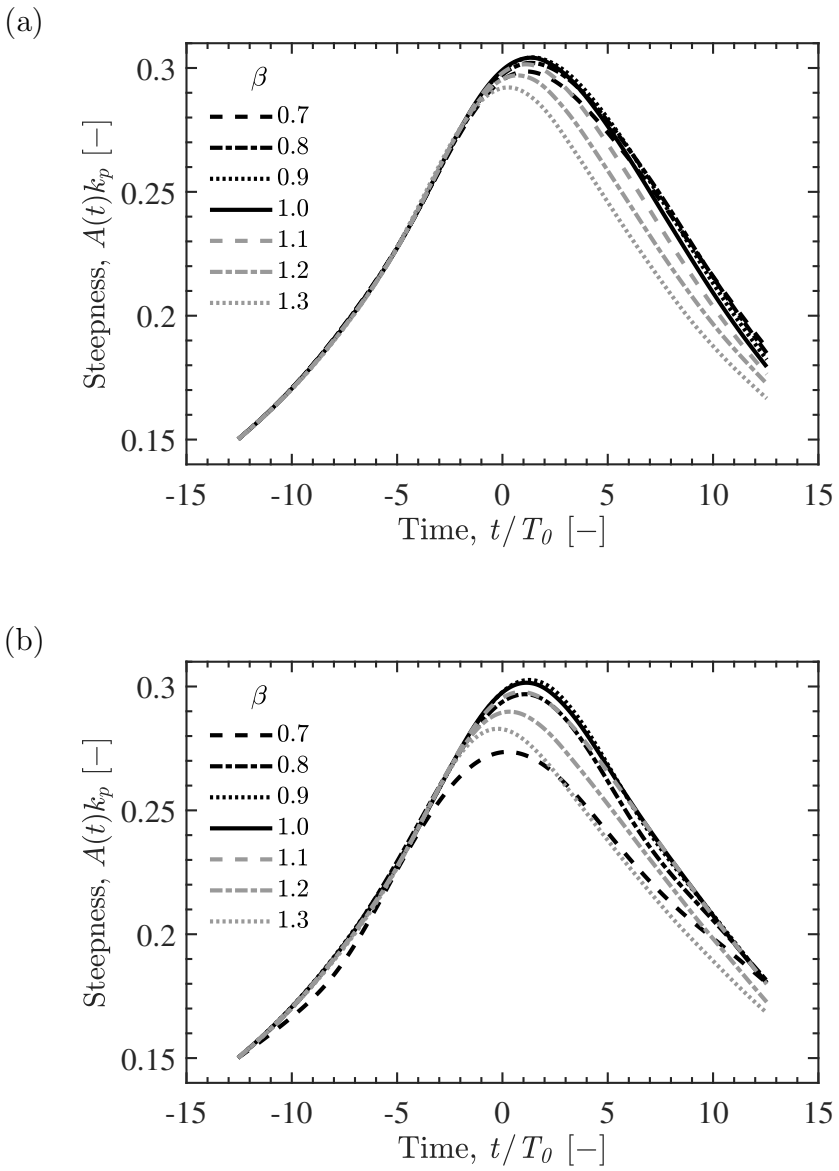

Figure 5.8: Envelope steepness over time for infinite-depth MNLS simulations, based on (5.13), with different characteristic wavenumbers ($\beta = k_0/k_p$), performed with: (a) exact linear dispersion operator; (b) truncated linear dispersion operator. The amplitude $A(t)$ is based on the maximum elevation of the wave envelope at time t.

less than unity do not significantly alter the evolution of the wave envelope if the exact dispersion operator is used. However, β values greater than unity do alter the evolution of the envelope for the exact dispersion operator; a β of 1.3 reduces the amplitude of the focused event by 4.0%. If the truncated dispersion operator is used, figure 5.8(b) reveals that β values both great and less than unity can impact the evolution of the wave group, indicating a 9.6% reduction in amplitude at focus for a β of 0.7. Thus, the truncated operator appears to be more sensitive than the exact operator to the selection of the β value. Selecting a carrier wavenumber above/below the spectral peak effectively tests the bandwidth limits of the equation since the largest amplitude wave components exist around the spectral peak. Moving the carrier wavenumber away from the spectral peak, thus, shifts some large amplitude components away from the characteristic wavenumber. The superior performance of the exact dispersion operator, thus, demonstrates the improved bandwidth limits of the MNLS equation with exact dispersion, as indicated by Trulsen *et al.* (2000).

The impact of the β value on spectral evolution is demonstrated by figure 5.9 and 5.10 with the results for the exact dispersion operator shown in figure 5.9 and the results for the truncated dispersion operator shown in figure 5.10. The amplitude spectrum of surface elevation is shown at the end of the simulation for various β values, including: $\beta = 0.7$ in figure 5.9(a) and 5.10(a); $\beta = 0.8$ in figure 5.9(b) and 5.10(b); $\beta = 1.0$ in figure 5.9(c) and 5.10(c); $\beta = 1.2$ in figure 5.9(d) and 5.10(d). Notably, both the exact and truncated dispersion operators appear to under predict oblique energy transfers for β values less than unity and both appear to over predict oblique energy transfers for β values greater than unity. As can be seen figure 5.9 and 5.10, the exact and truncated dispersion operators exhibit similar spectra for β values of 1.0 and 1.2. However, for β values less than unity, differences in the spectra arise between the exact and truncated dispersion operators. The truncated dispersion operator exhibits energy leakage to wavenumbers above the spectral peak forming a local peak at $k_x^*/k_p = 1.67$ for $\beta = 0.7$. However, no such energy leakage is apparent with the exact dispersion operator for β values of 0.7 and 0.8. Energy leakage in the MNLS equation, reported by Martin & Yuen (1980), is a source of

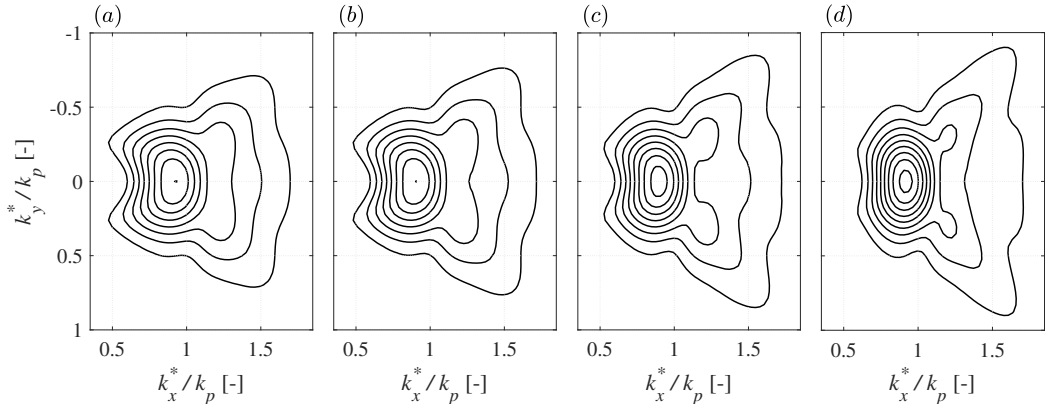

Figure 5.9: Amplitude spectra of surface elevation for infinite-depth MNLS simulations, based on (5.13), performed with the exact linear dispersion operator. The spectra correspond to the end of the simulations, $t/T_0 = 15$, performed with different characteristic wavenumbers ($\beta = k_0/k_p$): (a) $\beta = 0.7$; (b) $\beta = 0.8$; (c) $\beta = 1.0$; (d) $\beta = 1.2$. Contour levels are evenly distributed between 0.005 m and 0.150 m in intervals of 0.005 m.

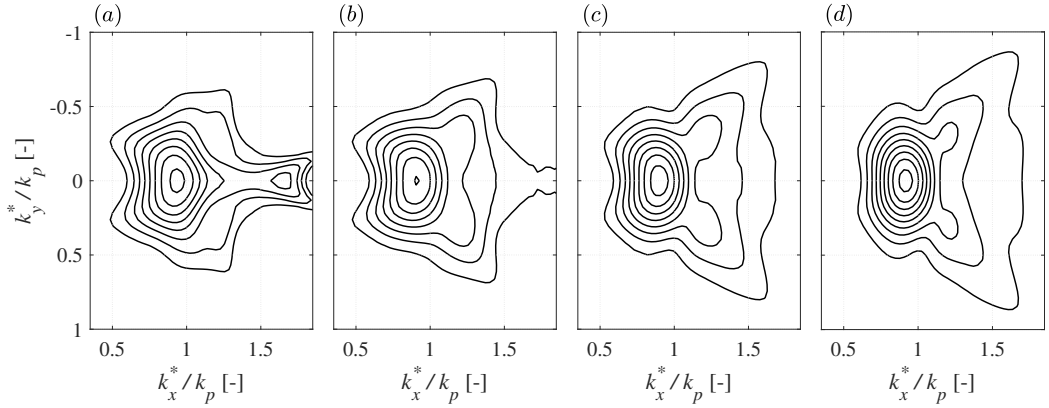

Figure 5.10: Amplitude spectra of surface elevation for infinite-depth MNLS simulations, based on (5.13), performed with the truncated linear dispersion operator. The spectra correspond to the end of the simulations, $t/T_0 = 15$, performed with different characteristic wavenumbers ($\beta = k_0/k_p$): (a) $\beta = 0.7$; (b) $\beta = 0.8$; (c) $\beta = 1.0$; (d) $\beta = 1.2$. Contour levels are evenly distributed between 0.005 m and 0.150 m in intervals of 0.005 m.

inaccuracy which can contaminate the solution, particularly in the context of long-term random sea simulation in which the effect accumulates over time. Trulsen *et al.* (2000) indicate that the exact dispersion operator eliminates energy leakage, and no significant evidence of energy leakage can be seen in figure 5.9 for all β values.

5.3.3 Direction of MNLS carrier wave

The impact of the carrier wave direction on the evolution of the wave envelope is shown in figure 5.11 for infinite-depth MNLS simulations based on (5.13). The results for the exact dispersion operator are shown in figure 5.11(a) and the results

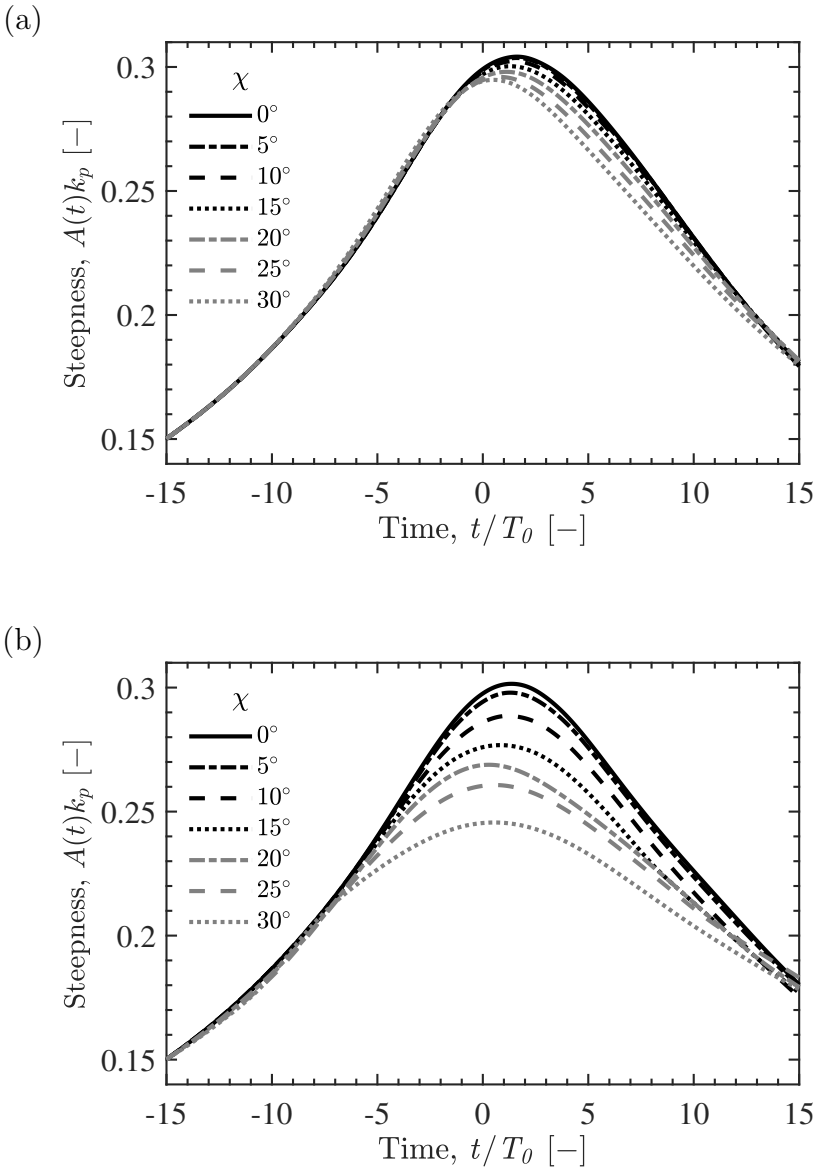

Figure 5.11: Envelope steepness over time for infinite-depth MNLS simulations, based on (5.13), with different carrier wave directions (χ), performed with: (a) exact linear dispersion operator; (b) truncated linear dispersion operator. The amplitude $A(t)$ is based on the maximum elevation of the wave envelope at time t.

for the truncated dispersion operator are shown in figure 5.11(b). The steepness of the wave envelope over time is shown for relative angles (χ) between 0° and 30° in intervals of 5°. The exact dispersion operator performs well even for a large relative angle between the carrier wave and direction of wave group propagation; an angle of 30° results in a 3.1% reduction in amplitude at focus. The truncated dispersion operator performs well for small relative angles, an angle of 10° results in a 4.5% reduction in amplitude at focus. However, the truncated dispersion operator performs less well for large relative angles; an angle of 30° results in a 18.5% reduction in amplitude at focus. A relative angle between the carrier wave and the direction of propagation for the wave group is another means of testing the bandwidth limits of the MNLS equations. Introducing an angle between the carrier wave and the components which comprise the wave group effectively shifts the characteristic wavenumber in the azimuthal direction away from the spectral peak. Thus, the lower sensitivity of the exact dispersion operator to the relative angle demonstrates the superior bandwidth limits of the MNLS equation based on exact dispersion.

The spectral evolution of the wave group for various angles of the carrier wave (χ) is shown in figure 5.12 and figure 5.13 for the exact dispersion operator and the truncated dispersion operator respectively. The amplitude spectrum at the end of the simulation is shown for various angles of the carrier wave, including: $\chi = 0°$ in figure 5.12(a) and 5.13(a); $\chi = 10°$ in figure 5.12(b) and 5.13(b); $\chi = 20°$ in figure 5.12(c) and 5.13(c) as well as $\chi = 30°$ in figure 5.12(d) and 5.13(d). The wave group is spatially symmetric about the y^*-axis, corresponding to spectral symmetry about the k_y^*-axis if all four-wave interactions are properly resolved. For the exact dispersion operator, figure 5.12 shows a low sensitivity to the angle of the carrier wave; an angle of $\chi = 10°$ introduces minor asymmetries into the spectral evolution but the result is highly consistent with the $\chi = 0°$ result. An angle of $\chi = 30°$ intensifies the asymmetries but the exact dispersion operator still facilitates the resolution of oblique energy transfers to positive and negative k_y components. The truncated dispersion operator shows a higher sensitivity to the angle of the carrier wave, as depicted in figure 5.13. Oblique energy transfers to positive and negative k_y compo-

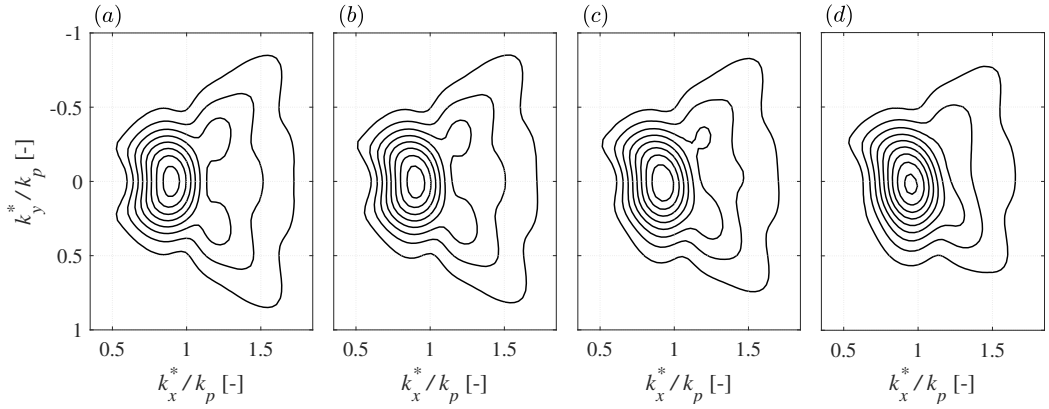

Figure 5.12: Amplitude spectra of surface elevation for infinite-depth MNLS simulations, based on (5.13), performed with exact linear dispersion operator. The spectra correspond to the end of the simulations, $t/T_0 = 15$, performed with different carrier wave directions: (a) $\chi = 0°$; (b) $\chi = 10°$; (c) $\chi = 20°$; (d) $\chi = 30°$. Contour levels are evenly distributed between 0.005 m and 0.150 m in intervals of 0.005 m.

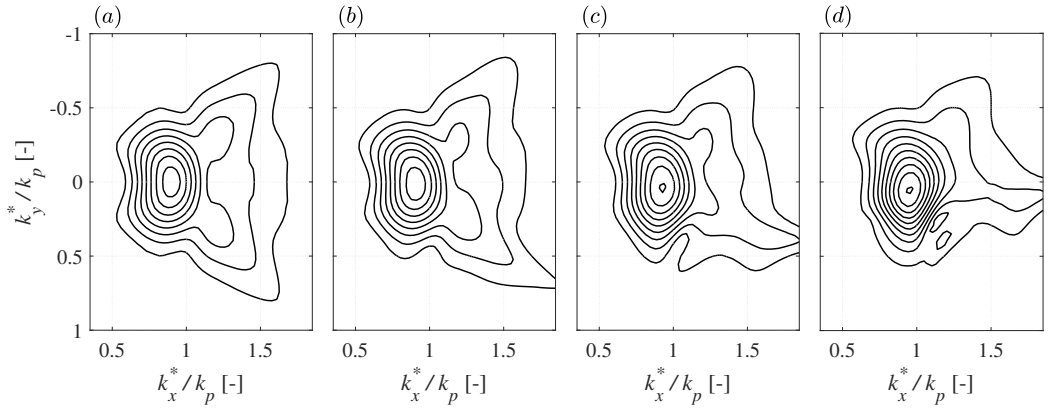

Figure 5.13: Amplitude spectra of surface elevation for infinite-depth MNLS simulations, based on (5.13), performed with truncated linear dispersion operator. The spectra correspond to the end of the simulations, $t/T_0 = 15$, performed with different carrier wave directions: (a) $\chi = 0°$; (b) $\chi = 10°$; (c) $\chi = 20°$; (d) $\chi = 30°$. Contour levels are evenly distributed between 0.005 m and 0.150 m in intervals of 0.005 m.

nents continue to be resolved for a relative angle of $\chi = 10°$. However, signs of energy leakage to oblique high-wavenumber components are apparent, resulting in significant asymmetry for $\chi = 20°$ and $\chi = 30°$. Thus, oblique energy transfers to positive k_y components are not resolved for large angles of χ with the truncated dispersion operator. Thus, the results shown in figure 5.12 and figure 5.13 demonstrate the superior bandwidth limits of the exact dispersion operator as well as the improved resolution of four-wave interactions. The resonance conditions of Phillips (1960) are based upon the linear dispersion relation. Thus, accurate resolution of four-wave interactions is expected to depend on the dispersion operator. Trulsen *et al.* (2000)

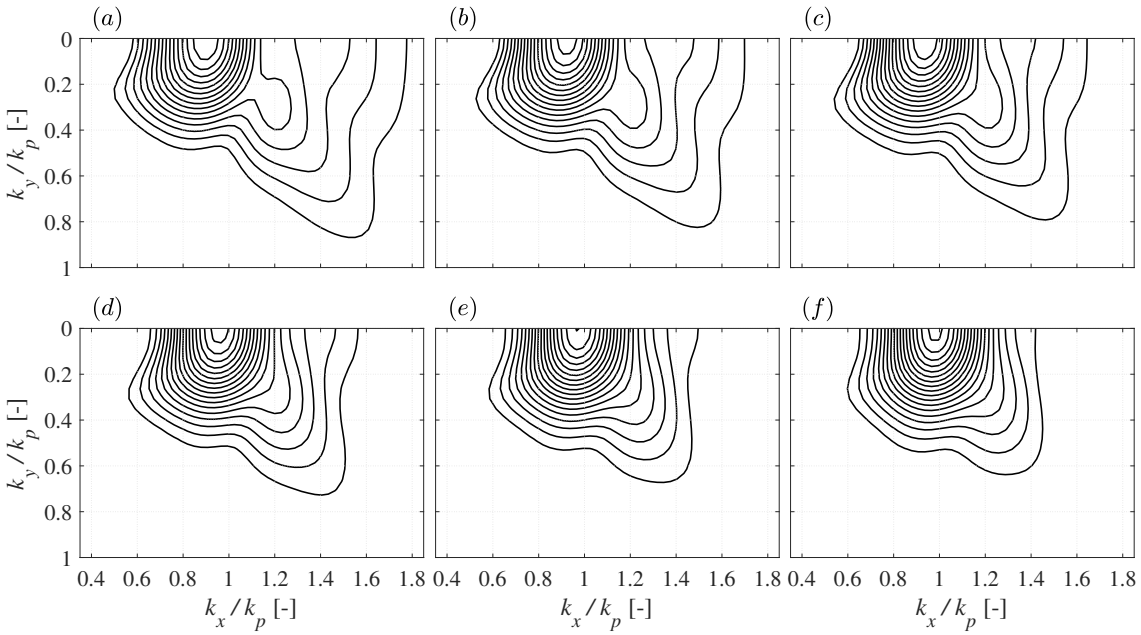

Figure 5.14: Amplitude spectra of surface elevation for OceanWave3D simulations. The spectra correspond to the end of the simulations, $t/T_0 = 15$, performed with different dimensionless depths: (a) $k_p d = 5.59$; (b) $k_p d = 3.14$; (c) $k_p d = 2.60$; (d) $k_p d = 2.00$; (e) $k_p d = 1.60$; (f) $k_p d = 1.36$. Contour levels are evenly distributed between 0.01 m and 0.105 m in intervals of 0.005 m.

indicate that improved resolution of four-wave interactions is expected for the exact dispersion operator, and figure 5.12 demonstrates that high-angle oblique energy transfers continue to be resolved if the MNLS equation is combined with an exact linear dispersion operator.

5.3.4 Finite-depth MNLS Simulations

We compare finite-depth MNLS simulations, based on (5.12) and (5.14), with the results of OceanWave3D for various dimensionless depths. Our comparison is based upon amplitude spectra of surface elevation at the end of simulation ($t/T_0 = 15$) for dimensionless depths ($k_p d$) of 5.59, 3.14, 2.60, 2.00, 1.60 and 1.36. The OceanWave3D results are shown in figure 5.14, demonstrating a weakening of wave-wave interactions with a reduction in depth as observed in previous studies. The spectra corresponding to $k_p d = 5.59$ show energy transfers along the k_x-axis and towards oblique high-wavenumber components, as expected in deep water—McLean (1982*b*) showed that deep-water waves of finite amplitude feature unidirectional as well as oblique instabilities. The unidirectional energy transfers are expected to be suppressed by depth due to an interplay between the modulation instability and the

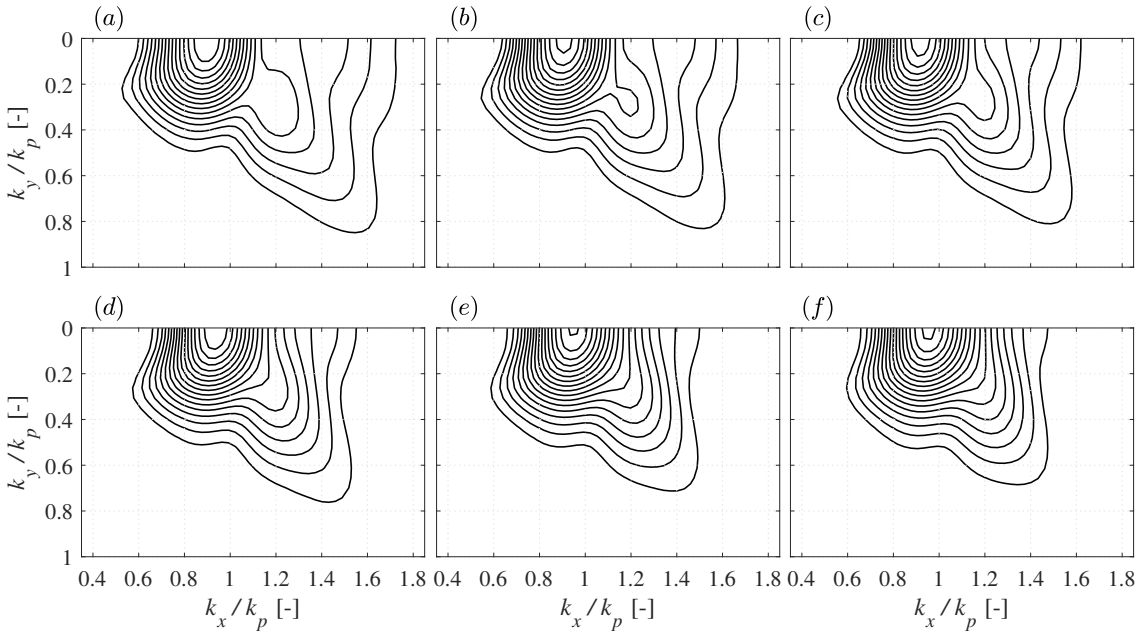

Figure 5.15: Amplitude spectra of surface elevation for finite-depth MNLS simulations based on Trulsen *et al.* (2000) with a depth-sensitive return current term. The spectra correspond to the end of the simulations, $t/T_0 = 15$, performed with different dimensionless depths: (a) $k_p d = 5.59$; (b) $k_p d = 3.14$; (c) $k_p d = 2.60$; (d) $k_p d = 2.00$; (e) $k_p d = 1.60$; (f) $k_p d = 1.36$. Contour levels are evenly distributed between 0.01 m and 0.105 m in intervals of 0.005 m.

return current, as found by Benjamin (1967) and Whitham (1974) and discussed by Janssen & Onorato (2007). Furthermore, Benney & Roskes (1969) and McLean (1982*a*) showed that the dominant/fastest component growth rates become oblique in waters of intermediate depth. In figure 5.14, the spectra all exhibit a significant reduction in energy transfers along the k_x-axis while the oblique energy transfers show less sensitivity to depth. Thus, the potential flow simulations exhibit an increasing dominance of oblique over unidirectional energy transfers as the water depth is reduced.

The corresponding MNLS results are shown in figure 5.15 and 5.16. Finite-depth MNLS simulations based on (5.12), the classic MNLS equation with arbitrary-depth linear dispersion and a depth-sensitive return current term, are shown in figure 5.15. Figure 5.16 shows the results based on (5.14), a combination of the exact version of (5.11), with arbitrary-depth linear dispersion, and the depth-dependent coefficients for the nonlinear terms proposed by Sedletsky (2003). Both finite-depth MNLS formulations exhibit weakening collinear energy transfers along the k_x-axis as depth is reduced from $k_p d = 5.59$ to $k_p d = 1.36$ accompanied by oblique energy

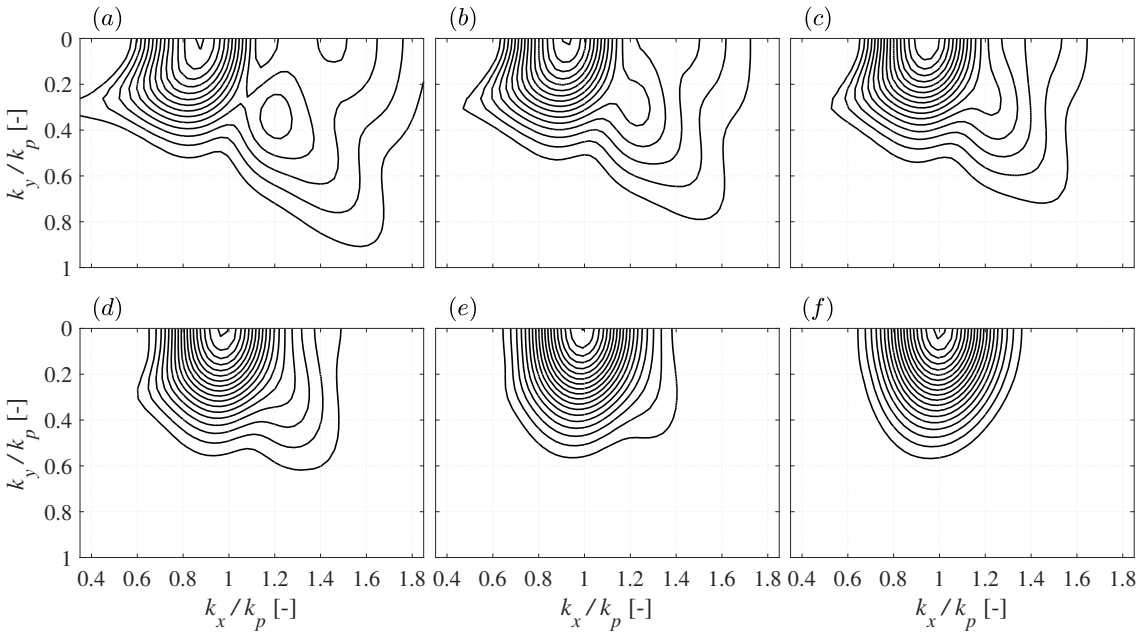

Figure 5.16: Amplitude spectra of surface elevation for finite-depth MNLS simulations. The spectra correspond to the end of the simulations, $t/T_0 = 15$, performed with different dimensionless depths: (a) $k_p d = 5.59$; (b) $k_p d = 3.14$; (c) $k_p d = 2.60$; (d) $k_p d = 2.00$; (e) $k_p d = 1.60$; (f) $k_p d = 1.36$. Contour levels are evenly distributed between 0.01 m and 0.105 m in intervals of 0.005 m.

transfers. Thus, both MNLS codes capture the shift of the dominant component growth rates away from the k_x-axis to oblique components as the dimensionless depth is reduced. However, the results based on the classic MNLS formulation in (5.12) show excellent agreement with OceanWave3D for the full range of depths, $1.36 \leq k_p d \leq 5.59$. In contrast, the results based on (5.14) agree well with OceanWave3D for depths in the range $2.00 \leq k_p d \leq 5.59$ but the agreement deteriorates for $k_p d < 2.00$. Figures 5.16(e) and 5.16(f) depict a clear suppression of the oblique energy transfers for depths of $k_p d = 1.60$ and $k_p d = 1.36$ with negligible changes to the spectrum, throughout the entirety of the simulation, for the case of $k_p d = 1.36$. Thus, the dimensionless depth $k_p d$ of 1.36 appears to be completely stable for the simulations based on (5.14), presumably since q_3 goes to zero and the two remaining nonlinear respectively diminish in amplitude or turn negative. In contrast, the potential flow simulations continue to feature oblique energy transfers for $k_p d = 1.60$ and $k_p d = 1.36$ and the case of $k_p d = 1.36$ still results in oblique energy transfers and significant changes to the spectrum during the focused wave event. Thus, the formulation presented in (5.14) appears to underestimate the extent of

the oblique energy transfers for $k_p d \leq 2.00$. The good agreement between figure 5.15 and figure 5.14 suggests that the coefficients of the nonlinear terms do not require modification for the range of finite-depths considered in this study. The scale of the return current beneath the wave group implies that the return current is especially sensitive to depth and the depth-sensitive return current term in (5.12) accounts for this effect. Combined with the arbitrary depth linear dispersion relation and the exact dispersion operator of Trulsen *et al.* (2000), the evidence suggests that (5.12) provides an excellent finite-depth MNLS model for narrow-banded wave groups with dimensionless depths between 5.59 and 1.36.

5.4 Conclusion

We have simulated directionally-spread surface gravity wave groups, formed by dispersive focusing, in deep and finite depths using the MNLS equation. We have compared the results with a fully nonlinear potential flow code and find that the fifth-order truncated dispersion operator of Trulsen & Dysthe (1996) and the exact linear dispersion operator of Trulsen *et al.* (2000) both perform well if the wavenumber of the carrier wave coincides with the spectral peak and the carrier wave direction is aligned with the direction of wave group propagation. The truncated dispersion operator shows marginally higher levels of diffusivity, impacting the steepness of the wave group after focus, but the spectral evolution agrees well between the truncated and exact dispersion operators. Selecting carrier wavenumbers above/below the spectral peak significantly impacts the results obtained with the truncated dispersion operator, reducing the steepness of the wave group at focus. Selecting a carrier wavenumber below the spectral peak can also aggravate energy leakage if the truncated dispersion operator is used. In contrast, the exact dispersion operator exhibits less sensitivity to the selection of the carrier wavenumber. Selecting a carrier wavenumber below the spectral peak does not significantly influence the steepness of the wave group at focus, if the exact dispersion operator is used, but carrier wavenumbers above the spectral peak can marginally reduce the steepness of the wave group at focus. Similarly, the truncated operator is more sensitive than the exact dispersion operator to misalignment between the carrier wave and the direction

of wave group propagation. The steepness of the wave group at focus is significantly impacted by misalignment of 10° or more, if the truncated operator is used. The exact dispersion operator demonstrates low sensitivity to misalignment, providing similar wave group steepnesses even for angles as large as 30°. The spectral evolution results show that misalignment aggravates energy leakage, if the truncated operator is used, reducing the resolution of oblique energy transfers. In contrast, the exact dispersion operator continues to resolve oblique energy transfers, even for the largest angles of misalignment, with no evidence of significant energy leakage. Thus, this study provides evidence that the exact dispersion operator of Trulsen *et al.* (2000) does extend the bandwidth limits of the MNLS equation for steep wave groups with directional spreading, while improving the resolution of four-wave interactions and suppressing energy leakage. We find that the MNLS equation of Trulsen *et al.* (2000) also works well at finite depths if the arbitrary depth linear dispersion relation is used to evaluate the dispersion operator and the bottom-boundary condition is imposed at finite depth. We observe good agreement with our fully-nonlinear potential flow code for narrow-banded wave groups with dimensionless depths between 5.59 and 1.36.

The Tail Wags the Dog

6 The Impact of the Spectral Tail on the Kurtosis of Random Seas

Abstract

We perform Modified Nonlinear Schrödinger (MNLS) simulations of random seas based on narrow-banded JONSWAP spectra ($\gamma = 6$) with directional spreading. Our wavefields are homogeneous in space and non-stationary in time, initialised with Gaussian statistics. We truncate the spectral tail for the initial conditions at different cut-off wavenumbers to assess the impact of the spectral tail on the kurtosis and spectral evolution. We consider two distinct cases based on truncation of the wavenumber tail at $|\boldsymbol{k}|/k_p = 2.4$ and $|\boldsymbol{k}|/k_p = 6$, where k_p is the wavenumber of the spectral peak. A comparison of our results with previous experiments and simulations yields good agreement, supporting the findings of our study. Our simulations indicate that the peak kurtosis value increases if the tail is truncated at $|\boldsymbol{k}|/k_p = 2.4$ rather than $|\boldsymbol{k}|/k_p = 6$. For the case with a wavenumber cut-off at $|\boldsymbol{k}|/k_p = 2.4$, augmented kurtosis is accompanied by comparatively more aggressive spectral changes including redevelopment of the spectral tail, rapid broadening of the spectrum and downshifting of the spectral peak. Similar trends are observed for the case with a wavenumber cut-off at $|\boldsymbol{k}|/k_p = 6$, but the spectral changes are less rapid and less substantial. Thus, the spectral tail appears to play an important role in a form of spectral equilibrium that reduces spectral changes and decreases the peak kurtosis value. Our findings suggest that care should be taken when truncating the spectral tail for the purpose of simulations/experiments. We also find that the kurtosis evolution equation of Fedele (2015, *J. Fluid Mech.*, vol. 782, pp. 25–36) provides an excellent estimate of the peak kurtosis value. However, the selected bandwidth parameter must account for the spectral tail to provide accurate estimates of the peak kurtosis.

6.1 Introduction

Rogue wave occurrence in random seas and the evolution of free-surface kurtosis remain active areas of research. Dispersive focusing based on wave components with different frequencies and directions can result in the formation of extreme waves (see, for example, Fedele *et al.* (2016)). Nonlinear interactions between wave components can also alter the dispersive characteristics of a wave field, allowing for self focusing (Janssen (2003)). The relative importance of nonlinear interactions in the formation of rogue waves has been a focus of previous studies with comprehensive reviews by Kharif & Pelinovsky (2003), Kharif *et al.* (2008*b*), Dysthe *et al.* (2008) and Adcock & Taylor (2014).

In the context of random seas, a deviation from Gaussian statistics indicates the presence of nonlinear interactions. The kurtosis of the free surface, Kur=$\langle\eta^4\rangle/\langle\eta^2\rangle^2$, has received particular attention, as an indicator of nonlinear interactions and rogue wave occurrence (see, e.g., Mori & Janssen (2006)). Here, η denotes the free-surface elevation and the angled brackets denote a statistical average. The *excess kurtosis*, denoted as C_4, quantifies the deviation from Gaussian statistics:

$$C_4 = \frac{\langle\eta^4\rangle}{3\langle\eta^2\rangle^2} - 1, \tag{6.1}$$

yielding $C_4 = 0$ for a Gaussian process, associated with linear seas. The excess kurtosis C_4 is comprised of dynamic (C_4^d) and bound (C_4^b) contributions such that $C_4 = C_4^d + C_4^b$ where the dynamic contribution accounts for the build-up of phase correlation and the bound contribution accounts for the presence of bound harmonics (see, e.g., Dalzell (1999) and Madsen & Fuhrman (2012) for a more detailed discussion on bound harmonics). Dynamics excess kurtosis values of $C_4^d > 0$ and $C_4^d < 0$ are respectively indicative of focusing and defocusing due to nonlinear interactions.

An analytical solution for dynamic kurtosis (C_4^d) has been presented by Fedele (2015), based on narrow-band directional waves with a Gaussian-type spectrum. The initial condition is based upon Gaussian statistics, $C_4^d(t_0) = 0$, with random component phases and amplitudes. Fedele (2015) assumes that the wave field is

spatially homogeneous and non-stationary in time. Analysis of this problem originates from Janssen (2003), providing an expression for the dynamic excess kurtosis of weakly nonlinear unidirectional seas. Mori & Janssen (2006) extended the work of Janssen (2003) based on the assumption of narrow-bandedness. Janssen & Bidlot (2009) and Mori *et al.* (2011) considered the role of directional effects. Fedele (2015) provides an expression for dynamic kurtosis in the directional case, based on:

$$\frac{\mathrm{d}C_4^d(\tau)}{\mathrm{d}\tau} = \mathrm{BFI}^2 \frac{\mathrm{d}J}{\mathrm{d}\tau}. \tag{6.2}$$

Here, τ represents nondimensional time, $\tau = \nu^2\omega_0 t$, where ν is the spectral width and $\omega_0 = 2\pi/T_0$ is the characteristic frequency based on the characteristic wave period T_0. The Benjamin-Feir index (BFI) is given by:

$$\mathrm{BFI} = \frac{\mu\sqrt{2}}{\nu}, \tag{6.3}$$

based on the wave steepness $\mu = k_0\sigma$ where k_0 is the characteristic wavenumber and σ is the standard deviation of the free surface, $\sigma^2 = \langle\eta^2\rangle$. Note that the definition in (6.3) is a factor of $\sqrt{2}$ smaller than the one used in some other studies, e.g., Onorato *et al.* (2009). The function $J(\tau, R)$ in (6.2) depends upon the short-crestedness parameter R:

$$R = \frac{1}{2}\frac{\sigma_\theta^2}{\nu^2}. \tag{6.4}$$

Here, σ_θ is the angular width of the spectrum which quantifies the directional spreading of the waves. Fedele (2015) calculates the angular width σ_θ based on the spreading function of the spectrum, $D(\theta)$:

$$\sigma_\theta = \sqrt{\frac{\int_0^{\pi/2} \theta^2 D(\theta)\mathrm{d}\theta}{\int_0^{\pi/2} D(\theta)\mathrm{d}\theta}}. \tag{6.5}$$

Using the short-crestedness parameter R and nondimensional time τ, Fedele (2015) found the expression:

$$\frac{\mathrm{d}J}{\mathrm{d}\tau} = 2\mathrm{Im}\left(\frac{1}{\sqrt{1-2i\tau+3\tau^2}\sqrt{1+2iR\tau+3R^2\tau^2}}\right), \tag{6.6}$$

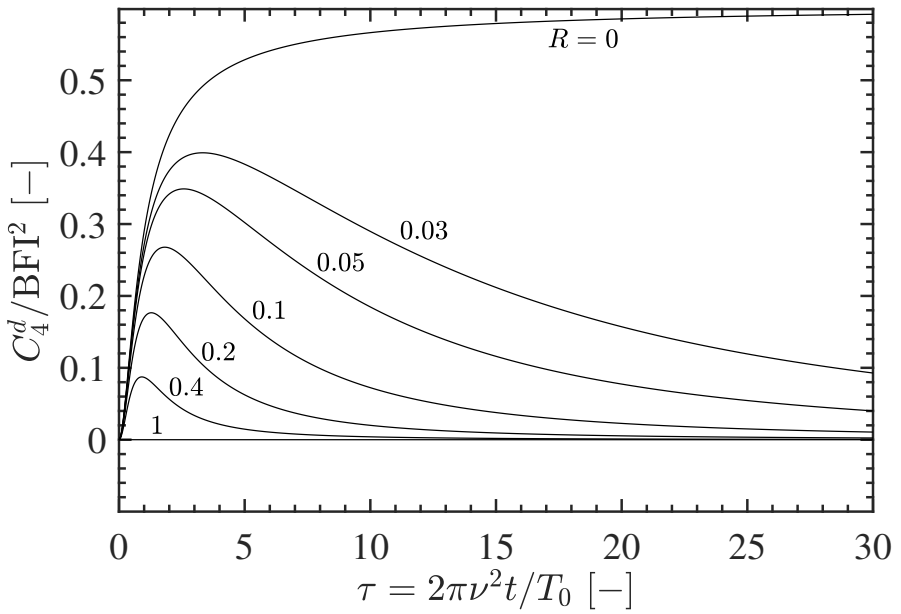

Figure 6.1: Dynamic excess kurtosis normalized by the square of the Benjamin-Feir index (C_d^4/BFI^2) as a function of nondimensional time ($\tau = \nu^2\omega_0 t$) for different values of R, based on Fedele (2015).

required to evaluate (6.2). Here, $\mathrm{Im}(x)$ denotes the imaginary part of x. Figure 6.1 shows the evolution in kurtosis predicted for a range of R values. As can be seen, the peak kurtosis value is significantly impacted by the value of R, suggesting a strong dependency on the bandwidth and spreading of the waves, as well as the steepness.

Previous studies have investigated the evolution of kurtosis for random seas, including the experiments of Onorato *et al.* (2009) as well as the Higher-Order Spectral (HOS) and Modified Nonlinear Schrödinger (MNLS) simulations of Toffoli *et al.* (2010*a*) and Xiao *et al.* (2013). In this study, we perform random seas simulations using the MNLS equation of Trulsen *et al.* (2000), a modified version of the Trulsen & Dysthe (1996) equation, based on an exact linear dispersion operator. Our simulations are based on the sea-state parameters used in Experiment B of Onorato *et al.* (2009), a case also considered by Toffoli *et al.* (2010*a*) and Xiao *et al.* (2013). Thus, we compare our results with those of previous studies. We note that the experiments of Onorato *et al.* (2009) are based upon wave fields which are inhomogeneous in space but stationary in time for a given location. In contrast, our simulations are based upon a spatially homogeneous random sea which is non-stationary in time, as simulated by Xiao *et al.* (2013) and Toffoli *et al.* (2010*a*). However, for narrow-

banded seas with low directional spreading, mapping between space and time can be performed with the group velocity, although we note this is an extra approximation. Toffoli *et al.* (2010*a*) performed MNLS simulations of both types (spatially homogeneous and non-stationary as well as spatially inhomogenous and stationary) and found that the kurtosis curves agreed well for the narrow-banded case considered in this study. Thus, we use the experimental results of Onorato *et al.* (2009) in our comparisons. Our investigation focuses on the impact of the spectral tail on kurtosis evolution, exploring the role of the tail in establishing a form of spectral equilibrium that reduces the peak kurtosis.

The concept of spectral equilibrium has been considered by previous studies. Non-equilibrium sea states are characterised by comparatively rapid spectral changes that eventually slow down as the sea state moves towards a better representation of equilibrium for the given conditions. As discussed by Trulsen (2018), wave-current interactions, sudden changes in bathymetry and meteorological conditions are all possible causes of non-equilibrium, provoking the occurrence of rapid spectral changes (see, e.g., Waseda *et al.* (2001), Viotti & Dias (2014), Rapizo *et al.* (2016)). The investigation of Barratt *et al.* (2021*a*) showed that steep wave groups formed under non-equilibrium conditions may exhibit augmented kinematics and a prolonged lifespan—the presence of a fully-developed spectral tail was found to reduce the nonlinear features of the wave groups. Physical mechanisms which may impact the development of the spectral tail have also been identified by previous studies. Background currents have been shown by Waseda *et al.* (2015) to possibly suppress the development of the spectral tail. As shown by Toffoli *et al.* (2015) and Meylan *et al.* (2018), ice sheets also tend to dissipate the energy associated with high-wavenumber components in the spectral tail. Simulations based on initial spectra that do not include a fully-developed tail also tend to exhibit rapid spectral evolution in the early stages (see, e.g., Dysthe *et al.* (2003), Xiao *et al.* (2013)). Our simulations are focused on the impact of the spectral tail on the evolution of random seas initialised with Gaussian statistics.

We perform simulations based on JONSWAP spectra truncated at different

wavenumbers to alter the bandwidth and prominence of the spectral tail. We monitor the consequent kurtosis evolution and explain the trends based on the spectral evolution we observe. Lastly, we calculate approximate R values and compare our results to (6.2) to assess the extent of the agreement.

6.2 Numerical Details

We perform random-sea MNLS simulations using the formulation of Trulsen *et al.* (2000), based on Rayleigh distributed component amplitudes with a uniform phase distribution. We consider two distinct cases, each with a different cut-off wavenumber for the spectral tail. Each case has been simulated a total of 20 times with a new random seed generated for each instance. Our analysis of the spectral evolution is based upon ensemble averaging of the resultant spectra.

6.2.1 Initial Conditions

We define the variance density spectrum $F(\omega, \theta)$ as the product of a frequency spectrum $S(\omega)$ and a spreading function $D(\theta)$, where ω represents the angular frequency and θ represents the direction of the wave component:

$$F(\omega, \theta) = S(\omega)D(\theta). \tag{6.7}$$

Following Onorato *et al.* (2009), we use the JONSWAP formulation as the frequency spectrum:

$$S(\omega) = \frac{\alpha g^2}{\omega^5} \exp\left[-\frac{5}{4}\left(\frac{\omega}{\omega_p}\right)^{-4}\right] \gamma^{\exp[-(\omega-\omega_p)^2/(2\sigma^2\omega_p^2)]}, \tag{6.8}$$

where ω is the angular frequency and ω_p the peak frequency, α the Phillips parameter, γ the peak enhancement factor, and the parameter σ is frequency dependent: $\sigma = 0.07$ for $\omega \leq \omega_p$ and $\sigma = 0.09$ for $\omega > \omega_p$. We use the cosine-squared spreading function:

$$D(\theta) = \begin{cases} \dfrac{2}{\Theta}\cos^2\left(\dfrac{\pi\theta}{\Theta}\right) & \text{for } |\theta| \leq \Theta/2. \\ 0 & \text{for } |\theta| > \Theta/2. \end{cases} \tag{6.9}$$

Here, θ is the wave propagation direction and Θ is the directional spreading width of the cosine-squared function. We note the relationship between σ_θ in (6.5) and Θ in (6.9), given by:

$$\sigma_\theta = \Theta\sqrt{\frac{\pi^2 - 6}{12\pi^2}}. \tag{6.10}$$

The product of (6.8) and (6.9) yields the variance density spectrum in the (ω, θ) coordinate system. The corresponding wavenumber spectrum in (k_x, k_y) can be calculated with a Jacobian: $\hat{S}(k_x, ky) = (1/k)(d\omega/dk)S(\omega, \theta) = (g^2/(2\omega^3))S(\omega, \theta)$, where $\boldsymbol{k}$ is the wavenumber vector $\boldsymbol{k} = (k_x,\, k_y)$ and we have used the deep-water dispersion relationship.

To perform random-sea simulations, we require Rayleigh distributed component amplitudes, a_i, with expected values, μ_i, that are consistent with the defined wavenumber spectrum, $\hat{S}(\boldsymbol{k})$. The expected amplitude for component $\boldsymbol{k}_i$ follows from the wavenumber spectrum:

$$\mu_i = \sqrt{2\hat{S}(\boldsymbol{k}_i)}. \tag{6.11}$$

Thus, the scale parameter of the Rayleigh distribution is given by $\sqrt{2/\pi}\,\mu_i$ and we generate the random amplitude, a_i, for component $\boldsymbol{k}_i$ using:

$$a_i = \sqrt{2/\pi}\ \mu_i \sqrt{-2\ln\chi}, \tag{6.12}$$

where χ is a uniformly distributed random variable within the range $[0, 1]$ and ln is the natural logarithm. A random phase offset φ_i is also generated for each wavenumber component $\boldsymbol{k}_i$ in the range $[0, 2\pi]$. We compute the linear surface elevation at each point in space $\boldsymbol{x} = (x,\, y)$ as a superposition of the components:

$$\eta_L(\boldsymbol{x}, t) = \sum_i a_i \cos\left(\boldsymbol{k}_i \cdot \boldsymbol{x} - \omega_i t + \varphi_i\right), \tag{6.13}$$

using the deep-water linear dispersion relationship $\omega_i = \sqrt{g|\boldsymbol{k_i}|}$ to calculate the component frequencies. For the MNLS simulations, we calculate the initial complex envelope $B(\boldsymbol{x}, t_0)$ using the linear surface elevation η_L and the corresponding Hilbert

Table 6.1: Sea-state parameters.

γ	ω_p	k_p	Θ	H_s	ϵ
6.0	0.5257 s^{-1}	0.02796 m^{-1}	12°	11.2 m	0.16

transform η_L^H following Osborne (2010):

$$B(\boldsymbol{x}, t_0) = \left\{\eta_L + i\eta_L^H\right\} \exp\left(-i[\boldsymbol{k}_0 \cdot \boldsymbol{x} - \omega_0 t_0]\right). \tag{6.14}$$

Here, $\boldsymbol{k}_0$ and ω_0 represent the characteristic wavenumber and frequency of the carrier wave.

The parameters used in this study are listed in table 6.1. We use a peak enhancement factor (γ) of 6.0. The spectral peak of the JONSWAP, in terms of angular frequency (ω_p) and wavenumber (k_p) are both listed in table 6.1 (note that ω_p and k_p are not simply related by the linear dispersion relation due to the presence of a Jacobian). The characteristic time and length scales associated with k_p are also listed in table 6.3. We use a directional spreading width (Θ) of 12°, based on the spreading function defined in (6.9), the same value as used by Xiao *et al.* (2013). Our significant wave height (H_s) of 11.2 m corresponds to a wave steepness ($\epsilon = k_p H_s/2$) of 0.16. As calculated by Fedele (2015), the parameters listed in table 6.1 correspond to a Benjamin-Feir index (BFI $= \mu\sqrt{2}/\nu$) of 0.78, where $\mu = \epsilon/2$ and ν is a measure of spectral bandwidth.

We use an exponential low-pass filter to truncate the tail of the spectrum, see Xiao *et al.* (2013):

$$\Omega(|\boldsymbol{k}|/k_p, \beta_1, \beta_2) = \exp\left(- \left[\frac{|\boldsymbol{k}|}{\beta_1 k_p}\right]^{\beta_2} \right). \tag{6.15}$$

We consider two test cases labelled Case ST and Case LT, where 'ST' refers to a short tail and 'LT' refers to a long tail for the spectrum. The β_1 and β_2 values are listed in table 6.2 together with the corresponding cut-off wavenumbers. Case ST and LT feature truncation of the spectral tail at approximately $|\boldsymbol{k}|/k_p = 2.4$ and $|\boldsymbol{k}|/k_p = 6$, respectively, based on the β_1 and β_2 listed in table 6.2. The resultant

Table 6.2: Low-pass filter parameters for spectral tail truncation.

Case	β_1	β_2	Cut-off wavenumber
ST	2.4	20	$\lvert\boldsymbol{k}\rvert/k_p = 2.4$
LT	6	35	$\lvert\boldsymbol{k}\rvert/k_p = 6.0$

initial conditions are shown in figure 6.3(a) for Case ST and figure 6.4(a) for Case LT. We note that approximately 21% of the total energy for Case LT is associated with wavenumber components with $|\boldsymbol{k}|/k_p > 2.4$.

6.2.2 MNLS Simulations

We perform our random-sea simulations using the MNLS equation of Trulsen *et al.* (2000), a modified version of the Trulsen & Dysthe (1996) equation:

$$\begin{aligned}\frac{\partial B}{\partial t} + \mathfrak{L}\,B + \frac{1}{2}i\omega_0 k_0^2|B|^2 B + \frac{3}{2}\omega_0 k_0 |B|^2\frac{\partial B}{\partial x} \\ + \frac{1}{4}\omega_0 k_0 B^2\frac{\partial B^*}{\partial x} + ik_0\frac{\partial \overline{\phi}}{\partial x}B = 0.\end{aligned} \tag{6.16}$$

Here, B^* denotes the conjugate of the complex envelope and $\overline{\phi}$ denotes the mean flow potential. The carrier wave is aligned with the x-axis, $\boldsymbol{k}_0 = (k_0, 0)$, so that k_0 in (6.16) represents the carrier wavenumber and the characteristic frequency ω_0 is related to the carrier wavenumber k_0 by the deep-water linear dispersion relationship, $\omega_0 = \sqrt{gk_0}$. The dispersion operator $\mathfrak{L}$ in (6.16) is based upon a pseudo-differential operator that preserves the exact linear dispersion relationship, as explained by Trulsen *et al.* (2000):

$$\begin{aligned}&\mathfrak{L}\,B = \\ &\frac{1}{4\pi^2}\int_{-\infty}^{\infty} i[\omega(\boldsymbol{k_0}+\boldsymbol{\mu}) - \omega_0]\exp\left(i\boldsymbol{\mu}\cdot(\boldsymbol{x}-\boldsymbol{y})\right)B(\boldsymbol{y},t)\mathrm{d}\boldsymbol{y}\mathrm{d}\boldsymbol{\mu}.\end{aligned} \tag{6.17}$$

Here, $\boldsymbol{\mu} = (\lambda, \mu)$ is the modulation wavenumber. Direct numerical evaluation of (6.17) avoids expansion and truncation of the linear dispersion relation, increasing the bandwidth limits of the MNLS equation and improving the resolution of four-wave interactions while reducing energy leakage (see Martin & Yuen (1980) and Yuen

& Lake (1980) for a discussion on MNLS energy leakage), with almost no additional computational cost. Barratt *et al.* (2021*b*) performed a detailed comparison of the exact and truncated versions of the dispersion operator for focused wave groups. The MNLS equation in (6.17) is subject to free surface and bottom boundary conditions, as well as continuity for the mean flow potential $\overline{\phi}$:

$$\frac{\partial \overline{\phi}}{\partial z} = \frac{\omega_0}{2}\frac{\partial}{\partial x}|B|^2 \quad \text{at} \quad z = 0, \tag{6.18}$$

$$\frac{\partial \overline{\phi}}{\partial z} = 0 \quad \text{at} \quad z = -\infty, \tag{6.19}$$

$$\nabla^2 \overline{\phi} = 0 \quad \text{for} \quad -\infty < z < 0. \tag{6.20}$$

We incorporate the boundary conditions, (6.18) and (6.19), directly into the MNLS equation, (6.16), using the continuity condition for the mean flow, (6.20), as done with the fourth-order envelope equation of Janssen (1983). A single governing equation is, thus, obtained:

$$\begin{aligned}\frac{\partial B}{\partial t} + \mathfrak{L}\, B + \frac{1}{2}i\omega_0 k_0^2 |B|^2 B + \frac{3}{2}\omega_0 k_0 |B|^2 \frac{\partial B}{\partial x} \\ + \frac{1}{4}\omega_0 k_0 B^2 \frac{\partial B^*}{\partial x} + ik_0 B \mathcal{F}^{-1}\left\{ \frac{ik_x}{|\boldsymbol{k}|}\mathcal{F}\left\{ \frac{\omega_0}{2}\frac{\partial}{\partial x}|B|^2 \right\} \right\} = 0.\end{aligned} \tag{6.21}$$

where $\mathcal{F}$ denotes a 2D Fourier transform in x and y and $\mathcal{F}^{-1}$ denotes the inverse operation. The expression in (6.21) is based upon the evaluation of the bottom boundary condition (6.19) at $z = -\infty$ and is, therefore, a deep-water equation. Thus, we obtain the initial complex envelope using (6.14) and the envelope is marched forward in time with (6.21). We discretize and numerically solve (6.21) using a split-step algorithm. We use spectral methods to evaluate the linear dispersion operator $\mathfrak{L}B$ in (6.17) and we use fourth-order finite differencing with symmetric stencils for the spatial derivatives in the nonlinear terms. Time marching is performed with the classic fourth-order Runge-Kutta scheme. The details of the discretisation are listed in table 6.3, including the length (L) and width (W) of the domain. The number of grid points in the x-direction and y-direction are listed, denoted as N_x and N_y respectively, together with the corresponding grid spacings, Δx and Δy. The size of the domain ensures 136 characteristic wavelengths (λ_0) in the x-direction and $91\lambda_0$

Table 6.3: Discretization Parameters.

Characteristic scales	Wavelength (λ_0) 225 m Wave period (T_0) 12.0s
Numerical domain	Length (L) 30.72 km Width (W) 20.48km
Discretisation	$N_x = 2049$, $\Delta x = 15$ m $N_y = 1025$, $\Delta y = 20$ m $N_t = 4501$, $\Delta t = 0.4$ s

in the y-direction, where $\lambda_0 = 2\pi/k_0$. The characteristic length scales of the wave envelope can be approximated with:

$$\Lambda_x = \frac{2\pi}{k_w}, \qquad \Lambda_y = \frac{2\pi}{k_0 \sigma_\theta}, \tag{6.22}$$

based on the characteristic length scales for the wavenumber (k_0), bandwidth (k_w) and spreading parameter (ς_0). Dimensionless metrics for grid resolution, in the x and y-directions can, thus, be defined as:

$$n_x = \frac{\Lambda_x}{\Delta x}, \qquad n_y = \frac{\Lambda_y}{\Delta y}, \tag{6.23}$$

which approximately represent the number of grid points spanning the length scale of the wave envelope in the x and y-directions. Based on the initial conditions, we use the peak of the wavenumber spectrum, $k_0 = 0.02796$ m^{-1}, and we use (6.5) to obtain $\sigma_\theta = 0.04$ rad. We estimate the bandwidth k_w for Case ST and Case LT using the spectral half-width and obtain $k_w = 0.004$ m^{-1}. Combined with the grid resolution listed in table 6.3, we obtain $n_x \approx 105$ and $n_y \approx 281$. The simulations are time marched for a total of 150 wave periods (T_0), where $T_0 = 2\pi/\omega_0$, with a time step (Δt) of 0.4 s. Using the group velocity of the wave envelope as the characteristic velocity, we calculate a Courant–Friedrichs–Lewy (CFL) condition of 0.25 for our MNLS simulations, based on the discretisation parameters listed in table 6.3. To assess the diffusivity of our simulations, we have considered the conserved quantity

I_2 (see Zakharov & Shabat (1972)):

$$I_2 = \sum_{i,j} |B(x_i, y_j)|^2, \tag{6.24}$$

typically associated with energy conservation. We found the quantity I_2 to be conserved within 1% of the initial value over the entire duration of all our simulations, indicating permissibly low levels of diffusivity. We find that the $|B|^2\,\partial B/\partial x$ term in (6.16) is particularly prone to causing simulation divergence. Thus, we apply spectral filtering to eliminate high-frequency contributions from this term—we set all components above $|\boldsymbol{k}|/k_p = 5$ to zero when calculating $|B|^2\,\partial B/\partial x$.

6.2.3 Spectral parameters

We analyse the spectral evolution of Case ST and Case LT using statistical parameters to characterise the spectral peak, bandwidth and directional spreading. Our selection of the spectral parameters is largely based on the review by Serio *et al.* (2005). For each simulation, we perform a two-dimensional discrete Fourier transform (in x and y) on the surface elevation once per wave period, and use the result to calculate the variance density spectrum in terms of wavenumber $S(k_x, k_y, t)$ based on a Cartesian co-ordinate system:

$$S(k_x, k_y, t) = \frac{1}{2}|\hat{\eta}(k_x, k_y, t)|^2, \tag{6.25}$$

where $\hat{\eta}$ represents the Fourier components of the surface elevation. Arithmetic averaging over the ensemble ($N_i = 20$) at time t yields the ensemble-averaged spectrum $\overline{S}(k_x, k_y, t)$:

$$\overline{S}(k_x, k_y, t) = \frac{1}{N_i}\sum_{i}^{N_i} S_i(k_x, k_y, t). \tag{6.26}$$

Converting to a polar co-ordinate system with the use of a Jacobian, $\overline{S}(k, \theta, t) = k\overline{S}(k_x, k_y, t)$, we characterise the directional spreading of the ensemble-averaged variance density spectrum:

$$\varsigma(t) = \sqrt{\frac{\sum_j \theta_j^2\ \overline{S}(k_j, \theta_j, t)}{\sum_j \overline{S}(k_j, \theta_j, t)}}. \tag{6.27}$$

Here, k represents the magnitude of the component wavenumber $|\boldsymbol{k}|$ for convenience of notation. To characterise the spectral peak and the bandwidth, we calculate the frequency spectrum $\overline{S}(f,\theta,t) = J\ \overline{S}(k,\theta,t)$ where $J = 4\pi\sqrt{k/g}$. Integration over θ yields the omnidirectional frequency spectrum $\overline{S}(f,t)$ used to estimate the peak frequency:

$$f_p(t) = \frac{\sum_j f_j\,[\,\overline{S}(f_j,t)\,]^4}{\sum_j\,[\,\overline{S}(f_j,t)\,]^4}, \tag{6.28}$$

based on the omnidirectional frequency spectrum raised to the fourth power, as recommended by Young *et al.* (1995). We also estimate the bandwidth based on the omnidirectional frequency spectrum, using the peakedness parameter introduced by Goda (1985):

$$Q_p(t) = \frac{2}{m_0^2}\int_0^\infty f[\,\overline{S}(f,t)\,]^2\mathrm{d}f, \tag{6.29}$$

where,

$$m_0 = \int_0^\infty \overline{S}(f,t_0)\mathrm{d}f. \tag{6.30}$$

We use the trapezoidal method to perform the numerical integration in (6.29) based on unequal point spacing. Our estimate of spectral bandwidth (ν) relates inversely to the peakedness parameter Q_p:

$$\nu(t) = \frac{1}{\sqrt{\pi}\,Q_p}, \tag{6.31}$$

consistent with the bandwidth metric used by Serio *et al.* (2005) to calculate the Benjamin-Feir index (BFI). We also use ν in (6.31) as our bandwidth metric when calculating the BFI. The spectral parameters defined in (6.27), (6.28) and (6.31) thus form the basis of our spectral evolution analysis.

6.3 Results and Discussion

We analyse the kurtosis evolution for Case ST and Case LT and explain the observations based on the spectral evolution, using contour plots of the ensemble-averaged spectra as well as the parameters defined in (6.27), (6.28) and (6.31). Lastly, we compare the simulation results for kurtosis with the theory of Fedele (2015) and we briefly discuss the selection of an appropriate bandwidth parameter.

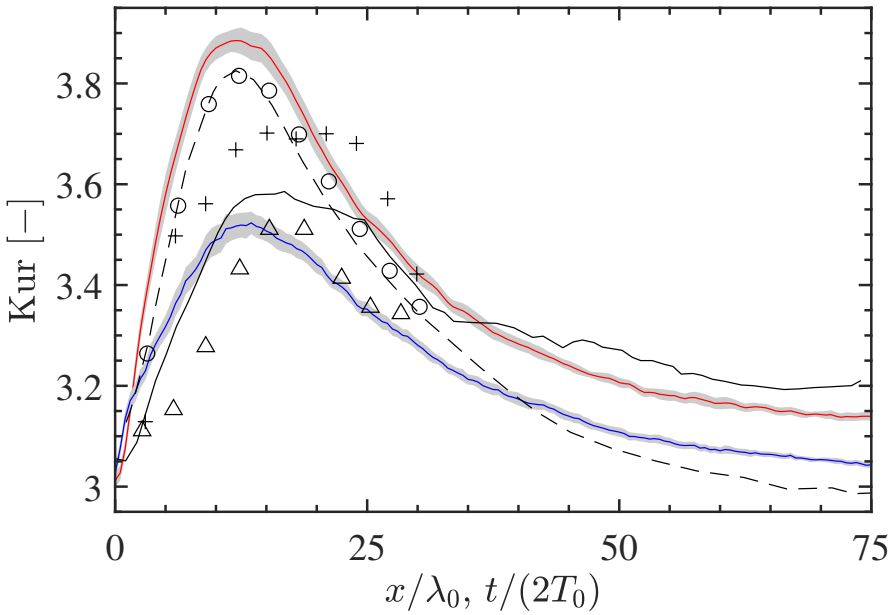

Figure 6.2: Kurtosis evolution for Case ST (red line) and Case LT (blue line) compared against other studies, including (△) the experiments of Onorato *et al.* (2009). The shaded grey bands represent 95% confidence intervals. The simulation results of Xiao *et al.* (2013) are shown: (− − −) MNLS and (——) HOS as well as the simulation results of Toffoli *et al.* (2010*a*): (○) MNLS and (+) HOS. All the results are based upon JONSWAP spectra ($\gamma = 6$) with steepness $\epsilon = 0.16$ and a Benjamin-Feir index (BFI) of 0.78 based on the definition in (6.3).

6.3.1 Kurtosis Evolution

The evolution of kurtosis for our MNLS simulations is shown in figure 6.2, including both dynamic and bound contributions up to the third order. The shaded grey bands represent 95% confidence intervals for the ensemble-averaged MNLS results. The experimental results of Onorato *et al.* (2009) are also shown. Both Toffoli *et al.* (2010*a*) and Xiao *et al.* (2013) performed similar simulations to those in this study, using the MNLS equation as well as a Higher-Order Spectral (HOS) code, and the results are depicted in figure 6.2. As discussed in the introduction, the results of Onorato *et al.* (2009) are based on waves propagating along a tank. We perform space/time mapping with the group velocity for the purposes of comparing our simulation results to the experiments of Onorato *et al.* (2009). The x-axis in figure 6.2 shows the corresponding spatial x/λ_0 or temporal $t/(2T_0)$ parameter with kurtosis shown on the y-axis (excluding the contribution of bound harmonics). Here, λ_0 and T_0 represent the characteristic wavelength and wave period, respectively. We see good agreement between the MNLS simulations results of Toffoli *et al.* (2010*a*),

Xiao *et al.* (2013) and Case ST of this study. A peak kurtosis value of 3.89 is observed for Case ST and agreement between the MNLS simulations appears to be particularly good in the vicinity of the peak. Similar to Case ST of this study, the MNLS simulations of both Toffoli *et al.* (2010*a*) and Xiao *et al.* (2013) effectively truncated the wavenumber spectrum of the surface elevation at $|\boldsymbol{k}|/k_p = 2$, by limiting the modulation wavenumber of the envelope to $|\boldsymbol{\mu}|/k_p \leq 1$. Here, $\boldsymbol{\mu} = (\lambda, \mu)$ is the modulation wavenumber defined relative to the wavenumber of the carrier wave, $\boldsymbol{k} = (k_p, 0)$. Thus, figure 6.2 also serves to verify our simulations. The HOS results of Toffoli *et al.* (2010*a*) and Xiao *et al.* (2013) differ, however, from the MNLS results for Case ST and agree better with the MNLS results for Case LT as well as the experimental results of Onorato *et al.* (2009). Case LT is based upon a spectral tail truncated at $|\boldsymbol{k}|/k_p = 6$ and, thus, features a more prominent spectral tail. Likewise, the experiments of Onorato *et al.* (2009) and the HOS simulations of Toffoli *et al.* (2010*a*) and Xiao *et al.* (2013) all included a fully-developed spectral tail in the initial conditions. Thus, the differences between Case ST and Case LT appear to be the result of the spectral tail and the findings are consistent other studies. Case LT, in this study, reaches a peak kurtosis value of 3.52, approximately 10% lower than the peak kurtosis value for Case ST. Inclusion of the spectral tail up to $|\boldsymbol{k}|/k_p = 6$ in the initial conditions, thus, appears to reduce the peak kurtosis value while artificial truncation of the spectral tail at $|\boldsymbol{k}|/k_p = 2.4$ augments the peak kurtosis value. The relatively good agreement between Case LT and the experiments/HOS results also suggests that the MNLS equation provides better kurtosis estimates if the spectral tail is included, despite the narrow-bandwidth limitations of the equation.

6.3.2 Spectral Evolution

To clarify the trends in kurtosis observed in the previous section, we have analysed the evolution of the ensemble-averaged variance density spectrum, $\overline{S}(k_x, k_y)$, for Case ST and Case LT with the results shown in figure 6.3 and 6.4 respectively. The wavenumbers k_x and k_y have been normalised by the characteristic wavenumber $k_0 = 0.02796$ m^{-1}, the initial spectral peak listed in table 6.1. The contour plots in each figure are shown at times: (a) $t/T_0 = 0$; (b) $t/T_0 = 50$; and (c) $t/T_0 = 100$.

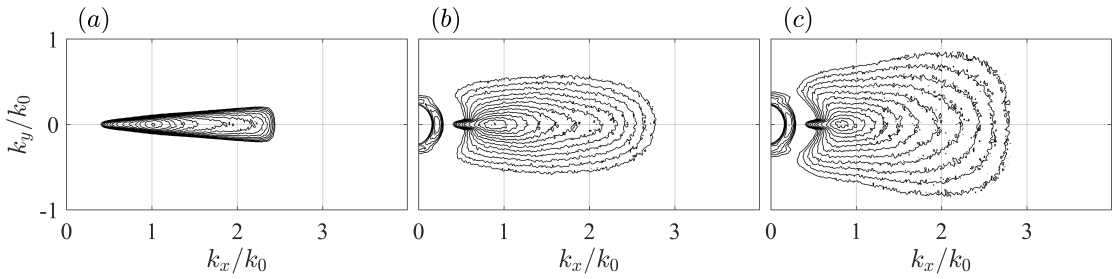

Figure 6.3: Contour plots of the ensemble-averaged variance density spectrum $\overline{S}(k_x, k_y)$ for Case ST featuring truncation of the spectral tail in the vicinity of $|\boldsymbol{k}|/k_p = 2.4$: (a) $t/T_0 = 0$; (b) $t/T_0 = 50$; (c) $t/T_0 = 100$. The contour levels are logarithmic, ranging from 1×10^{-5} to 1×10^{-2}.

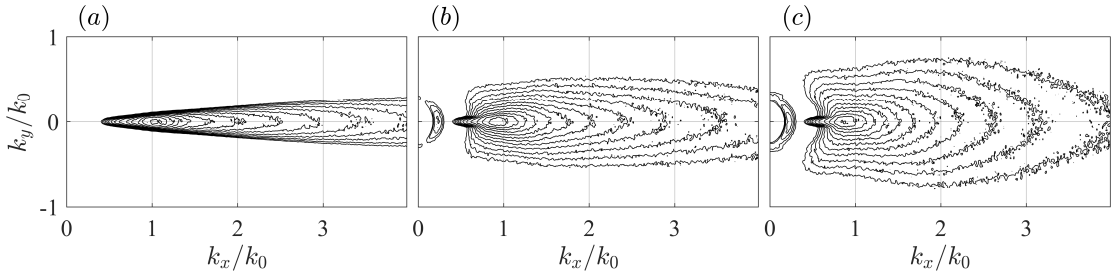

Figure 6.4: Contour plots of the ensemble-averaged variance density spectrum $\overline{S}(k_x, k_y)$ for Case LT featuring truncation of the spectral tail in the vicinity of $|\boldsymbol{k}|/k_p = 6$: (a) $t/T_0 = 0$; (b) $t/T_0 = 50$; (c) $t/T_0 = 100$. The contour levels are logarithmic, ranging from 1×10^{-5} to 1×10^{-2}.

Note that the contour levels are logarithmically distributed. As can be seen in figure 6.3(a), Case ST features a narrow-banded spectrum with truncation of the tail in the vicinity of $|\boldsymbol{k}|/k_p = 2.4$. Figure 6.3(b) and 6.3(c) reveal the rapid broadening of the spectrum which occurs during the simulation—the truncated tail partially redevelops and the directional spreading increases. Similar features are apparent for Case LT, shown in figure 6.4. Case LT features a more prominent spectral tail for the initial conditions since truncation is performed in the vicinity of $|\boldsymbol{k}|/k_p = 6$. However, rapid broadening of the spectrum over time is also observed for Case LT, although less directional spreading is apparent in figure 6.4(b) and 6.4(c) than the corresponding plots in figure 6.3. The differences in spectral evolution between Case ST and Case LT are best captured by the statistical parameters defined in (6.27), (6.28) and (6.31).

Figure 6.5 shows the evolution of the ensemble-averaged spectral parameters for Case ST and Case LT. The spectral bandwidth parameter ν, defined in (6.31), is shown in figure 6.5(a). The spreading parameter ς, defined in (6.27), is shown in fig-

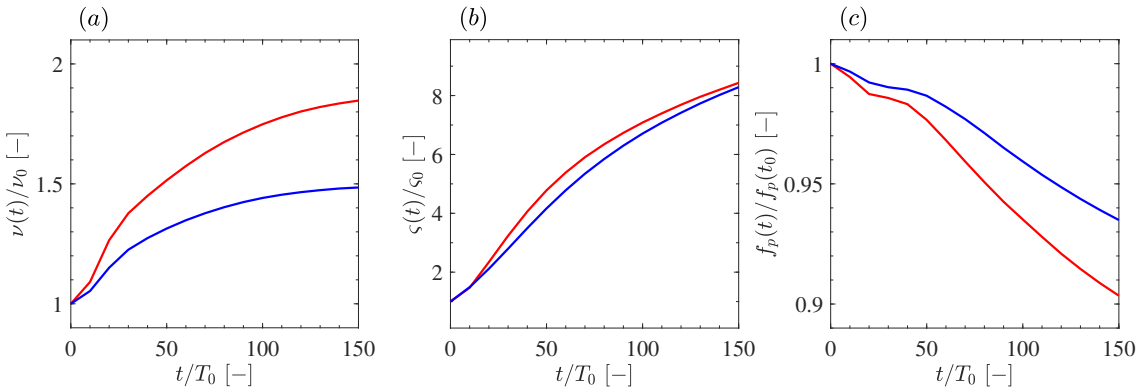

Figure 6.5: Evolution of ensemble-averaged spectral parameters for Case ST (red line) and Case LT (blue line): (a) spectral bandwidth ν defined in (6.31); (b) spreading parameter ς defined in (6.27); (c) peak frequency f_p defined in (6.28).

ure 6.5(b). The peak frequency f_p, defined in (6.28), is shown in figure 6.5(c). All of the parameters have been normalised by their initial value, at time t_0. Figure 6.5(a) shows that Case ST and Case LT both exhibit an increase in spectral bandwidth, however the increase in ν/ν_0 is more rapid for Case ST and the final value of 1.85 exceeds the final value of 1.48 for Case LT by approximately 25%. Similarly, the spreading parameter in figure 6.5(b) also exhibits an increase in ς/ς_0 for both cases—the values are similar towards the start and end of the simulations however Case ST exhibits a more rapid increase in between. Lastly, figure 6.5(c) demonstrates a reduction in the peak frequency for both cases, consistent with the downshift of the spectral peak observed in other studies (see, e.g., Lake *et al.* (1977), Tulin & Waseda (1999) and Dysthe *et al.* (2003)). The frequency downshift is also observed to occur more rapidly for Case ST than Case LT and the final value of 0.903 for Case ST is approximately 4% lower than the final value of 0.935 observed for Case LT. Thus, all the spectral parameters indicate that the spectral changes for Case ST occur more rapidly and are more pronounced than those of Case LT. Inclusion of a more prominent spectral tail in Case LT thus appears to reduces the spectral changes observed during the simulations. Truncation of the spectral tail close to the spectral peak in Case ST conversely augments the spectral changes which occur during the simulations. Thus, the spectral tail appears to play an important role in establishing the spectral equilibrium of the sea state and care should be taken when truncating the tail in a simulation or laboratory setting. The kurtosis results

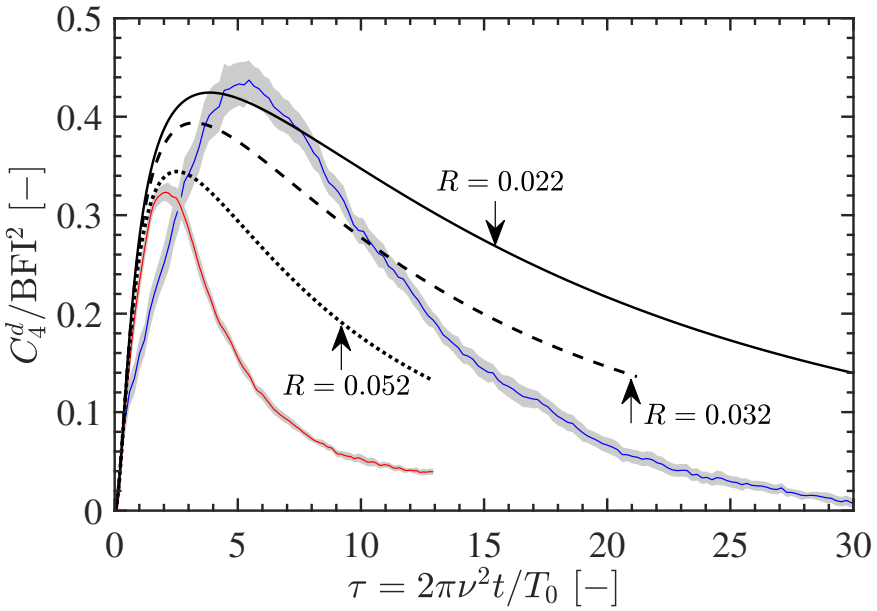

Figure 6.6: Kurtosis evolution for Case ST (red line) and Case LT (blue line) compared against the solution of Fedele (2015) based on different bandwidth parameters: (dashed, − − −) bandwidth based on spectral half-width for both Case ST and Case LT yields $R = 0.031$; (dotted, · · · · ·) bandwidth based on (6.31) for Case ST yields $R = 0.052$; (solid, ——) bandwidth based on (6.31) for Case LT yields $R = 0.022$. The shaded grey bands represent 95% confidence intervals for the ensemble-averaged results.

shown in figure 6.2 indicate that the rapid spectral changes in Case ST augment the peak kurtosis value, relative to Case LT, demonstrating the importance of the tail in determining the peak kurtosis.

6.3.3 Comparison with Theory

We compare our ensemble-averaged kurtosis results with the solution of Fedele (2015), with the results shown in figure 6.6. The kurtosis curves for Case ST and Case LT are both shown, expressed as dynamic excess kurtosis, see (6.1), normalised by the square of the Benjamin-Feir index, see (6.3). The kurtosis curves have been plotted against non-dimensional time, $\tau = \nu^2\omega_0 t$, based on the spectral bandwidth (ν) and the characteristic frequency (ω_0). Our calculation of the shortcrestedness parameter R is based upon (6.4) using the angular width in (6.5). The dashed line in figure 6.6, calculated by Fedele (2015), bases the bandwidth parameter ν on the spectral half-width and, thus, yields $R = 0.032$ with the same curve for Case ST and Case LT (since the spectral half-width is not altered by truncation of the tail). The solid ($R = 0.022$) and dotted ($R = 0.052$) lines in figure 6.6 are based on the

bandwidth parameter in (6.31), which does account for truncation of the spectral tail. As can be seen, the kurtosis curves based on (6.31) provide better agreement with the simulation results, compared with the curve based on the spectral half-width. We note that the peak kurtosis value is particularly well predicted, although the long-term behaviour differs—the kurtosis decline after the peak occurs faster for the simulations than predicted by the theoretical results. Thus, we find that Fedele (2015) provides an excellent estimate for the peak kurtosis value in our simulations. However, the bandwidth parameter ν must account for the spectral tail to accurately predict the kurtosis peak. We find that the bandwidth parameter in (6.31), based on the peakedness parameter of Goda (1985), appears to be suitable for this purpose, consistent with the recommendations of Serio *et al.* (2005).

6.4 Conclusion

Our findings indicate that artificial truncation of the spectral tail augments the peak kurtosis value of a random sea initialised with Gaussian statistics. Truncation of the tail results in more aggressive spectral changes during the simulation, characterised by spectral broadening in terms of bandwidth and spreading as well as downshifting of the spectral peak. The spectral tail is also observed to redevelop during the course of the simulation. Thus, the spectral tail appears to play an important role in establishing a form of spectral equilibrium that reduces spectral changes and decreases the peak kurtosis value. Care should, thus, be taken when artificially truncating the tail for the purpose of simulations/experiments. We find that the MNLS equation of Trulsen *et al.* (2000) can be used to estimate the peak kurtosis value, by including the spectral tail in the initial conditions, despite the bandwidth limits of the equation. Fedele (2015) also provides an excellent estimate for the peak kurtosis value if the bandwidth parameter accounts for truncation of the spectral tail and the peakedness parameter of Goda (1985) appears to provide a suitable choice of bandwidth parameter.

7 Thesis Conclusions

In this section, we address the four thesis objectives listed in section 1.1 and summarise the thesis conclusions relevant to each objective.

Objective 1 *To characterise the nonlinear wave-wave interactions which dominate the spectral evolution of a steep wave group formed by dispersive focusing*

We have found that the nonlinear wave-wave interactions are dominated by Class I interactions of McLean (1982*b*), formed by a quartet of resonant components, with no significant evidence of Class II interactions, formed by a quintet of resonant components, consistent with the findings Fujimoto & Waseda (2016). Our results indicate that the interactions resemble a degenerate quartet if the wave group is narrow-banded, resulting in directional energy transfers at $\pm 35°$ to the spectral peak as described by the figure-of-eight resonance loop of Phillips (1960). We term these interactions *quasi-degenerate* since the interactions qualitatively resemble a degenerate quartet but the interactions may not meet the strict resonance condition of degeneracy (see section 2.8). We find that the quasi-degenerate interactions cause the wave group to become more broad-banded, worsening the qualitative resemblance to a degenerate quartet. The increase in bandwidth facilitates *non-degenerate* interactions which manifest as energy transfers at $\pm 55°$ to the spectral peak for the wave groups considered in this study. All our simulations also exhibit downshifting of the spectral peak, as observed by Melville (1982), Tulin & Waseda (1999), Trulsen & Dysthe (1997) and others. For unidirectional waves, the downshift due to wave-wave interactions has been found by Tulin & Waseda (1999) to be largely reversible in the absence of breaking. Our three-dimensional wave simulations do not include breaking but we observe a permanent downshift of the spectral peak in all cases. The nonlinear interactions have been shown to impact the shape, kinematics and lifespan of the focused wave groups. The directional energy transfers result in the formation of *wing waves* that form at the edges of the wave group and propagate in an oblique

direction relative to the wave group. The existence of obliquely propagating coherent waves has recently been observed in simulations based on field data as presented by Waseda *et al.* (2021), suggesting this phenomenon may also arise in a random sea. Our simulations confirm that the formation of wing waves is accompanied by contraction of the wave group in the direction of propagation and expansion of the wave group in the transverse direction, forming the 'wall of water' studied by Gibbs & Taylor (2005) and Adcock & Taylor (2016). We also observe front-rear asymmetry as found by previous studies (see, e.g., Adcock & Taylor (2016) and Fujimoto *et al.* (2019)). We find that the lifespan of the focused events is increased by nonlinear interactions that alter the dispersive characteristics of the wave group, as discussed by Gibson & Swan (2007) and Houtani *et al.* (2018) and observed by Fujimoto *et al.* (2019) in the context of random seas. We note that suppressed linear dispersion has been observed by Steer *et al.* (2019) for modulations which propagate at $\pm 35.26°$ to the wave group, suggesting that oblique energy transfers at $\pm 35.26°$ may extend the lifespan of the wave events. Energy transfers to higher-wavenumbers augment both the velocities and accelerations of the wave field while the transverse contraction of the wave group at focus increases the in-line velocity component. Consequently, both the drag and inertial forces increase, as calculated by the Morison equation.

Objective 2 *To determine the impact of steepness, finite depth, spreading and the spectral tail on the dominant nonlinear interactions of a steep wave group*

We find that both the quasi-degenerate and non-degenerate interactions strengthen with increasing steepness. However, we observe that energy transfers along the unidirectional k_x direction can be suppressed by high steepnesses, consistent with the findings of Longuet-Higgins (1978), McLean (1982*b*), Francius & Kharif (2003) and Fedele (2014). Thus, we observe a biasing towards oblique energy transfers amongst the highest steepness wave groups. We find that a reduction in depth severely suppresses the quasi-degenerate interactions with evidence of complete suppression at $k_p d = 1.363$, consistent with the original results of Benjamin (1967) and Whitham (1967), due to detuning of the interactions by the return current. However, the

non-degenerate interactions are found to be more depth resilient with evidence of directional energy transfers to oblique components persisting at $k_p d = 1.363$, consistent with the findings of Benney & Roskes (1969) and McLean (1982*a*). We find that the in-line contraction and transverse expansion of the wave group also persists as the depth of the water is reduced, suggesting that the 'wall of water' effect may also arise at intermediate depths. A major theme in this thesis is the role of directional spreading and the spectral tail in establishing *spectral equilibrium* that reduces nonlinear energy transfers between wave components, as discussed by Trulsen (2018). Linear theory reveals that broad-banded wave events focus for a shorter time duration thereby reducing energy transfers in an integral sense. Our results demonstrate that the rate of energy transfer itself is also slower for broad-banded events, suggesting that directional spreading contributes to a form of spectral equilibrium that reduces nonlinear energy transfers. We find that focused wave groups with low directional spreading tend to broaden rapidly as the wave group focuses, due to directional energy transfers that increase the directional spreading—crucially, the increase in spreading is largely permanent and does not reverse after focus. Conversely, we find that steep wave events with high amounts of directional spreading become less spread as the wave group focuses, due to contraction of the wavenumber spectrum in the transverse direction—the contraction is, however, largely temporary and reverses after focus. Thus, extreme wave events in a long-crested sea may contribute to the global development of directional spreading through the accumulated contributions of individual events. The local spectral changes of individual wave events could, thus, play an important role in determining the global spectral evolution of long-crested seas. The same cannot be said for short-crested seas since our results suggest that spectral changes are largely temporary for steep wave events in short-crested seas. We also find that the spectral tail may be integral to the establishment of spectral equilibrium. Our simulations reveal that steep wave groups that are based on wave spectra without a tail tend to redevelop the tail during the simulation. Redevelopment of the tail is associated with rapid spectral changes and augmented rates of energy transfer resulting in a prevalence of nonlinear fea-

tures for the wave groups. Truncating the tail of the spectrum for the purpose of simulations/experiments could, thus, result in artificially exaggerated nonlinear energy transfers. Thus, truncation of the tail should be handled with care. We note that certain physical mechanisms may also suppress the tail of the spectrum. For example, ice sheets disproportionately dissipate the energy associated with high-wavenumber components, potentially suppressing the tail of the spectrum (see, e.g., Toffoli *et al.* (2015) and Meylan *et al.* (2018)). Similarly, 'wave blocking' by currents could suppress the tail of the spectrum by allowing the long-wavelength components to propagate through the current while convecting short-wavelength components downstream (see, e.g., Chawla & Kirby (2002) and Ma *et al.* (2010)). Notably, currents have also been shown by Waseda *et al.* (2015) to suppress the development of the tail by detuning the wave-wave interactions. Thus, ice sheets and currents could cause a local suppression of the spectral tail resulting in focused wave events with augmented energy transfers in the immediate vicinity.

Objective 3 *To assess the suitability of the Modified Nonlinear Schrödinger (MNLS) equation for simulating steep wave groups*

We have focused upon two aspects of the MNLS equation in particular. The bandwidth limits of the equation and the ability to cope with finite depth. Use of the MNLS equation for engineering purposes is hindered by concerns about the bandwidth limits of the equation and the existing finite-depth formulations often include lengthy expressions for the coefficients of the nonlinear terms (see, e.g., Sedletsky (2003)). Thus, we assess the bandwidth and finite-depth limits of the 'classic' MNLS formulations (see Trulsen & Dysthe (1996) and Trulsen *et al.* (2000)) which remain attractive in their simplicity and low computational expense. Our analysis of the MNLS bandwidth limits has focused on the relative advantages of the exact dispersion operator of Trulsen *et al.* (2000) compared with the truncated dispersion operator of Trulsen & Dysthe (1996). We found that both dispersion operators perform well if: (i) the carrier wave is aligned with direction of wave group propagation and (ii) the characteristic wavenumber of the carrier wave coincides with the spec-

tral peak. Although, we found the truncated dispersion operator to be slightly more diffusive than the exact dispersion operator. Under conditions (i) and (ii), both dispersion operators yield good agreement with our high-fidelity potential flow simulations, in terms of the amplitude of the wave envelope and the spectral evolution of the wave group. In practice, the selection of the MNLS carrier wave properties is likely to be based on the underlying wave spectrum. However, steep wave events in a random sea may form at an angle to the dominant wave direction, as evidenced by Waseda *et al.* (2021), in violation of condition (i). Steep wave events also feature local spectral distortions which implies that the characteristic wavenumber of an individual wave event may differ from the global characteristic wavenumber of the sea state, in violation of condition (ii). The interplay between the spectral content of an individual wave event and the background sea state is a major theme in this thesis and the concept is again relevant to our analysis of the MNLS equation. Thus, we have investigated the sensitivity of the MNLS equation to directional misalignment of the carrier wave and the selection of the characteristic wavenumber to ascertain the ability of the MNLS equation to resolve steep wave events with different spectral content to the background sea state. The violation of conditions (i) and (ii) tests the bandwidth limits of the MNLS equation by placing large amplitude components at modulation wavenumbers away from the carrier wavenumber. We find that the exact dispersion operator significantly improves the bandwidth limits of the MNLS equation. While the truncated dispersion operator produces significant errors for a misalignment greater than 10°, the exact dispersion operator performs well with a misalignment up to 30°. The truncated dispersion operator also shows signs of aggravated energy leakage if the carrier wavenumber falls below the spectral peak while the exact dispersion operator shows few signs of energy leakage in any of our simulations. Our results also indicate that the exact dispersion operator improves the finite-depth capabilities of the MNLS equation, allowing the arbitrary-depth dispersion relation to be implemented in the dispersion operator. We found that the arbitrary-depth dispersion relation, combined with evaluation of the bottom boundary condition at finite depth, allows the MNLS equation to capture the evo-

lution of focused wave groups at finite depths. We observe good agreement with our high-fidelity potential flow simulations for $k_p d$ between 5.592 and 1.363. Thus, modification of the coefficients for the nonlinear terms appears to be unnecessary within this range of depths. Thus, our results suggest that the exact dispersion operator significantly improves the bandwidth limits of the MNLS equation and inclusion of the arbitrary-depth dispersion allows the equation to be used at intermediate depths, representing positive steps towards the possible use of the MNLS equation for engineering purposes.

Objective 4 *To determine whether our local observations, based on individual wave groups, are consistent with the global statistics of a random wave field*

Using our MNLS code, we considered the kurtosis evolution of random seas because the free-surface kurtosis is indicative of the formation of 'rogue' wave events. Our focus has been the impact of the spectral tail on the peak kurtosis value achieved after initialisation with Gaussian statistics and we use the test case defined by Experiment B of Onorato *et al.* (2009). Our potential flow simulations of isolated wave groups revealed that truncation of the spectral tail resulted in focused wave events with a greater prevalence of nonlinearity, accompanied by redevelopment of the spectral tail and augmented rates of energy transfer. Analogously, our random sea simulations indicate that truncation of the spectral tail results in an augmented peak kurtosis values, accompanied by redevelopment of the spectral tail and augmented rates of energy transfer. Thus, our observation on the local scale of an individual wave event resembles our observation on the global scale of a random sea. This observation suggests that the spectral evolution of the background sea state may be the accumulated result of the local spectral distortions produced by individual steep wave events. We observe qualitatively similar trends in the spectral evolution of our isolated wave groups and random sea simulations, including downshifting of the spectral peak, an increase in bandwidth and the development of increased directional spreading in the tail due to directional energy transfers to oblique components. However, the trends in our random sea simulations are all more prominent

if the spectral tail is truncated. Thus, we conclude that the spectral tail plays an important role in establishing the spectral equilibrium of random seas. Truncation of the tail for the purpose of simulations/experiments should, thus, be performed with care. A comparison of our MNLS simulations with HOS simulations and experiments performed by other studies (see Onorato *et al.* (2009), Toffoli *et al.* (2010*a*) and Xiao *et al.* (2013)) indicates that the MNLS equation can be used to estimate the peak kurtosis value despite the bandwidth limits of the equation. We also find that the kurtosis evolution equation of Fedele (2015) provides a good estimate of the peak kurtosis. However, the selected bandwidth parameter must account for the spectral tail to provide accurate estimates of the peak kurtosis value and we find that the bandwidth parameter of Goda (1985) appears to provide a suitable choice, consistent with the recommendations of Serio *et al.* (2005).

Appendix A

A Linearization of the wave spectrum: a comparison of methods

Abstract

The relative contributions of free waves and bound waves to the formation of an extreme wave event remains a topic of interest in offshore engineering. A variety of methods have been proposed for identifying and removing the bound wave components. The method of 'phase separation' or 'phase manipulation' repeats simulations/experiments of a wave field with an offset in the initial phase of the wave components and relies upon summation of the resulting wave fields to isolate the bound harmonics, following from a Stokes expansion in steepness; the method has proven effective in isolating bound harmonics but requires that all cases be repeated. Alternatively, the bound harmonics can be removed using a three-dimensional fast Fourier transform (3D-FFT) of the wave field. However, the Fourier transform requires periodicity in the signal and assumes homogeneity in space and stationarity in time, producing spurious modes otherwise. We compare the phase separation and 3D-FFT approaches for a steep, focusing wave group in deep water using the numerical simulation tool, OceanWave3D, and discuss the effectiveness of both methods.

A.1 Introduction

A variety of mechanisms have been associated with the formation of steep ocean waves, as discussed by Kharif & Pelinovsky (2003), Dysthe *et al.* (2008) and Adcock & Taylor (2014). The formation of a steep ocean wave can result from linear dispersion as well as nonlinear self-focusing. Nonlinear wave-wave interactions can facilitate resonant energy transfers, altering the amplitude and phase velocity of interacting wave components. Another nonlinear feature of ocean waves is the formation of 'bound harmonics' which can increase the crest height of a focused wave (see, e.g., the second-order formulation of Dalzell (1999)). Surface gravity waves in the ocean can be approximately modelled, to first-order accuracy, as a linear superposition of 'free harmonics', which adhere to the linear dispersion relation and yield Fourier coefficients that are independent of each other. However, the linear treatment of ocean waves only satisfies the free-surface boundary conditions to the first-order and higher-order nonlinear analyses indicate the presence of bound harmonics, which feature Fourier coefficients that depend on the free wave components and also propagate with dynamics slaved to the free wave components. Accurate calculation of the growth rates and dispersion characteristics of the free wave components requires that the bound harmonics be removed from the wave spectrum.

Figure A.1 demonstrates the significance of the nonlinear terms in the free surface boundary conditions, from the simulations of Barratt *et al.* (2020). The two wave groups shown in figure A.1(a) and figure A.1(b) are based upon identical initial conditions and both achieve a steepness (Ak) of approximately 0.3 at focus, based on the amplitude (A) and characteristic wavenumber (k). However, figure A.1(a) shows the result obtained by neglecting the nonlinear terms in the free-surface boundary conditions and figure A.1(b) shows the result obtained with the fully-nonlinear free-surface boundary conditions. Both the linear and nonlinear versions of the event are shown at the time of maximum crest elevation, $t/T_p = 0$ for the linear case and $t/T_p = 1.3$ for the nonlinear case. Inclusion of the nonlinear terms alters the shape of the wave group; the nonlinear case features the largest crest at the front of the wave group rather than the center and the formation of oblique localised protrusions,

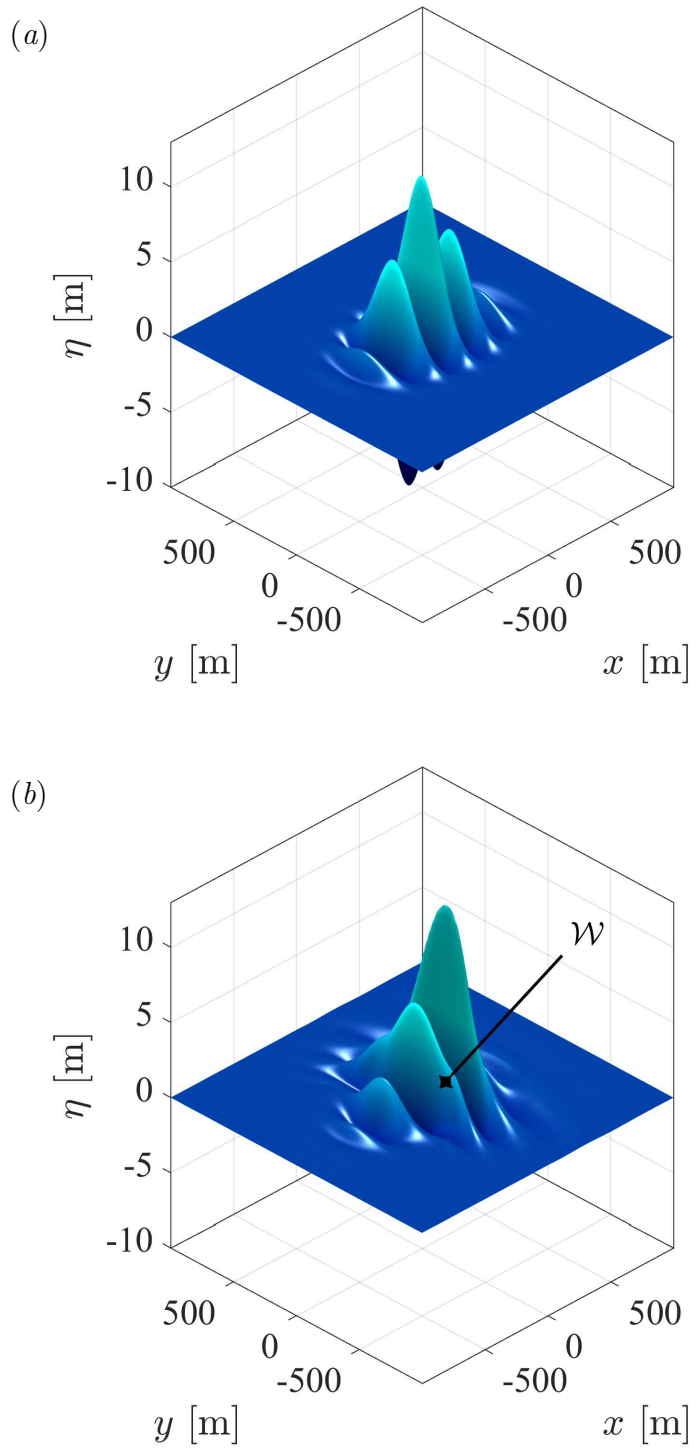

Figure A.1: Surface elevation of wave groups at focus with a steepness (Ak) of 0.3, simulated with identical initial conditions in *OceanWave3D*: (a) time-marched without nonlinear terms in free surface boundary conditions; (b) time-marched with nonlinear terms in free surface boundary conditions. The formation of *wing waves* is demarcated with $\mathcal{W}$.

termed *wing waves*, can be observed at the periphery of the wave group for the nonlinear case. Second-order bound harmonics are associated with the development of higher, sharper crests and shallower, flatter troughs as well as a 'set-down' in surface elevation, all observed in the second-order simulations of Dalzell (1999). The combined influences of nonlinearity cause the maximum crest height in figure A.1(b) to be 13% higher than figure A.1(a).

In this study, we simulate steep focused wave groups, formed by dispersive focusing, using the fully-nonlinear potential flow solver *OceanWave3D*, described in Engsig-Karup *et al.* (2009). Using the results, we contrast two different methods of linearizing the wave spectrum: (I) the technique of *phase separation* used by Gibbs & Taylor (2005) for focusing wave groups with directional spreading and; (II) a three-dimensional Fourier transform (3D-FFT) technique applied by Slunyaev & Kokorina (2019) to random wave fields. We perform the comparison on wave groups with different amounts of directional spreading and discuss the limitations of both techniques.

A.2 Numerical Details

The initial conditions for the simulations have been calculated 15 characteristic wave periods before the linear focus time, using the linear dispersion relationship. Time marching of the initial conditions has been performed with *OceanWave3D* for 30 wave periods, terminating each simulation 15 wave periods after the linear focus time.

A.2.1 Code Description

OceanWave3D solves the governing equations of potential flow for surface gravity waves (see, e.g., Currie (1993)) and a detailed description of the code can be found in Engsig-Karup *et al.* (2009), extending the work of Bingham & Zhang (2007). A non-conformal transform maps the solution to a time-invariant domain:

$$\sigma \equiv \frac{z + d(x, y)}{\eta(x, y, t) + d(x, y)}, \tag{A.1}$$

discretized with a flexible-order finite difference scheme and time marched with the classic fourth-order Runge–Kutta (RK4) scheme. Here, η denotes the surface elevation, d the depth of the domain and z the vertical coordinate. We employ grid stretching in the vertical direction, to cluster nodes near the free surface, using the symmetric half of a Chebyshev-Gauss-Lobatto (CGL) distribution: $\sigma_j = \sin((\pi[j-1])/(2[N_z-1]))$. A single layer of ghost nodes lines all boundaries except the free surface. The discrete linear system is solved with a preconditioned iterative scheme, based on the Generalized Minimal Residual (GMRES) method without restarts. Preconditioning has been performed with multi-grid Gauss-Seidel relaxation to ensure optimal scaling of the solution effort as demonstrated by Engsig-Karup *et al.* (2009).

A.2.2 Simulation Parameters

A numerical wave tank 7.68 km in length, 2.56 km in width and 112 m in depth (d) has been used. All simulations possess a characteristic wavelength (λ_0) of 225 m and characteristic period of 12 s—based on the initial peak of the wavenumber spectrum, $k_p = 0.02796$ m^{-1}. The water is approximated as deep with a dimensionless depth of $k_p d = 3.142$. A symmetry plane has been utilised in the transverse (y) direction, along the centreline of the wave group (see figure A.1), to reduce the size of the numerical domain. Barratt *et al.* (2020) have confirmed that the symmetry plane does not significantly aggravate numerical diffusion for the wave group.

A.2.3 Initial Conditions

We calculate the variance density spectrum, $F(k,\theta)$, as the product of an omni-directional spectrum $S(k)$ in terms of wavenumber (k) and a spreading function $D(\theta)$ based on the angle of propagation (θ) for each component. We use a Gaussian wavenumber spectrum:

$$S(k) = \exp\left(\frac{-(k-k_p)^2}{2{k_w}^2}\right), \tag{A.2}$$

in combination with a frequency-independent Gaussian spreading function:

$$D(\theta) = \frac{1}{\varsigma\sqrt{2\pi}} \exp\left(\frac{-\theta^2}{2\varsigma^2}\right). \tag{A.3}$$

Here, the initial peak of the omnidirectional wavenumber spectrum (k_p) as well as the bandwidth (k_w) are required as inputs, and values of $k_p = 0.02796$ m^{-1} and $k_w = 0.004606$ m^{-1} have been used in this study. The spreading function also includes a spreading parameter (ς) and we have used values of 15°, 20° and 25° in this study, to assess the bandwidth sensitivity of phase separation. Based on the theory of quasi-determinism (see Boccotti (1983)), the scaled-autocorrelation function of the variance density spectrum, $F(k, \theta)$, has been calculated to obtain the surface elevation of the wave group, $\eta(x, y, t)$:

$$\eta = A_L \frac{\sum_i F(k_i, \theta_i) \cos\left(k_i \cos\theta_i \, x + k_i \sin\theta_i \, y - \omega_i t + \varphi_0\right)}{\sum_i F(k_i, \theta_i)}, \tag{A.4}$$

also known as the *NewWave* model of an extreme wave (see Tromans *et al.* (1991)). Here, k_i is the wavenumber magnitude for each component, θ_i is the propagation angle, A_L is the amplitude of the group at linear focus ($t/T_0 = 0$) and the angular frequency of each component (ω_i) is based on the linear dispersion relationship, $\omega_i = \sqrt{g k_i \tanh\left(k_i d\right)}$, dependent upon the gravitational constant (g) and the domain depth (d). A linear steepness of $A_L k_p = 0.24$ has been used for all cases in this study. The phase offset (φ_0) is defined relative to a 0° baseline and values of 0°, 90°, 180° and 270° have been simulated for application of the four-phase separation technique. The scaled autocorrelation function is known to represent the average shape of the largest waves in a linear sea, as described by Boccotti (1983), and has thus been used in this study as a model for a steep wave group.

A.2.4 Linearization of the Wave Spectrum

The method of phase separation has been shown by Gibbs & Taylor (2005) to effectively linearize the wave spectrum for a narrow-banded wave group with directional spreading. However, the method requires that each simulation be repeated with an offset in the initial phase, increasing the required number of test cases. Conversely, the 3D-FFT approach we use, motivated by Slunyaev & Kokorina (2019), does not require additional cases to perform the linearization. However, the use of Fourier transforms requires periodicity in the signal and also assumes homogeneity in space

as well as stationarity in time, in contrast to the local and rapid distortions of the wave spectrum surrounding a steep wave.

Phase Separation The technique of *phase separation* derives from the general solution form of Stokes' expansion, shown here to the fourth-order in steepness for a single amplitude component, a_i, with phase $\vartheta_i(t)$:

$$\begin{aligned}\eta_i(t) = &+ a_i \cos\vartheta_i(t) \\ &+ C_{22}a_i^2 \cos 2\vartheta_i(t) + C_{20}a_i^2 \\ &+ C_{31}a_i^3 \cos\vartheta_i(t) + C_{33}a_i^3 \cos 3\vartheta_i(t) \\ &+ C_{42}a_i^4 \cos 2\vartheta_i(t) + C_{44}a_i^4 \cos 4\vartheta_i(t),\end{aligned} \tag{A.5}$$

Here, $\vartheta_i(t) = k_i\, x \cos\theta_i + k_i\, y \sin\theta_i - \omega_i\, t + \varphi_0$. The initial phase φ_0 is defined relative to a 0° baseline and the coefficients, C_{ij}, determine sensitivity to depth, listed to fifth-order in Fenton (1985). Particular terms of the Stokes expansion can be isolated by performing simulations with an offset in the initial phase, φ_0, followed by addition/subtraction of the resultant wave fields, a method introduced by Baldock *et al.* (1996). A phase offset of 180°, for example, reverses the sign of the first-order and third-order terms in (A.5) but does not change the sign of the second-order and fourth-order terms. Addition of the surface elevation for the 0° and 180° cases, thus, allows the second-order and fourth-order bound harmonics to be isolated and used to linearize the surface elevation. The same approach can also be applied to the velocity potential. Fitzgerald *et al.* (2014) demonstrate the *four-phase* approach, performing simulations with 0°, 90°, 180° and 270° phase offsets to isolate the first-order free harmonic and the third-order principal harmonic (usually considered negligible), yielding the linearised surface elevation (η_L):

$$\eta_L(t) = a_i \cos\vartheta_i(t) + C_{31}a_i^3 \cos\vartheta_i(t). \tag{A.6}$$

In this study, we also apply the four-phase separation technique to linearize the wave spectrum using the expressions of Fitzgerald *et al.* (2014). An *eight-phase* version

of phase separation has also been formulated by Hann *et al.* (2014).

Note, the phase of the first-order and third-order terms in (A.6) always match. Thus, the first-order free harmonic and third-order principal harmonic cannot be further separated by any combination of phase offsets, an inherent limitation of the phase separation technique.

Three-Dimensional Fourier Transform We simulate focused wave groups with directional spreading. The surface elevation $\eta(x, y, t)$ at a particular time step ($t = t_s$) can, thus, be transformed with a two-dimensional Fast Fourier Transform ($\mathcal{F}_{xy}$), in x and y, to obtain the Fourier components in the wavenumber domain.

$$\hat{\eta}(k_x,\, k_y,\, t_s) = \mathcal{F}_{xy}\{\eta(x,\, y,\, t_s)\}. \tag{A.7}$$

The process can be repeated at every time step, yielding a vector of Fourier components for each wavenumber component (k_x, k_y) with a length equivalent to the number of time steps (N_t). We reflect the signal to ensure periodicity,

$$\hat{\eta}[N_t + 1 : 1 : 2(N_t - 1)]\Big|_{k_x,\, k_y} = \hat{\eta}[N_t - 1 : -1 : 2]\Big|_{k_x,\, k_y}, \tag{A.8}$$

producing a vector of length $2(N_t - 1)$ for every wavenumber component (k_x, k_y). Subsequent application of a third Fourier transform to the reflected vector resulting from (A.8):

$$\tilde{\eta}(\omega)\big|_{k_x,\, k_y} = \mathcal{F}_t\big\{\hat{\eta}\big|_{k_x,\, k_y}\big\}, \tag{A.9}$$

yields a further vector of Fourier components, also of length $2(N_t - 1)$, indicating the amplitudes associated with various frequencies for a specific wavenumber component (k_x, k_y). According to the linear dispersion relation, the frequency associated with a free wave component (k_x, k_y) is given by $\omega_n^2 = g|k| \tanh\{|k|d\}$ and the bound wave components associated with the same wavenumber appear as *superharmonics*, $\omega > \omega_n$, and *subharmonics*, $\omega < \omega_n$. We apply top-hat filters to the $\tilde{\eta}$ vectors calculated with (A.9), preserving the free wave components ($\omega \approx \omega_n$), while eliminating both superharmonic and subharmonic bound wave components. The steps defined

in (A.7-A.9) are thereafter reversed, to reconstruct the linearised surface elevation $\eta_L(x, y, t)$.

Note, however, that (A.9) assumes stationarity in time, implying that the various harmonics associated with a specific wavenumber (k_x, k_y) possess amplitudes and angular frequencies which do not change in time. Nonlinear wave-wave interactions will, however, alter both the amplitude and angular frequency of the free wave components during the course of the simulation. Thus, (A.9) is susceptible to aliasing and the production of spurious modes which may overlap with the bound harmonics and obstruct filtering/linearization of the results. Reflection of the signal in (A.8) ensures a smooth periodic signal but may also result in aliasing. The 3D-FFT technique requires the surface elevation of the entire wave field, which is usually only available for numerical simulations due to the experimental challenges of such a measurement, and automation of the filtering process involves assumptions about the characteristics of the free and bound waves. Additional simulation are not, however, required to perform the linearization, in contrast to the phase separation approach.

A.3 Results and Discussion

We assess the effectiveness of phase separation and the 3D-FFT approach for linearizing the wave spectrum, using wave groups with different amounts of directional spreading—based on the spreading parameter (ς) of the Gaussian spreading function in (A.3). Figure A.2 shows the results for a wave group with a spreading parameter of 15°. Application of the 3D-FFT approach described in (A.7-A.9) has produced the contour plots shown figure A.2, indicating the amplitudes associated with different frequency harmonics for wavenumbers up to $5k_p$. A logarithmic scale (base-10) has been used for the contours in figure A.2 to emphasise the bound harmonics. Note, however, that figure A.2 only includes wavenumber components with $k_y = 0$. Oblique components, $k_y \neq 0$, are not included in figure A.2 for clarity of the plot. However, qualitatively similar results have also been observed for oblique wavenumber components. Figure A.2(a) depicts the result for the 0° baseline case, before any linearization technique has been applied. A black line indicates the lin-

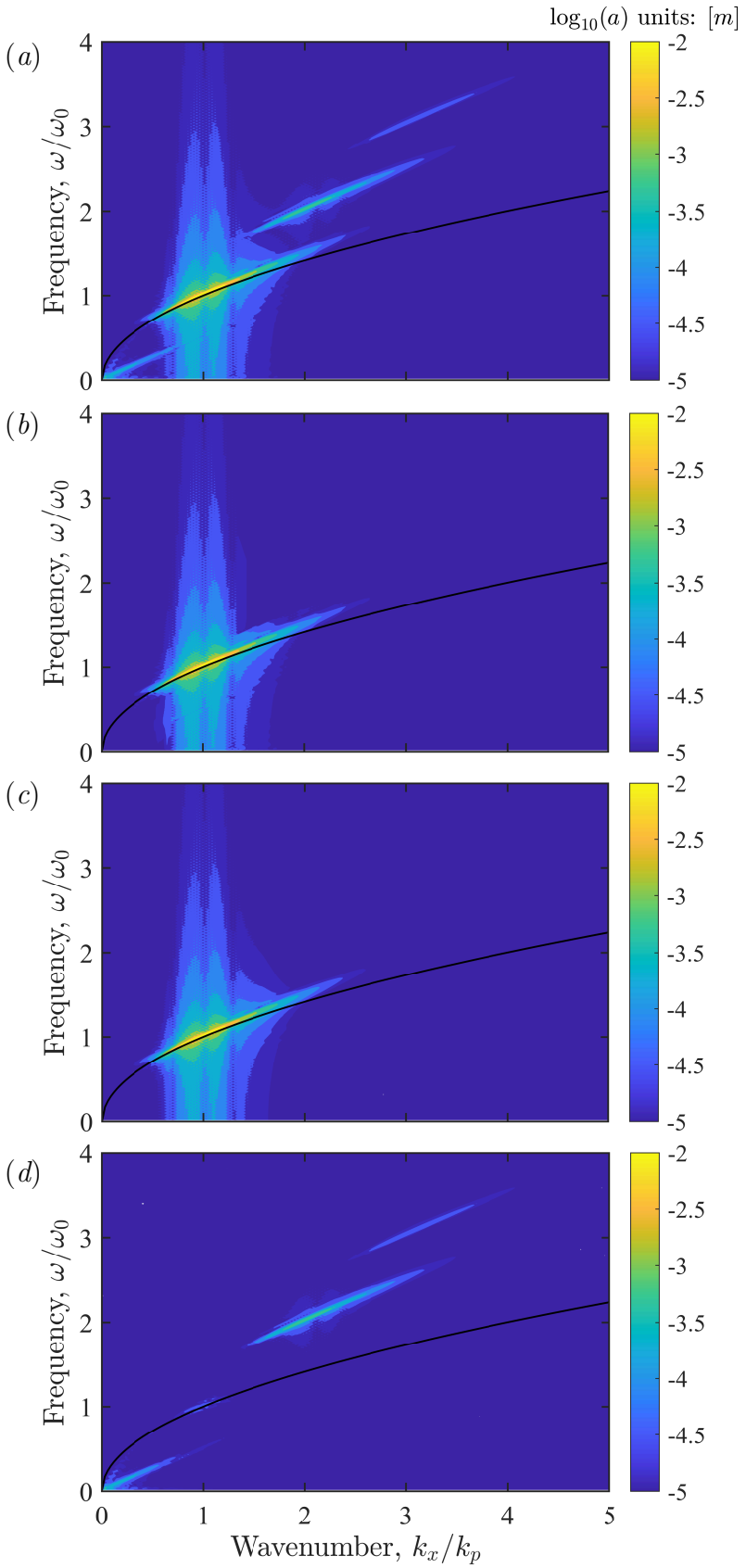

Figure A.2: Contour plots of component amplitude, calculated with the 3D-FFT, for a wave group with a steepness (Ak) of 0.24 and an initial spreading parameter (ς) of 15°: (a) nonlinear wave spectrum including all bound harmonics; (b) linearized result based on filtering of 3D-FFT; (c) linearized result based on phase separation; (d) bound harmonics isolated with phase separation. Only components with $k_y = 0$ are included for the sake of clarity.

ear dispersion relationship. The wavenumber on the abscissa has been normalised by the wavenumber of the initial spectral peak (k_p) and the frequency on the ordinate has been normalised by $\omega_0 = \sqrt{gk_p}$. A concentration of harmonics can be seen around $k = k_p$, representing the free wave components associated with the narrow-banded wave group. However, a 'smearing' of amplitudes can be seen for the free-wave components with a local peak near the linear dispersion line and diminising amplitudes extending to both higher and lower wavenumbers—this effect can be attributed to the production of spurious modes by (A.9), since the processed signals are not strictly stationary in time. Despite the spurious modes, both subharmonic and superharmonic bound waves are clearly visible in figure A.2(a): second-order subharmonics occupy the wavenumber range of $0-0.7k_p$ at frequencies of $0-0.3\omega_0$; second-order superharmonics occupy the wavenumber range of $1.2-3.5k_p$ at frequencies of $1.7-2.7\omega_0$ and; third-order superharmonics occupy the wavenumber range of $2.5-4.2k_p$ at frequencies of $2.7-3.5\omega_0$. As can be seen in figure A.2(a), a small amount of overlap exists between the free wave components and the fringes of the second-order subharmonics and superharmonics. However, the extent of the overlap is not severe and selective application of top-hat filters to the harmonics shown in figure A.2(a) yields the linearised result shown in figure A.2(b). The corresponding linearised result obtained with phase separation is shown in figure A.2(c). The agreement between figure A.2(b) and figure A.2(c) is generally good, although slight differences can be perceived where the overlap between free waves and bound waves arose. We note that filtering of figure A.2(a) would have proven significantly more challenging if a JONSWAP wavenumber spectrum, including the high-wavenumber tail, had been used since the overlap between the free waves and bound waves would be more substantial. Figure A.2(d) shows all the bound harmonics, isolated with the method of phase separation; the bound harmonics have been successfully isolated with phase separation even in the regions of overlap with the free harmonics. The method of filtering applied to figure A.2(b) has been applied to all wavenumber components in the range of $0 < k_x < 5k_p$ and $0 < k_y < 5k_p$, followed by reconstruction of the surface elevation to obtain a fully-linearised result with the 3D-FFT

approach.

Figure A.3 compares the linearised surface elevation obtained with the 3D-FFT approach against the linearised surface elevation obtained with the phase separation technique and the nonlinear result (with all bound harmonics included). The analysis has also been repeated for wave groups with different values for the spreading parameter: $\varsigma = 15^{\circ}$ in figure A.3(a); $\varsigma = 20^{\circ}$ in figure A.3(b) and; $\varsigma = 25^{\circ}$ in figure A.3(c). The time history of surface elevation (η_0) is shown on the ordinate, for the spatial location where nonlinear focus of the wave group occurs. The location of focus (x_f, y_f) varies for all the cases, dependent upon the nonlinear dispersive characteristics of the wave group, but always occurs along the centreline of the domain ($y_f = 0$) due to symmetry. The x-coordinate of nonlinear focus is listed in table A.1, alongside the time of nonlinear focus (t_f), for each case. The spatial x-coordinate is defined relative to the location where linear focus of the wave group would occur ($x = 0$) and the time of focus is similarly defined relative to the time of linear focus ($t = 0$), normalised by the characteristic wavelength (λ_0) and characteristic wave period (T_0) respectively. All three cases in figure A.3 show excellent agreement between the two methods of linearization. Removal of the bound harmonics diminishes the amplitude of the crests and deepens the troughs, in accordance with the known characteristics of the second-order bound harmonics (see Dalzell (1999)) expected to dominate the bound wave contributions. The maximum crest height occurring at the location of nonlinear focus is listed in table A.1 for the nonlinear case with all bound harmonics included (η_{NL}), the linearised case based on filtering of the 3D-FFT (η_{LF}) and the linearised case based on phase separation (η_{LP}). The difference between the two linearised cases, normalised by the linear amplitude of the focused wave event (A_L):

$$\delta[\%] = \frac{|\eta_{LF}^{Max} - \eta_{LP}^{Max}|}{A_L} \times 100, \tag{A.10}$$

is also listed in table A.1. All three cases list differences (δ) less than 0.7% with the best agreement for the least spread case ($\varsigma = 15^{\circ}$), presumably because the overlap between the free waves and bound waves is less severe for the least spread case which

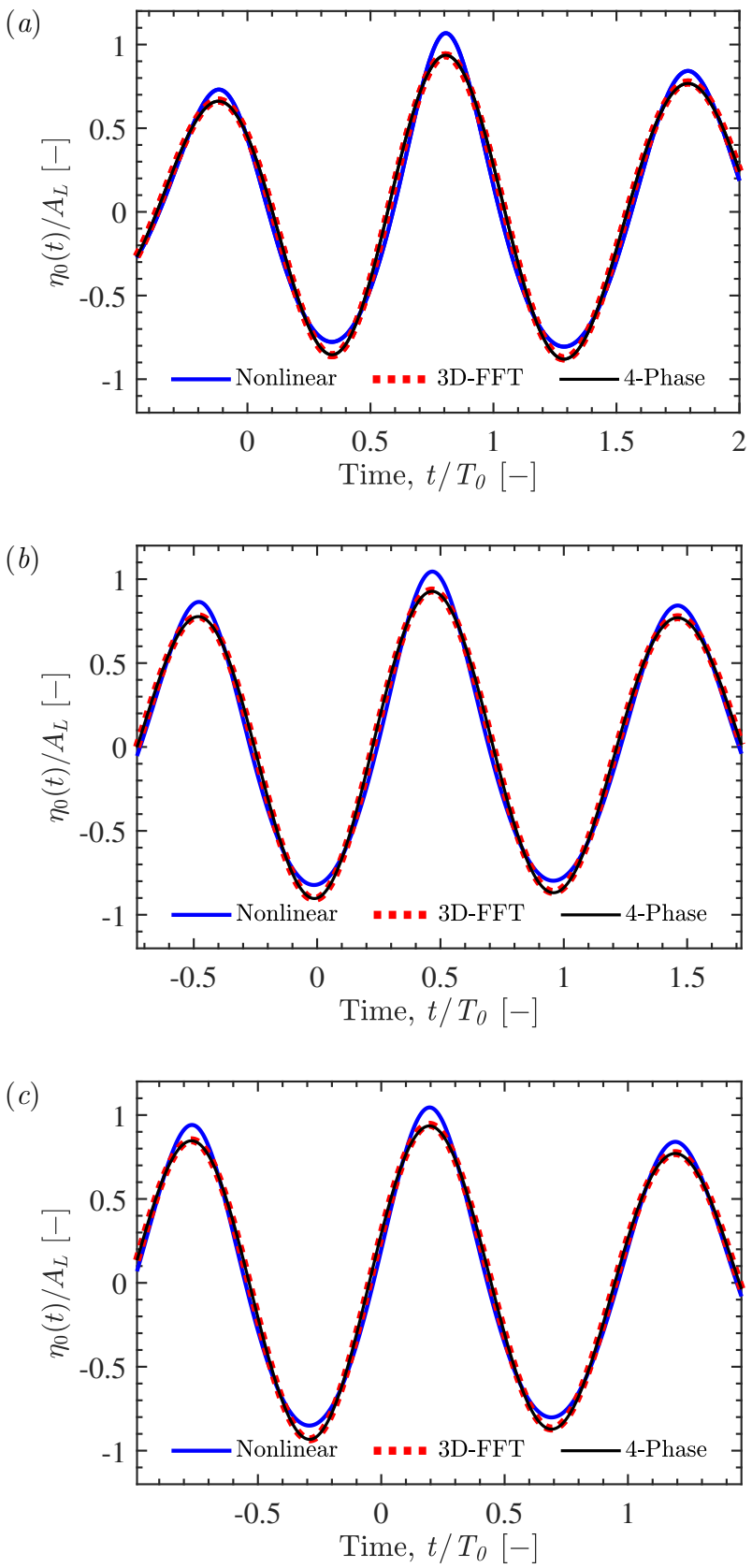

Figure A.3: Time history of surface elevation, $\eta_0(t)$, at the location of nonlinear focus for wave groups of steepness $Ak = 0.24$ with initial spreading parameters of: (a) $\varsigma = 15°$; (b) $\varsigma = 20°$; and (c) $\varsigma = 25°$. Normalisation has been performed with the linear focus amplitude (A_L). The nonlinear surface elevation, including all bound harmonics, is shown together with the linearized results based on filtering of the 3D-FFT and phase separation. The location and time of nonlinear focus for each case is listed in table A.1 together with the max crest elevation.

Table A.1: Max crest elevation for nonlinear and linearized cases.

ς	x_f/λ_0 [-]	t_f/T_0 [-]	η_{NL}^{Max} [m]	η_{LF}^{Max} [m]	η_{LP}^{Max} [m]	δ [%]
15°	0.93	0.80	9.153	8.038	8.033	0.06
20°	0.57	0.47	8.972	8.004	7.963	0.48
25°	0.27	0.20	8.968	8.082	8.024	0.68

facilitates better filtering of the bound waves. The results listed in table A.1 could likely be improved with windowing of the processed signals and a more sophisticated filtering scheme, especially for the cases with more directional spreading. Wavelets could also resolve the issue of non-stationarity in (A.9), reducing the aliasing effect of the free waves in figure A.2 and eliminating overlap between the free wave and bound wave components.

A.4 Conclusion

Linearization of the wave spectrum has been successfully performed for potential flow simulations of focusing wave groups using both the 3D-FFT and phase separation techniques. The methods have been compared for wave groups with spreading parameters of 15°, 20° and 25° and quantitative agreement has been obtained within 0.7% for the maximum crest elevation. The 3D-FFT approach requires the entire wave field at every time step and, thus, is most appropriate for numerical simulation data. In this study, we have directly filtered the bound harmonics from the 3D-FFT results, which proved possible because the wave groups have been constructed from narrow-banded Gaussian spectra. However, filtering of the 3D-FFT would be significantly more challenging with a JONSWAP wavenumber spectrum. Phase separation proved able to separate the bound harmonics, even in instances of overlap with the free waves, and thus can be used with a JONSWAP wavenumber spectrum. However, linearization with the four-phase technique requires additional simulations which are not required by the 3D-FFT approach.

References

Adcock, T. A. A., Gibbs, R. H. & Taylor, P. H. 2012 The nonlinear evolution and approximate scaling of directionally spread wave groups on deep water. *Proc. R. Soc. A* **468**, 2704–2721.

Adcock, T. A. A. & Taylor, P. H. 2014 The physics of anomalous ('rogue') ocean waves. *Rep. Prog. Phys.* **77**, 105901.

Adcock, T. A. A. & Taylor, P. H. 2016 Fast and local non-linear evolution of steep wave-groups on deep water: A comparison of approximate models to fully-nonlinear simulations. *Phys. Fluids* **28**, 016601.

Adcock, T. A. A., Taylor, P. H. & Draper, S. 2015 Nonlinear dynamics of wave-groups in random seas: Unexpected walls of water in the open ocean. *Proc. R. Soc. A* **471**, 20150660.

Akhmediev, N., Dudley, J. M., Solli, D. R. & Turitsyn, S. K. 2013 Recent progress in investigating optical rogue waves. *J. Opt.* **15** (6), 060201.

Alber, I. E. 1978 The effects of randomness on the stability of two-dimensional surface wavetrains. *Proc. R. Soc. A* **363**, 525–546.

Alberello, A., Chabchoub, A., Monty, J. P., Nelli, F., Lee, J. H., Elsnab, J. & Toffoli, A. 2018 An experimental comparison of velocities underneath focussed breaking waves. *Ocean Eng.* **155**, 201–210.

Annenkov, S. Y. & Shrira, V. I. 2006 Role of non-resonant interactions in the evolution of nonlinear random water wave fields. *J. Fluid Mech.* **561**, 181–207.

Annenkov, S. Y. & Shrira, V. I. 2018 Spectral evolution of weakly nonlinear random waves: Kinetic description versus direct numerical simulations. *J. Fluid Mech.* **844**, 766–795.

Baldock, T. E., Swan, C. & Taylor, P. H. 1996 A laboratory study of nonlinear surface waves on water. *Proc. R. Soc. A* **354** (1707), 649–676.

Banner, M. L. & Young, I. R. 1994 Model spectral dissipation in the evolution of wind waves. Part I: Assessment of existing model performance. *J. Phys. Oceanogr.* **24** (7), 1550–1571.

Barratt, D., Bingham, H. B. & Adcock, T. A. A. 2020 Nonlinear evolution of a steep, focusing wave group in deep water simulated with *OceanWave3D*. *J. Offshore Mech. Arct. Eng.* **142**, 021201.

Barratt, D., Bingham, H. B., Taylor, P. H., van den Bremer, T. S. & Adcock, T. A. A. 2021*a* Rapid spectral evolution of steep surface wave groups with directional spreading. *J. Fluid Mech.* **907**.

Barratt, D., van den Bremer, T. S. & Adcock, T. A. A. 2021*b* MNLS simulations of surface wave groups with directional spreading in deep and finite depth waters. *J. Ocean Eng. Mar. Energy* pp. 1–15.

Barthelemy, X., Banner, M. L., Peirson, W. L., Fedele, F., Allis, M. & Dias, F. 2018 On a unified breaking onset threshold for gravity waves in deep and intermediate depth water. *J. Fluid Mech.* **841**, 463–488.

Bateman, W. J. D., Katsardi, V. & Swan, C. 2012 Extreme ocean waves. Part I. The practical application of fully nonlinear wave modelling. *Appl. Ocean Res.* **34**, 209–224.

Bateman, W. J. D., Swan, C. & Taylor, P. H. 2001 On the efficient numerical simulation of directionally spread surface water waves. *J. Comp. Phys.* **174**, 277–305.

Benjamin, T. B. 1967 Instability of periodic wavetrains in nonlinear dispersive systems. *Proc. R. Soc. A* **299** (1456), 59–76.

Benney, D. J. & Roskes, G. J. 1969 Wave instabilities. *Stud. Appl. Math.* **48** (4), 377–385.

Bingham, H. B. & Zhang, H. 2007 On the accuracy of finite-difference solutions for nonlinear water waves. *J. Eng. Math.* **58** (1-4), 211–228.

Boccotti, P. 1983 Some new results on statistical properties of wind waves. *Appl. Ocean Res.* **5** (3), 134–140.

Boccotti, P. 2000 *Wave mechanics for ocean engineering*. Elsevier: Amsterdam.

van den Bremer, T. S. & Taylor, P. H. 2015 Estimates of Lagrangian transport by surface gravity wave groups: The effects of finite depth and directionality. *J. Geophys. Res. Oceans* **120** (4), 2701–2722.

Brinch-Nielsen, U. & Jonsson, I. G. 1986 Fourth order evolution equations and stability analysis for Stokes waves on arbitrary water depth. *Wave Motion* **8** (5), 455–472.

Chawla, A. & Kirby, J. T. 2002 Monochromatic and random wave breaking at blocking points. *J. Geophys. Res. Oceans* **107** (C7), 4–1.

Crawford, D. R., Lake, B. M., Saffman, P. G. & Yuen, H. C. 1981 Stability of weakly nonlinear deep-water waves in two and three dimensions. *J. Fluid Mech.* **105**, 177–191.

Currie, I. G. 1993 *Fundamental Mechanics of Fluids*, 3rd edn. McGraw-Hill, New York.

Dalzell, J. F. 1999 A note on finite depth second-order wave–wave interactions. *Appl. Ocean Res.* **21** (3), 105–111.

Davey, A. & Stewartson, K. 1974 On three-dimensional packets of surface waves. *Proc. R. Soc. A* **338**, 101–110.

Ducrozet, G., Bingham, H. B., Engsig-Karup, A. P., Bonnefoy, F. & Ferrant, P. 2012 A comparative study of two fast nonlinear free-surface water wave models. *Int. J. Numer. Meth. Fluids* **69** (11), 1818–1834.

Dudley, J. M., Dias, F., Erkintalo, M. & Genty, G. 2014 Instabilities, breathers and rogue waves in optics. *Nature Photon.* **8** (10), 755–764.

Dysthe, K., Krogstad, H . E. & Müller, P. 2008 Oceanic rogue waves. *Annu. Rev. Fluid Mech.* **40**, 287–310.

Dysthe, K. B. 1979 Note on a modification to the nonlinear Schrödinger equation for application to deep water waves. *Proc. R. Soc. A* **369** (1736), 105–114.

Dysthe, K. B., Trulsen, K., Krogstad, H. E. & Socquet-Juglard, H. 2003 Evolution of a narrow-band spectrum of random surface gravity waves. *J. Fluid Mech.* **478**, 1–10.

Engsig-Karup, A. P., Bingham, H. B. & Lindberg, O. 2009 An efficient flexible-order model for 3D nonlinear water waves. *J. Comp. Phys.* **228** (6), 2100–2118.

Ewans, K. C. 1998 Observations of the directional spectrum of fetch-limited waves. *J. Phys. Oceanogr.* **28** (3), 495–512.

Fadaeiazar, E., Alberello, A., Onorato, M., Leontini, J., Frascoli, F., Waseda, T. & Toffoli, A. 2018 Wave turbulence and intermittency in directional wave fields. *Wave Motion* **83**, 94–101.

Fedele, F. 2014 On certain properties of the compact Zakharov equation. *J. Fluid Mech.* **748**, 692–711.

Fedele, F. 2015 On the kurtosis of deep-water gravity waves. *J. Fluid Mech.* **782**, 25–36.

Fedele, F., Brennan, J., León, S. P. De, Dudley, J. & Dias, F 2016 Real world ocean rogue waves explained without the modulational instability. *Sci Rep* **6**, 27715.

Fenton, J. D. 1985 A fifth-order Stokes theory for steady waves. *J. Waterw. Port Coast. Ocean Eng.* **111** (2), 216–234.

Fitzgerald, C. J., Taylor, P. H., Eatock Taylor, R. E., Grice, J. & Zang, J. 2014 Phase manipulation and the harmonic components of ringing forces on a surface-piercing column. *Proc. R. Soc. A* **470**, 105901.

Forristall, G. Z. 2000 Wave crest distributions: Observations and second-order theory. *J. Phys. Oceanogr.* **30** (8), 1931–1943.

Francius, M. & Kharif, C. 2003 On the disappearance of the lowest-order instability for steep gravity waves in finite depth. *Phys. Fluids* **15** (8), 2445–2448.

Fujimoto, W. & Waseda, T. 2016 The relationship between the shape of freak waves and nonlinear wave interactions. In *ASME 2016 35th International Conference on Ocean, Offshore and Arctic Engineering*. American Society of Mechanical Engineers.

Fujimoto, W., Waseda, T. & Webb, A. 2019 Impact of the four-wave quasi-resonance on freak wave shapes in the ocean. *Ocean Dyn.* **69**, 101–121.

Gandzha, I. S. & Sedletsky, Y. V. 2017 Bright and dark solitons on the surface of finite-depth fluid below the modulation instability threshold. *Phys. Lett. A* **381** (21), 1784–1790.

Gibbs, R. H. & Taylor, P. H. 2005 Formation of walls of water in 'fully' nonlinear simulations. *Appl. Ocean Res.* **27**, 142–157.

Gibson, R. S. & Swan, C. 2007 The evolution of large ocean waves: The role of local and rapid spectral changes. *Proc. R. Soc. A* **463**, 21–48.

Goda, Y. 1985 *Random Seas and Design of Marine Structures*. University of Tokyo Press: Tokyo.

Gramstad, O. & Trulsen, K. 2007 Influence of crest and group length on the occurrence of freak waves. *J. Fluid Mech.* **582**, 463–472.

Hann, M., Greaves, D. & Raby, A. 2014 A new set of focused wave linear combinations to extract nonlinear wave harmonics. In *Twenty-ninth International Workshop on Water Waves and Floating Bodies,* Osaka, Japan, Mar. 30 – Apr. 2, pp. 61–64.

Hara, T. & Mei, C. C. 1991 Frequency downshift in narrowbanded surface waves under the influence of wind. *J. Fluid Mech.* **230**, 429–477.

Hasselmann, K. 1962 On the non-linear energy transfer in a gravity-wave spectrum. Part 1: General theory. *J. Fluid Mech.* **12**, 481–500.

Hasselmann, K. & others 1973 Measurements of wind-wave growth and swell decay during the Joint North Sea Wave Project (JONSWAP). *Deutch Hydrogr. Z.* **A8**, 1–95.

Holthuijsen, L. H. 2007 *Waves in oceanic and coastal waters*. Cambridge University Press: Cambridge, UK.

Houtani, H., Waseda, T. & Tanizawa, K. 2018 Experimental and numerical investigations of temporally and spatially periodic modulated wave trains. *Phys. Fluids* **30**, 034101.

Hwang, P. A., Wang, D. W., Walsh, E. J., Krabill, W. B. & Swift, R. N. 2000 Airborne measurements of the wavenumber spectra of ocean surface waves. Part II: Directional distribution. *J. Phys. Oceanogr.* **30** (11), 2768–2787.

Janssen, P. A. E. M. 1983 On a fourth-order envelope equation for deep-water waves. *J. Fluid Mech.* **126**, 1–11.

Janssen, P. A. E. M. 2003 Nonlinear four-wave interactions and freak waves. *J. Phys. Oceanogr.* **33**, 863–884.

Janssen, P. A. E. M. & Bidlot, J. R. 2009 On the extension of the freak wave warning system and its verification. *ECMWF Tech. Mem.* **588**.

Janssen, P. A. E. M. & Onorato, M. 2007 The intermediate water depth limit of the Zakharov equation and consequences for wave prediction. *J. Phys. Oceanogr.* **37** (10), 2389–2400.

Kharif, C., Giovanangeli, J. P., Touboul, J., Grare, L., & Pelinovsky, E. 2008*a* Influence of wind on extreme wave events: Experimental and numerical approaches. *J. Fluid Mech.* **594**, 209–247.

Kharif, C. & Pelinovsky, E. 2003 Physical mechanisms of the rogue wave phenomenon. *Eur. J. Mech. B/Fluids* **22**, 603–634.

Kharif, C., Pelinovsky, E. & Slunyaev, A. 2008*b* *Rogue waves in the ocean*. Springer Science & Business Media: Berlin/Heidelberg.

Komen, G. J., Cavaleri, L., Donelan, M., Hasselmann, K., Hasselmann, S. & Janssen, P. A. E. M. 1994 *Dynamics and Modelling of Ocean Waves*. Cambridge University Press.

Lake, B. M., Yuen, H. C., Rungaldier, H. & Ferguson, W. E. 1977 Nonlinear deep-water waves: Theory and experiment. Part 2. Evolution of a continuous wave train. *J. Fluid Mech.* **83** (1), 49–74.

Lannes, D. 2013 *The water waves problem: Mathematical analysis and asymptotics (Mathematical Surveys and Monographs)* vol. 188. American Mathematical Society.

Latheef, M., Swan, C. & Spinneken, J. 2017 A laboratory study of nonlinear changes in the directionality of extreme seas. *Proc. R. Soc. A* **473**, 20160290.

Leckler, F., Ardhuin, F., Peureux, C., Benetazzo, A., Bergamasco, F. & Dulov, V. 2015 Analysis and interpretation of frequency-wavenumber spectra of young wind waves. *J. Phys. Oceanogr.* **45** (10), 2484–2496.

Lindgren, G. 1970 Some properties of a normal process near a local maximum. *Ann. Math. Stat* **41** (6), 1870–1883.

Lo, E. & Mei, C. C. 1985 A numerical study of water-wave modulation based on a higher-order nonlinear Schrödinger equation. *J. Fluid Mech.* **150**, 395–416.

Longuet-Higgins, M. S. 1962 Resonant interactions between two trains of gravity waves. *J. Fluid Mech* **12**, 321–332.

Longuet-Higgins, M. S. 1976 On the nonlinear transfer of energy in the peak of a gravity-wave spectrum: A simplified model. *J. Fluid Mech.* **347**, 311–328.

Longuet-Higgins, M. S. 1978 The instabilities of gravity waves of finite amplitude in deep water. II. Subharmonics. *Proc. R. Soc. A* **360**, 489–505.

Ma, Y., Dong, G., Perlin, M., Ma, X., Wang, G. & Xu, J. 2010 Laboratory observations of wave evolution, modulation and blocking due to spatially varying opposing currents. *J. Fluid Mech.* **661**, 108–129.

Madsen, P. A. & Fuhrman, D. R. 2012 Third-order theory for multi-directional irregular waves. *J. Fluid Mech.* **698**, 304–334.

Martin, D. U. & Yuen, H. C. 1980 Quasi-recurring energy leakage in the two-space-dimensional nonlinear Schrödinger equation. *Phys. Fluids* **23**, 881–883.

McLean, J. W. 1982*a* Instabilities of finite-amplitude gravity waves on water of finite depth. *J. Fluid Mech.* **114**, 331–341.

McLean, J. W. 1982*b* Instabilities of finite-amplitude water waves. *J. Fluid Mech.* **114**, 315–330.

Melville, W. K. 1982 The instability and breaking of deep-water waves. *J. Fluid Mech.* **115**, 165–185.

Meylan, M. H., Bennetts, L. G., Mosig, J. E. M., Rogers, W. E., Doble, M. J. & Peter, M. A. 2018 Dispersion relations, power laws, and energy loss for waves in the marginal ice zone. *J. Geophys. Res. Oceans* **123** (5), 3322–3335.

Mori, N. & Janssen, P. A. E. M. 2006 On kurtosis and occurrence probability of freak waves. *J. Phys. Oceanogr.* **36** (7), 1471–1483.

Mori, N., Onorato, M. & Janssen, P. A. E. M. 2011 On the estimation of the kurtosis in directional sea states for freak wave forecasting. *J. Phys. Oceanogr.* **41**, 1484–1497.

Onorato, M., Cavaleri, L., Fouques, S., Gramstad, O., Janssen, P. A. E. M., Monbaliu, J., Osborne, A. R., Packozdi, C., Serio, M., Stansberg, C. T. & Toffoli, A. 2009 Statistical properties of mechanically generated surface gravity waves: A laboratory experiment in a three-dimensional wave basin. *J. Fluid Mech.* **627**, 235–257.

Onorato, M., Osborne, A. R., Serio, M. & Bertone, S. 2001 Freak waves in random oceanic sea states. *Phys. Rev. Lett* **86** (25), 5831.

Onorato, M., Osborne, A. R., Serio, M., Resio, D., Pushkarev, A., Zakharov, V. E. & Brandini, C. 2002 Freely decaying weak turbulence for sea surface gravity waves. *Phys. Rev. Lett* **89** (14), 144501.

Onorato, M., Residori, S., Bortolozzo, U., Montina, A. & Arecchi, F. T. 2013 Rogue waves and their generating mechanisms in different physical contexts. *Phys. Rep.* **528** (2), 47–89.

Onorato, M. & Suret, P. 2016 Twenty years of progresses in oceanic rogue waves: The role played by weakly nonlinear models. *Natural Hazards* **84** (2), 541–548.

Osborne, A. 2010 *Nonlinear Ocean Waves and the Inverse Scattering Transform*. Academic Press: New York.

Paulsen, B. T., Bredmose, H., Bingham, H. B. & Jacobsen, N. G. 2014 Forcing of a bottom-mounted circular cylinder by steep regular water waves at finite depth. *J. Fluid Mech.* **755**, 1–34.

Perlin, M., Choi, W. & Tian, Z. 2013 Breaking waves in deep and intermediate waters. *Annu. Rev. Fluid Mech.* **45**, 115–145.

Peureux, C., Benetazzo, A. & Ardhuin, F. 2018 Note on the directional properties of meter-scale gravity waves. *Ocean Sci.* **14** (1), 41–52.

Phillips, O. M. 1960 On the dynamics of unsteady gravity waves of finite amplitude. Part 1. The elementary interactions. *J. Fluid Mech.* **9** (2), 193–217.

Pinar, Z., Rezazadeh, H. & Eslami, M. 2020 Generalized logistic equation method for kerr law and dual power law Schrödinger equations. *Opt. Quant. Electron.* **52** (504), 1–16.

Rapizo, H., Waseda, T., Babanin, A. V. & Toffoli, A. 2016 Laboratory experiments on the effects of a variable current field on the spectral geometry of water waves. *J. Phys. Oceanogr.* **46** (9), 2695–2717.

Sedletsky, Y. V. 2003 The fourth-order nonlinear Schrödinger equation for the envelope of Stokes waves on the surface of a finite-depth fluid. *J. Exp. Theor. Phys.* **97** (1), 180–193.

Segur, H., Henderson, D., Carter, J., Hammack, J., Li, C., Pheiff, D. & Socha, K. 2005 Stabilizing the Benjamin–Feir instability. *J. Fluid Mech.* **539**, 229–271.

Serio, M., Onorato, M., Osborne, A. R. & Janssen, P. A. E. M. 2005 On the computation of the Benjamin-Feir index. *Nuovo Cimento* **28** (6), 893–903.

Sharma, J. N. & Dean, R. G. 1981 Second-order directional seas and associated wave forces. *Soc. Pet. Eng. J.* **21**, 129–140.

Shemer, L., Sergeeva, A. & Liberzon, D. 2010 Effect of the initial spectrum on the spatial evolution of statistics of unidirectional nonlinear random waves. *J. Geophys. Res. Oceans* **115**, C12039.

Simanesew, A., Krogstad, H. E., Trulsen, K. & Nieto Borge, J. C. 2016 Development of frequency-dependent ocean wave directional distributions. *Appl. Ocean Res.* **59**, 304–312.

Simanesew, A., Krogstad, H. E., Trulsen, K. & Nieto Borge, J. C. 2018 Bimodality of directional distributions in ocean wave spectra: A comparison of data-adaptive estimation techniques. *J. Atmos. Ocean Tech.* **35** (2), 365–384.

Slunyaev, A. & Kokorina, A. 2019 The method of spectral decomposition into free and bound wave components. Numerical simulations of the 3D sea wave states. In *Geophysical Research Abstracts,* EGU General Assembly, Vienna, Austria, Apr. 7–12. EGU2019-546.

Slunyaev, A. V. 2005 A high-order nonlinear envelope equation for gravity waves in finite-depth water. *J. Exp. Theor. Phys.* **101** (5), 926–941.

Socquet-Juglard, H., Dysthe, K., Trulsen, K., Krogstad, H. E. & Liu, J. 2005 Probability distributions of surface gravity waves during spectral changes. *J. Fluid Mech.* **542**, 195–216.

Steer, J. N., Borthwick, A. G. L, Onorato, M., Chabchoub, A. & van den Bremer, T. S. 2019 Hydrodynamic X waves. *Phys. Rev. Lett* **123** (18), 184501.

Stiassnie, M. 1984 Note on the modified nonlinear Schrödinger equation for deep water waves. *Wave Motion* **6**, 431–433.

Stiassnie, M. 2001 Nonlinear interactions of inhomogenous random water waves. In *ECMWF report of the Workshop on Ocean Waves Forecasting,* European Centre for Medium-Range Weather Forecasts, Reading, UK, pp.39–52.

Stiassnie, M. 2017 On the strength of the weakly nonlinear theory for surface gravity waves. *J. Fluid Mech.* **810**, 1–4.

Stiassnie, M & Shemer, L. 2005 On the interaction of four water-waves. *Wave Motion* **41**, 307–328.

Stuhlmeier, R. & Stiassnie, M. 2017 Evolution of statistically inhomogenous degenerate water wave quartets. *Proc. R. Soc. A* **376**, 20170101.

Su, M. Y., Bergin, M., Marler, P. & Myrick, R. 1982 Experiments on nonlinear instabilities and evolution of steep gravity-wave trains. *J. Fluid Mech.* **124**, 45–72.

Toffoli, A., Bennetts, L. G., Meylan, M. H., Cavaliere, C., Alberello, A., Elsnab, J. & Monty, J. P. 2015 Sea ice floes dissipate the energy of steep ocean waves. *Geophys. Res.* **42** (20), 8547–8554.

Toffoli, A., Benoit, M., Onorato, M. & Bitner-Gregersen, E. M. 2009 The effect of third-order nonlinearity on statistical properties of random directional waves in finite depth. *Nonlinear Proc. Geoph.* **16** (1), 131.

Toffoli, A., Gramstad, O., Trulsen, K., Monbaliu, J., Bitner-Gregersen, E. & Onorato, M. 2010*a* Evolution of weakly nonlinear random directional waves: laboratory experiments and numerical simulations. *J. Fluid Mech.* **664**, 313–336.

Toffoli, A., Onorato, M., Bitner-Gregersen, E. M. & Monbaliu, J. 2010*b* Development of a bimodal structure in ocean wave spectra. *J. Geophys. Res. Oceans* **115**, C03006.

Tromans, P. S., Anaturk, A. & Hagemeijer, P. 1991 A new model for the kinematics of large ocean waves—application as a design wave. In *Proceedings of the First International Offshore and Polar Engineering Conference (ISOPE),* Edinburgh, UK, Aug. 11–16. ISOPE-I-91-154.

Trulsen, K. 2018 Rogue waves in the ocean, the role of modulational instability, and abrupt changes of environmental conditions that can provoke non equilibrium wave dynamics. In *The Ocean in Motion*, pp. 239–247. Springer: Zug, CH.

Trulsen, K. & Dysthe, K. B. 1990 Frequency down-shift through self modulation and breaking. In *Water wave kinematics*, pp. 561–572. Springer: Zug, CH.

Trulsen, K. & Dysthe, K. B. 1996 A modified nonlinear Schrödinger equation for broader bandwidth gravity waves on deep water. *Wave Motion* **24** (3), 281–289.

Trulsen, K. & Dysthe, K. B. 1997 Frequency downshift in three-dimensional wave trains in a deep basin. *J. Fluid Mech.* **352**, 359–373.

Trulsen, K., Kliakhandler, I., Dysthe, K. B. & Velarde, M. G. 2000 On weakly nonlinear modulation of waves on deep water. *Phys. Fluids* **12** (10), 2432–2437.

Tulin, M. P. & Waseda, T. 1999 Laboratory observations of wave group evolution, including breaking effects. *J. Fluid Mech.* **378**, 197–232.

Viotti, C. & Dias, F. 2014 Extreme waves induced by strong depth transitions: Fully nonlinear results. *Phys. Fluids* **26** (5), 051705.

Walker, D. A. G., Taylor, P. H. & Eatock Taylor, R. 2004 The shape of large surface waves on the open sea and the Draupner new year wave. *Appl. Ocean Res.* **26** (3-4), 73–83.

Waseda, T., Kinoshita, T., Cavaleri, L. & Toffoli, A. 2015 Third-order resonant wave interactions under the influence of background current fields. *J. Fluid Mech.* **784**, 51–73.

Waseda, T., Toba, Y. & Tulin, M. P. 2001 Adjustment of wind waves to sudden changes of wind speed. *J. Oceanogr.* **57**, 519–533.

Waseda, T., Watanabe, S., Fujimoto, W., Nose, T., Kodaira, T. & Chabchoub, A. 2021 Directional coherent wave group from an assimilated nonlinear wavefield. *Front. Phys.* **9**, 127.

Whitham, G. B. 1967 Non-linear dispersion of water waves. *J. Fluid Mech.* **27** (2), 399–412.

Whitham, G. B. 1974 *Linear and Nonlinear Waves*. John Wiley and Sons: New York.

Xiao, W., Liu, Y., Wu, G. & Yue, D. K. P. 2013 Rogue wave occurrence and dynamics by direct simulations of nonlinear wave-field evolution. *J. Fluid Mech.* **720**, 357–392.

Young, I. R., Verhagen, L. A. & Banner, M. L. 1995 A note on the bimodal directional spreading of fetch-limited wind waves. *J. Geophys. Res. Oceans* **100**, 773–778.

Yuen, H. C. & Lake, B. M. 1980 Instabilities of waves on deep water. *Ann. Rev. Fluid Mech.* **12**, 303–334.

Zakharov, V. E. 1968 Stability of periodic waves of finite amplitude on the surface of a deep fluid. *J. Appl. Mech. Tech. Phys.* **9**, 190–194.

Zakharov, V. E. & Shabat, A. B. 1972 Exact theory of two-dimensional self-focusing and one-dimensional self-modulation of waves in nonlinear media. *Soviet Physics JETP* **34** (1), 62–69.